Computational multiscale modeling of fracture problems and its model order reduction

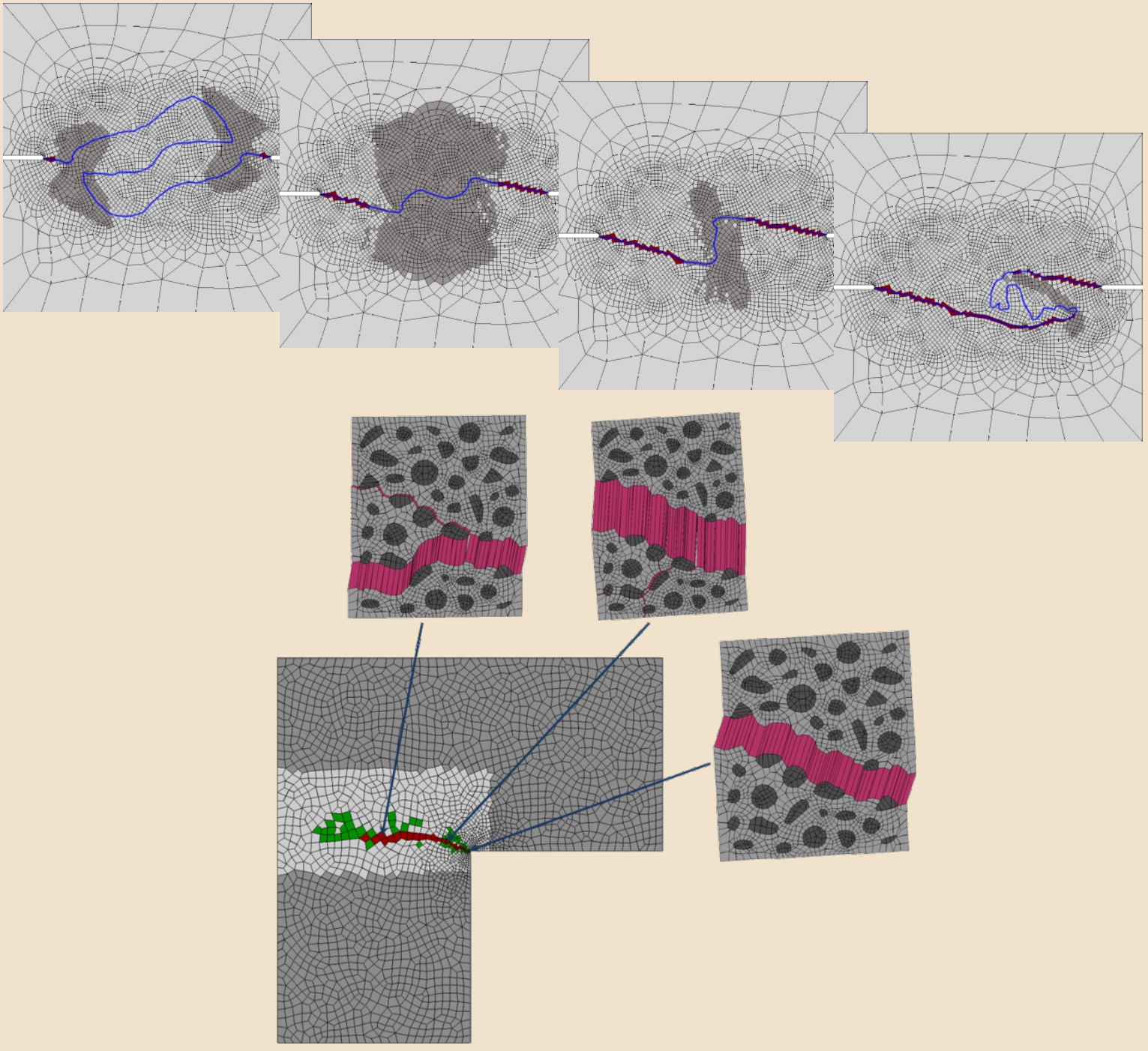

PhD. Thesis by:

Manuel Alejandro Caicedo Silva

UNIVERSITAT POLITÈCNICA
DE CATALUNYA
BARCELONATECH

Computational multiscale modeling of fracture problems and its model order reduction

by

Manuel Alejandro Caicedo Silva

Universitat Politècnica de Catalunya
Escola Tècnica Superior d'Enginyers
de Camins, Canals i Ports

DEPARTAMENT D'ENGINYERIA CIVIL I AMBIENTAL (DECA)

INTERNATIONAL CENTER FOR NUMERICAL METHODS IN ENGINEERING

PhD Thesis:

COMPUTATIONAL MULTISCALE MODELING OF FRACTURE PROBLEMS AND ITS MODEL ORDER REDUCTION

By

Manuel Alejandro Caicedo Silva

Advisors:

Prof. Xavier Oliver

Dr. Alfredo E. Huespe

Barcelona, January 2017

UNIVERSITAT POLITÈCNICA DE CATALUNYA
BARCELONATECH
Escola de Doctorat

Curso académico: 2016-2017

Acta de calificación de tesis doctoral

Nombre y apellidos
MANUEL ALEJANDRO CAICEDO SILVA

Programa de doctorado
ANALISIS ESTRUCTURAL

Unidad estructural responsable del programa
DEPARTAMENT D'ENYINYERIA CIVIL I AMBIENTAL (DECA)

Resolución del Tribunal

Reunido el Tribunal designado a tal efecto, el doctorando / la doctoranda expone el tema de su tesis doctoral titulada COMPUTATIONAL MULTISCALE MODELING OF FRACTURE PROBLEMS AND ITS MODEL ORDER REDUCTION.

Acabada la lectura y después de dar respuesta a las cuestiones formuladas por los miembros titulares del tribunal, éste otorga la calificación:

☐ NO APTO ☐ APROBADO ☐ NOTABLE ☐ SOBRESALIENTE

(Nombre, apellidos y firma) Presidente/a		(Nombre, apellidos y firma) Secretario/a
(Nombre, apellidos y firma) Vocal	(Nombre, apellidos y firma) Vocal	(Nombre, apellidos y firma) Vocal

BARCELONA, _____ de _____ de 2017

El resultado del escrutinio de los votos emitidos por los miembros titulares del tribunal, efectuado por la Comisión Permanente de la Escuela de Doctorado, otorga la MENCIÓN CUM LAUDE:

☐ SÍ ☐ NO

(Nombre, apellidos y firma) Presidente/a de la Comisión Permanente de la Escuela de Doctorado	(Nombre, apellidos y firma) Secretario/a de la Comisión Permanente de la Escuela de Doctorado

BARCELONA, _____ de _____ de 2017

RESUMEN

Esta Tesis se enfoca en el modelamiento numérico de la fractura y su propagación en materiales heterogéneos sujetos a degradación, mediante modelos multiescala jerárquicos basados en la técnica FE^2, abordando a su vez la problemática del coste computacional excesivo mediante el desarrollo, la implementación y validación de un conjunto de herramientas computacionales basadas en técnicas de modelos reducidos.

Para la modelización de problemas de fractura, se desarrolló, implementó y validó, un modelo multiescala de fallo con las siguientes características:

- En la macroescala, se adaptaron los últimos avances de la *Aproximación de Discontinuidades Fuertes del Continuo (CSDA)*, hasta el momento desarrollados para modelos monoescala. Se formula un nuevo elemento finito con alta capacidad de capturar y modelar localización de deformaciones en bandas que pueden interceptar al elemento finito en direcciones arbitrarias. Para evaluar la dirección de propagación de falla se utiliza la técnica del *crack-path field* (Oliver et al., 2014).
- En la microescala, en aras de usar mecanismos de fallo que sean simples de implementar y calcular, y de cara al posterior desarrollo de una formulación de modelos reducidos, se propone el uso de elementos cohesivos tipo banda, equipados con un modelo constitutivo de daño isótropo regularizado, capaz de representar la decohesión del material. Estos elementos cohesivos son distribuidos entre los diferentes componentes de la microestructura, y en sus fronteras, cumpliendo a su vez el papel de elementos de interfase.

Se verificó la objetividad de los resultados del modelo con respecto al tamaño de la *celda de fallo*, y al tamaño del elemento finito de la macroestructura. De igual forma, también se verificó la consistencia del modelo multiescala por medio de la comparación de resultados obtenidos con el mismo, y soluciones obtenidas mediante *Simulaciones Numéricas Directas (DNS)*.

En cuanto a la reducción del coste computacional en los modelos multiescala jerárquicos del tipo FE^2. Se propone reformular el problema de valores de contorno de la microescala, mediante el uso de dos técnicas sucesivas de reducción, definidas como *Modelo de Orden Reducido MOR* y *Modelo de Orden Hiper-reducido (HROM ó HPROM)*, respectivamente.

En primer lugar, para el Modelo de Orden Reducido, el problema de elementos finitos estándar (*de alta fidelidad*) de la microestructura, es proyectado y resuelto

en un subespacio de menor dimensión mediante el método de la *Descomposición Ortogonal Propia (POD)*. En segundo lugar, para el desarrollo del Modelo de Orden Hiper-reducido, dos técnicas han sido estudiadas y desarrolladas, a saber: los métodos de *interpolación* y los métodos de *Cuadratura de Orden Reducido ROQ* (An et al., 2009). Las bases reducidas para la proyección de las *variables primales*, son calculadas por medio de la *Descomposición en Valores Singulares SVD* de *snapshots* captados de trayectorias de *entrenamiento* previamente definidas.

Para modelar problemas de materiales heterogéneos caracterizados por relaciones constitutivas que poseen endurecimiento material, las fluctuaciones de desplazamiento y las tensiones de la microestructura fueron seleccionadas como variables primales para la primera y segunda reducción, respectivamente. En este caso, la segunda reducción se realizó por medio de la interpolación del campo de tensiones. Sin embargo, se puede observar que el operador de proyección de las tensiones, al ser calculado a partir de la selección de *snapshots* de pasos numéricamente convergidos, produce un malcondicionamiento del problema. Este malcondicionamiento es estudiado en profundidad y es corregido para dar lugar a una solución robusta y consistente.

Para la reducción en modelos de fractura, se propuso como punto de partida la formulación multiescala de fallo desarrollada en esta Tesis. Al igual que en la modelización de problemas de materiales que poseen endurecimiento material, se preserva el esquema de dos reducciones sucesivas.

Teniendo en cuenta el caracter discontinuo de las deformaciones en la microescala en problemas de fractura. Se propone la descomposición de la celda de fallo en dos partes, un dominio *cohesivo* que contiene la totalidad de bandas cohesivas, y un dominio *regular* compuesto por el dominio disjunto remanente de la microcelda. Cada uno de estos dominios tiene un tratamiento individual. El modelo de la microescala, es reformulado como un problema de *punto de silla* en el cual se busca minimizar el potencial de energía libre, sujeto a restricciones para que cumpla los postulados básicos de la modelización multiescala.

En una primera reducción, se propone como variable primal el campo de deformaciones fluctuantes, que por medio del método de la *Descomposición Ortogonal Propia (POD)*, se proyecta y resuelve el problema en un espacio de dimensión reducida. La segunda reducción se basa en integrar los términos que resultan del problema variacional de equilibrio mediante una *Cuadratura de Orden Reducido (ROQ)*, conformada por un conjunto de puntos de integración, considerablemente inferior con respecto a la cantidad de puntos de integración requeridos por la cuadratura de Gauss convencional en el modelo de *alta fidelidad*.

Esta metodología de hiperreducción mediante cuadraturas de orden reducido (ROQ), provó ser considerablemente mas eficiente y robusta que los métodos de interpolación, siendo además, aplicable a problemas multiescala con endurec-

imiento.

Para la validar los modelos reducidos desarrollados en esta Tesis, se realizaron múltiples pruebas variando la cantidad de bases para ambas reducciones, observando la convergencia del modelo reducido con respecto a la respuesta del modelo de alta fidelidad, incrementando la cantidad de modos y puntos de integración. Igualmente se puede concluir que, para errores admisibles (inferiores al 5%), las aceleraciones del costo computacional involucrado respecto al tiempo requerido por el modelo de alta fidelidad (speed-up) son del orden de 110 veces. Lo que constituye aceleraciones considerablemente superiores a lo reportado por la literatura.

ABSTRACT

This Thesis focuses on the numerical modeling of fracture and its propagation in heterogeneous materials by means of hierarchical multiscale models based on the FE^2 method, addressing at the same time, the problem of the excessive computational cost through the development, implementation and validation of a set of computational tools based on reduced order modeling techniques.

For fracture problems, a novel multiscale model for propagating fracture has been developed, implemented and validated. This multiscale model is characterized by the following features:

- At the macroscale level, were adapted the last advances of the *Continuum Strong Discontinuity Approach (CSDA)*, developed for monoscale models, devising a new finite element exhibiting good ability to capture and model strain localization in bands which can be intersect the finite element in random directions; for failure propagation purposes, the adapted *Crack-path field* technique (Oliver et al., 2014), was used.
- At the microscale level, for the sake of simplicity, and thinking on the development of the reduced order model, the use of cohesive-band elements, endowed with a regularized isotropic continuum damage model aiming at representing the material decohesion, is proposed. These cohesive-band elements are distributed within the microscale components, and their boundaries.

The objectivity of the solution with respect to the *failure cell* size at the microscale, and the finite element size at the macroscale, was checked. In the same way, its consistency with respect to *Direct Numerical Simulations (DNS)*, was also tested and verified.

For model order reduction purposes, the microscale *Boundary Value Problem (VBP)*, is rephrased using *Model Order Reduction* techniques. The use of two subsequent reduction techniques, known as: *Reduced Order Model (ROM)* and *HyPer Reduced Order Model (HPROM or HROM)*, respectively, is proposed.

First, the standard microscale finite element model *High Fidelity (HF)*, is projected and solved in a low-dimensional space via *Proper Orthogonal Decomposition (POD)*. Second, two techniques have been developed and studied for multiscale models, namely: a) *interpolation* methods, and b) *Reduced Order Cubature (ROQ)* methods (An et al., 2009). The reduced bases for the projection of the *primal variables*, are computed by means of a judiciously training, defining a set of pre-defined

training trajectories.

For modeling materials exhibiting hardening behavior, the microscale displacement fluctuations and stresses have been taken as *primal variables* for the first and second reductions, respectively. In this case, the second reduction was carried out by means of the stress field interpolation. However, it can be shown that the stress projection operator, being computed with numerically converged snapshots, leads to an ill-possed microscale reduced order model. This ill-poseddness is deeply studied and corrected, yielding a robust and consistent solution.

For the model order reduction in fracture problems, the developed multiscale formulation in this Thesis was proposed as point of departure. As in hardening problems, the use of two successive reduced order techniques was preserved.

Taking into account the discontinuous pattern of the strain field in problems exhibiting softening behavior. A domain separation strategy, is proposed. A *cohesive* domain, which contains the cohesive elements, and the *regular* domain, composed by the remaining set of finite elements. Each domain has an individual treatment. The microscale Boundary Value Problem (BVP) is rephrased as a *saddle-point* problem which minimizes the potential of free-energy, subjected to constraints fulfilling the basic hypotheses of multiscale models.

The strain flucuations are proposed as the primal variable for the first reduction, where the high fidelity model is projected and solved into a low-dimensional space via *POD*. The second reduction is based on integrating the equilibrium equations by means of a *Reduced Order Quadrature (ROQ)*, conformed by a set of integration points considerably smaller than the classical Gauss quadrature used in the *high fidelity* model.

This methodology had been proven to be more robust and efficient than the interpolation methods, being applicable not only for softening problems, but also for hardening problems.

For the validation of the reduced order models, multiple test have been performed, changing the size of the set of reduced basis functions for both reductions, showing that convergence to the high fidelity model is achieved when the size of reduced basis functions and the set of integration points, are increased. In the same way, it can be concluded that, for admissible errors (lower than 5%), the reduced order model is $\sim$ 110 times faster than the high fidelity model, considerably higher than the speedups reported by the literature.

CONTENTS

ACRONYMS

BVP	Boundary Value Problem
CSDA	Continuum Strong Discontinuity Approach
DNS	Direct Numerical Simulation
EFEM	Embedded Finite Element Methodology
EIM	Empirical Interpolation Method
FE	Finite Element method
FE^2	FE$\times$FE hierarchical multiscale technique
HF	High Fidelity
HPROM	High-Performance Reduced Order Model
HROM	Hyper-Reduced Order Model
MOR	Model Order Reduction
POD	Proper Orthogonal Decomposition
ROM	Reduced Order Model
ROQ	Reduced Optimal Quadrature
RUC	Repeating Unit Cell
RVE	Representative Volume Element
SVD	Singular Value Decomposition

Part I

RESEARCH SUMMARY

1

INTRODUCTION

1.1 State of the Art

1.1.1 *Multiscale modeling of heterogeneous materials*

During the last decades, a large variety of multiscale strategies focusing on the study and analysis of the mechanical behavior of heterogeneous materials, have been proposed by the computational mechanics community. Based on the work of (Böhm, 2013), these strategies may be divided into three main groups:

- *Mean-Field approaches*: based on the seminal contributions developed by (Eshelby, 1957) and (Mori and Tanaka, 1973). In these approaches, the microfields within each constituent of an heterogeneous material, are approximated by their phase averages, typically, *phase-wise* uniform stress and strain fields are employed. Recently, the application of these approaches to nonlinear modeling in composites has become a subject of active research.

- *Bounding Methods:* Variational principles are used to obtain upper and lower bounds of the overall mechanical properties (e. g. elastic tensors, secant moduli, yield thresholds, among others). Bounding Methods are closely related with Mean-Field approaches, because many analytical bounds are obtained on the basis of phase-wise constant fields.

  The formal treatments were provided by, i. e., (Nemat-Nasser and Hori, 1999; Bornert, 1999; Ponte Castañeda and Suquet, 1998; Markov, 2000; Milton, 2002; Torquato, 2002). Two of the most relevant results of this kind of models are, the *upper bounds* of (Voigt, 1889), and the *lower bounds* of (Reuss, 1929). Posteriorly, Hill extends those bounds to tensorial entities, particularly, for constitutive tangent tensors (Hill, 1952).

- *Representative Volume Element (RVE) based approaches:* these approximations are based on studying discrete microstructures, aiming at evaluating the microscale fields, fully accounting for the interactions between different phases. *Homogenization* is used as a strategy to upscale the resulting averaged variables. This homogenization strategy uses *representative volumes*, which copy as much as possible the material heterogeneities. These representative volume elements must be large enough to capture a statistically

representative solution of the material behavior, but, also their size must be limited in comparison with the macroscopic characteristic length - (separation of scales).

The hypothesis of these approaches are properly fulfilled if there is a marked scale separation between those phenomena observed at the macroscale, and the ones observed at the microscale. However, nowadays, new approaches have been proposed which overcome this limitation.

Models based on the existence of a RVE can be divided into two main groups:

- *Hierarchical models:* The RVE, subjected to consistent boundary conditions[1] is used to obtain a detailed microscale response. The link between scales is reached by means of an energetic identity, such as the Hill-Mandel Principle of Macro-Homogeneity (Hill, 1965; Mandel, 1971), or even on more general approaches, like the Principle of Multiscale Virtual Power (Blanco et al., 2016). In the context of the Finite Element Method this methodology is known as FE×FE hierarchical multiscale technique (FE^2) (Feyel and Chaboche, 2000).

  In virtue of the potential applications in microstructures with complex morphologies, the FE^2 technique is suitable to deal with problems facing material instabilities, like fracture processes. In this sense, some approaches have been proposed (Belytschko et al., 2008; Song and Belytschko, 2009; Nguyen et al., 2010a,b; Matous et al., 2008; Coenen et al., 2012; Toro et al., 2014), among others. One of the main contributions of this Thesis, is an alternative approach with marked differences with respect to the previous ones.

- *Concurrent models:* the RVE is embedded into the macroscale geometry, and the corresponding kinematic compatibility is guaranteed via Lagrange multipliers, similar to Domain Decomposition approaches.

  As the above mentioned models, concurrent models are widely applied. In approaches based on the finite element method, the embedded meshes are not necessarily compatible. However, its computational viability is only for cases with small scale separation, this feature becomes into its main disadvantage. Some concurrent approaches in the field of fracture mechanics have been recently developed, i. e., (Lloberas-Valls et al., 2012).

1.1.2 *Fracture mechanics*

1.1.2.1 *Monoscale Fracture Approaches*

The study and analysis of fracture in solids is a topic of research since the last centuries. The seminal works on this topic were focussed on the Elastic Fracture

1 Consistent in the sense that, all possible boundary conditions have to be compatible with the strains obtained at the macroscale.

Mechanics. However, its generalization to nonlinear material behavior is a non trivial task.

Departing from the concept of fracture energy, which has become a central issue in non-linear fracture mechanics modeling, several techniques have been developed:

- *Cohesive models:* are based on the introduction of interfaces embedded into a continuum medium. These interfaces admit the development of displacements discontinuities. Cohesive forces across the interfaces act opposing to the crack opening, and diminishing as material degradation takes place. The energy consumed to produce a crack is equal to the fracture energy. Some applications of this kind of models are found in (Pandolfi et al., 1999; Molinari et al., 2007; Toro et al., 2016; Rodrigues et al., 2016).

- *Continuum regularized models:* Characterized by a continuum constitutive law displaying a softening response. These kind of approaches are subjected to material instabilities and bifurcation processes, causing ill-possedness of the problem from the mathematical point of view. As a remedy to this flaw, it is introduced a constitutive law regularization (localization limiters), ensuring mesh objective solutions. Some proposed models can be found in (Pijaudier-Cabot and Bazant, 1987; Tvergaard and Needleman, 1995; Pijaudier-Cabot and Bazant, 1987; Aifantis, 1984; de Borst and Mühlhaus, 1992; Peerlings et al., 1996, 2001, 2002; Steinmmann and Willam, 1991; Muhlhaus and Vardoulakis, 1987), among others.

- *Continuum Strong Discontinuity Approach (CSDA):* This approach establishes a link between *cohesive models* and *continuum models*. Its fundamentals have been presented in the seminal work (Simo et al., 1993), and posteriorly, improved and applied to many applications, in static and dynamic scenarios (Oliver, 2000; Oliver et al., 2002; Oliver and Huespe, 2004b,a; Oliver et al., 2014). This approach provides an unified theory, which goes from the continuum description to the degradation and posterior material failure exhibiting displacement discontinuities (cracks). In this context, the continuum constitutive model subjected to a kinematics inducing displacement discontinuities represents also a "projected" cohesive law on the crack surface.

1.1.2.2 *Multiscale Fracture Approaches*

The study of heterogeneous materials subjected to softening, and, therefore, to degradation and failure, through multiscale approaches brings additional challenges. The fundamental reason lies in two aspects: (a) it becomes imperative the use of regularized constitutive theory at both scales in order to ensure the well-possednes of the multiscale problem. (b) *The size effect*, intrinsically related to the fracture energy, which has been extensively studied by (Bazant and Planas, 1998). As a result of this, the homogenized stress tensor, in the post-citrical

regime, becomes extremely sensible to the RVE size.

The second issue is the existence of the representative volume element (Gitman et al., 2007), and the fulfillment of the basic hypothesis in multiscale modeling.

The necessity to develop specific homogenization techniques, becomes a starting point for obtaining consistent multiscale formulations. (Belytschko et al., 2008) has proposed a methodology that excludes the localization domain in the homogenization process. More recently, (Song and Belytschko, 2009) proposed a predetermined size of representative volume elements. (Matous et al., 2008) describe a novel methodology, based on the existence of a macroscopic adhesive interface, which links the macroscale jump of displacements with an equivalent jump at the microscale, imposed by consistent boundary conditions.

Recent works (Nguyen et al., 2010a,b), describe the material failure by means of non-local gradient theories. In this kind of approaches, and, in contrast with other alternatives, the homogenization of the stress field during the post-critical regime, is carried out at the localization zone (this zone corresponds to a subdomain of the RVE). However, other authors claimed some inconsitencies related to this kind of approaches, particularly, about the fact that kinematics at the macroscale is not equivalent with the one modeled at the microscale.

1.1.3 *Model Order Reduction*

In general, the FE^2 method involving fine space-time discretization and time-dependent homogenization procedures, involves an enormous computational cost, being even larger when facing fracture mechanics problems.

The idea of exploiting the combination of dimensionality reduction and multiscale modeling is certainly not new. A survey of the related literature reveals that, over the last decade, researchers from various scientific disciplines dealing with multiscale problems have begun to consider the model reduction as a potential route – complementary to improvements in software and hardware power – to diminish the often unaffordable cost of multiscale simulations. In the specific context of homogenization-based multiscale methods, the application of model reduction techniques has been addressed by several authors, namely, (Ganapathysubramanian and Zabaras, 2004; Yvonnet and He, 2007; Boyaval, 2007; Monteiro et al., 2008; Nguyen, 2008). The strategy adopted in all these works for constructing a cost efficient model of the micro-cell is the standard reduced basis method, whose gist is to project the governing equations onto a low-order subspace spanned by carefully chosen bases (Amsallem et al., 2009).

1.1.3.1 *Reduced basis techniques (ROM)*

Reduced basis methods, in its standard form, suffer from an important limitation when handling non-linear problems: they reduce notably the number of degrees

of freedom –and thus the pertinent equation solving effort–, yet the computational cost associated to the evaluation of the internal forces and jacobians at quadrature points remains the same. Standard reduction methods only prove, thus, effective in dealing with micro-cells whose constituents obey simple constitutive laws (linear elasticity). In a general inelastic case, the calculation of the stresses at each gauss point is, on its own, a computationally expensive operation and dominates the total cost of the computation. As a consequence, the speed up provided by standard model reduction methods in non-linear scenarios is practically negligible, and may not compensate for the cost associated to the offline construction of the reduced-order bases.

1.1.3.2 *High-performance reduced order modeling techniques (HPROM)*

The origin of the first effective proposal on this issue can be traced back to the seminal work of (Barrault et al., 2004), who suggested to approximate the nonlinear term in the reduced-order equations by a linear combination of a few, carefully chosen basis functions. In the spirit of a offline/online strategy, in the standard reduced basis approach, these spatial bases are computed offline from full-order snapshots of the non-linear term, whereas the corresponding parameter-dependent modal coefficients are determined online by interpolation at a few (as many as basis functions), judiciously pre-selected spatial points. As in classical reduced bases methods, the efficiency of this second or collateral reduction is predicated on the existence of a moderate number $M \ll N$ (N is the original dimension of the problem) of basis functions whose span accurately approximate the manifold induced by the parametric dependence of the nonlinear contribution. The interpolation method developed by (Barrault et al., 2004) is known as the Empirical Interpolation Method (EIM); the main ingredients of this method are: a) the use of a greedy algorithm to generate a set of maximally independent bases from the collection of snapshots of the nonlinear term, on the one hand; and b) the recursive selection – also via a greedy algorithm – of spatial locations where the error between the full-order bases and their reconstructed counterparts is maximum[2].

Solution methods in which the governing equations are used in its variational form (as in the Finite Element method (FE)), reduction of the computational complexity arising from nonlinearities can be, alternatively, achieved by approximating the integrals in which the offending nonlinear function appears, rather than the function itself, as done in the interpolatory and least-square reconstruction techniques discussed above. Based on this observation, (An et al., 2009) propose a quadrature scheme devised for fast-run integration of the subspace spanned by a representative set of snapshots of the nonlinear integrand.

2 Maximum in the sense that, the selected points have to be taken from components in which the error between the high fidelity and the High-Performance Reduced Order Model (HPROM) solutions is greater.

In what follows, we shall use as equivalent the appellations *HPROM* and *Hyper-Reduced Order Model (HROM)* to refer to reduced basis methods combined with interpolatory or least-square reconstruction schemes.

1.1.3.3 *Reduction Order Modeling in fracture problems*

The development of reduced models for non-homogeneous materials has been tackled in numerous previous contributions, such as (Michel et al., 2001), where the proposed reduction techniques are based on Fourier's transforms, or (Yvonnet and He, 2007), where a reduced model is applied the homogenization analysis of hyperelastic solids subjected to finite strains. Also, the work in (Ryckelynck, 2009) develops a hyper-reduced model of a monoscale analysis considering non-linear material behavior. However, the existing literature barely considers reduced order modeling of non-smooth problems, as is the case of fracture, where discontinuous displacements occur. The multiscale case, when fracture takes place at both scales of the problem, makes the task even much heavier. Indeed, only very few contributions have been presented in the literature about this topic, see for example: (Oskay and Fish, 2007), which follows an eigendeformation-based methodology, or (Zhang and Oskay, 2016; Kerfriden et al., 2013) that resort to global–local approaches.

The previous approaches combine projection techniques and, in some cases, empirical criteria to integrate the equilibrium equations in the domain. However, these techniques are usually derived in an ad-hoc manner, and applied to problems with relatively simple crack propagation schemes. Currently, some researchers consider the effective model order reduction of fracture processes, an insolvable problem. This Thesis will reconsider this statements, by developing a robust HPROM formulation, for multiscale fracture problems resulting in high computational speedups.

1.2 Adopted Approach

The approach adopted in this work, uses a FE method and multiscale hierarchical models. Particularly the FE^2 approach is used, which involves two scales (*macroscale* and *micro/meso-scale*) both discretized via finite elements. *Infinitesimal strain* setting, and *first-order homogenization* are assumed.

For fracture modeling purposes, the CSDA is adapted to the multiscale setting, and used for modeling propagating fracture at the macroscale level. At the microscale level, the use of predefined cohesive bands, distributed within the components and its interfaces, is proposed. These cohesive bands are endowed with regularized continuum damage models, which induce the crack initiation and propagation.

The Model Order Reduction techniques used in this Thesis, are based on the *Proper Orthogonal Decomposition (POD)*, defining the projection of the *full order*

model into a low-dimension small space, and, on the use of novel *interpolation* and *Reduced Optimal Quadrature (ROQ)* schemes to diminish the computational cost generated by the multiscale problem.

1.3 Objectives and Scope

The central goals of this Thesis are:

- *To develop a consistent and minimally intrusive multiscale hierarchical approach for propagating fracture with proper transfer of energy across scales.*
- *To develop, implement and validate a set of computational tools to efficiently reduce, the unaffordable computational cost associated to the FE^2 approach.*

1.4 Outline

The remainder of this manuscript is organized in four chapters. Chapter 2 is devoted to the derivation of the multiscale model for propagating fracture, including a brief introduction of the fundamentals of the computational homogenization used in the proposed approach. Chapter 3 deals with the derivation of reduced order models for multiscale, smooth and non-smooth (fracture), problems, and in addition, some numerical results obtained from the developed models, are presented. Chapter 4 provides some concluding remarks and identifies areas for future research. In Appendix A, the participations in national and international conferences, and specialized workshops are listed. In Appendix B, a short summary of the supporting papers is presented. Finally, in Appendix C, all scientific contributions supporting this Thesis, and co-authorized by the author, are annexed.

2

MULTISCALE MODELING APPROACH TO FRACTURE PROBLEMS

2.1 Computational Homogenization

In the context of two scale (macro scale – micro/meso scale) problems, computational homogenization of materials is generally regarded as a way of obtaining point-wise stress–strain constitutive models at the macroscale, accounting for complex micro/mesoscopic material morphology.

The homogenization approach used in this Thesis –commonly know as *first-order* homogenization– is only valid for materials that display either *statistical homogeneity* or *spatial periodicity*.

In consequence, depending on the morphology and random distribution of constituents at the microscale, the definition and existence of a *representative sample (RVE)* plays an important role in the material characterization of heterogeneities at the macroscale.

This representative sample, hereafter denoted $\mathcal{B}_\mu \in \mathbb{R}^d (d = 2, 3)$, is assumed to exhibit several features. One of those corresponds to the *size indifference* property (Terada et al., 2000; Kouznetsova, 2002; Drago and Pindera, 2007), which states that if the size of this sample is increased, the response remains identical regardless the *admissible* boundary conditions on the RVE. The lower size limit for the RVE satisfying the size indifference property is represented by the *characteristic length-scale* denoted as h_μ, giving rise to the existence of the RVE, whereas in micro-structures that display periodicity, it is known as *Repeating Unit Cell (RUC)*, or simply *unit cell*. Furthermore, $\mathcal{B}_\mu$ has to be small enough to be regarded as a point at the macro-scale (Gross and Seelig, 2011) (i. e., $h_\mu \ll L$, being L the characteristic length of the macroscale $\mathcal{B}$, see Fig. 1), this is the so-called *scale separation* hypothesis.

This section presents a summary of the multiscale variational formulation used in this Thesis. This approach is based on the following fundamental hypotheses:

- The infinitesimal strains setting is used.
- Quasiestatic problems are considered[1]. A pseudo-time variable t is used which increases monotonically, with $t \in [0, t_f]$, being t_f the final time of the analysis. In the development of the multiscale model for fracture modeling, the incremental form of the equilibrium equations is used, due to the fact that the kinematic enhancement is modified along time. This issue is fully detailed in Sec. 2.2.
- The multiscale problem is restricted to two scales, although it can be easily extended to additional scales. The upper scale (*macroscale*), usually identified as the structural scale, is denoted as $\mathcal{B}$, and its material points are denoted as $\boldsymbol{x}$. The lower scale is denoted as (*meso/microscale*) $\mathcal{B}_\mu$, in which, every material point is denoted by $\boldsymbol{y}$. In addition, for the sake of clarity, entities at the small scale, are identified by the subindex μ, see Fig. 1.
- The body at the macroscale, $\mathcal{B}$, is subjected to either force or displacement predefined actions, applied along its boundary $\boldsymbol{\Gamma}$. This boundary $\boldsymbol{\Gamma}$ is supposed to be smooth by parts, and it can be splitted into two parts, $\boldsymbol{\Gamma}_D$ and $\boldsymbol{\Gamma}_N$, representing the domains in which *Dirichlet* and *Newman* boundary conditions are imposed and, fulfilling $\boldsymbol{\Gamma}_D \cap \boldsymbol{\Gamma}_N = \emptyset$.
- Every point $\boldsymbol{x}$ at the macroscale, is related with a corresponding heterogeneous microstructural representative domain (the *RVE*), assuming the existency of a *scale separation*, so that the representative length at the microscale h_μ is considerably smaller than that representing the macroscale L ($h_\mu \ll L$).
- The body at the macroscale, $\mathcal{B}$, is idealized as a statistically homogeneous media, in which the mechanical state at a generic point $\boldsymbol{x}$ is characterized by the strain, $\boldsymbol{\varepsilon}$, and stress, $\boldsymbol{\sigma}$, tensors. The macroscale strain tensor $\boldsymbol{\varepsilon}$ is the input variable for the small scale, and, the corresponding output variables are the homogenized stress $\boldsymbol{\sigma}$ and the homogenized tangent constitutive $\mathbb{C}$ tensor ($\dot{\boldsymbol{\sigma}} = \mathbb{C} : \dot{\boldsymbol{\varepsilon}}$). In this way, the multiscale model can be interpreted as a constitutive model that, given a strain history, returns the stress and tangent constitutive tensors histories, accounting for the morphology and the interaction of the different components at the small scale, see Fig. 1.
- The *Hill-Mandel Variational Principle of Macro-Homogeneity* (Hill, 1965; Mandel, 1971), which states an equivalence between the virtual power densities between micro and macro scales, and requires the adoption of specific kinematically admissible displacement fluctuations at the RVE is adopted.

1 However, in one article supporting this Thesis, dynamic problems are also considered. See (Hernández et al., 2017)

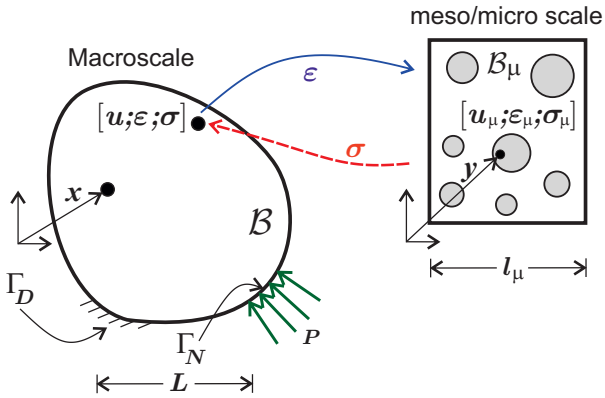

Figure 1: Macrosctructure with an embedded local microstructure.

2.1.1 *RVE kinematics and strain tensor*

In the context of the adopted first-order homogenization setting, the microscopic velocity field $\dot{\boldsymbol{u}}_\mu$, can be splitted as follows:

$$\dot{\boldsymbol{u}}_\mu = \dot{\boldsymbol{u}}(x,t) + \dot{\boldsymbol{\varepsilon}}(\boldsymbol{x},t)\cdot\boldsymbol{y} + \dot{\tilde{\boldsymbol{u}}}_\mu(\boldsymbol{y},t) \tag{2.1}$$

where $\dot{\boldsymbol{u}}$ stands for the velocity at the macroscale, $\dot{\boldsymbol{\varepsilon}}$ stands for the rate of infinitesimal macroscopic strain tensor, the term $\dot{\boldsymbol{\varepsilon}}\cdot\boldsymbol{y}$ is a velocity term that varies linearly with $\boldsymbol{y}$, and the *velocity fluctuations* is denoted as $\dot{\tilde{\boldsymbol{u}}}_\mu$. The decomposition of the rate of microscopic strain tensor $\dot{\boldsymbol{\varepsilon}}_\mu$ in the finite element framework yields, from spatial differentiation of Eq. (2.1):

$$\dot{\boldsymbol{\varepsilon}}_\mu(\boldsymbol{x},\boldsymbol{y},t) = \dot{\boldsymbol{\varepsilon}}(\boldsymbol{x},t) + \boldsymbol{\nabla}^s_{\boldsymbol{y}}\dot{\tilde{\boldsymbol{u}}}_\mu(\boldsymbol{y},t) \tag{2.2}$$

The starting point of multi-scale constitutive settings, is the assumption that the rate of macroscopic strain $\dot{\boldsymbol{\varepsilon}}$, at a point $\boldsymbol{x}$ of the macro-continuum, is the *volume average* of the rate of microscopic strain (2.2), over the RVE associated with $\boldsymbol{x}$. This assumption is also interpreted as the fact that the fine-scale deformations only influence the coarse-scale behavior through its volume average.

$$\dot{\boldsymbol{\varepsilon}}(\boldsymbol{x},t) = \frac{1}{\Omega_\mu}\int_{\mathcal{B}_\mu}\dot{\boldsymbol{\varepsilon}}_\mu(\boldsymbol{y},t)\,dV \tag{2.3}$$

In virtue of (2.2) and (2.3), this condition is equivalent to impose the volume average of the symmetric gradient of the velocity fluctuations $\boldsymbol{\nabla}^s_{\boldsymbol{y}}\dot{\tilde{\boldsymbol{u}}}_\mu$ to vanish. This condition can be written using the Gauss theorem as a constraint over $\dot{\tilde{\boldsymbol{u}}}_\mu$, involving the whole volume of the RVE, as follows:

$$\dot{\tilde{\boldsymbol{u}}}_\mu \in \tilde{\mathcal{V}}^u_\mu \qquad \text{where} \qquad \tilde{\mathcal{V}}^u_\mu := \left\{ \dot{\tilde{\boldsymbol{u}}}_\mu \;\middle|\; \int_{\Gamma_\mu}\dot{\tilde{\boldsymbol{u}}}_\mu \otimes^s \boldsymbol{\nu}_\mu\,d\Gamma = \boldsymbol{0} \right\} \tag{2.4}$$

where $\tilde{\mathcal{V}}^u_\mu$, is defined as the space of admissible microscale velocity fluctuations in the RVE, Γ_μ stands for the boundary of the domain $\mathcal{B}$, and $\boldsymbol{\nu}_\mu$ is the unit normal

vector on Γ_μ. Equation (2.4) is also known as the *minimum constraint condition*.

The actual set of kinematically admissible velocity fields $\tilde{\mathcal{V}}_\mu$, together with the associated space of *virtual kinematically* admissible velocities at the microscale, denoted by $\mathcal{W}_\mu^u$, play a fundamental role in the variational formulation of the equilibrium problem of the microscale. This space $\mathcal{W}_\mu^u$ can be defined as follows:

$$\mathcal{W}_\mu^u := \left\{ \boldsymbol{\eta} = \boldsymbol{v}_1 - \boldsymbol{v}_2 \quad | \quad \boldsymbol{v}_1, \boldsymbol{v}_2 \in \tilde{\mathcal{V}}_\mu \right\} \tag{2.5}$$

In virtue of (2.4), and the fact that $\tilde{\mathcal{V}}_\mu^u$ is itself a vector space, it can be concluded from (2.4) that:

$$\mathcal{W}_\mu^u = \tilde{\mathcal{V}}_\mu^u \tag{2.6}$$

Furthermore, the same arguments can be applied to the *total* form, and establish that any *kinematically admisible displacement fluctuation* $\tilde{\boldsymbol{u}}_\mu$ belongs also to $\tilde{\mathcal{V}}_\mu^u$.

2.1.2 *Hill-Mandel Principle of Macro-Homogeneity*

The scale bridging equations are completed by introducing the *Hill-Mandel Principle of Macro-Homogeneity* (Hill, 1965; Mandel, 1971). Based on physical arguments, this Principle states that the macroscopic stress power equates the volume average over the RVE of the microscopic stress power, making both, macroscale and microscale, continuum descriptors *energetically equivalent*. Thus, departing from:

$$\delta\boldsymbol{\varepsilon}_\mu = \delta\boldsymbol{\varepsilon} + \boldsymbol{\nabla}_{\boldsymbol{y}}^s \delta\tilde{\boldsymbol{u}}_\mu \qquad \forall \delta\boldsymbol{\varepsilon} \in \mathcal{E} \quad \forall \delta\tilde{\boldsymbol{u}}_\mu \in \tilde{\mathcal{V}}_\mu \tag{2.7}$$

where $\mathcal{E}$, stands for the space of all second order macroscopic strain tensor functions, Eq. (2.7) is similar to Eq. (2.2), but for admissible strain variations. Therefore, the following identity holds:

$$\boldsymbol{\sigma} \cdot \delta\boldsymbol{\varepsilon} \;=\; \frac{1}{\Omega_\mu} \int_{\mathcal{B}_\mu} \boldsymbol{\sigma}_\mu : \delta\boldsymbol{\varepsilon}_\mu \, d\mathcal{B}_\mu \qquad \forall \delta\boldsymbol{\varepsilon}_\mu \tag{2.8}$$

In particular, taking $\delta\tilde{\boldsymbol{u}}_\mu = \boldsymbol{0}$, and $\forall \delta\boldsymbol{\varepsilon} \in \mathcal{E}$, yields:

$$\boldsymbol{\sigma} = \frac{1}{\Omega_\mu} \int_{\mathcal{B}_\mu} \boldsymbol{\sigma}_\mu(\boldsymbol{y}, t) \, d\mathcal{B}_\mu \tag{2.9}$$

where, $\boldsymbol{\sigma}$ stands for the *macroscopic stress tensor*, which turns out to be as the volume average of the microscopic stress $\boldsymbol{\sigma}_\mu$. Clearly equation is also fulfilled in rate form. In addition to Eq. (2.9), the following condition emerges from the variational equation (2.8) solving for $\delta\boldsymbol{\varepsilon} = \boldsymbol{0}$:

$$\int_{\mathcal{B}_\mu} \boldsymbol{\sigma}_\mu : \boldsymbol{\nabla}_{\boldsymbol{y}}^s \delta\tilde{\boldsymbol{u}}_\mu \, d\mathcal{B}_\mu = \boldsymbol{0} \qquad \forall \delta\tilde{\boldsymbol{u}}_\mu \in \tilde{\mathcal{V}}_\mu \tag{2.10}$$

Eq. (2.10) defines the variational microscale equilibrium problem (or *microscale virtual power principle*).

2.2 Multiscale Fracture Mechanics issues

In the computational Fracture Mechanics, hierarchical multiscale methods involve additional issues. In particular:

- The existence of the RVE has been questioned, arguing that for fracture cases, the material loses its statistical homogeneity (Gitman et al., 2007; Nguyen et al., 2010a).
- The fact that the homogenized constitutive model lacks an internal length (Bazant, 2010), raising similar issues than in classical phenomenological monoscale problems.

Mesh-bias dependence, and the proper fracture energy dissipation issues (Rots, 1988), via regularized constitutive models (Oliver, 1989; Oliver et al., 2002; Oliver and Huespe, 2004a; Oliver et al., 2015) are also crucial issues to be considered at each scale.

Along this section, the most important aspects of the proposed multiscale approach are summarized, this multiscale approach is fully detailed in Paper #2 in Sec. B.2.

2.2.1 *Multi-scale modeling setting*

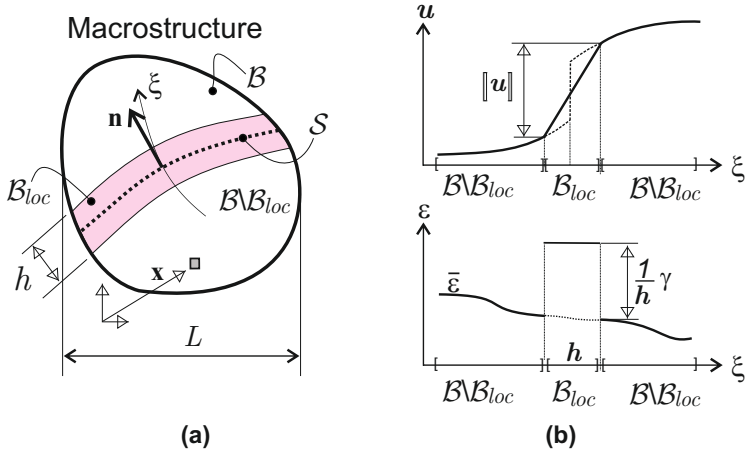

Figure 2: Macroscopic (Structural scale) body $\mathcal{B}$ **(a)** subdivision in a non-smooth domain $\mathcal{B}_{\text{loc}}(t)$, and a smooth domain $\mathcal{B} \setminus \mathcal{B}_{\text{loc}}(t)$ **(b)** h-regularized displacement and strain discontinuity kinematics.

2.2.1.1 *Macro Scale Model*

Considering the body $\mathcal{B}$, at the macroscopic (structural) scale (see Fig. 2). it is assumed that material points, $\boldsymbol{x}$, of the macroscopic body belong, at the current time t, to either of the two subdomains:

- Domain $\mathcal{B} \setminus \mathcal{B}_{\text{loc}}(t)$: the set of points at the macroscale, exhibiting smooth behavior. The infinitesimal strain field $\boldsymbol{\varepsilon}(\boldsymbol{x}, t)$ is described, in rate form, as:

$$\dot{\boldsymbol{\varepsilon}}(\boldsymbol{x}, t) = (\boldsymbol{\nabla}_{\boldsymbol{x}} \otimes \dot{\boldsymbol{u}}(\boldsymbol{x}, t))^{s} \equiv \boldsymbol{\nabla}^{s}_{\boldsymbol{x}} \dot{\boldsymbol{u}}(\boldsymbol{x}, t) \qquad \forall \boldsymbol{x} \in \mathcal{B} \setminus \mathcal{B}_{\text{loc}}(t) \tag{2.11}$$

  where $\boldsymbol{u}(\boldsymbol{x}, t)$ is the macroscopic displacement field, t stands for the time or *pseudo-time* parameter and $(\cdot)^{s}$ stands for the symmetric counterpart of $(\cdot)$.

- Domain $\mathcal{B}_{\text{loc}}(t)$: the set of points exhibiting material failure and, therefore, a non-smooth behavior. The strain field at these points is assumed to be captured by a h-regularized *strong-weak* discontinuity kinematics, h being the width of the corresponding strain localization band (see Fig. 2-(b)).

See: ***Sec.2.1*** ***Paper 2***

$$\dot{\boldsymbol{\varepsilon}}(\boldsymbol{x}, t) = \dot{\tilde{\boldsymbol{\varepsilon}}}(\boldsymbol{x}, t) + \frac{\kappa_{\mathcal{B}_{\text{loc}}}(\boldsymbol{x})}{h} \dot{\boldsymbol{\gamma}}(\boldsymbol{x}, t) = \dot{\tilde{\boldsymbol{\varepsilon}}}(\boldsymbol{x}, t) + \delta^{h}_{s}(\boldsymbol{x}) \dot{\boldsymbol{\gamma}}(\boldsymbol{x}, t) \quad \forall \boldsymbol{x} \in \mathcal{B}_{\text{loc}}(t) \tag{2.12}$$

  In Eq. (2.12), $\dot{\tilde{\boldsymbol{\varepsilon}}}(\boldsymbol{x}, t)$ stands for the regular (smooth) counterpart of the strain, $\kappa_{\mathcal{B}_{\text{loc}}}$ is a colocation (*characteristic*) function on $\mathcal{B}_{\text{loc}}$ (See. Fig. 3), so that the term $\kappa_{\mathcal{B}_{\text{loc}}}(\boldsymbol{x})$ becomes a h-regularized Dirac's delta function shifted to the center-line, $S(t)$ (the macroscopic discontinuity-path at the current time t), see Fig. 2-(a). Thus, in Eq. (2.12), the term $\delta^{h}_{s}(\boldsymbol{x}) \dot{\boldsymbol{\gamma}}(\boldsymbol{x}, t)$ corresponds to the non-smooth (discontinuous and h-regularized) localized counterpart of the strains; a space-discontinuous second order tensor for the *weak-discontinuity case*.

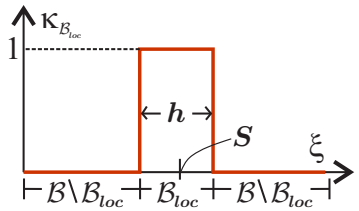

Figure 3: Colocation Function $\kappa_{\mathcal{B}_{\text{loc}}}(\boldsymbol{x})$

2.2.1.2 *Micro Scale Model*

Now we assume that the fracture at the macroscale is arisen, in turn, by the appearance of failure mechanisms at the microscale level, originated by some type of material failure. Therefore, next step is to endow the small scale model with mechanisms to capture the onset and propagation of this material failure.

Therefore, and without introducing further details, it is considered that the microstructure shall be able to capture some dominant failure mechanisms of the material.

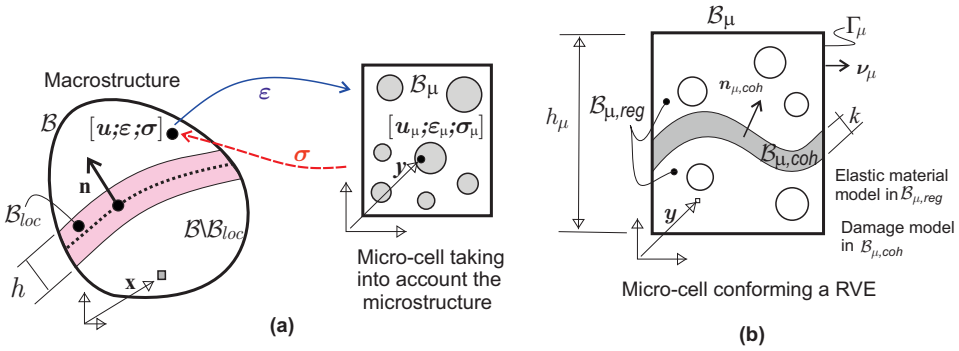

Figure 4: Outline of the multiscale model for propagating fracture: **a)** macro and micro-scales; **b)** micro-cell model accounting for material failure.

For this purpose, a micro *failure cell*, $\mathcal{B}_\mu$, of characteristic size h_μ, is considered to exist at every material point $\boldsymbol{x} \in \mathcal{B}$. It accounts for the material morphology at the lower scale (voids, inclusions etc.), in addition, it is endowed with a set of *cohesive bands*, ($\mathcal{B}_{\mu,\text{coh}} \subset \mathcal{B}_\mu$), of very small width ($k \ll h_\mu$), whose position and other geometric properties (typically the normal n_μ, see Fig. 4) are predefined. Activation (de-cohesion) at the current time t, of a number of those bands, defines the current subset of active bands, $\mathcal{B}_{\mu,\text{act}}(t) \subset \mathcal{B}_{\mu,\text{coh}} \subset \mathcal{B}_\mu$ which constitutes the "active" microscopic failure mechanism, at the current time, for the considered point $\boldsymbol{x} \in \mathcal{B}$ of the macro-scale.

In principle, there is no intrinsic limitation on the number of the "candidate" cohesive bands to be considered at the failure cell. On one hand, their number and spatial position have to be sufficient to capture the dominant material failure mechanisms at the macro-scale, and, on the other hand, the associated computational cost sets a limitation on the number of such bands. In this context, the following domains at the microscale are considered (see Fig. 4):

- Domain $\mathcal{B}_\mu \setminus \mathcal{B}_{\mu,\text{coh}}$: the set of points $\boldsymbol{y}$, which do not belong to the cohesive bands. They are compelled to exhibit a smooth behavior described by a *Continuum hardening model*, typically:

$$\dot{\boldsymbol{\sigma}}_\mu = \Sigma^{\text{hard}}(\dot{\boldsymbol{\varepsilon}}_\mu) \equiv \mathbb{C}_\mu^{\text{hard}} : \dot{\boldsymbol{\varepsilon}}_\mu \qquad \forall \boldsymbol{x} \in \mathcal{B}; \quad \forall \boldsymbol{y} \in \mathcal{B}_\mu \setminus \mathcal{B}_{\mu,\text{coh}} \tag{2.13}$$

  where $\boldsymbol{\sigma}_\mu$ and $\boldsymbol{\varepsilon}_\mu$ stand, respectively, for the stress and strain fields at the microscale point, $\boldsymbol{y}$, of the failure cell (corresponding to the macroscale point $\boldsymbol{x}$), being $\mathbb{C}_\mu^{\text{hard}}$ the microscopic inelastic constitutive tensor derived from the hardening constitutive model.

- Domain $\mathcal{B}_{\mu,\text{coh}}$: the set of microscale cohesive bands. As for the material behavior, in this case one has to make distinction of two cases:

– The failure cell, $\mathcal{B}_\mu$ is associated to a non-smooth material point at the macroscale ($\boldsymbol{x} \in \mathcal{B}_{\text{loc}}$). Without limiting the use of any other inelastic constitutive model, this domain is endowed with an *isotropic continuum damage model*, exhibiting inelasticity with regularized strain softening only for tensile stress - *tensile-damage continuum damage model* (Oliver, 1995b; Faria et al., 1998; Oliver et al., 2005). Its constitutive response is represented in a general form as:

See: ***Sec.2.2*** ***Paper 2***

$$\dot{\boldsymbol{\sigma}}_\mu = \Sigma^{\text{inelas}}(\dot{\boldsymbol{\varepsilon}}_\mu, \boldsymbol{\mu}) \qquad \forall \boldsymbol{x} \in \mathcal{B}_{\text{loc}}(t); \quad \forall \boldsymbol{y} \in \mathcal{B}_{\mu,\text{coh}} \tag{2.14}$$

where $\boldsymbol{\mu}$ stands for a set of *internal variables* accounting for the inelastic behavior evolution.

– The failure cell, $\mathcal{B}_\mu$ is associated to a smooth material point at the macroscale, ($\boldsymbol{x} \in \mathcal{B} \setminus \mathcal{B}_{\text{loc}}(t)$). In this case, the inelastic model, in Eq. (2.14) is enforced to behave instantaneously elastic at the cohesive bands domain, $\mathcal{B}_{\mu,\text{coh}}$, i. e.:

$$\dot{\boldsymbol{\sigma}}_\mu = \Sigma^{\text{elastic}}_{\text{inst}}(\dot{\boldsymbol{\varepsilon}}_\mu) = \mathbb{C}^{\text{elastic}}_{\text{inst}} : \dot{\boldsymbol{\varepsilon}}_\mu \quad \forall \boldsymbol{x} \in \mathcal{B} \setminus \mathcal{B}_{\text{loc}}(t); \quad \forall \boldsymbol{y} \in \mathcal{B}_{\mu,\text{coh}} \tag{2.15}$$

where, in continuum damage models, $\mathbb{C}^{\text{elastic}}_{\text{inst}} = (1 - d_\mu) \cdot \mathbb{C}_\mu$ with $\dot{d}_\mu = 0$, and being $\dot{d}_\mu$ the rate of the damage internal variable (a scalar for isotropic damage cases).

An advantage of this methodology, in the previous setting, is that the same failure cell morphology is considered to represent the microstructure at every macroscopic point of $\mathcal{B}$, both for $\boldsymbol{x} \in \mathcal{B}_{\text{loc}}(t)$ and $\boldsymbol{x} \in \mathcal{B} \setminus \mathcal{B}_{\text{loc}}(t)$. The only difference is the considered constitutive behavior at the cohesive bands $\mathcal{B}_{\mu,\text{coh}}$, defined in Eqs. (2.13),(2.14) and (2.15).

Displacement fluctuations in the CSDA: Considering Eq. (2.1), with a local coordinate system (ξ, η) aligned with the domain $\mathcal{B}_{\mu,\text{coh}}$ (see Fig. 4), and, exhibiting the de-cohesive behavior allocated to the cohesive bands, the smooth part of the microscopic displacement fluctuation field, $\bar{\boldsymbol{u}}_\mu$, can be expressed as:

$$\begin{aligned}
\dot{\bar{\boldsymbol{u}}}_\mu(\xi,\eta,t) &= \dot{\tilde{\boldsymbol{u}}}_\mu(\xi,\eta,t) - \mathcal{H}_{\mathcal{B}_{\mu,\text{coh}}}(\xi)\dot{\boldsymbol{\beta}}_\mu(\eta,t) && (a)\\
\mathcal{H}_{\mathcal{B}_{\mu,\text{coh}}}(\xi) &= \begin{cases} 0 & \forall \boldsymbol{y} \in (\mathcal{B}_\mu \setminus \mathcal{B}_{\mu,\text{coh}})^- \\ \frac{\xi}{k} & \forall \boldsymbol{y} \in \mathcal{B}_{\mu,\text{coh}} \\ 1 & \forall \boldsymbol{y} \in (\mathcal{B}_\mu \setminus \mathcal{B}_{\mu,\text{coh}})^+ \end{cases} && (b)\\
\dot{\boldsymbol{\beta}}_\mu(\eta(\boldsymbol{y}),t)\Big|_{\boldsymbol{y}\in\mathcal{B}_{\mu,\text{coh}}} &\equiv [\![\dot{\tilde{\boldsymbol{u}}}_\mu(\xi,\eta,t)]\!]^+_- && (c)
\end{aligned} \tag{2.16}$$

where $\mathcal{H}_{\mathcal{B}_{\mu,\text{coh}}}(\xi)$ is the k-regularized Heaviside function shifted to $\mathcal{B}_{\mu,\text{coh}}$, and $\dot{\boldsymbol{\beta}}_\mu(\eta,t)$ is a (smooth) function arbitrarily defined except for the restriction in Eq. (2.16)-(c), In Eq. (2.16) $[\![(\cdot)(\xi,\eta,t)]\!]^+_- \equiv (\cdot)(\xi,\eta,t)|_{\xi=k} - (\cdot)(\xi,\eta,t)|_{\xi=0}$, is the

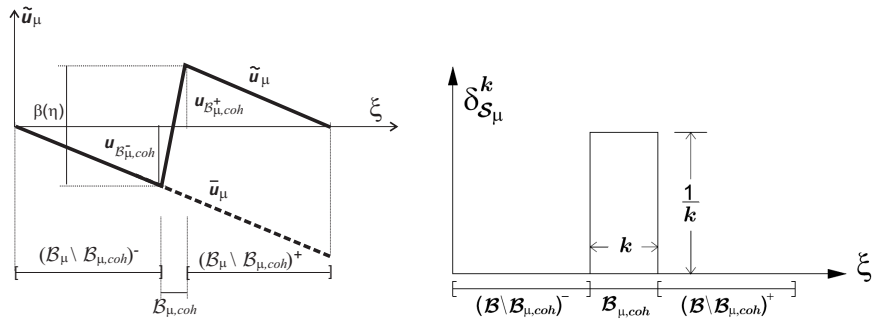

(a) Microscopic displacement fluctuation field.

(b) k-regularized Dirac Delta function.

Figure 5: Cohesive Band behavior.

apparent jump of $(\cdot)(\xi,\eta,t)$ across the cohesive band.

Following these statements, the microscale displacement fluctuation is given by (see Fig. 5):

$$\dot{\tilde{\boldsymbol{u}}}_\mu(\xi,\eta,t) = \underbrace{\dot{\bar{\boldsymbol{u}}}_\mu(\xi,\eta,t)}_{\text{smooth}} + \mathcal{H}_{\mathcal{B}_{\mu,\text{coh}}}(\xi)\dot{\boldsymbol{\beta}}_\mu(\eta,t) \tag{2.17}$$

Eq. (2.17) constitutes the displacement counterpart of a k-regularized strong discontinuity kinematics (Oliver, 1996a), and proves that the herein proposed cohesive-bands approach, is consistent with a k-regularized strong discontinuity at the cohesive domain $\mathcal{B}_{\mu,\text{coh}}$. In consequence, the corresponding microscopic strain fluctuation field is given by:

$$\boldsymbol{\nabla}^s_{\boldsymbol{y}}\dot{\tilde{\boldsymbol{u}}}_\mu(\boldsymbol{y},t) = \underbrace{\boldsymbol{\nabla}^s_{\boldsymbol{y}}\dot{\bar{\boldsymbol{u}}}_\mu(\boldsymbol{y},t) + \mathcal{H}_{\mathcal{B}_{\mu,\text{coh}}}(\xi)\boldsymbol{\nabla}^s_{\boldsymbol{y}}\dot{\boldsymbol{\beta}}_\mu(\boldsymbol{y},t)}_{\dot{\bar{\boldsymbol{\varepsilon}}}_\mu(\boldsymbol{y},t)} + \delta^k_{s_\mu}(\dot{\boldsymbol{\beta}}_\mu \otimes \boldsymbol{n}_\mu)^s \tag{2.18}$$

where $\delta^k_{s_\mu}$ stands for the k-regularized Dirac's delta function, placed at the center line, S_μ, of $\mathcal{B}_{\mu,\text{coh}}$ (see Fig. 5-(b)). Thus, the rate of microscopic strain field $\dot{\boldsymbol{\varepsilon}}_\mu$ can be written in terms of the rate of macroscopic strain $\dot{\boldsymbol{\varepsilon}}$, and the rate of microscopic displacement fluctuations $\dot{\tilde{\boldsymbol{u}}}_\mu$, as follows:

$$\dot{\boldsymbol{\varepsilon}}_\mu(\boldsymbol{x},\boldsymbol{y},t) = \underbrace{\dot{\boldsymbol{\varepsilon}}(\boldsymbol{x},t) + \dot{\bar{\boldsymbol{\varepsilon}}}_\mu(\boldsymbol{y},t)}_{\text{bounded}} + \underbrace{\delta^k_{s_\mu}(\dot{\boldsymbol{\beta}}_\mu \otimes \boldsymbol{n}_\mu)^s}_{\text{unbounded}} \tag{2.19}$$

From Eq. (2.19), it can be concluded, that the second term at the right hand-side becomes unbounded in the limit $k \to 0$. In multiscale modeling, this expression is equivalent to the one given, in phenomenological monoscale models, in the context of the *Continuum Strong Discontinuity Approach* (CSDA) of material failure (Oliver et al., 2002).

2.2.2 *Homogenized (induced) constitutive equation*

One of the most specific features of the proposed multiscale approach, is that the same homogenization setting is used in points of both domains, smooth ($\boldsymbol{x} \in \mathcal{B}_\mu \setminus \mathcal{B}_{\mu,\text{coh}}$), and non-smooth ($\boldsymbol{x} \in \mathcal{B}_{\mu,\text{coh}}$), coinciding with the approach presented in Sec. 2.1. Other approaches (Toro et al., 2014), redefine the failure cell along time, fulfilling conditions of material bifurcation induced by instabilities at the microscale. More complex approaches (Kouznetsova, 2002; Geers et al., 2010; Otero et al., 2015; Lesicar et al., 2015) propose the use of *second-order* computational homogenization schemes in order to get better accuracy in the prediction of high strain gradients. In this Thesis it is claimed the ability of the proposed approach to induce discrete failure in a *first-order homogenization* setting, giving rise to objective responses, and proper energy transfer through scales.

An issue appearing in this scenario, widely known in hierarchical multiscale approaches, is the high computational cost. In this context, the proposed model was also conceived to be combined with the use of *model order reduction techniques* (Paper #3) (Oliver et al., 2017b). These techniques have been deeply studied in this Thesis, and their main features are presented in Chapter 3.

In the following, the consequences of the homogenization procedure based on the Hill-Mandel Principle of Macro-homogeneity are analyzed. The fact that the regularized strong discontinuities appear also at the small scale, being captured by the cohesive bands $\mathcal{B}_{\mu,\text{coh}}$, is one of the most relevant features of the proposed approach.

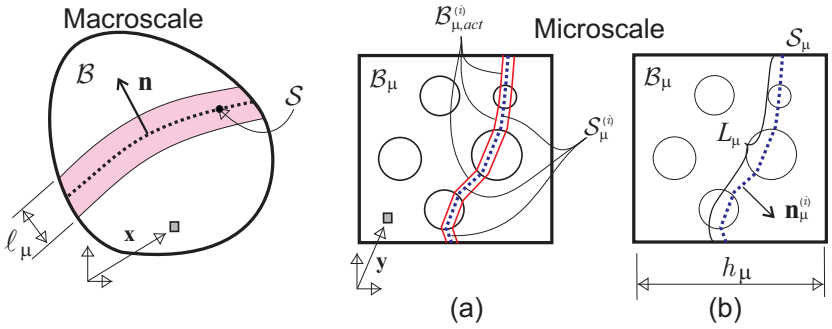

Figure 6: Multiscale model: **(a)** failure cell with activated failure mode; **(b)** geometrical characterization of the failure mode.

For the sake of generality, the RVE is considered composed by several components: a matrix, and randomly distributed inclusions and voids. In addition, a number of cohesive bands are considered defining the set $\mathcal{B}_{\mu,\text{coh}}$ (a sketch is presented in Fig. 6); those cohesive bands allow failure within the matrix, across the aggregates and at the matrix/aggregate interface.

See: ***Sec.2.4*** ***Paper 2***

Following the previous domain decomposition (smooth and non-smooth subdomains) in Sec. 2.2.1.2, the Eq. (2.9) can be integrated in the two separated subdomains:

$$\dot{\boldsymbol{\sigma}} = \frac{1}{\Omega_\mu}\int_{\mathcal{B}_\mu} \dot{\boldsymbol{\sigma}}_\mu \, dV = \frac{1}{\Omega_\mu}\left[\int_{\mathcal{B}_\mu \setminus \mathcal{B}_{\mu,\text{coh}}} \dot{\boldsymbol{\sigma}}_\mu \, dV + \int_{\mathcal{B}_{\mu,\text{coh}}} \dot{\boldsymbol{\sigma}}_\mu \, dV\right] \tag{2.20}$$

In consonance with the definition of $\dot{\boldsymbol{\sigma}}_\mu$ (in particular, the bounded behavior of the microscopic stress field), the second term on the right hand side can be neglected assuming a small enough width of the cohesive bands ($k \to 0$).

Finally, after some manipulations of Eq. (2.20), and following the definitions of microscale kinematics in Eq. (2.19), and the lemma in Eq. 23 in Paper #2 (Oliver et al., 2015), the resulting homogenized constitutive equation fulfills the following:

$$\dot{\boldsymbol{\sigma}}(\boldsymbol{x},t) = \bar{\mathbb{C}} : \left[\dot{\boldsymbol{\varepsilon}}(\boldsymbol{x},t) + \dot{\boldsymbol{\chi}}(\boldsymbol{x},t) - \dot{\boldsymbol{\varepsilon}}^{(i)}(\boldsymbol{x},t)\right] \qquad \bar{\mathbb{C}} \equiv \frac{1}{\Omega_\mu}\int_{\mathcal{B}_\mu} \mathbb{C}_\mu(\boldsymbol{y}) \, dV \tag{2.21}$$

$$\dot{\boldsymbol{\varepsilon}}^{(i)}(\boldsymbol{x},t) = \frac{1}{\Omega_\mu}\int_{S_\mu} (\dot{\boldsymbol{\beta}}_\mu \otimes \boldsymbol{n}_\mu)^s \, dS = \frac{1}{l_\mu}\overline{(\dot{\boldsymbol{\beta}}_\mu \otimes \boldsymbol{n}_\mu)^s}_{S_\mu} \tag{2.22}$$

$$\overline{(\dot{\boldsymbol{\beta}}_\mu \otimes \boldsymbol{n}_\mu)^s}_{S_\mu} = \frac{1}{L_\mu}\int_{S_\mu} (\dot{\boldsymbol{\beta}}_\mu \otimes \boldsymbol{n}_\mu)^s \, dS \qquad l_\mu(\boldsymbol{x},t) \equiv \frac{\Omega_\mu}{L_\mu} = \mathcal{O}(h_\mu) \tag{2.23}$$

where, l_μ stands for a *characteristic length*, depending on the activated microscopic failure pattern. The tensorial entities $\dot{\boldsymbol{\chi}}(\boldsymbol{x},t)$ and $\dot{\boldsymbol{\varepsilon}}^{(i)}(\boldsymbol{x},t)$, are inelastic strains, and play the same role than internal variables in phenomenological models. However, unlike them, here, their evolution is determined, at every macroscopic sampling point $\boldsymbol{x}$, by homogenized values of entities at the corresponding microscopic failure cell $\mathcal{B}_\mu$. This extends to non-smooth problems, some theoretical results already derived for smooth problems, see (Michel and Suquet, 2003, 2004). In addition, a characteristic length l_μ emerges naturally in Eq. (2.22), as the ratio between the measure of the failure cell (area in 2D and volume in 3D), and the measure (length/surface) of the activated microscopic failure mechanism. In consequence this length is of the order of the failure cell size. For a deeper review of the analytical results of this induced homogenized constitutive model, the reader is addressed to Sec. 2.4 in Paper #2.

See: ***Sec.2.4 Paper 2***

The role of the characteristic length, l_μ, *naturally derived* from the present formulation, is not only computational, but it has also other very relevant physical and mechanical implications. Consideration of such a characteristic length, for multiscale based approaches, has been claimed from the material mechanics community (Bazant, 2010), and sometimes introduced in a heuristic way in other approaches (Unger, 2013). This characteristic length depends on both the specific data of the problem and the local microscopic failure state. Through its consideration, the correct energy transfer between scales and mesh

size objectivity can be achieved.

In summary, Eq. (2.21) and Eq. (2.22) retrieve the format of a *constitutive model equipped with an internal length and with internal variables whose evolution is described by the microstructure behavior*. Although this model will never be used for computational purposes[2], it supplies relevant insights on the properties of the resulting homogenized constitutive model.

2.2.3 *Energy dissipation*

Let us consider, on one hand the fracture energy, $G_\mu^f(\boldsymbol{y})$ corresponding to points $\boldsymbol{y} \in \mathcal{B}_\mu$, defined as a material property specific for every compound of the heterogeneous RVE, and, on the other hand, the macroscale fracture energy $G^f(\boldsymbol{x})$, obtained as an output from the homogenization procedure. According to their definitions, those fracture energies can be computed in terms of fracture energy densities, in terms of the energy dissipation that takes place in bands with bandwidth k (at the microscale) and l_μ (at the macroscale), respectively.

$$g^f(\boldsymbol{x}) = \frac{G^f(\boldsymbol{x})}{l_\mu(\boldsymbol{x})} = \int_0^\infty \boldsymbol{\sigma}(\boldsymbol{x},t) : \dot{\boldsymbol{\varepsilon}}(\boldsymbol{x},t)\, dt \quad \forall \boldsymbol{x} \in \mathcal{B}_{\text{loc}} \tag{2.24}$$

$$g_\mu^f(\boldsymbol{x}) = \frac{G_\mu^f(\boldsymbol{x})}{k} = \int_0^\infty \boldsymbol{\sigma}_\mu(\boldsymbol{y},t) : \dot{\boldsymbol{\varepsilon}}_\mu(\boldsymbol{y},t)\, dt \quad \forall \boldsymbol{y} \in \mathcal{B}_{\mu,\text{coh}} \tag{2.25}$$

See: ***Sec.2.6*** ***Paper 2***

In virtue of the Hill-Mandel Principle of Macro-Homogeneity, it can be concluded that the macroscopic fracture energy G^f is equivalent to the average of microscopic fracture energy $G_\mu^f(\boldsymbol{y})$, along the activated failure mechanism at the microscale S_μ. Replacing (2.24) into Eq. (2.8), and after some manipulations, the macroscopic fracture energy is given by the expression (Oliver et al., 2015):

$$\frac{G^f(\boldsymbol{x})}{l_\mu(\boldsymbol{x})} = \underbrace{\frac{L_\mu}{\Omega_\mu}}_{\frac{1}{l_\mu(\boldsymbol{x})}} \cdot \frac{1}{L_\mu} \int_{S_\mu} G_\mu^f(\boldsymbol{y})\, dS_\mu = \frac{1}{l_\mu(\boldsymbol{x})} \overline{G_\mu^f(\boldsymbol{y})}_{S_\mu} \tag{2.26}$$

$$G^f(\boldsymbol{x}) = \overline{G_\mu^f(\boldsymbol{y})}_{S_\mu} \tag{2.27}$$

where $\overline{G_\mu^f(\boldsymbol{y})}_{S_\mu}$ is the mean value of the microscopic fracture energy varying along the active failure path. Eq. (2.28) provides the relationship of fracture energies at both scales. In case of an homogeneous fracture energy at the active cohesive bands of the microscale, Eq. (2.26) translates into an exact equivalence of fracture energies along the scales, i. e.:

$$G^f(\boldsymbol{x}) = G_\mu^f \tag{2.28}$$

2 Instead, the homogenized value of the stress in Eq. (2.9) is point-wise used to evaluate the current macroscopic stress in terms of the corresponding macroscopic strain.

In the light of this result, it can be easily concluded that the fracture energies at the small scale, determine in average, the effective fracture energy at the macroscale. It is stressed the importance of the characteristic length l_μ in order to guarantee the proper dissipation between scales. For more details, the reader is addressed to Appendix B in Paper #2.

2.2.4 *Numerical Aspects: Finite Element model*

The proposed multiscale formulation has been implemented in a Finite Element model following the setting of a FE^2 strategy. Accordingly, two *nested* finite element models are used:

- At the macroscale level, an Embedded Finite Element Methodology (EFEM) based on the CSDA is used, aiming at capturing propagating cracks. As described in (Oliver et al., 2014), this technology consists of the insertion, during specific stages of the simulation, of goal oriented specific strain fields via mixed finite element formulations. This allows modeling propagating cracks through the macroscale finite element mesh.
- A standard Finite Element model is used at the microscale level, combining standard elements endowed with continuum hardening constitutive models and cohesive-band elements endowed with regularized constitutive softening models. These are placed in the edges of every finite element, capturing the crack onset and strain localization, similar to the cohesive interface elements in (Pandolfi et al., 1999), and more recently in (Rodrigues et al., 2016). This approach benefits the simplicity of the algorithmic and, the non-intrusive character of its implementation.

In what follows, these two finite element models are described.

2.2.4.1 *Failure cell finite element model*

Standard quadrilateral finite elements are adopted for the numerical simulation of the cell response. The cohesive bands $\mathcal{B}_{\mu,\text{coh}}$ are also modeled by quadrilateral isoparametric finite elements of very small thickness (high aspect ratio) ($k \ll h_\mu$), as shown in Fig. 7-(a), endowed with constitutive models whose behavior is sketched in Fig. 7-(b) and defined through equations (2.13) to (2.15). The remaining finite elements of the cell are endowed with either elastic or inelastic hardening responses. Therefore, only elements on the cohesive bands can exhibit strain localization.

The corresponding non-linear problem in the failure cell is then solved for the discretized version of the microscale displacement fluctuations, using Eq. (2.10). Dirichlet boundary conditions precluding rigid body motions, and, minimal boundary conditions, in Eq. (2.4), are also imposed.

Material failure propagates naturally through the RVE, strain localization takes place at the finite elements defining the cohesive bands. At every time step of the

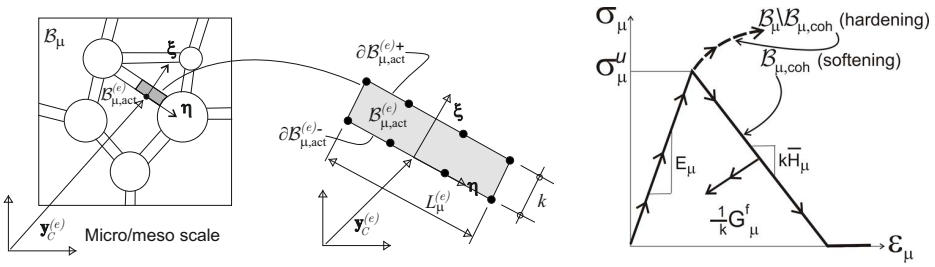

(a) Cohesive bands (b) Constitutive equation

Figure 7: Multiscale model: finite element discretization at the microscale.

analysis, those finite elements who are in loading state, define the active set of cohesive bands $\mathcal{B}_{\mu,\text{act}}$ conforming the active failure mechanism.

2.2.4.2 *Finite Element model at the macroscale: material failure propagation*

One of the most critical issues in computational modeling of material failure is the appropriate capture of the crack onset and propagation. *When does failure trigger at a given material point?* and *how does it propagate?*. These two questions are the cornerstone of material failure propagation algorithms.

At the microscale, where the morphology and the position of candidate propagation mechanisms are predefined, the two issues are of minor relevance due to the adopted simplified failure-bands model. However, at the macroscale, there is not a predefined failure path, and, in principle, any material point may fail and propagate in any direction. To adequately solve the previous questions, the procedure for modeling onset and propagation of discontinuities recently developed for monoscale problems (Oliver et al., 2014) has been extended to the multiscale setting. The proposed methodology is based on the use of the following specific techniques:

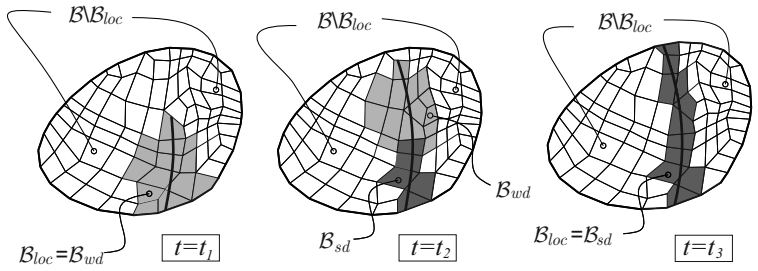

Figure 8: Evolution of the injection domains for three typical stages of the discontinuity propagation. $t_1 < t_2 < t_3$

- ***Strain injection techniques***: based on the use of goal oriented assumed-strain fields injected in selected domains, via mixed formulations (Simo and

Hughes, 1986; Simo and Riffai, 1990; Reddy and Simo, 1995; Zienkiewicz and Taylor, 2000). The standard (four points) Gauss quadrature rule, corresponding to full integration of two-dimensional quadrilaterals, is complemented with two additional sampling points, placed at the barycenter of the element, see Fig. 9, termed the *singular* and *regular* sampling points. These two additional quadrature points sample the stresses similarly to the standard Gauss points. Therefore, for the injected elements, numerical integration (typically evaluation of the incremental internal forces in terms of the stresses), is based on those two additional sampling points, by defining the weight indicated in **Table 3** - in Appendix B in Paper #2.

As for propagation purposes, two different enhanced strain injection stages, are considered[3]:

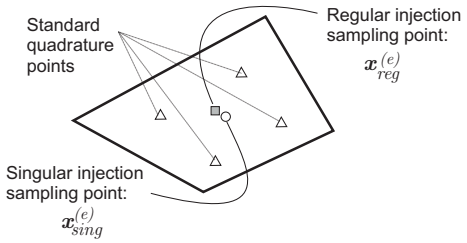

Figure 9: Sampling points involved in the numerical integration.

– In a *first stage, the* ***weak discontinuity stage***, embedded localization bands with bandwidth l_μ, at the macroscale, are incrementally injected (prior to development of displacement discontinuities) in an evolving subdomain. These embedded localization bands have no preferred orientation (they have an isotropic character), and exhibit a great ability to propagate material failure in the proper directions. This so-injected elements are used for a very short time in order to avoid stress locking effects. Once the crack propagation remains stable, and the crack path is well defined, the injection stage is switched to the second stage.

  The injected strain rate at element e, with n_{node} nodes, is the following:

$$\dot{\boldsymbol{\varepsilon}}^{(e)}(\boldsymbol{x},t) \equiv \underbrace{\sum_{i=1}^{i=n_{node}} \boldsymbol{\nabla} N_i(\boldsymbol{x}) \otimes \dot{\boldsymbol{u}}_i(t)}_{\text{regular}} + \underbrace{\zeta_{\mathcal{S}}^{h^{(e)},l_\mu^{(e)}}(\boldsymbol{x})\dot{\boldsymbol{\gamma}}^{(e)}(t)}_{\text{singular}} \tag{2.29}$$

  where N_i are the standard shape functions, $\dot{\boldsymbol{u}}(t)$, the macroscale nodal displacements, and $\zeta_{\mathcal{S}}^{h^{(e)},l_\mu^{(e)}}$ is the regularized *dipole-function* in the element (e). A description of the weak enhanced mode is presented in

3 To switch between stages, a set of *control variables* are defined, all those detailed in Sec. 3 and Appendix B in Paper #2

Fig. 10, In addition, the variational problem for the weak-discontinuity regime, in rate form, is presented in **Box A1** in the Appendix B in Paper #2.

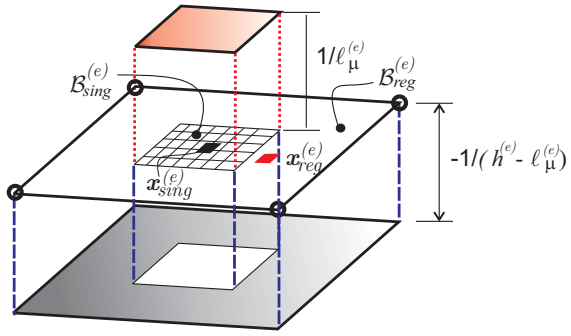

Figure 10: Weak discontinuity mode. Elemental regularized dipole function $\zeta_{\mathcal{S}}^{h^{(e)},l_\mu^{(e)}}$.

– In a *second stage, the* ***strong discontinuity stage***, the obtained crack path field, S, is used to determine the appropriate placement of an elemental embedded strong-discontinuity strain field, which is incrementally injected in the appropriated set of elements, $\mathcal{B}_{\text{sd}}$.

  In the present multiscale context, the proposed second stage consists of, the incremental injection of the following *elemental strong discontinuity mode*:

$$\dot{\boldsymbol{\varepsilon}}^{(e)}(\boldsymbol{x},t) \equiv \underbrace{\sum_{i=1}^{i=n_{node}} \boldsymbol{\nabla} N_i(\boldsymbol{x}) \otimes \dot{\boldsymbol{u}}_i(t)}_{\text{regular}} + \underbrace{\delta_s^{l_\mu^{(e)}} (\dot{\boldsymbol{\beta}}^{(e)} \otimes \boldsymbol{n}^{(e)})^S}_{\text{singular}} \tag{2.30}$$

  in terms of the ${l_\mu}^{(e)}$-regularized Dirac's delta function, $\delta_s^{l_\mu^{(e)}}$, displayed in Fig. 11, being $\boldsymbol{n}^{(e)}$ the direction of the element normal, provided by the solution of the discontinuous bifurcation problem presented in Sec. 2.5 in Paper #2. The resulting variational problem for the injection procedure is summarized in **Box A2** - Appendix B in Paper #2.

- ***Crack-path-field techniques***: their goal is the identification of the trace of the propagating crack by means of the so-called crack-path field. It is denoted as, $\mu(\boldsymbol{x},t)$, and obtained from a selected localized scalar variable $\alpha(\boldsymbol{x},t)$, which identifies the crack path as the locus where $\alpha(\boldsymbol{x},t)$ takes its transversal maximum value. In order to define this locus $\mathcal{S}_t$, some alternatives have been developed in this multiscale framework, see Eqs. $55-56$ in Paper #2 (Oliver et al., 2015). The variational statement for the crack-path field model is fully detailed in **Box 3.1** in Paper #2.

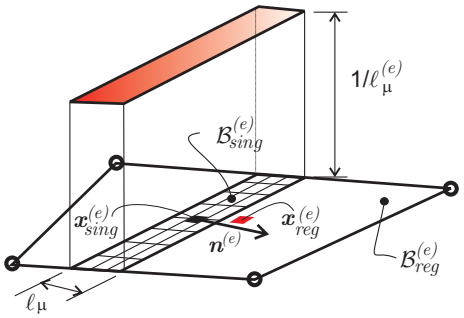

Figure 11: Strong discontinuity mode. Elemental regularized Dirac's delta function $\delta_s^{l_\mu^{(e)}}$.

The resulting procedure is a robust and efficient technique to model propagating material failure in a finite element setting. It is especially appropriate for capturing material failure propagation in coarse meshes, in contraposition of the alternative extra elemental character techniques (i. e. *phase-field*, *gradient* or *non-local damage* models), where several elements span the localization band. In addition, its implementation in an existing finite element code has a little intrusive character.

In regards to the space and time integrations, as commented above, injection of weak-discontinuity and strong-discontinuity modes requires, in principle, specific integration rules in space, i. e.: a standard four-point Gauss quadrature rule, and two additional sampling points, for injected elements, $\mathcal{B}^{(e)} \subset \mathcal{B}_{\text{wd}}$ and $\mathcal{B}^{(e)} \subset \mathcal{B}_{\text{sd}}$ so that $\mathcal{B}_{\text{loc}} = \mathcal{B}_{\text{wd}} \cup \mathcal{B}_{\text{sd}}$. Since those domains evolve along time (see Fig. 8), some additional problems on the time-integration of the resulting equilibrium equations are found. To tackle this issue, in (Oliver et al., 2014) and (Oliver et al., 2015) is proven that defining some "equivalent" stress entities, at the standard Gauss points, the spatial integration can be rephrased as a standard four Gauss points integration rule in the integration domain. This space-time integration rule is fully explained in Appendix B3 in Paper #2, and the corresponding stress evaluation is also summarized in Box A3.

3

MODEL ORDER REDUCTION IN MULTISCALE ANALYSIS

3.1 General Framework

Along this Thesis, some techniques for reducing the unaffordable computational cost inherent to the numerical simulation of multiscale fracture problems have been developed. Those techniques are combined to obtain a hyper-reduced order model HPROM, based on a two-stage strategy:

- First Stage: also termed Reduced Order Model (ROM), consists of a Galerkin projection, via *Proper Orthogonal Decomposition* (POD), onto a small space (*reduced-order manifold*), in which the set of modes conforming the projection basis are computed off-line.
- Second Stage: also called *HyPer-Reduced Order Model* (HPROM). Two different techniques have been developed here. The first one is based on *interpolation methods*, widely applied in problems exhibiting hardening behavior (see Paper #1) (Hernández et al., 2014b). The second one, based on a Reduced Optimal Quadrature (ROQ) rule, has been applied to fracture (non-smooth) problems. Similarly to the previous stage, the reduced modes functions used to reconstruct the state variables, are computed off-line.

In what follows, these techniques have been applied to the microscale Boundary Value Problem (BVP), while the finite element model at the macroscale remains as the standard one.

3.2 Reduced-order modeling (ROM) of the RVE problem

The model order reduction concept relies on the premise that, for any input parameter $\boldsymbol{\mu} \in \mathcal{D}$ governing the microscale displacement fluctuations $\tilde{\boldsymbol{u}}_{\mu}$, the solution can be approximated by a set of n linearly independent basis functions

$\boldsymbol{\Phi}$ approximately spanning the *primal variable*[1] space.

Following this idea, the *off-line stage* is devoted to determine via a POD technique, the reduced basis in which the High Fidelity (HF) solution is projected. Once this basis has been obtained, a subsequent *online stage* in the *reduced-space* is considered.

3.2.1 *Computation of the reduced basis functions*

Taking as a primal variable the displacement fluctuations, and departing from the problem depicted in Sec. 2.1, a first step consists of determining an approximation[2] of the finite element space of kinematically admissible microscale displacement fluctuations $\tilde{\mathcal{V}}_\mu^h$. This approximation is obtained as the span of the displacement fluctuation solutions obtained, for a judiciously chosen set of n_{hst} input strain *trajectories*, every trajectory being discretized into a number of steps n_{stp}. These set of finite element solutions are stored into the snapshot matrix $\mathbf{X}_u$ as column vectors:

$$\mathbf{X}_u = [\mathbf{U}^1, \mathbf{U}^2, \mathbf{U}^3, \cdots, \mathbf{U}^{n_{snp}}] \tag{3.1}$$

In consequence, the approximating space for $\tilde{\mathcal{V}}_\mu^h$, henceforth called the *snapshot space*, is then defined as:

$$\tilde{\mathcal{V}}_u^{snp} = \text{span}\{\tilde{\boldsymbol{u}}_\mu^1(\boldsymbol{y}), \tilde{\boldsymbol{u}}_\mu^2(\boldsymbol{y}), \tilde{\boldsymbol{u}}_\mu^3(\boldsymbol{y}), \cdots, \tilde{\boldsymbol{u}}_\mu^{n_{snp}}(\boldsymbol{y})\} \subseteq \tilde{\mathcal{V}}_\mu^h \tag{3.2}$$

where, $n_{snp} = n_{stp} \cdot n_{hst}$ is the total number of snapshosts.

Once the snapshot matrix $\mathbf{X}_u$ has been computed, the *Elastic-Inelastic decomposition* technique is used to determine the *reduced basis functions*. The reason for it relies on the fact that the Singular Value Decomposition (SVD) applied to the whole matrix $\mathbf{X}_u$, may produce basis with a large number of elements, which makes difficult to retrieve the response of the RVE in some specific cases. Particularly, the elastic response[3], might request a much larger number of basis functions, this translating into a significant waste of computational cost.

To eliminate this shortcoming, in this Thesis, it is proposed a time partition of the space of snapshots $\tilde{\mathcal{V}}_u^{snp}$ into *elastic* ($\tilde{\mathcal{V}}_{u,el}^{snp}$), and *inelastic* ($\tilde{\mathcal{V}}_{u,inel}^{snp}$) subspaces.

$$\tilde{\mathcal{V}}_u^{snp} = \tilde{\mathcal{V}}_{u,el}^{snp} \oplus \tilde{\mathcal{V}}_{u,inel}^{snp} \tag{3.3}$$

See: ***App. B*** ***Paper # 1***

obtaining the reduced basis as the combination (spatial sum) of both sub-bases. An orthonormal basis for $\tilde{\mathcal{V}}_{u,el}^{snp}$ is determined by taking a low number of elastic snapshots (at a minimum, $n_{snp}^e = 3$ for 2D problems, $n_{snp}^e = 6$ for 3D problems),

1 *Primal variable* is known as the selected variable to perform the reduction process.

2 In general, $\tilde{\mathcal{V}}_\mu^h$ cannot be precisely determined, such a task will require finite element analyses of the cell under *all conceivable* strain paths. Rather, one has to be content to construct an *approximation* of it.

3 Under an infinitesimal strain framework, this response is exactly recovered with only three basis (Hernández et al., 2014b).

and computing the corresponding orthonormal basis.

Once this set of elastic basis is known, the orthogonal projection of each snapshot $\tilde{\boldsymbol{u}}^k$ onto the orthogonal complement of $\tilde{\mathcal{V}}_{u,el}^{snp}$ is computed; with this new set of snapshots, the inelastic basis functions are obtained via SVD. Finally, the assembled basis results the following:

$$[\boldsymbol{\Phi}] = [\ \underbrace{\boldsymbol{\Phi}_1, \boldsymbol{\Phi}_2, \boldsymbol{\Phi}_3}_{\text{elastic modes basis}} \qquad \underbrace{\boldsymbol{\Phi}_4, \boldsymbol{\Phi}_5, \boldsymbol{\Phi}_6, \cdots, \boldsymbol{\Phi}_{n_u}}_{\text{"essential" inelastic modes basis}}\ ] \tag{3.4}$$

and the reduced-order space $\tilde{\mathcal{V}}_u^*$, spanned by this base, is:

$$\tilde{\mathcal{V}}_u^* = \tilde{\mathcal{V}}_{u,el}^{snp} \oplus \tilde{\mathcal{V}}_{u,inel}^{snp,*} = \text{span}\left\{ \underbrace{\boldsymbol{\Phi}_1, \boldsymbol{\Phi}_2, \boldsymbol{\Phi}_3}_{\text{elastic modes}} \quad \underbrace{\boldsymbol{\Phi}_4, \boldsymbol{\Phi}_5, \boldsymbol{\Phi}_6, \cdots, \boldsymbol{\Phi}_{n_u}}_{\text{"essential" inelastic modes}} \right\} \subseteq \tilde{\mathcal{V}}_\mu^h \tag{3.5}$$

Placing the m_e elastic modes in the first m_e positions, followed by the *essential*[4] inelastic modes, ensures the reduced-order model to deliver linear elastic solutions with the same accuracy than the HF solutions. For more details, the reader is encouraged to sent to the Appendix B in (Hernández et al., 2014b).

3.2.1.1 *Formulation of the reduced order model*

Once the reduced basis $[\boldsymbol{\Phi}]$ is computed, the online stage consists of solving the discrete version of the microscale equilibrium equation (via FE), projected onto the reduced-order space $\tilde{\mathcal{V}}_u^* \subseteq \tilde{\mathcal{V}}_\mu^h$ spanned by $[\boldsymbol{\Phi}]$. To this end, the test and trial functions, $\boldsymbol{\eta}$ and $\tilde{\boldsymbol{u}}_\mu$, are approximated by the following linear expansions:

See: ***Sec. 4 Paper # 1***

$$\tilde{\boldsymbol{u}}_\mu(\boldsymbol{y}) \approx \tilde{\boldsymbol{u}}_\mu^*(\boldsymbol{y}) = \sum_{i=1}^{n_u} \boldsymbol{\Phi}_i(\boldsymbol{y}) \boldsymbol{c}_i \tag{3.6}$$

$$\boldsymbol{\eta}(\boldsymbol{y}) \approx \boldsymbol{\eta}^*(\boldsymbol{y}) = \sum_{i=1}^{n_u} \boldsymbol{\Phi}_i(\boldsymbol{y}) \boldsymbol{c}_i^* \tag{3.7}$$

where, $\tilde{\boldsymbol{u}}_\mu^*$ and $\boldsymbol{\eta}^*$ stand for the *low-dimensional* approximations of trial and test functions, respectively.

Introducing expressions (3.6) and (3.7) into the discrete version of the microscale BVP (see Sec. 4 in (Hernández et al., 2014b)), and multiplying the resulting expression by $\boldsymbol{\Phi}^T$ (Galerkin projection), it yields:

4 Essential based on a threshold given by an *a-priori* error estimation, see Sec. 9.4 in (Hernández et al., 2014b), thus, $\tilde{\mathcal{V}}_{u,inel}^{snp,*}$ corresponds to the truncated version of the full base with $n_u - 3$ dominant modes.

PROBLEM A (ROM) (*Microscale reduced problem via POD*):
Given the macroscale strain, $\boldsymbol{\varepsilon}$, and the reduced basis for displacement fluctuations $\boldsymbol{\Phi}$, find $\boldsymbol{c} \in \mathbb{R}^{n_\varepsilon}$ satisfying:

$$\int_{\mathcal{B}_\mu} \mathbf{B}^{*T}(\boldsymbol{y})\boldsymbol{\sigma}_\mu(\boldsymbol{y}, \boldsymbol{\varepsilon} + \mathbf{B}^*\boldsymbol{c}, \boldsymbol{\mu})\, d\mathcal{B}_\mu \approx \sum_{i=1}^{n_g} \mathbf{B}^{*T}(\boldsymbol{y}_g, :)\boldsymbol{\sigma}_\mu(\boldsymbol{y}_g, :)\, w_g = \mathbf{0} \qquad (3.8)$$

where $\boldsymbol{c} = [c_1, c_2, \cdots, c_{n_u}] \in \mathbb{R}^{n_u}$ denotes the vector containing the coefficients associated to each basis function $\boldsymbol{\Phi}_i$, being $\boldsymbol{c}$ the basic unknowns for the standard reduced-order problem. $\mathbf{B}^*$ stands for the *reduced* strain-displacement matrix "B-matrix" defined as $\mathbf{B}^*(\boldsymbol{y}) = \mathbf{B}(\boldsymbol{y}) \cdot \boldsymbol{\Phi}(\boldsymbol{y})$. When using a Gauss quadrature integration scheme, $n_g = \mathcal{O}(n)$ is the total number of Gauss points of the mesh; w_g denotes the weight associated to the g-th Gauss point $\boldsymbol{y}_g$; $\mathbf{B}(\boldsymbol{y}_g, :)$ and $\boldsymbol{\sigma}_\mu(\boldsymbol{y}_g, :)$ stand for the reduced B-matrix and the stress vector at Gauss point $\boldsymbol{y}_g$, respectively (Hernández et al., 2014a).

3.2.2 *Specific issues in non-smooth (fracture) problems*

3.2.2.1 *Domain separation strategy*

Taking advantage of the unbounded character of the microscale strain field typically observed in this kind of problems, the failure cell is splitted into a *regular domain* (made of elastic matrix and possible inclusions) and a *cohesive domain* (cohesive bands exhibiting a softening cohesive behavior). Details on this issue can be found in Sec. 3.2.2 in Paper #3 (Oliver et al., 2017b).

3.2.3 *Formulation of the microscale saddle-point problem*

In addition to this proposal, the ROM of the failure cell is formulated in an unconventional manner, i. e.: *in terms of strain fluctuations rather than in terms of conventional displacement fluctuations*.

As it will be shown later, it is convenient to rephrase the original problem, posed in terms of displacement fluctuations (*PROBLEM-I* in Paper #3). The primary unknowns of the rephrased problem are now the microscale strain fluctuations instead of its displacement fluctuations, while the constrained original minimum problem (of the standard micro-cell BVP) is rewritten in terms of a Lagrange functional. The resulting formulation is a variationally consistent *saddle-point* formulation.

Considering the material free energy φ_μ for the isotropic damage model in $\mathcal{B}_{\mu,\text{coh}}$, the microscale stress field $\boldsymbol{\sigma}_\mu$ can be expressed as:

$$\boldsymbol{\sigma}_\mu(\boldsymbol{\varepsilon}_\mu, \boldsymbol{\mu}) = \frac{\partial \varphi_\mu(\boldsymbol{\varepsilon}_\mu, \boldsymbol{\mu})}{\partial \boldsymbol{\varepsilon}_\mu} = \frac{\partial \varphi_\mu(\boldsymbol{\varepsilon} + \tilde{\boldsymbol{\varepsilon}}_\mu, \boldsymbol{\mu})}{\partial \boldsymbol{\varepsilon}_\mu} \qquad (3.9)$$

complemented by the evolution laws of the internal variables (Simo and Hughes, 1998). Thus, in consonance with the hierarchical multiscale approach, the following parametrized functional can be defined:

$$\Pi_{[\varepsilon,\mu]}(\tilde{\boldsymbol{\varepsilon}}_\mu, \boldsymbol{\lambda}) = \int_{\mathcal{B}_\mu} \varphi_\mu(\tilde{\boldsymbol{\varepsilon}}_\mu)\, d\mathcal{B}_\mu + \boldsymbol{\lambda} : \int_{\mathcal{B}_\mu} \tilde{\boldsymbol{\varepsilon}}_\mu\, d\mathcal{B}_\mu \tag{3.10}$$

where, $\boldsymbol{\lambda}(t) \in \mathbb{S}^{n\times n}$, is a symmetric second order tensor Lagrange multiplier enforcing condition (2.4) on the microscale strain fluctuations $\tilde{\boldsymbol{\varepsilon}}_\mu$. With this parametrized functional $\Pi_{[\varepsilon,\mu]}(\tilde{\boldsymbol{\varepsilon}}_\mu, \boldsymbol{\lambda})$, a *saddle-point* problem can be stated as:

PROBLEM II (HF) (*Microscale saddle-point problem)*: Given the macroscale strain, $\boldsymbol{\varepsilon}$, find $\tilde{\boldsymbol{\varepsilon}}_\mu$ and $\boldsymbol{\lambda}$ satisfying:

$$\{\tilde{\boldsymbol{\varepsilon}}_\mu(\boldsymbol{\varepsilon}, \boldsymbol{\mu}), \boldsymbol{\lambda}(\boldsymbol{\varepsilon}, \boldsymbol{\mu})\} = \arg\Big\{\min_{\tilde{\boldsymbol{\varepsilon}}_\mu \in \mathcal{E}_\mu} \max_{\boldsymbol{\lambda}\in\mathbb{S}^{n\times n}} \Pi_{[\varepsilon,\mu]}(\tilde{\boldsymbol{\varepsilon}}_\mu, \boldsymbol{\lambda})\Big\} \tag{3.11}$$

Such that:

$$\dot{\boldsymbol{\mu}} = f(\boldsymbol{\varepsilon}_\mu, \boldsymbol{\mu})$$

where $\mathcal{E}_\mu$ stands for the space of microscale kinematically compatible strain fluctuations and, f stands for the evolution equation of the internal variables. After considering that the microscale stress field $\boldsymbol{\sigma}_\mu$ is given by Eq. (3.9), the following optimality conditions emerge:

$$\int_{\mathcal{B}_\mu} [\boldsymbol{\sigma}_\mu(\tilde{\boldsymbol{\varepsilon}}_\mu)(\boldsymbol{y}) + \boldsymbol{\lambda}] : \hat{\boldsymbol{\varepsilon}}_\mu\, d\mathcal{B}_\mu = 0; \qquad \forall \hat{\boldsymbol{\varepsilon}}_\mu \in \mathcal{E}_\mu \tag{3.12}$$

$$\hat{\boldsymbol{\lambda}} : \int_{\mathcal{B}_\mu} \tilde{\boldsymbol{\varepsilon}}_\mu\, d\mathcal{B}_\mu = \mathbf{0}; \qquad \forall \hat{\boldsymbol{\lambda}} \in \mathbb{S}^{n\times n} \tag{3.13}$$

Eqs. (3.12) and (3.13) provide the solution of the saddle-point problem stated in Eq. (3.11). It can be proven that Eqs. (3.12) and (3.13) make *PROBLEM II* equivalent to the original problem in Eq. (2.10), but now rephrased in terms of the microscale strain fluctuations $\tilde{\boldsymbol{\varepsilon}}_\mu$ (see *PROBLEM I-R* in Paper #3).

3.2.3.1 *Computation of the reduced basis functions*

The transition from the high-dimensional finite element space to the reduced-order space, is accomplished by applying the POD technique, now for non-smooth problems. The standard reduced order model is based on the reduction of the strain fluctuation field $\tilde{\boldsymbol{\varepsilon}}_\mu$, and, for these purposes, the first step consists of generating a collection of solutions (samples) from different trial loading cases, representatives of all possible loading cases.

In each trial case, the microscale strain fluctuation $\tilde{\boldsymbol{\varepsilon}}_\mu$, at every Gauss point, is collected and stored in the snapshot matrix as a column vector:

$$\mathbf{X}_k = [\tilde{\boldsymbol{\varepsilon}}_\mu(\boldsymbol{y}_1), \tilde{\boldsymbol{\varepsilon}}_\mu(\boldsymbol{y}_2), \cdots, \tilde{\boldsymbol{\varepsilon}}_\mu(\boldsymbol{y}_{N_g})]^T$$

$$\mathbf{X} = [\mathbf{X}_1, \mathbf{X}_2, \mathbf{X}_3, \cdots, \mathbf{X}_{n_{snp}}] \in \mathbb{R}^{(N_g \cdot n_\sigma) \times n_{snp}} \tag{3.14}$$

See: ***Sec.4 Paper 3***

where, n_{snp} is the number of snapshots vectors. Therefore, $\mathbf{X}$ represents a number of sampled solutions obtained with the HF model, under different loading conditions. For more details, the reader is addressed to Sec. 4 in (Oliver et al., 2017a).

In order to get a more accurate estimation of the dominant modes of the microscale strain fluctuations, it is convenient to separate the microscale into specific *sub-blocks* in accordance with the type of material response observed during the load history. The procedure is sketched in Fig. 12:

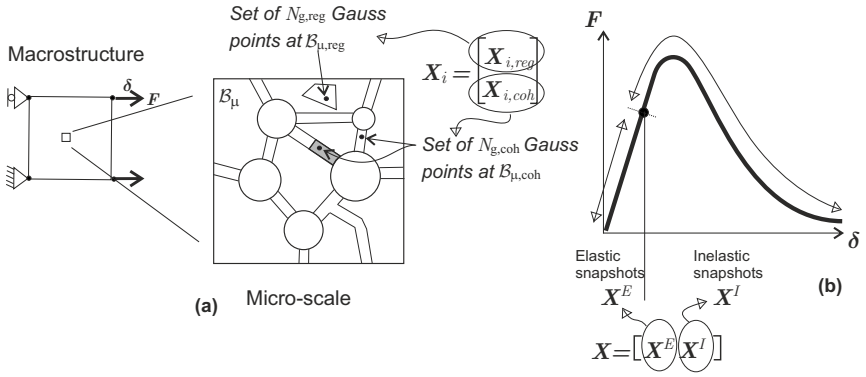

Figure 12: (a) All entries of $\mathbf{X}$ are partitions into two sub-blocks: $\mathbf{X}_{reg}$ and $\mathbf{X}_{coh}$, the strain fluctuations from points at *regular* and *cohesive* domains, respectively. (b) Snapshots taken from the elastic regime of the failure cell correspond to the sub-block $\mathbf{X}^E$. Snapshots taken during the inelastic regime (at least one Gauss point at $\mathcal{B}_{\mu,\text{coh}}$ is in inelastic state) correspond to the sub-block $\mathbf{X}^I$.

In addition, the *Elastic-Inelastic snapshot decomposition* above explained (Hernández et al., 2014b), is also applied to each sub-block. Thus, without loss of generality, the snapshot entries are organized so that the first, $N_{g,reg}$ entries correspond to Gauss points in $\mathcal{B}_\mu \setminus \mathcal{B}_{\mu,\text{coh}}$, while the remaining $N_{g,coh}$ entries correspond to Gauss points in $\mathcal{B}_{\mu,\text{coh}}$.

See: ***Sec.3.2.2 Paper 3***

In accordance with this criterion, the snapshot matrix (3.14) can now be partitioned into sub-matrices as follows:

$$[\mathbf{X}] = \begin{bmatrix} \mathbf{X}_{\text{reg}} \\ \mathbf{X}_{\text{coh}} \end{bmatrix} = \begin{bmatrix} \mathbf{X}^E_{\text{reg}} & \mathbf{X}^I_{\text{reg}} \\ \mathbf{X}^E_{\text{coh}} & \mathbf{X}^I_{\text{coh}} \end{bmatrix} \qquad N_g = N_{g,reg} + N_{g,coh} \tag{3.15}$$

where $\mathbf{X}_{\text{reg}}$ and $\mathbf{X}_{\text{coh}}$ collect the strain fluctuations located outside and inside the cohesive bands, respectively. The second matrix in (3.15) emphasizes the double partition performed in accordance with elastic-inelastic regimes.

After some additional manipulations, the corresponding set of orthonormal basis is obtained as:

$$\boldsymbol{\Psi}_G = [\boldsymbol{\Psi}_G^E \;\; \boldsymbol{\Psi}_G^I] \tag{3.16}$$

The number of reduced basis in $\boldsymbol{\Psi}_G$ is: $n_\varepsilon = 6 + n^I_{\varepsilon,reg} + n^I_{\varepsilon,coh}$, where the values $n^I_{\varepsilon,reg}$ and $n^I_{\varepsilon,coh}$ are obtained from the SVD applied to the inelastic projected snapshots. Additional details can be found in Sec. 3.2.2 in Paper #3.

3.2.3.2 *Formulation of the reduced order model*

Once the reduced basis $\boldsymbol{\Psi}_G$ is known, the strain fluctuations are interpolated as a linear combination of the elements of this basis as:

$$\tilde{\boldsymbol{\varepsilon}}_{\boldsymbol{\mu}}(\boldsymbol{y}, t) = \sum_{i=1}^{n_\varepsilon} \boldsymbol{\Psi}_i(\boldsymbol{y}) \cdot c_i(t) = \boldsymbol{\Psi}_G(\boldsymbol{y}) \cdot \boldsymbol{c}(t) \tag{3.17}$$

where each element $\boldsymbol{\Psi}_i$, of the basis $\boldsymbol{\Psi}_G$, is a micro-strain fluctuation mode and the vector of time dependent coefficients $\boldsymbol{c}(t) = [c_1, c_2, \cdots, c_{n_\varepsilon}]$ ($\boldsymbol{c} \in \mathbb{R}^{n_\varepsilon}$) represents their corresponding amplitudes (the actual unknowns of the problem). In the same way, the variations of the microscopic strain fluctuations are expressed similar to (3.17) as:

See: ***Sec.3.1 Paper 3***

$$\hat{\boldsymbol{\varepsilon}}_{\boldsymbol{\mu}}(\boldsymbol{y}, t) = \boldsymbol{\Psi}_G(\boldsymbol{y}) \cdot \hat{\boldsymbol{c}}(t) \tag{3.18}$$

The problem solved in the online stage is then the following:

PROBLEM III (ROM) (RVE *saddle point problem)*:
Given the macroscale strain, $\boldsymbol{\varepsilon}$, find $\mathbf{c} \in \mathbb{R}^{n_\varepsilon}$ and $\boldsymbol{\lambda} \in \mathbb{R}^{n_\sigma}$ satisfying:

$$\{\boldsymbol{c}(\boldsymbol{\varepsilon}, \boldsymbol{\mu}), \boldsymbol{\lambda}(\boldsymbol{\varepsilon}, \boldsymbol{\mu})\} = \arg\Big\{\min_{\boldsymbol{c} \in \mathbb{R}_{n_\varepsilon}} \max_{\boldsymbol{\lambda} \in \mathbb{R}^{n_\sigma}} \Pi_{[\boldsymbol{\varepsilon}, \boldsymbol{\mu}]}(\boldsymbol{\Psi c}, \boldsymbol{\lambda})\Big\} \tag{3.19}$$

$$\text{with} \quad \Pi_{[\boldsymbol{\varepsilon}, \boldsymbol{\mu}]}(\boldsymbol{\Psi c}, \boldsymbol{\lambda}) = \int_{\mathcal{B}_\mu} \varphi_\mu(\boldsymbol{\varepsilon} + \boldsymbol{\Psi c})\, d\mathcal{B}_\mu + \boldsymbol{\lambda}^T \left(\int_{\mathcal{B}_\mu} \boldsymbol{\Psi}\, d\mathcal{B}_\mu \right) \boldsymbol{c}$$

such that:

$$\dot{\boldsymbol{\mu}} = f(\boldsymbol{\varepsilon}_\mu, \boldsymbol{\mu})$$

The optimality conditions for the problem above yield:

$$\frac{\partial}{\partial \boldsymbol{c}} \Pi_{[\boldsymbol{\varepsilon}, \boldsymbol{\mu}]}(\boldsymbol{\Psi c}, \boldsymbol{\lambda}) = \int_{\mathcal{B}_\mu} \boldsymbol{\Psi}^T \boldsymbol{\sigma}_\mu(\boldsymbol{\varepsilon} + \boldsymbol{\Psi c})\, d\mathcal{B}_\mu + \left(\int_{\mathcal{B}_\mu} \boldsymbol{\Psi}^T\, d\mathcal{B}_\mu \right) \boldsymbol{\lambda} = \mathbf{0} \tag{3.20}$$

$$\frac{\partial}{\partial \boldsymbol{\lambda}} \Pi_{[\boldsymbol{\varepsilon}, \boldsymbol{\mu}]}(\boldsymbol{\Psi c}, \boldsymbol{\lambda}) = \left(\int_{\mathcal{B}_\mu} \boldsymbol{\Psi}^T\, d\mathcal{B}_\mu \right) \boldsymbol{c} = \mathbf{0} \tag{3.21}$$

which, expressed in matrix notation, yield:

$$\boldsymbol{\Psi}_G^T [\mathbb{W}] \left([\boldsymbol{\sigma}_\mu(\boldsymbol{c})]_G + [\boldsymbol{\lambda}]_G \right) = \mathbf{0} \tag{3.22}$$

$$[W] \cdot [\boldsymbol{\Psi}_G] \boldsymbol{c} = \mathbf{0} \tag{3.23}$$

where $[\boldsymbol{\sigma}_\mu(\boldsymbol{c})]_G \in \mathbb{R}^{(n_\sigma \cdot N_g)}$ is the column vector constituted by piling-up the N_g stress vectors, $\boldsymbol{\sigma}_\mu(\boldsymbol{c}) \in \mathbb{R}^{(n_\sigma)}$, evaluated at the integration Gauss points. The column vector $[\boldsymbol{\lambda}]_G$ is also the pilled-up of N_g repeated values of the same constants vector $\boldsymbol{\lambda} \in \mathbb{R}^{(n_\sigma)}$. The square diagonal matrix $[\mathbb{W}] \in \mathbb{R}^{(N_g n_\sigma \times N_g n_\sigma)}$, and the rectangular matrix $[W] \in \mathbb{R}^{(n_\sigma \times N_g n_\sigma)}$, collect the Gauss weights: $w_1, w_2, ..., w_{N_g}$, which for plane strain cases ($n_\sigma = 4$) are distributed in sub-block matrices $\mathbb{W}_i \in \mathbb{R}^{(4\times 4)} (i = 1, 2, 3, 4, ..., N_g)$, as follows:

See: ***Sec. 3.2 Paper 3***

$$\mathbb{W} = \begin{bmatrix} \mathbb{W}_1 & \mathbb{O} & \dots & \mathbb{O} \\ \mathbb{O} & \mathbb{W}_1 & \dots & \mathbb{O} \\ \vdots & \vdots & \ddots & \vdots \\ \mathbb{O} & \mathbb{O} & \dots & \mathbb{W}_{N_g} \end{bmatrix}; \quad [W] = [\mathbb{W}_1 \dots \mathbb{W}_{N_g}] \tag{3.24}$$

being $\mathbb{W}_i$ a matrix with the corresponding i-th Gauss weight placed at the diagonal.

Now, the unknowns for the reduced order model are, the modal amplitudes $\boldsymbol{c}(t)$, and the Lagrange multiplier $\boldsymbol{\lambda}$.

Now considering the system of equations (3.22) and (3.23) for $\boldsymbol{c}$ and $\boldsymbol{\lambda}$, it could be expected that this problem, with $n_\varepsilon + n_\sigma$ equations, should be less computationally costly, than the HF model. However, this is not the case: the numerical simulations with the ROM model do not substantially reduce the computational cost, and little (or even smaller than one) speedups are obtained. This fact highlights that the actual *bottleneck* for fast online computation is not the solution of the balance equations but, rather, the determination of the stresses, internal forces and stiffness matrices at every integration point of the underlying finite element mesh. Therefore, an additional technique is proposed to reduce the amount of integration points in which the constitutive equation is evaluated.

3.3 Numerical Integration: Reduced Order Quadrature Technique (ROQ)

Attention is then focused on reducing the computational cost arisen by the use of a classical Gauss quadrature for the numerical integration of the optimality conditions (Eqs. (3.20) and (3.21)).

For this purpose, a *reduced integration technique* has been developed by resorting to a nonconventional method, termed Reduced Optimal Quadrature (ROQ), to integrate the term involving the microscale free energy $\varphi_\mu(\boldsymbol{\varepsilon} + \boldsymbol{\Psi}\boldsymbol{c})$ in (3.19):

$$\int_{\mathcal{B}_\mu} \varphi_\mu(\boldsymbol{\varepsilon} + \boldsymbol{\Psi}\boldsymbol{c}, \boldsymbol{\mu})\, d\mathcal{B}_\mu \approx \sum_{j=1}^{N_r} \varphi_\mu(\boldsymbol{\varepsilon} + \boldsymbol{\Psi}\boldsymbol{c}, \boldsymbol{\mu})\, w_j := \int_* \varphi_\mu(\boldsymbol{\varepsilon} + \boldsymbol{\Psi}\boldsymbol{c}, \boldsymbol{\mu})\, d\mathcal{B}_\mu \tag{3.25}$$

Where $\int_*(\cdot)\, d\mathcal{B}_\mu$ stands for he reduced order quadrature.

The reduced quadrature technique is based on selecting, from the initial set of "Gauss" sampling points, and through an adequate algorithm, an "equivalent" subset of sampling points $z_j;\ j = 1, 2, \ldots, N_r$, and their new corresponding weights $w_j;\ j = 1, 2, \ldots, N_r$. The success of the reduced integration numerical scheme, in front of the conventional Gauss quadrature, lies on the fact that it is possible to reduce notably the number of involved quadrature points to $N_r \ll N_g$, being N_g the number of integration points for the Gauss quadrature scheme, keeping under strict control, or even reducing to zero, the numerical error introduced by the reduced quadrature rule. Then, the microscale potential energy in Eq. (3.25), is re-expressed as:

$$\Pi^*_{[\boldsymbol{\varepsilon},\boldsymbol{\mu}]}(\boldsymbol{\Psi c}, \boldsymbol{\lambda}) = \int_* \varphi_\mu(\boldsymbol{\varepsilon} + \boldsymbol{\Psi c})\, d\mathcal{B}_\mu + \boldsymbol{\lambda}^T \left(\int_{\mathcal{B}_\mu} \boldsymbol{\Psi}\, d\mathcal{B}_\mu \right) \boldsymbol{c} \tag{3.26}$$

In consequence, the corresponding optimality conditions (equilibrium equations) to be solved during the online stage are:

PROBLEM IV (HPROM) (*Microscale reduced saddle-point problem)*: Given the macroscale strain, $\boldsymbol{\varepsilon}$, find $\boldsymbol{c} \in \mathbb{R}^{n_\varepsilon}$ and $\boldsymbol{\lambda} \in \mathbb{R}^{n_\sigma}$ satisfying:

$$\underbrace{\int_* \boldsymbol{\Psi}^T \boldsymbol{\sigma}_\mu(\boldsymbol{\varepsilon} + \boldsymbol{\Psi c})\, d\mathcal{B}_\mu}_{\text{Reduced O. Quadrature}} + \underbrace{\left(\int_{\mathcal{B}_\mu} \boldsymbol{\Psi}^T\, d\mathcal{B}_\mu \right)}_{\text{Gauss Quadrature}} \boldsymbol{\lambda} = \boldsymbol{0} \tag{3.27}$$

$$\underbrace{\left(\int_{\mathcal{B}_\mu} \boldsymbol{\Psi}^T\, d\mathcal{B}_\mu \right)}_{\text{Gauss Quadrature}} \boldsymbol{c} = \boldsymbol{0} \tag{3.28}$$

A similar procedure could also be used for the integral terms (underlined as "Gauss quadrature") in Eqs. (3.27) and (3.28). However, this would not produce a substantial computational cost gain due to the fact that those terms are constant (not depending neither on the unknowns of the problem nor on the constitutive internal variables). They are required to be integrated only once, via the standard Gauss quadrature, and the result can be stored, and retrieved when necessary, during the online stage execution.

3.3.1 *Reduced Optimal Quadrature*

In spite that the goal of the ROQ is to develop a reduced cost interpolation scheme as a general framework for both static and dynamic problems, attention is focussed here on the multiscale quasi-static fracture problems. The minimum number of quadrature points providing an admissible integration error in the free energy integral, (3.25) is based on the optimal linear expansion of φ_μ in terms of the free energy modes $\boldsymbol{\Phi}_i\, (i = 1, 2, 3, \ldots, n_\varphi)$ and its corresponding

amplitudes f_i, i. e., (a similar expression to that adopted for constructing the reduced microscopic strain fluctuations in Eq. (3.17)), as follows:

$$\varphi_\mu(\boldsymbol{\Psi}(\boldsymbol{y})\boldsymbol{c}) = \sum_{i=1}^{n_\varphi} \boldsymbol{\Phi}_i(\boldsymbol{y}) f_i(\boldsymbol{\varepsilon}, \boldsymbol{c}, \boldsymbol{\mu}) \tag{3.29}$$

With the previous approximation in hand, the total microscale free energy can be expressed as:

$$\int_{\mathcal{B}_\mu} \varphi_\mu(\boldsymbol{\varepsilon} + \boldsymbol{\Psi}\boldsymbol{c}, \boldsymbol{\mu})\, d\mathcal{B}_\mu \approx \sum_{i=1}^{n_\varphi} \underbrace{\left(\int_{\mathcal{B}_\mu} \boldsymbol{\Phi}_i(\boldsymbol{y})\, d\mathcal{B}_\mu \right)}_{\text{“Gauss Quadrature”}} f_i(\boldsymbol{\varepsilon}, \boldsymbol{c}, \boldsymbol{\mu}) \approx \sum_{i=1}^{n_\varphi} \underbrace{\left(\int_{*} \boldsymbol{\Phi}_i(\boldsymbol{y})\, d\mathcal{B}_\mu \right)}_{\text{Reduced O. Quadrature}} f_i(\boldsymbol{\varepsilon}, \boldsymbol{c}, \boldsymbol{\mu}) \tag{3.30}$$

3.3.2 *A Greedy algorithm for obtaining a reduced quadrature rule*

In order to obtain the reduced optimal numerical quadrature rule, the following optimization problem is considered:

OPTIMIZATION PROBLEM : Given the expanded reduced basis $\boldsymbol{\Phi}$, and the set of sampling points $\mathcal{S} = \{\boldsymbol{y}_1, \boldsymbol{y}_2, \ldots, \boldsymbol{y}_{N_g}\}$, find $\boldsymbol{\omega} \in \mathbb{R}_+^{N_r}$ and $\mathcal{Z} \in \mathbb{N}^{N_r}$ satisfying:

$$(\boldsymbol{\omega}, \mathcal{Z}) = \arg\min_{(\mathbf{w} \in \mathbb{R}_+^m, \bar{\mathcal{Z}}_g \in \mathcal{B}_\mu)} \sqrt{\sum_{i=1}^{n_\varphi} (e_i)^2 + (e_{vol})^2} \tag{3.31}$$

being:

$$e_i := \sum_{j=1}^{N_r} \omega_j \boldsymbol{\Phi}_i(\bar{\boldsymbol{y}}_j) - \int_{\mathcal{B}_\mu} \boldsymbol{\Phi}_i(\boldsymbol{y})\, d\mathcal{B}_\mu \qquad e_{vol} := \sum_{j=1}^{N_r} \omega_j - \Omega_\mu \tag{3.32}$$

Where, e_i and e_{vol} stand for the error committed through the reduced integration of every free energy reduced basis function, and the error in the integration of the volume Ω_μ, respectively. The resulting algorithm (described in the flowchart of **Box IV** in (Paper #4) (Hernández et al., 2017)) returns a sub-set of optimal Gauss-points, and the corresponding weights, that integrate “exactly” the basis $\boldsymbol{\Phi}(\boldsymbol{y})$ and, therefore, the free energy in Eq. (3.29).

See: ***Sec. 5*** ***Paper 4***

3.3.2.1 *Computation of the reduced basis functions*

Regarding the computation of the microscale energy reduced basis $\boldsymbol{\Phi}$, a SVD-based strategy is used in the off-line stage, similar to that described in Sec. 3.2.1.

The method is based again on the construction of a snapshots matrix, in this case, for the free energy, and the computation of its corresponding reduced basis via SVD. For this purpose, two options appear:

- Consruct the microscale energy snapshots by collecting solutions of the ROM in (3.19). This strategy implies the following actions: (a) the ROM is constructed considering a number of microscale strain fluctuation modes n_ε. In consequence, the obtained energy snapshots matrix $\mathbf{X}^\varphi$ provides a reduced basis, which spans a space determined by the selected set of strain fluctuation modes.
- Construct the microscale energy snapshots by collecting solutions of the HF model in (3.11). This strategy computes *simultaneously* the microscale energy and the strain fluctuation snapshots. The resulting reduced bases are consequently independent from each other, but they converge to the HF solution as the number of strain basis functions, n_ε, and energy basis functions, n_ψ, increase.

The first method is considered as the algorithmically *consistent* strategy. However, it is also more expensive than the second one. The reason relies on the fact that, in order to get the reduced basis for the microscale energy $\mathbf{\Phi}$, training trajectories have to be computed twice: a) First using the HF model to obtain the strain modes $\mathbf{\Psi}$, 2) Second, using the ROM model to obtain the corresponding free-energy modes $\mathbf{\Phi}$.

Both strategies have been tested and both provide accurate results. However, the later, being the cheaper and simpler one, was adopted as the most convenient.

In summary, both the strains and the free energies of the microscale are sampled simultaneously at the off-line stage, for different sampling trajectories with the HF model, and a series of q_{snp} snapshots of energy, φ_μ, are evaluated and collected for each Gauss point. Then, the microscale energy snapshot matrix $\mathbf{X}^\varphi$ is built as:

$$\mathbf{X}^\varphi = [\mathbf{X}_1^\varphi, \mathbf{X}_2^\varphi, \cdots, \mathbf{X}_{p_{snp}}^\varphi] \in \mathbb{R}^{(N_g \cdot n_\sigma) \times p_{snp}} \qquad \mathbf{X}_k^\varphi = [\varphi_\mu(\boldsymbol{y}_1), \varphi_\mu(\boldsymbol{y}_2), \ldots, \varphi_\mu(\boldsymbol{y}_{N_g})]_k^T \tag{3.33}$$

In accordance with the position of the Gauss point, in the finite element mesh, and following a similar procedure to that adopted in Eq. (3.15), this snapshot matrix is also partitioned into components associated to the domains $\mathcal{B}_\mu \setminus \mathcal{B}_{\mu,\text{coh}}$ and $\mathcal{B}_{\mu,\text{coh}}$ as:

*See: **Sec. 3.4** **Paper 3***

$$[\mathbf{X}^\varphi] = \begin{bmatrix} \mathbf{X}_\varphi^{\text{reg}} \\ \mathbf{X}_\varphi^{\text{coh}} \end{bmatrix} = \begin{bmatrix} \mathbf{X}_\varphi^{\text{reg},E} & \mathbf{X}_\varphi^{\text{reg},I} \\ \mathbf{X}_\varphi^{\text{coh},E} & \mathbf{X}_\varphi^{\text{coh},I} \end{bmatrix} \qquad N_g = N_{g,reg} + N_{g,coh} \tag{3.34}$$

and the SVD technique is then separately applied to both partitions of $\mathbf{X}_\varphi^E$ to obtain two distinct (orthogonal) bases, for the elastic regime of both subdomains:

$$\mathbf{\Phi}^E = \begin{bmatrix} \mathbf{\Phi}^{\text{reg},E} & \mathbf{0} \\ \mathbf{0} & \mathbf{\Phi}^{\text{coh},E} \end{bmatrix}; \quad \mathbf{\Phi}^{\text{reg},E} \in \mathbb{R}^{(N_{g,reg} \times \text{n}_{elas})}; \; \mathbf{\Phi}^{\text{coh},E} \in \mathbb{R}^{(N_{g,coh} \times \text{n}_{elas})} \tag{3.35}$$

The corresponding inelastic reduced basis functions are also computed via SVD, following a procedure similar to the one described in Sec. 3.2.1. The complete reduced basis for the energy field $\mathbf{\Phi}$, is made of the union of $\mathbf{\Phi}^E$ and $\mathbf{\Phi}^I$:

$$\boldsymbol{\Phi} = [\boldsymbol{\Phi}^E \;\; \boldsymbol{\Phi}^I] \tag{3.36}$$

The number of basis vectors in $\boldsymbol{\Phi}$ is: $n_\varphi = 12 + n^I_{\varphi,reg} + n^I_{\varphi,coh}$, where the values of $n^I_{\varphi,reg}$ and $n^I_{\varphi,coh}$ are obtained from the solution of the SVD applied to the inelastic projected snapshots.

3.4 Numerical assessment and approximation errors

The accuracy of the reduced models, ROM and HPROM, depends on several aspects. In order to assess it, three different sets of tests are done:

- *Consistency tests:* A set of trajectories already sampled with the HF model during the microscale sampling process in the off-line stage, are re-evaluated using the ROM and HPROM strategies. This kind of assessment provides an estimation of the quality and richness of the basis to reproduce the stored snapshots, and the accuracy of the ROQ scheme. It is expected that the error with respect to the HF solutions (*consistency error*) tends to zero as the number of considered modes, for each reduction strategies, are increased.
- *Accuracy tests:* Similarly to the aforementioned consistency tests, the representative cell is subjected to a *unsampled loading trajectory*. In these cases, the quality of the reduced bases and the ROQ scheme is also tested. In contrast with the previous case, unsampled trajectories during the off-line stage, are not supposed to be exactly captured, due to the underlying *sampling error*.
- *Multiscale structural tests:* These kind of tests are based on multiscale benchmarks. The aim is to evaluate the accuracy of the solutions when the proposed overall HPROM strategy is applied, and to obtain the corresponding speed-ups.

Details on this issue can be found in Sec. 5 in Paper #3.

3.5 Representative example

A squared microscale model, made of a matrix and randomly distribuited aggregates, is devised and tested (see figure 14) to simulate the meso-structure of a cementitious-like material (concrete). Some details about the finite element model are presented in Table 1. Trying to mimic the concrete material response, the failure cell is modeled with three components: *aggregates*, which are assumed to be elastic, *bulk matrix*, which is also assumed elastic, and *interfaces* (matrix-matrix and matrix-aggregates), which are modelled with cohesive-band equipped with an isotropic damage constitutive law. The properties of the components in the microscale are defined in Table 2.

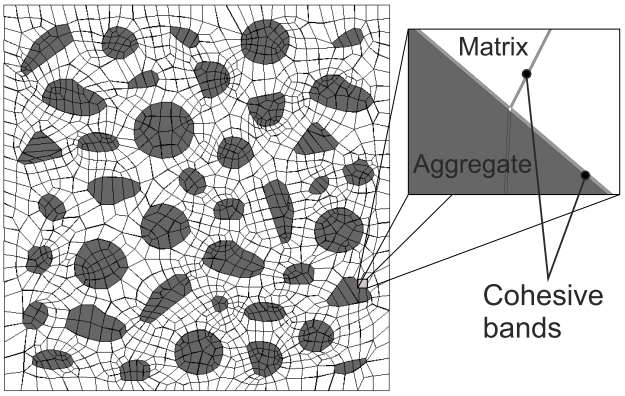

Figure 13: Failure cell

Number of FE	Number of D.o.f.'s	Number of Cohesive Bands	Total number of Gauss points (N_g)
5409	14256	2189	21636

Table 1: Finite element models for the tested microstructure.

3.5.1 *Design of the HPROM Strategy*

Figure 14 shows the summary of a number of results obtained by running the HPROM strategy in a number of cases for the microstructure in Fig. 13.

The plots can be used as an "abacus" for a-priori selection by the user of the HPROM strategy in a multiscale problem (for a given microstructure at the RVE). For instance, by selecting the admissible error, in the top figure, (say error=3,5%), the number of strain modes, ($n_\varepsilon = 80$) is obtained. Entering in the lower plot, with this result, ($n_\varepsilon = 80$), one obtains the suitable number of integration points ($OQN \simeq 200$) and the speedup that can be expected ($speedup \simeq 110$).

The availability of such an abacus (constructed off-line) for a specific RVE microstructure, allows the user's a-priori selection of the appropriated HPROM strategy, by balancing the admissible error vs. the desired speedup.

3.5.2 *Multiscale crack propagation problem: L-shaped panel*

The panel in Figure 15 is a benchmark commonly used for testing macroscale propagating fracture models. This concrete specimen is considered here to test the qualitative results and convergence properties of the proposed HPROM approach, when utilized in real FE^2 multiscale crack propagation problems.

	E_μ [MPa]	ν_μ	$\sigma_{\mu u}$ [MPa]	$G_{\mu f}$ [N/m]
Elastic matrix	1.85×10^4	0.18	—	—
Elastic aggregate	3.70×10^4	0.18	—	—
Cohesive bands of matrix-matrix interface	1.85×10^4	0.18	2.60	140
Cohesive bands of matrix-aggregate interface	1.85×10^4	0.18	—	—

Table 2: Material properties of the sampled microcell. Properties are: E_μ (Young's modulus), ν_μ (Poisson ratio), $\sigma_{\mu u}$ (ultimate tensile stress) and $G_{\mu,f}$ (fracture energy).

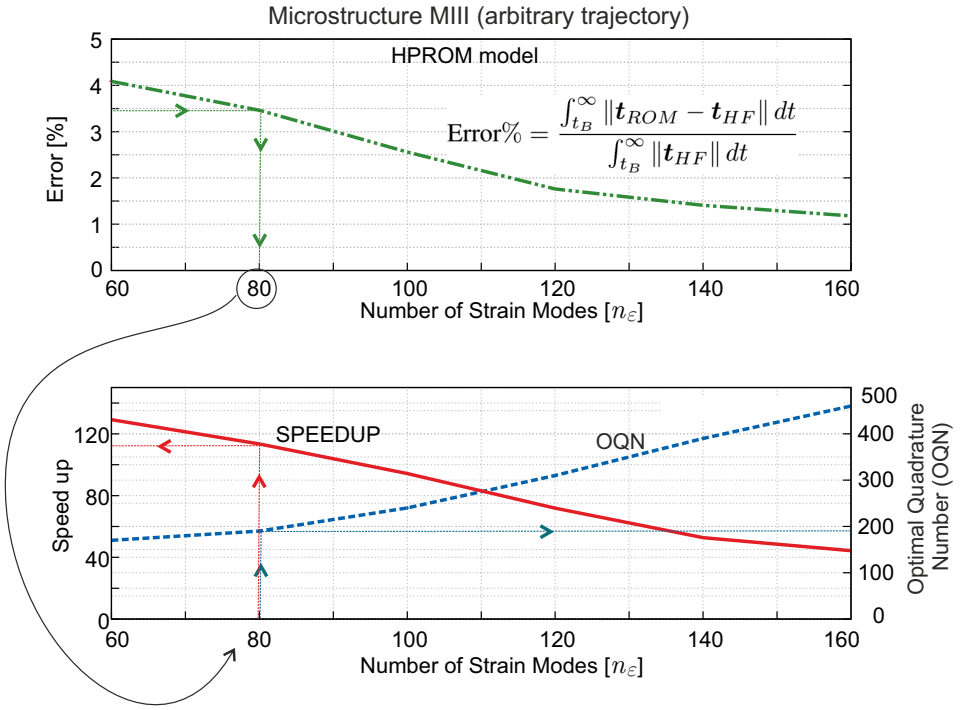

Figure 14: HPROM design diagrams. *Top*: HPROM error in terms of the number of strain modes. *Bottom:* OQN and obtained speedup in terms of the number of strain modes. By selecting the admissible error (say 3,5%) in the upper diagram, one obtains the requested number of strain modes, $n_\varepsilon = 80$. Entering with this result in the lower diagram one obtains the suitable number of integration points ($OQN = 200$) and the resulting speedup ($speedup = 110$).

The geometry of the simulated specimen is depicted in Figure 15-a. As shown in Figure 15-b, the domain of the L-shaped panel is split into two domains: 1) the multiscale domain (with 721 finite elements) corresponding to the region where the crack is expected to propagate, modeled with the HPROM of the microstructure

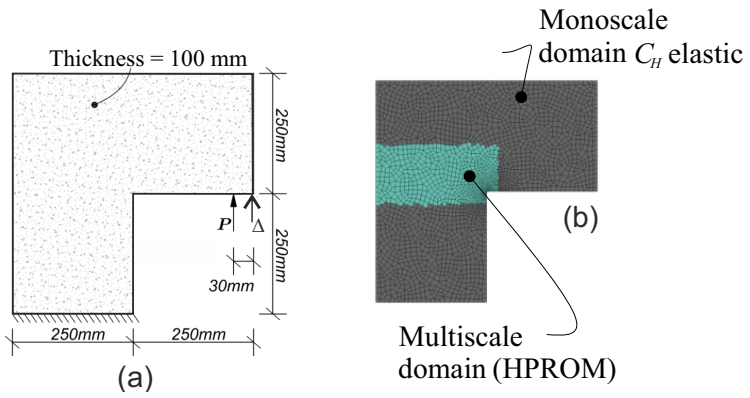

Figure 15: L-shaped panel: a) Specimen geometry; b) Finite element mesh

depicted in Figure 13, and 2) the remaining part of the panel, which is modeled with an elastic monoscale approach (using 1709 finite elements), where the elasticity tensor is obtained through an *elastic homogenization* of the microstructure elastic properties. Even for this (rather coarse) multiscale problem the high fidelity HF computational solution is extremely costly to handle, until the point that, with the available computational resources[5], it was not possible to display the complete action-response curve (in Fig. 16).

However, the remaining structural responses in figure 16, obtained through a number of HPROM strategies, involve very reasonable computational costs, and they were obtained in advance *with no previous knowledge of the HF* results. The accuracies are very good, and a response indistinguishable from the HF can be obtained 60 times faster ($speedup = 60$). A less accurate response, but with a fairly good agreement with the HF can be obtained with $speedup = 130$.

In Fig. 17, the evolution of the microscale crack opening is shown. It is worth noting that, both, the microscale failure mechanism and displacement jump vary along the macroscale in agreement with the crack propagation direction observed at the macroscale.

This illustrates the new paradigm that is set and the computational possibilities open by the HPROM strategies in computational multiscale modeling explored in this Thesis.

5 A cluster of 500 cores, of recent generation, is used. The multiscale finite element code is written in a Matlab©environment.

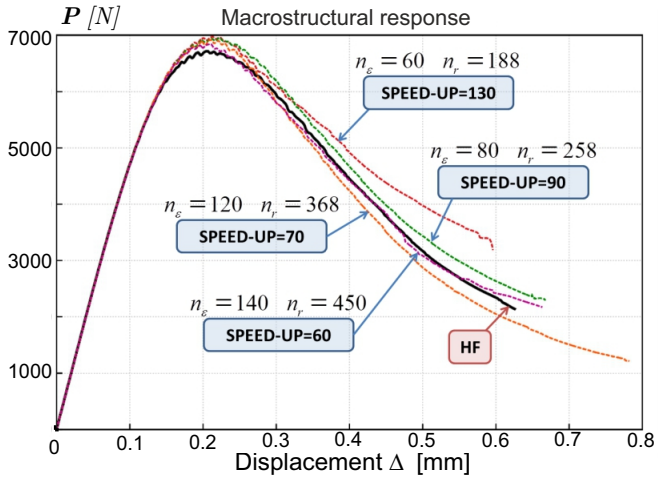

Figure 16: L-shaped panel: Structural responses in terms of force P vs. vertical displacement Δ, for different RVE HPROM strategies, and obtained speed-ups.

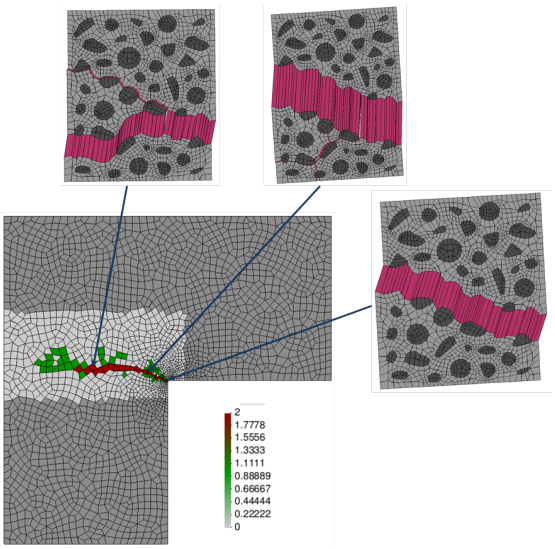

Figure 17: L-shaped panel: Microscale crack activation along the crack-path field, using $n_\varepsilon = 80$ and $n_r = 258$.

4

DISCUSSION, CONCLUSIONS AND FUTURE WORK

4.1 Discussion and Conclusions

4.1.1 *Overview of the work*

Multiscale modeling is foreseen to become a key approach to enable the next wave of design paradigms for engineering materials and structures. Indeed, it has an excellent potential to account for the physical links between different scales, involving the diverse phenomenologies intervening in the mechanical response of materials (grains, particles, defects, inclusions, etc.).

Quoting from a report by a group of experts to the US National Science Foundation (Oden et al., 2006):

". . . . In recent years, a large and growing body of literature in physics, chemistry, biology, and engineering has focused on various methods to fit together simulation models of two or more scales, and this has led to the development of various multi-level modeling approaches. . . .. To date, however, progress on multiscale modeling has been agonizingly slow. Only a series of major breakthroughs will help us establish a general mathematical and computational framework for handling multiscale events and reveal to us the commonalities and limitations of existing methods . . . .".

In this sense, the effort invested in developing and using multiscale models, has been, in many cases, fruitless, due to the involved computational cost in this kind of methodologies. This limitation, becomes a *bottleneck* for multiscale modeling, usually discarded, or, in other cases, relegated to the availability of supercomputers, and, therefore, not always accessible to the whole computational mechanics community.

In addition, while multiscale models exhibiting material hardening behavior have widely been studied, multiscale models dealing with material softening behavior are in an early stages of development.

Therefore, the development of a reliable, and minimal intrusive multiscale fracture models, becomes a crucial task, not only in order to have a robust and consistent multiscale fracture numerical tools, but also for developing their related reduced order models that allow their use in complex (*industrial*) cases with an affordable cost. These are the fundamental reasons for the research and development about this issues.

A sketch of the overall work carried out in this thesis is shown in Fig. 18. In there, contributions are chronologically numbered and highlighted with a blue arrow. Contributed papers are numbered from P1, corresponding to the the first contribution (Paper #1), to P6 (Paper #6) the last one; in this context, CB means *Chapter in Book*.

In what follows, they are specifically commented, and the corresponding conclusions and achievements, are presented.

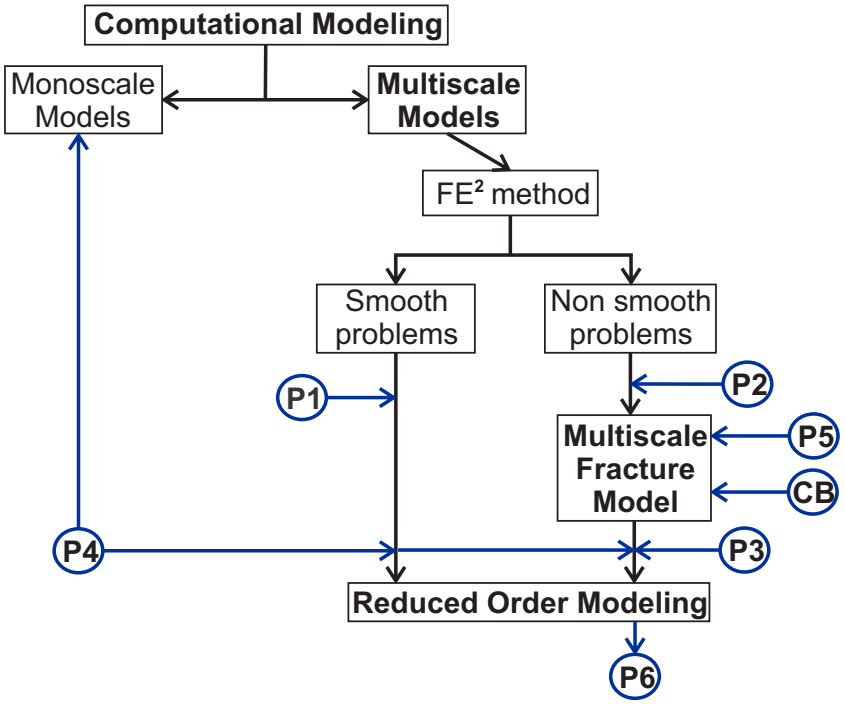

Figure 18: Global Flow Chart of the Thesis

4.1.2 *Paper #1: J. A. Hernández, J. Oliver, A. E. Huespe, M. A. Caicedo, J. C. Cante. High-performance model reduction techniques in computational multiscale homogenization, Computer Methods in Applied Mechanics and Engineering - 2014, Volume 276, Pages 149–189*

This Article presents the first research developments in this Thesis on Model Order Reduction (MOR) techniques applied to multiscale modeling. The scope of this publication is limited to smooth problems and exclude fracture processes. Techniques like *interpolation* methods via HPROM have been studied.

The concept of a two-stage reduction (ROM-HPROM) is presented. The first reduction, denoted as ROM, is performed via POD, taking the displacement fluctuation field as a primal variable. The second reduction, denoted as HPROM, is performed via *interpolation* techniques (DEIM) of the microscale stress field.

It is shown that the interpolation-based HPROM obtained in this way, leads to an ill-posed mathematical formulation when the reduction process involves an interpolant constructed using POD modes provided by the primal variable (microscale stress field). This issue has been studied in the paper, and a robust and consistent solution has been proposed.

An additional aspect in this contribution, is the selection of the interpolation points for the stress field. These interpolation points are chosen guided, not only by accuracy requirements, but also by stability considerations.

The method of selection of the interpolation points (*Greedy Algorithm*) is, at the present, an intensive research field. However, although in the literature there are several alternative algorithms, none of them offers a robust and general treatment to handle this Thesis purposes.

Different measures of error have been presented to test the accuracy and the convergence. The work is assessed by the homogenization of a highly complex porous metal material. The results show that, the speed-up factor is about three orders of magnitude, for an error in stress smaller than 10%.

As conclusions of this work, it can be stated that:

- The hyper-reduced form of the RVE equilibrium equation has a conceptual simplicity, and the corresponding solution scheme is also very simple to implement. Taking as departure point an existing FE code, one only has to replace the typical loop over elements in the FE code by a loop over the pre-selected sampling points.
- Storage of history data (internal variables) is only required at the pre-selected sampling points.
- Consistency with respect to the HF solution is achieved when the amount of reduced order basis functions, for both reductions, is increased.

In consequence, the numerical results suggest that this HPROM provides accurate solutions to problems exhibiting hardening behavior. However, some questions need to be further analyzed. For example:

- *Can the model order reduction techniques capture the RVE solution in problems displaying crack propagation processes?*
- *Will the number of modes necessary to accurately replicate its solution, increase with the number of potential crack paths (i.e., with the geometrical complexity of the RVE)?*

These questions motivated the next research work: i. e.the development of a reduced order model applied to problems exhibiting discontinuous fields, and in particular, the case of the quasi-brittle fracture.

4.1.3 *Paper #2: J. Oliver, M. Caicedo, E. Roubin, A. E. Huespe, J. A. Hernández. Continuum approach to computational multiscale modeling of propagating fracture, Computer Methods in Applied Mechanics and Engineering - 2015, Volume 294, Pages 384–427*

This work presents a novel approach to two-scale modeling of propagating fracture, based on computational homogenization FE^2. The specific features of this contribution are:

- Extends the homogenization paradigms for smooth problems presented in Paper #1 – typically the Hill–Mandel principle and the stress-strain homogenization procedures – to non-smooth problems.
- In both scales of analysis, a continuum (stress–strain) constitutive relationship is considered, instead of making use of the most common discrete traction/separation-law. This contributes to provide a unified setting for smooth and non-smooth, problems. This is achieved by resorting to the well-established Continuum Strong Discontinuity Approach (CSDA).
- As for the multiscale modeling issue, it involves a new and crucial additional entity: a *characteristic length*, which is point-wise obtained from the geometrical features of the failure mechanism developed at the low scale. As a specific feature of the presented approach, this characteristic length is exported, in addition to the homogenized stresses and the tangent constitutive operator, to the macroscale, and considered as the bandwidth of a propagating strain localization band, at that scale.
- Consistently with the characteristic length, a specific computational procedure is used for modeling the onset and propagation of this localization band at the macro-scale. It is based on the crack-path-field and strain injection techniques, developed (Oliver et al., 2014). This computational procedure ensures the macroscale mesh-size and microscale RVE-size objectivity of the results, and a consistent energy dissipation at both scales.

The approach has been validated and tested using classical benchmarks in fracture mechanics. After validation, some aspects of the proposed approach can be emphasized:

- From the computational point of view, the proposed technique is minimally invasive with regards to procedures well established in the literature on multiscale modeling of materials. In fact, in terms of the computational homogenization, the proposed approach displays no substantial difference with respect to the ones used for smooth (continuous) problems. In terms of material failure propagation, existing algorithms for monoscale crack propagation modeling can be easily extended to this multiscale case. In addition, this multiscale approach is extensible to other families of propagation schemes.
- Consistency has been assessed by comparison, with a number of representative cases, through results obtained with the proposed FE^2 and the ones obtained by Direct Numerical Simulation (DNS). In the same way, objectivity have been also checked in terms of finite element mesh size and bias, at the macro-scale, and the failure-cell (size and shape) at the micro/meso-scale.

As mentioned, multiscale computational fracture problems and their extension to 3D cases, face a great challenge: the enormous involved computational cost. In consequence, next step is the development of a reduced order model aiming at diminishing the computational burden of the developed multiscale fracture model.

4.1.3.1 *HPROM for hardening processes applied to quasi-brittle fracture*

The reduced order model described in Paper #1 was used as a first attempt. However, the results were very unsatisfactory. The conclusions of this interpolation-based approach to multiscale reduced order modeling in fracture cases were:

- The reduced basis for the microscale displacement fluctuations obtained via SVD does not make a clear distinction between smooth and non-smooth domains. Hence, a large set of displacement modes (considerably larger than the one requested in hardening problems) has to be used to retrieve accurate solutions.
- The stress snapshots, taken from high localized strain stages with released near-to-zero stresses, are numerically neglected by the SVD[1], this taking interpolation-based HPROM methods to fail in reproducing the post-critical stages.
- To obtain a good approximation with the HPROM, it is necessary to largely increase the number of displacement and stress modes, but, in this scenario, the interpolation method is not longer robust.

1 The SVD strategy, gives importance to repeated snapshots, and mainly, snapshots which euclidean norm is considerably high.

This suggests additional research and exploration of specific model order reduction techniques for multiscale fracture problems.

4.1.4 *Paper #3: J. Oliver, M. Caicedo, A. E. Huespe, J. A. Hernández, E. Roubin. Reduced Order Modeling strategies for Computational Multiscale Fracture, Computer Methods in Applied Mechanics and Engineering - 2016, Volume 313, Pages 560–595*

This article proposes a set of new computational techniques to solve multiscale problems via HPROM techniques. These techniques have been applied to the multiscale model described in 4.1.3, and they are summarized next:

- A *domain separation* strategy. The RVE is split into the *regular domain* (made of the elastic matrix and possible inclusions) and the *singular domain* (the cohesive bands exhibiting a softening cohesive behavior). These are designed to provide a sufficiently good representation of the microscopic fracture and of its effects on the homogenized material behavior (Oliver et al., 2015). The distinct constitutive behavior of both domains suggests a specific ROM strategy for each of them, in order to obtain a reduction strategy with information on the mechanical variables in every specific subdomain. Therefore, selection of the ROM low-dimensional projection space is made independently for each of these domains.

- In combination with the previous strategy, the ROM for the RVE is formulated in an *unconventional manner* i. e.: in terms of the strain fluctuations rather than in terms of the conventional displacement fluctuations. The reduced strain fluctuation space is spanned by basis functions satisfying, by construction, the strain compatibility conditions, this guaranteeing that, after reduction, the solution in the strain fluctuation space also satisfies the strain compatibility.

- A specific Reduced Optimal Quadrature (ROQ) is used as a key technique to obtain relevant computational cost reduction from the ROM. This technique consists of replacing the standard Gauss integration rule by an optimal quadrature, involving much less sampling points, has been proposed in other works (Farhat et al., 2015; Hernández et al., 2017) as an ingredient of HyPer-Reduced Order Modeling (HPROM) strategies. In these works, the reduced numerical integration technique is applied to the variational equations of the problem (i.e. internal forces, involving n-dimensional vector entities) whereas, in the herein proposed approach, a similar reduced integration technique is applied, again unconventionally, to the primitive problem, i.e: the functional (a scalar entity) in the micro-scale saddle-point problem that supplies the RVE variational equations. In the present proposal, this functional turns out to be the stored energy (free energy) at the RVE, which, being a scalar entity, is much less demanding in terms of the integration rule.

In a first validation stage, in order to test the sensibility of the reduction techniques, a set of three different failure cells have been tested, by increasing the complexity and, consequently, the amount of cohesive bands. A-priori and a-posteriori errors analysis are performed, showing that, increasing the complexity (number of involved operations) at the microscale, the amount of required strain and free energy modes increases only slightly for a given error. This is a clearly promising scenario.

Finally, this reduced multiscale model was also validated and tested with the *L-Shape Panel* test, comparing the solution with the one given by the HF (obtained with the approach described in the Paper #2), and analyzing the impact on the use of different amounts of reduced order basis functions of both, the strain fluctuations and the free energy.

Several aspects of the proposed methodology can be highlighted as new contributions:

- The RVE domain separation technique: to account for distinct constitutive models used at the RVE and take the maximum advantage of this distinction.
- A strain-based formulation of the variational RVE problem allowing a simpler application of the previous technique, without the need of introducing compatibility constraints.
- A specific sampling program, for the construction of the sets of snapshots in the off-line stage of the HPROM procedure, in accordance with the rest of elements of the proposed strategy.
- The Reduced Optimal Quadrature (ROQ) technique, which resorts to the primitive formulation of the RVE problem as a saddle-point problem.

At this point it can be argued that only idealized, two-dimensional, problems have been considered. The real interest of many multiscale modeling problems residing on actual three-dimensional problems, the following question arises:

to what extent these techniques can be extended to three-dimensional problems, where the involved RVE complexity and the associated computational cost can be two or three orders of magnitudes larger than in 2D problems?

In Fig. 19, the results obtained from different kind of 2D microscale morphologies are presented. They show a very relevant property: **the obtained speedup "scales" linearly with the problem-complexity**. Therefore one could think of achievable values of $\approx 10^4$–10^5 for the speedup in 3D problems. This fact (in conjunction with, the additional usage of HPC procedures), could turn affordable 3D multiscale fracture modelling.

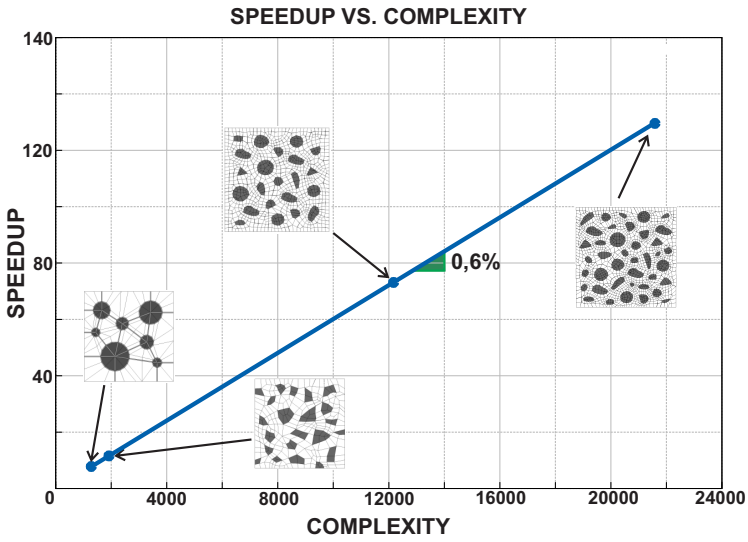

Figure 19: Speedup scalability.

4.1.5 *Paper #4: J. A. Hernández, M. A. Caicedo, A. Ferrer. Dimensional hyper-reduction of nonlinear finite element models via empirical cubature, Journal of Computer Methods in Applied Mechanics and Engineering - 2016, Volume 313, Pages 560–595*

This work has been developed in combination with the reduced order model for non-smooth problems (see 4.1.4). The main objective is to develop the algorithmic procedure in a general setting to be applied to different problems involving integral operators that can be sampled. Not only problems involving multiple scales can be analyzed, but also monoscale (static and dynamic) problems based on the Finite Element method.

It is presented a general framework for the dimensional reduction in terms of numbers of degrees of freedom as well as number of integration points of nonlinear parametrized finite element models.

As in previous cases (see 4.1.2 and 4.1.4), the reduction process is divided into two sequential stages, the first consists of a Galerkin projection of the strain fluctuations, via POD, and the second consists of a novel cubature rule also used in 4.1.4. In this case, this method is deeply studied and analyzed. The distinguish features of the proposed method to be highlighted are:

- The minimization method is set in terms of orthogonal basis vectors (obtained via Singular Value Decomposition SVD) rater than in terms of snapshots taken from the integrand.
- The volume of the domain is exactly integrated.

- The selection algorithm does not require solve, in all iterations, a non-negative least-squares problem to obtain positive weights.

This model is tested through two structural examples, (quasi-static bending, and resonant vibration of elasto-plastic composite plates). The total amount of integration points is reduced three order of magnitudes, this methodology can be applied to different primary variables, in 4.1.4, attention was focused on use the free energy to determine the reduced integration rule.

Several issues have been improved by this research: firstly, the *robustness*, one of the most attractive features of the proposed hyper-reduced order model (and in general, of all cubature-based ROMs) is that it preserves the spectral properties of the Jacobian matrix of the finite element motion equations. Secondly, the improved version of the *Empirical cubature method*, in contrast with other similar techniques proposed in the literature, in which the weights at almost all iterations of the greedy algorithm are calculated with a standard, unconstrained least-squares. In fact, the nonnegative least squares problem is included to filter out small negative weights caused by roundoff errors. And finally, for implementation purposes, the "format" of the finite element method is conserved.

4.1.6 *Paper #5: J. Oliver, M. Caicedo, E. Roubin, A. E. Huespe. Continuum Approach to Computational Multi-Scale Modeling of Fracture, Key Engineering Materials - 2014, Volume 627, Pages 349–352*

This work presents a brief summary of the two-scale approach for modeling failure propagation, providing details about propagation at the macro and micro levels. This publication is centered in exploring the applicability of the method to structural problems. The four-point bending and the *Nooru-Mohamed* problems have been chosen as benchmarks, taking the material properties form experimental tests.

In the case of the Nooru-Mohamed test, it has been shown, the influence of the horizontal load (shear force) in the microscale behavior, and the activation of different crack patterns, representing the macroscale changes in the crack propagation scheme. In the four-point bending test, it is displayed the influence on the macroscale propagation scheme, when critical failure mechanisms at the microscale are precluded.

4.1.7 *Paper #6: M. Caicedo, J. Oliver, A. E. Huespe, O. Lloberas-Valls. Model Order Reduction in computational multiscale fracture mechanics, Key Engineering Materials - 2016, Volume 713, Pages 248–253*

This work has a similar objective than the previous one. A brief summary about the reduced order model based on the two-scale approach for modeling failure propagation, has been presented. This work also presents a summary about the results obtained in the *L-Shaped Panel*, and the influence of the size of reduced

order basis functions (for strain fluctuations and free energy) is presented and analyzed.

4.1.8 *Chapter In Book (CB): J. Oliver, M. Caicedo, E. Roubin, J. A. Hernández, A. E. Huespe. Multi-scale (FE^2) analysis of material failure in cement-aggregate-type composite structures, Computational Modeling of Concrete Structures - 2014, Pages 39–49*

This work focuses on exploring different issues of the two-scale approach for modeling failure propagation. Particularly, the total energy dissipation and its relation at both scales is analyzed in some specific fracture problems.

4.2 Ongoing work and future research lines

4.2.1 *Ongoing work*

- Most of the real industrial problems require 3D modelling. This is the reason because an immediate task is to extend all procedures developed in this Thesis to 3D problems. This extension is carried out in Kratos Multi-Physics, an open-source code developed at CIMNE (International Center for Numerical Methods in Engineering).
- The approach developed in Paper #3 is being extended to nonlinear geometrical multiscale problems. Considering an elasto-plastic constitutive model endowed, with hardening behavior, the goal is to study and analyze geometric bifurcation at the macroscale. Some early results have been obtained, exhibiting the potential uses of this methods in nonlinear geometric multiscale problems.
- Fracture processes of composite materials via multiscale modeling, are being studied by using the formulations developed in Paper #2 and Paper #3. The main goals are: to reproduce the experimental behavior of composite sublaminates of ultra-thin plies (Arteiro et al., 2014) and, to devise some design alternatives based on the material failure analysis, taking advantage of the reduced order model techniques.
- In order to obtain an optimum performance of the reduced order models developed in this Thesis, it is convenient to optimize the tasks performed in the *offline stage*, particularly, the Singular Value Decomposition performed after sampling the training trajectories. This method can be highly computational demanding in very fine meshes. Therefore, the study of SVD partitioned procedures, and iterative strategies are presently explored.

4.2.2 *Future research lines*

- Extension of the developed multiscale model to propagating fracture in non-linear dynamic cases. This includes modeling more complex phenomena like branching and multiscale dynamic processes. This field was also studied via monoscale phenomenological modeling in (Belytschko et al., 2003; Prabel et al., 2007; Linder and Armero, 2009; Lloberas-Valls et al., 2016). In addition, inclusion of non-linear hardening behavior, before the onset of material failure in the considered damage model, and consideration of other families of constitutive behavior, like plasticity, rate dependence etc., should be studied.

- The use, in the developed multiscale model for propagating fracture, of other crack propagation models at the microscale, either based on continuum methods (CSDA, non-local models or gradient-regularized models), or discrete methods (cohesive interfaces equipped with traction-separation laws).

- Extension of the reduced order model described in Paper #3 to other microscale failure methodologies, i. e., gradient damage models, Enhanced finite element methods (EFEM), etc. In the same way, the extension of the reduced order model to other multiscale strategies involving fracture processes, i. e., concurrent models (Lloberas-Valls et al., 2012).

CONTRIBUTED PUBLICATIONS

	NAME	JOURNAL	QUARTIL INDEX in JCR	IMPACT FACTOR
Paper #1	High-performance model reduction techniques in computational multiscale homogenization	Computer M. in Applied Mechanics and Engineering	Q1	3.467
Paper #2	Continuum approach to computational multiscale modeling of propagting fracture	Computer M. in Applied Mechanics and Engineering	Q1	3.467
Paper #3	Reduced Order Modeling strategies for Computational Multiscale Fracture	Computer M. in Applied Mechanics and Engineering	Q1	3.467
Paper #4	Dimensional hyper-reduction of nonlinear finite element models via empirical cubature	Computer M. in Applied Mechanics and Engineering	Q1	3.467
Paper #5	Continuum Approach to Computational Multi-Scale Modeling of Fracture	Key Engineering Materials	–	0.39
Paper #6	Model Order Reduction in computational multiscale fracture mechanics	Key Engineering Materials	–	0.39

Table 3: Scientific Contributions in specialized journals

	NAME	BOOK	CONGRESS
CB	Multi-scale (FE^2) analysis of material failure in cement-aggregate-type composite structures	Computational Modeling of Concrete Structures	EURO-C 2014

Table 4: Book Chapters

BIBLIOGRAPHY

E. Aifantis. On the microestructural origin of certain inelastic models. *ASME J. Engrg Mat. Tech.*, 106:326–334, 1984.

David Amsallem, Julien Cortial, Kevin Carlberg, and Charbel Farhat. A method for interpolating on manifolds structural dynamics reduced-order models. *International Journal for Numerical Methods in Engineering*, 80(9):1241–1258, 2009. ISSN 1097-0207. doi: 10.1002/nme.2681. URL http://dx.doi.org/10.1002/nme.2681.

S. An, T. Kim, and D. James. Optimizing cubature for efficient integration of subspace deformations. *ACM transactions on graphics*, 27(5):165, 2009.

A. Arteiro, G. Catalanotti, A.R. Melro, P. Linde, and P.P. Camanho. Micro-mechanical analysis of the in situ effect in polymer composite laminates. *Composite Structures*, 116:827–840, 2014. ISSN 0263–8223. doi: http://dx.doi.org/10.1016/j.compstruct.2014.06.014. URL http://www.sciencedirect.com/science/article/pii/S0263822314002839.

Maxime Barrault, Yvon Maday, Ngoc Cuong Nguyen, and Anthony T. Patera. An 'empirical interpolation' method: application to efficient reduced-basis discretization of partial differential equations. *Comptes Rendus Mathematique*, 339(9):667 – 672, 2004. ISSN 1631-073X. doi: http://dx.doi.org/10.1016/j.crma.2004.08.006. URL http://www.sciencedirect.com/science/article/pii/S1631073X04004248.

Z. Bazant. Can Multiscale-Multiphysics Methods Predict Softening Damage and Structural Failure? *International Journal for Multiscale Computational Engineering*, 8(1):61–67, 2010. ISSN 1543-1649.

Z.P. Bazant and J. Planas. *Fracture and size efect in concrete and other quasibrittle materials*. CRC Press, Boca Raton, FL, 1998.

T. Belytschko, H. Chen, J.X. Xu, and G. Zi. Dynamic crack propagation based on loss of hyperbolicity and a new discontinuous enrichment. *Int. J. Numer. Methods Engrg.*, 58:1873–1905, 2003.

T. Belytschko, S. Loehnert, and J.H. Song. Multiscale aggregating discontinuities: A method for circumventing loss of material stability. *Int. J. Numer. Meth. Engng.*, 73:869–894, 2008.

Pablo J. Blanco, Pablo J. Sánchez, Eduardo A. de Souza Neto, and Raúl A. Feijóo. Variational foundations and generalized unified theory of rve-based multiscale models. *Archives of Computational Methods in Engineering*, 23(2):191–253, 2016.

ISSN 1886-1784. doi: 10.1007/s11831-014-9137-5. URL http://dx.doi.org/10.1007/s11831-014-9137-5.

H. Böhm. Short introduction to basic aspects of continuum micromechanics. *Technical Report. Institute of Lightweight Design and Structural Biomechanics (ILSB). Vienna University of Technology*, 27(206), 2013.

M. Bornert. *Morphologie microstructurale et comportement mécanique; charactérisations expérimentales, approches par bornes et estimations autocohérentes généralisées*. PhD. Thesis, Ecole Nationale des Ponts et Chaussées, 1999.

S. Boyaval. Reduced-basis approach for homogenization beyond the periodic setting. *Arxiv preprint math/0702674*, 2007.

E.W.C. Coenen, V.G. Kouznetsova, E. Bosco, and M.G.D. Geers. A multi-scale approach to bridge microscale damage and macroscale failure: a nested computational homogenization-localization framework. *Int. J. Fracture*, 178(1-2):157–178, 2012.

R. de Borst and H. Mühlhaus. Gradient-dependent plasticity: formulation and algorithmic aspects. *Int J. Numer. Meth. Engrg.*, 35(3):521–539, 1992.

A. Drago and M. J. Pindera. Micro-macromechanical analysis of heterogeneous materials: Macroscopically homogeneous vs periodic microstructures. *Composites science and technology*, 67(6):1243–1263, 2007.

J.D. Eshelby. The determination of the field of an ellipsoidal inclusion and related problems. *Proc. R. Soc. Lond A*, 241:376–396, 1957.

C. Farhat, T. Chapman, and P. Avery. Structure-preserving, stability, and accuracy properties of the energy-conserving sampling and weighting method for the hyper reduction of nonlinear finite element dynamic models. *International Journal for Numerical Methods in Engineering*, 2015.

R. Faria, J. Oliver, and M. Cervera. A strain-based plastic viscous-damage model for massive concrete structures. *International Journal of Solids and Structures*, 35(14):1533–1558, 1998. ISSN 0020-7683. doi: 10.1016/S0020-7683(97)00119-4. URL http://www.sciencedirect.com/science/article/pii/S0020768397001194.

F. Feyel and J.L. Chaboche. FE^2 multiscale approach for modelling the elastoviscoplastic behaviour of long fibre SiC/Ti composite materials. *Comput. Meth. App. Mech. Eng.*, 183:309–330, 2000.

Shankar Ganapathysubramanian and Nicholas Zabaras. Design across length scales: a reduced-order model of polycrystal plasticity for the control of microstructure-sensitive material properties. *Computer Methods in Applied Mechanics and Engineering*, 193(45-47):5017 – 5034, 2004. ISSN 0045-7825. doi: http://dx.doi.org/10.1016/j.cma.2004.04.004. URL http://www.sciencedirect.com/science/article/pii/S0045782504002567.

M.G.D. Geers, V.G. Kouznetsova, and W.A.M. Brekelmans. Multi-scale computational homogenization: Trends and challenges. *Journal of Computational and Applied Mathematics*, 234:2175–2182, 2010.

I.M. Gitman, H. Askes, and L.J. Sluys. Representative volume: Existence and size determination. *Engineering Fracture Mechanics*, 74:2518–2534, 2007.

D. Gross and T. Seelig. *Fracture mechanics: with an introduction to micromechanics*. Springer–Verlag, Berlin Heidelberg, 2nd edition, 2011.

J.A. Hernández, J. Oliver, A.E. Huespe, M.A. Caicedo, and J.C. Cante. *Computational Homogenization of Inelastic Materials using Model Order Reduction*, volume 141. International Center for Numerical Methods in Engineering (CIMNE) Monograph, 2014a.

J.A. Hernández, J. Oliver, A.E. Huespe, M.A. Caicedo, and J.C. Cante. High-performance model reduction techniques in computational multiscale homogenization. *Computer Methods in Applied Mechanics and Engineering*, 276: 149–189, 2014b.

J.A. Hernández, M.A. Caicedo, and Ferrer A. Dimensional hyper-reduction of nonlinear finite element models via empirical cubature. *Computer Methods in Applied Mechanics and Engineering*, 313:687–722, 2017. ISSN 0045–7825. doi: http://dx.doi.org/10.1016/j.cma.2016.10.022. URL `http://www.sciencedirect.com/science/article/pii/S004578251631355X`.

R. Hill. The elastic behavior of a crystalline aggregate. *Proc. Phys. Soc. London*, A65:349–354, 1952.

R. Hill. A self-consistent mechanics of composite materials. *J. Mech. Phys. Solids*, 13:213–222, 1965.

P. Kerfriden, O. Goury, T. Rabczuk, and S.P. Bordas. A partitioned model order reduction approach to rationalise computational expenses in nonlinear fracture mechanics. *Computer methods in applied mechanics and engineering*, 256:169–188, 2013.

V.G. Kouznetsova. *Computational homogenization for the multi-scale analysis of multi-phase materials*. PhD thesis, Technische Universiteit Eindhoven, Netherlands, 2002.

T. Lesicar, Z. Tonković, and J. Sorić. Multi-Scale Modeling of Heterogeneous Materials and the Validation Challenge. *Key Engineering Materials*, 665:181–184, 2015. doi: 10.4028/www.scientific.net/AMM.70.345. URL `www.scientific.net/KEM.665.181`.

C. Linder and F. Armero. Finite elements with embedded branching. *Finite Elements in Analysis and Design*, 45(4):280–293, 2009. ISSN 0168-874X. doi: http://dx.doi.org/10.1016/j.finel.2008.10.012. URL `http://www.sciencedirect.com/science/article/pii/S0168874X08001595`. The Twentieth Annual Robert J. Melosh Competition.

O. Lloberas-Valls, D.J. Rixen, A. Simone, and L.J. Sluys. Multiscale domain decomposition analysis of quasi-brittle heterogeneous materials. *Int. J. Num. Meth. Eng.*, 89(11):1337–1366, 2012.

O. Lloberas-Valls, A.E. Huespe, J. Oliver, and I.F. Dias. Strain injection techniques in dynamic fracture modeling. *Computer Methods in Applied Mechanics and Engineering*, 308:499–534, 2016. ISSN 0045–7825. doi: http://dx.doi.org/10.1016/j.cma.2016.05.023. URL http://www.sciencedirect.com/science/article/pii/S0045782516304248.

J. Mandel. *Plasticité Classique et Viscoplasticité*. Springer–Verlag, Udine, Italy, 1971.

K. Markov. Elementary micromechanics of heterogeneous media. *Heterogeneous Media: Micromechanics Modeling Methods and Simulations*, pages 1–162, 2000.

K. Matous, M.G. Kulkarni, and P.H. Geubelle. Multiscale cohesive failure modeling of heterogeneous adhesives. *Journal of the Mechanics and Physics of Solids*, 56:1511–1533, 2008.

J.C. Michel and P. Suquet. Nonuniform transformation field analysis. *International Journal of Solids and Structures*, 40(25):6937–6955, 2003. ISSN 0020-7683. doi: 10.1016/S0020-7683(03)00346-9. URL http://www.sciencedirect.com/science/article/pii/S0020768303003469. Special issue in Honor of George J. Dvorak.

J.C. Michel and P. Suquet. Computational analysis of nonlinear composite structures using the nonuniform transformation field analysis. *Computer Methods in Applied Mechanics and Engineering*, 193(48–51):5477–5502, 2004. ISSN 0045-7825. doi: 10.1016/j.cma.2003.12.071. URL http://www.sciencedirect.com/science/article/pii/S004578250400283X. Advances in Computational Plasticity.

JC Michel, H Moulinec, and P Suquet. A computational scheme for linear and non-linear composites with arbitrary phase contrast. *International Journal for Numerical Methods in Engineering*, 52(1-2):139–160, 2001.

G. W. Milton. *The Theory of Composites*. Cambridge University Press, Cambridge, UK, 2002.

J.F. Molinari, G. Gazonas, R. Raghupathy, A. Rusinek, and F. Zhou. The cohesive element approach to dynamic fragmentation: the question of energy convergence. *Int. J. Num. Meth. Eng.*, 69(3):484–503, 2007.

E. Monteiro, J. Yvonnet, and Q.C. He. Computational homogenization for nonlinear conduction in heterogeneous materials using model reduction. *Computational Materials Science*, 42(4):704 – 712, 2008. ISSN 0927-0256. doi: http://dx.doi.org/10.1016/j.commatsci.2007.11.001. URL http://www.sciencedirect.com/science/article/pii/S0927025607003242.

T. Mori and K. Tanaka. Average stress in the matrix and average energy of materials with misfitting inclusions. *Acta Metall.*, 21:571–574, 1973.

H. Muhlhaus and I. Vardoulakis. The thickness of shear bands in granulars materials. *Geotechnic*, 37:271–283, 1987.

S. Nemat-Nasser and M. Hori. *Micromechanics: overall properties of heterogeneous materials*. Elsevier, 1999.

N.C. Nguyen. A multiscale reduced-basis method for parametrized elliptic partial differential equations with multiple scales. *Journal of Computational Physics*, 227(23):9807 – 9822, 2008. ISSN 0021-9991. doi: http://dx.doi.org/10.1016/j.jcp.2008.07.025. URL http://www.sciencedirect.com/science/article/pii/S0021999108004087.

V.P. Nguyen, O. Lloberas-Valls, M. Stroeven, and L.J. Sluys. On the existence of representative volumes for softening quasi-brittle materials - A failure zone averaging scheme. *Comput. Meth. App. Mech. Eng.*, 199:3028–3038, 2010a.

V.P. Nguyen, O.Lloberas-Valls, and L.J. Sluys M. Stroeven. Homogenization-based multiscale crack modelling: from micro diffusive damage to macro cracks. *Comput. Meth. App. Mech. Eng.*, 200:1220–1236, 2010b.

J. T. Oden, T. Fish J. Belytschko, T. J. R. Hughes, C. Johnson, L. A Keyes, L Petzold, L. Srolovitz, and S. Yip. Simulation-based engineering science. Report of the nsf sbes panel to the nsf engineering advisory committee, National Science Foundation (USA), 2006.

J. Oliver. A consistent characteristic length for smeared cracking models. *International Journal for Numerical Methods in Engineering*, 28(2):461–474, 1989. ISSN 1097-0207. doi: 10.1002/nme.1620280214. URL http://dx.doi.org/10.1002/nme.1620280214.

J. Oliver. Continuum modelling of strong discontinuities in solids mechanics using damage models. *Comput. Mech.*, 17(1-2):49–61, 1995b.

J. Oliver. Modelling strong discontinuities in solids mechanics via strain softening constitutive equations. Part 1: Fundamentals. *Int. j. numer. methods eng.*, 39(21):3575–3600, 1996a.

J. Oliver. On the discrete constitutive models induced by strong discontinuity kinematics and continuum constitutive equations. *Int. J. Solids Struct.*, 37:7207–7229, 2000.

J. Oliver and A. E. Huespe. Continuum approach to material failure in strong discontinuity settings. *Comp. Meth. Appl. Mech. in Engrg.*, 193:3195–3220, 2004a.

J. Oliver and A.E. Huespe. Theoretical and computational issues in modelling material failure in strong discontinuity scenarios. *Comput. Meth. App. Mech. Eng.*, 193:2987–3014, 2004b.

J. Oliver, A. E. Huespe, M. D. G. Pulido, and E. Chaves. From continuum mechanics to fracture mechanics: the strong discontinuity approach. *Engineering Fracture Mechanics*, 69:113–136, 2002.

J. Oliver, A.E. Huespe, S. Blanco, and D.L. Linero. Stability and robustness issues in numerical modeling of material failure with the strong discontinuity approach. *Comput. Meth. App. Mech. Eng.*, 195(52):7093–7114, 2005.

J. Oliver, I.F. Dias, and A.E. Huespe. Crack-path field and strain-injection techniques in computational modeling of propagating material failure. *Computer Methods in Applied Mechanics and Engineering*, 274:289–348, 2014. ISSN 0045-7825. doi: 10.1016/j.cma.2014.01.008. URL http://www.sciencedirect.com/science/article/pii/S0045782514000139.

J. Oliver, M. Caicedo, E. Roubin, A.E. Huespe, and J.A. HernÃ¡ndez. Continuum approach to computational multiscale modeling of propagating fracture. *Computer Methods in Applied Mechanics and Engineering*, 294:384–427, 2015. ISSN 0045-7825. doi: 10.1016/j.cma.2015.05.012. URL http://www.sciencedirect.com/science/article/pii/S0045782515001851.

J. Oliver, M. Caicedo, A.E. Huespe, J.A. Hernández, and E. Roubin. Reduced order modeling strategies for computational multiscale fracture. *Computer Methods in Applied Mechanics and Engineering*, 313:560–595, 2017a. ISSN 0045-7825. doi: 10.1016/j.cma.2016.09.039. URL http://www.sciencedirect.com/science/article/pii/S0045782516303322.

J. Oliver, M. Caicedo, A.E. Huespe, J.A. HernÃ¡ndez, and E. Roubin. Reduced order modeling strategies for computational multiscale fracture. *Computer Methods in Applied Mechanics and Engineering*, 313:560–595, 2017b. ISSN 0045-7825. doi: 10.1016/j.cma.2016.09.039. URL http://www.sciencedirect.com/science/article/pii/S0045782516303322.

C. Oskay and J. Fish. Eigendeformation-based reduced order homogenization for failure analysis of heterogeneous materials. *Comput. Meth. App. Mech. Eng.*, 196 (7):1216–1243, 2007.

F. Otero, X. Martínez, S. Oller, and O. Salomón. An efficient multi-scale method for non-linear analysis of composite structures. *Composite Structures*, 131:707–719, 2015. ISSN 0263-8223. doi: 10.1016/j.compstruct.2015.06.006. URL http://www.sciencedirect.com/science/article/pii/S0263822315004699.

A. Pandolfi, P. Krysl, and M. Ortiz. Finite element simulation of ring expansion and fragmentation: the capturing of length and time scales through cohesive models of fracture. *Int. J. Fracture*, 95(1-4):279–297, 1999.

R. Peerlings, R. de Borst, W. Brekelmans, and J. de Vree. Gradient Enhanced Damage for Quasi-Brittle Materials. *Int J. Numer. Meth. Engrg.*, 39:3391–3403, 1996.

R. Peerlings, M. Geers, R. de Borst, and W. Brekelmans. A critical comparison of nonlocal and gradient-enhanced softening continua. *Int J. Solids Struct.*, 38: 7723–7746, 2001.

R. Peerlings, R. de Borst, W. Brekelmans, and M. Geers. Localization issues in local and nonlocal continuum approaches to fracture. *European Journal of Mechanics A/Solids*, 21:175–189, 2002.

G. Pijaudier-Cabot and Z. Bazant. Nonlocal damage theory. *ASCE J. Engrg. Mech.*, 113(10):1512–1533, 1987.

P. Ponte Castañeda and P. Suquet. Nonlinear composites. *Advances in Applied Mechanics*, 34:171–302, 1998.

B. Prabel, A. Combescure, A. Gravouil, and S. Marie. Level set x-fem non-matching meshes: application to dynamic crack propagation in elastic-plastic media. *International Journal for Numerical Methods in Engineering*, 69(8):1553–1569, 2007. ISSN 1097-0207. doi: 10.1002/nme.1819. URL `http://dx.doi.org/10.1002/nme.1819`.

B. D. Reddy and J. Simo. Stability and convergence of a class of enhanced strain methods. *SIAM, Jornal on Numerical Analysis*, 32:1705–1728, 1995.

A. Reuss. Berechnung der Fließgrenze von Mischkristallen auf Grund der Plastizitätsbe–dingung für Einkristalle. *ZAMM*, 9:49–58, 1929.

E.A. Rodrigues, O.L. Manzoli, L.A.G. Bitencourt Jr, and T. Bittencourt. 2D mesoscale model for concrete based on the use of interface element with a high aspect ratio. *International Journal of Solids and Structures*, 94:112–124, 2016.

J. Rots. *Computational modelling of concrete fracture*. PhD thesis, Delft University, Netherlands, 1988.

D. Ryckelynck. Hyper-reduction of mechanical models involving internal variables. *International Journal for Numerical Methods in Engineering*, 77(1):75–89, 2009.

J. Simo and T. Hughes. *Computational inelasticity*. Springer-Verlag, 1998.

J. Simo and T. J. R. Hughes. On the variational foundations of assumed strain methods. *Journal of Applied Mechanics, ASME*, 53:51–54, 1986.

J. Simo and M. Riffai. A class of mixed assumed strain methods and the method of incompatible modes. *Int. J. Numer. Methods eng.*, 29:1595–1638, 1990.

J. Simo, J. Oliver, and F. Armero. An analysis of strong discontinuities induced by strain-softening in rate-independent inelastic solids. *Comput. Mech.*, 12:277–296, 1993.

J.H. Song and T. Belytschko. Multiscale aggregating discontinuities method for micro-macro failure of composites. *Composites*, Part B 40:417–426, 2009.

P. Steinmmann and K. Willam. Localization within the framework of micropolar elasto-plasticity. In V. Mannl et al., editor, *Advances in continuum mechanics*, pages 296–313, Berlin, 1991. Springer Verlag.

Kenjiro Terada, Muneo Hori, Takashi Kyoya, and Noboru Kikuchi. Simulation of the multi-scale convergence in computational homogenization approaches. *International Journal of Solids and Structures*, 37(16):2285–2311, 2000. ISSN 0020-7683. doi: 10.1016/S0020-7683(98)00341-2. URL http://www.sciencedirect.com/science/article/pii/S0020768398003412.

S. Toro, P.J. Sánchez, A.E. Huespe, S.M. Giusti, P.J. Blanco, and R.A. Feijóo. A two-scale failure model for heterogeneous materials: numerical implementation based on the finite element method. *Int. J. Num. Meth. Eng.*, 97(5):313–351, 2014.

S. Toro, P.J. Sánchez, P.J. Blanco, E.A. de Souza Neto, A.E. Huespe, and R.A. Feijóo. Multiscale formulation for material failure accounting for cohesive cracks at the macro and micro scales. *Int. J. of Plasticity*, 76:75–110, 2016.

S. Torquato. *Random Heterogeneous Media*. Springer–Verlag, New York, NY, 2002.

V. Tvergaard and A. Needleman. Efects of nonlocal damage in porous plastic solids. *Int J. Solids Struct.*, 32(8/9):1063–1077, 1995.

J. F. Unger. An FE2-X1 approach for multiscale localization phenomena. *Journal of the Mechanics and Physics of Solids*, 61(4):928–948, 2013. ISSN 0022-5096. doi: 10.1016/j.jmps.2012.12.010. URL http://www.sciencedirect.com/science/article/pii/S0022509613000069.

W. Voigt. Über die Beziehung zwischen den beiden Elasticitäts-Constanten isotroper Körper. *Ann.Phys.*, 38:573–587, 1889.

J. Yvonnet and Q-C. He. The reduced model multiscale method (R3M) for the non-linear homogenization of hyperelastic media at finite strains. *Journal of Computational Physics*, 223(1):341–368, 2007.

S. Zhang and C. Oskay. Reduced order variational multiscale enrichment method for elasto-viscoplastic problems. *Computer Methods in Applied Mechanics and Engineering*, 300:199–224, 2016.

O.C. Zienkiewicz and R.L. Taylor. *The Finite Element Method*. Butterworth-Heinemann, Oxford, UK, 2000.

Part II

APPENDIX

List of participations in national and international conferences.

A

CONTRIBUTIONS TO CONFERENCES AND WORKSHOP PROCEEDINGS

During the development of the Thesis, the partial advances and results have been presented in several national and international specialized conferences and whorshops. The list of attended conferences are:

- **Caicedo M., Oliver J., Huespe A. E., Hernández J., Ferdinand C.** Computational Multiscale Modelling of materials using Reduced-order modeling techniques, Whorkshop CIMNE-Lulea, Barcelona, Spain. May 2011.
- **Oliver J., Hernández J.A., Huespe A., Caicedo M.** High performance Model-Order-Reduction methods in computational multi-scale simulations of non-linear solids, European Congress on Computational Methods in Applied Sciences and Engineering (**ECCOMAS 2012**), Vienna, Austria, September 2012.
- **Oliver J., Hernández J.A., Huespe A., Caicedo M.** High performance Model-Order-Reduction methods in computational multi-scale simulations of non-linear solids, 1st Spain - Japan Whorkshop on Computational Mechanics, Barcelona, Spain, September 2012. **Link to Publisher**
- **Oliver J., Huespe A., Caicedo M., Hernández J.A.** Two-scale modeling of material failure based on the Continuum Strong Discontinuity Approach, The Third International Conference on Computational Modeling of Fracture and Failure of Materials and Structures (**CFRAC 2013**), Prague, Czech Republic, 5–7 June 2013.
- **Hernández J.A., Oliver J., Huespe A., Caicedo M., Cante J.C** Application of High-Performance Reduced-Order Modeling (HP-ROM) to two-scale homogenization problems, Congress of Numerical Methods in Engineering 2013, SEMNI, Bilbao, Spain, 25–28 June 2013.
- **Oliver J., Huespe A., Caicedo M., Hernández J.A.** Continuum Approach to Computational Multi-scale Modeling of Material Failure, XII International Conference on Computational Plasticity: Fundamentals and Applications (**COMPLAS 2014**), Barcelona, Spain, 3–5 September 2013.

- **Hernández J.A., Oliver J., Huespe A., Caicedo M., Cante J.C** On the application of high-performance model reduction techniques to homogenization of heterogeneous materials, XII International Conference on Computational Plasticity: Fundamentals and Applications (**COMPLAS 2014**), Barcelona, Spain, 3–5 September 2013.
- **Oliver J., Huespe A., Caicedo M., Roubin E.,Hernández J.A.** Multi-scale analysis of material failure in cement/aggregate composite structures, Computational modelling of Concrete and Concrete Structures (**EURO–C 2014**), St. Anton am Arlberg, Austria, 24–27 March 2014.
- **Hernández J.A., Oliver J., Huespe A., Caicedo M.** Computational homogenization using high-performance, reduced-order modeling, XI World Congress on Computational Mecnahics (**XI WCCM 2014**), Barcelona, Spain, 20–25 July 2014.
- **Caicedo M, Oliver J., Huespe A., Roubin E., Hernández J.A.** Continuum multi-scale (FE^2) Modeling of Material Failure, XI World Congress on Computational Mecnahics (**XI WCCM 2014**), Barcelona, Spain, 20–25 July 2014. **Link to Publisher**
- **Oliver J., Caicedo M., Roubin E., Huespe A.** Continuum approach to computational multi-scale modeling of fracture, 13th International Conference on Fracture and Damage Mechanics (**FDM-2014**), Sao Miguel Island, Azores, Portugal, September 23–25 2014.
- **Oliver J., Caicedo M., Roubin E., Huespe A.** Continuum Multi-scale modeling of propagating fracture in quasi-brittle materials, European Mechanics Congress (**EUROMECH-2015**), Eindhoven, The Netherlands, February 2015.
- **Oliver J., Huespe A. and Caicedo M.** Multiscale modelling of propagating fracture in quasi brittle materials: a continuum approach, IV International Conference on Computational Modeling of Fracture and Failure of Materials and Structures (**CFRAC 2015**), École Normale Superiéure de Cachan, France, 3–5 June 2015.
- **Caicedo M., Roubin E., Huespe A. and Oliver J.** Continuum multi-scale modeling of fracture in cementitious-like materials, Congress on Numerical Methods in Engineering (**CMN2015**), Lisbon, Portugal, Juny 29 - July 2, 2015.
- **Roubin E., Caicedo M., Hernández J., Huespe A. and Oliver J.** On POD based reduction-order modeling in multi-scale material failure simulation, Congress on Numerical Methods in Engineering (**CMN2015**), Lisbon, Portugal, Juny 29 - July 2, 2015.
- **Caicedo M., Oliver J., Roubin E., Huespe A. and Hernández J.** Continuum multi-scale (FE^2) modeling of material failure in concrete-like materials, XIII

International Conference on Computational Plasticity: Fundamentals and Applications (**COMPLAS 2015**), Barcelona, Spain, 1–3 September 2015.

- **Oliver J., Huespe A. and Caicedo M.** A continuum approach for multi-scale propagating material fracture modeling, VII European Congress on Computational Methods in Applied Sciences and Engineering (**ECCOMAS 2016**), Crete, Greece, June 5–10, 2016.

- **Caicedo M., Oliver J., Huespe A. and O. Lloberas-Valls.** Model Order Reduction in Computational Multiscale Fracture Mechanics, 15th International Conference on Fracture and Damage Mechanics (**FDM-2016**), Alicante, Spain, September 14–16, 2016.

- **Oliver J., Huespe A. and Caicedo M.** Hyper-reduced order modeling techniques in computational multiscale fracture, Colloquium 584 Multi-uncertainty and multi-scale methods and related applications (**EuroMesh 2016**), Porto, Portugal, September 14–16, 2016.

- **Oliver J., Huespe A. and Caicedo M.** High-performance model order reduction in computational multiscale fracture, XXII Congreso sobre Métodos Numéricos y sus aplicaciones (**ENIEF 2016**), Córdoba, Argentina, Noviembre 8–11, 2016.

- **Caicedo M., Toro S., Mroginski J. L., Oliver J. and Huespe A. E.** Model Order Reduction applied to Geometric Non-Linear Multiscale Modeling, XXII Congreso sobre Métodos Numéricos y sus aplicaciones (**ENIEF 2016**), Córdoba, Argentina, Noviembre 8–11, 2016.

B

PUBLISHED ARTICLES

B.1 Paper #1

Title: High-performance model reduction techniques in computational multiscale homogenization.
Authors:

- **J. A. Hernández**: Assistant Professor of Structural Engineering and Strength of Materials at the School of Industrial and Aeronautic Engineering of Terrassa, of the Technical University of Catalonia. Senior researcher at the International Center for Numerical Methods in Engineering (CIMNE).
- **J. Oliver**: Professor of Continuum Mechanics and Structural analysis at the Escola Tecnica Superior d'Enginyers de Camins, Canals i Ports (Civil Engineering School) of the Universitat Politècnica de Catalunya (Technical University of Catalonia BarcelonaTech). Senior researcher at the International Center for Numerical Methods in Engineering (CIMNE).
- **A. E. Huespe**: Professor of Mechanics at the Faculty of Chemical Engineering, Dept. of Materials, National University of Litoral, Santa Fe, Argentina. Independent researcher of Conicet at CIMEC (Centro de Investigaciones en Mecánica Computacional), National University of Litoral (UNL).
- **M. Caicedo**: PhD Candidate in Structural Analysis in UPC BarcelonaTech and International Center for Numerical Methods in Engineering (CIMNE).
- **J. C. Cante**: Associate Professor of Computational Engineering at the Escola Tècnica Superior d'Enginyeries Industrial i Aeronàutica de Terrassa – Universitat Politècnica de Catalunya (Technical University of Catalonia, BarcelonaTech). Associate researcher at the International Center for Numerical Methods in Engineering (CIMNE).

Journal of Computer Methods in Applied Mechanics and Engineering
Editors: Thomas J.R. Hughes, J. Tinsley Oden, Manolis Papadrakakis
ISSN: 0045-7825
Elsevier Editors
http://dx.doi.org/10.1016/j.cma.2014.03.011
Link to Publisher

High-performance model reduction techniques in computational multiscale homogenization

J.A. Hernández[a,c,*], J. Oliver[a,b], A.E. Huespe[b,d], M.A. Caicedo[a], J.C. Cante[a,c]

[a] *Centre Internacional de Mètodes Numèrics en Enginyeria (CIMNE), Technical University of Catalonia, Edificio C1, Campus Norte, Jordi Girona 1-3, Barcelona 08034, Spain*

[b] *E.T.S. d'Enginyers de Camins, Canals i Ports, Technical University of Catalonia, Edificio C1, Campus Norte, Jordi Girona 1-3, Barcelona 08034, Spain*

[c] *E.T.S. d'Enginyeries Industrial i Aeronàutica de Terrassa, Technical University of Catalonia, C/ Colom, 11, Terrassa 08222, Spain*

[d] *CIMEC, CONICET, Güemes 3450, 3000 Santa Fe, Argentina*

Abstract

A novel model-order reduction technique for the solution of the fine-scale equilibrium problem appearing in computational homogenization is presented. The reduced set of empirical shape functions is obtained using a partitioned version —that accounts for the elastic/inelastic character of the solution— of the Proper Orthogonal Decomposition (POD). On the other hand, it is shown that the standard approach of replacing the nonaffine term by an interpolant constructed using only POD modes leads to ill-posed formulations. We demonstrate that this ill-posedness can be avoided by enriching the approximation space with the span of the gradient of the empirical shape functions. Furthermore, interpolation points are chosen guided, not only by accuracy requirements, but also by stability considerations. The approach is assessed in the homogenization of a highly complex porous metal material. Computed results show that computational complexity is independent of the size and geometrical complexity of the representative volume element. The speedup factor is over three orders of magnitude —as compared with finite element analysis— whereas the maximum error in stresses is less than 10%.

*Corresponding author

Email address: jhortega@cimne.upc.edu (J.A. Hernández)

Keywords: Multiscale, homogenization, model reduction,
High-Performance reduced-order model, hyperreduction, POD

1. Introduction

1.1. Motivation and goal

The major challenge in the macro-scale continuum description of heterogeneous materials such as composites and polycrystalline metals (that exhibit a clear *heterogeneous* composition at the the micro-, or meso-, scale, but that can be regarded, for practical purposes, as *homogeneous* at the the macro-scale) lies in the determination of a constitutive connection, between macro-stresses and macro-strains, that accurately reflects the properties and geometrical arrangement of the distinct phases at the finer scale. It is well-known [34] that, under the hypotheses of either *periodicity or statistical homogeneity*, on the one hand; and *scale separation*, on the other hand, this constitutive link can be systematically established by solving, for *each* point at the coarse scale, a boundary value problem (BVP) on a certain representative microscopic subdomain. In a strain-driven formulation of this BVP, the macro-strain at a given point acts as "loading parameter", in the form of appropriate essential boundary conditions, whereas the associated macro-stress is obtained through volume averaging —i.e., *homogenization*— of the corresponding micro-stress field.

Methods dealing with the solution of this BVP range from purely analytical approaches to *direct computational methods*, such as the two-level, Finite Element (FE^2) method [29]. Analytical approaches are computationally inexpensive, but only valid for certain types of geometrically and constitutively simple micro-structures. By contrast, direct computational methods have no other limitation in scope than the imposed by the aforementioned hypotheses of statistical homogeneity and scale separation —in these methods, the microscopic BVP at each coarse-scale point is attacked using no other approximation than the spatial discretization of the pertinent solution strategy, thus, circumventing the need for introducing *ad-hoc*, simplifying assumptions regarding the topological arrangement of the micro-phases and/or their collective constitutive behavior. Needless to say, the versatility of direct computational homogenization comes at a significant price: its enormous computational cost.

Between these two extremes (purely analytical and direct computational methods), there are homogenization strategies that can be termed *semi-analytical*, since they combine analytical results with numerical computations. Such is the case of the *Transformation Field Analysis* (TFA) [25] and variants thereof [49, 50, 56, 30], which are based on the *pre-computation* of certain characteristic operators (strain localization and influence tensors) using the information obtained from solving a carefully chosen battery of fine-scale BPVs. Although these methods have notably widen the scope of classical analytical approaches —while maintaining their low computational cost—, they are still predicated, to a lesser or greater extent, on ad-hoc assumptions connected with the constitutive description of the involved phases. Consideration of new materials with unstudied compositions using semi-analytical approaches, thus, requires additional research efforts by specialists in the field and eventual modifications of the corresponding mathematical and numerical formulations —in contrast to direct computational homogenization approaches, such as the FE^2 method, in which the formulation is "material-independent", and hence more versatile.

The current state of affairs in the field of two-scale homogenization seems to call, thus, for a unified homogenization approach that combines somewhat the advantages of direct computational homogenization and analytical and semi-analytical techniques. It would be desirable to have a homogenization method with a computational cost virtually *independent of the geometric complexity* of the considered representative volume, as in analytical and semi-analytical techniques. At the same time, it would be also interesting to arrive at a method whose mathematical formulation dispenses with *ad-hoc*, simplifying assumptions related with the composition of the heterogeneous material; i.e, one enjoying the versatility, unrestricted applicability and "user-friendliness" —insofar as it would totally relieve the modeler from the often exceedingly difficult task of visualizing such assumptions — of direct computational homogenization methods. The goal of the present paper is to show that these desirable attributes can be achieved, for arbitrarily complex heterogeneous materials *well into the inelastic range*, by using the so-called [47] *Reduced-Basis* (RB) *approximation* in the solution of the fine-scale BVPs.

1.2. The reduced-basis method

Generally speaking, the reduced-basis approximation is a class of *Galerkin* approximation procedure that employs, as opposed to the FE method, but

similarly to classical Rayleigh-Ritz solution techniques [19], *globally supported basis functions*. The main difference with respect to classical Rayleigh-Ritz schemes is that these basis functions *or modes* are not constructed from either polynomials or transcendental functions (sines, cosines ...), but rather are determined from a larger set of *previously* computed —using *the finite element* (FE) method or other classical solution techniques— solutions of the BVP at appropriately selected values of the input of interest. These functions are commonly termed *empirical basis functions* [41], the qualifier empirical meaning "derived from computational experiments".

1.2.1. Dimensionality reduction

As noted earlier, the input of interest or "loading" parameter in the fine-scale problem is the macro-scale strain tensor. Accordingly, the starting point for constructing the basis functions consists in solving, using the FE method, a battery of BVPs for various, representative *macro-strain histories*. The outcome of these FE calculations is a data set comprising an ensemble of hundred or even thousand (depending on the number of time steps into which the strain histories are discretized) displacement field solutions (also called *snapshots*). Were all these snapshots barely correlated with each other, the dimension of the manifold spanned by them would prove overly high, rendering the entire approach impractical —it would no longer qualify as a truly *reduced* basis method. Fortunately, as we show in the present paper, in general, most of these snapshots do display strong linear correlations between each other —i.e., they have redundant information—, and, in addition, contain deformation modes that are *irrelevant* to the quality of coarse-scale predictions. All that is required to obtain a much lower dimensional representation of the solution data set, and therewith the desired reduced basis, is an automatic means to identify and remove this redundant and irrelevant information, while preserving, as much as possible, its *essential* features. The problem of removing unnecessary complexity from huge data sets so as to uncover *dominant patterns* is the central concern of disciplines such as digital image compression [60] and patter recognition [8], to name but a few, and thereby many efficient *dimensionality reduction* (or *data compression*, in more common parlance) algorithms already exist to deal with it. In the present work, we employ one of the simplest and most popular of these di-

mensionality reduction algorithms: the Proper Orthogonal Decomposition[1] (POD).

It may be inferred from the above that the proposed homogenization method, like analytical and semi-analytical strategies, does introduce *simplifications* in solving the fine-scale BVP. However, as opposed to analytical, and to a lesser extent, semi-analytical procedures, these simplifications are not introduced by the modeler, but rather are automatically carried out by the abovementioned dimensionality reduction methods (in an offline stage, prior to the overall multiscale analysis). In other words, in the proposed method, the *task of discerning what is essential and what is not*[2] *is entirely delegated to the computer* itself, and hence, its success does not depend upon the depth of insight, experience, and knowledge base of the modeler —only some discretion is to be exercised in choosing appropriate strain paths for the offline FE analyses. This feature naturally confers the advantages of versatility and "user-friendliness" enjoyed by direct computational methods.

1.2.2. Numerical integration

Once the global shape functions have been determined, the next step is to introduce an *efficient* method for *numerically evaluating the integrals* appearing in the weak form of the cell BVP. Of course one can simply use the same Gauss quadrature formulae and the same sampling points (a total number of $n_g = \mathcal{O}(n)$, n being the number of mesh nodes) as the underlying finite element model. But this would be akin to integrating, say, a third-order polynomial function using thousand of sampling points—a profligate waste of computational resources. Since displacement solutions for the cell BVP are constrained to lie in a reduced-order space of dimension $n_u << n$, it is reasonable to expect that the corresponding stresses, internal forces and Jacobians will also reside in reduced-order spaces of dimensions of order $\mathcal{O}(n_u)$, and consequently, *only* $p = \mathcal{O}(n_u) << n_g$ *sampling points* would suffice in principle to accurately evaluate the corresponding integrals. The challenging questions that have to be confronted are where to locate these p sampling points and, loosely speaking, how to determine their associated

[1] By constraining the cell to deform only into the deformation modes determined by the POD, one automatically obtains a genuine *reduced-order model* (ROM) of the cell.

[2] Discerning what is essential and what is not is, according to M.Ashby [4], the key to any successful computational model (i.e., one that strikes the right balance between accuracy and simplicity)

weighting functions so that maximum accuracy in the integration is attained.

Approaches found in the model reduction literature that, directly or indirectly, deal with these fundamental questions can be broadly classified either as *interpolatory* methods [7, 33, 54, 18, 5] or *Gauss-type quadrature* strategies [3, 39]. In both types of approaches, the integrand or part of the integrand is approximated by a linear combination of a reduced set of empirical modes. In interpolatory approaches, the coefficients in this approximation are obtained by *interpolation* at a set of pre-selected sampling points; the criterion for choosing the location of such points is the *minimization of the interpolation error* over the finite element snapshots. In Gauss-type quadrature procedures, on the other hand, the selection of sampling points and the calculation of the accompanying weighting factors are *simultaneously* carried out, guided by a criterion of *minimum integration* error over the snapshots.

In the BVP under consideration, the *output of interest* is the volume average of the stresses over the cell domain and, therefore, accuracy is required not only in the integration of the equilibrium equation, but also on the approximation of the stresses themselves. This is the reason why attention is focused here on interpolatory integration strategies, the variable subject to spatial interpolation being precisely the stresses.

1.3. Originality of this work

The idea of exploiting the synergistic combination of multiscale modeling and reduced basis approximation is admittedly not new. In the specific context of two-scale homogenization, it has been recently explored by Boyaval [10], Yvonnet et al. [62], and Monteiro et al. [51]. Traces of this idea can also be found in articles dealing with more general hierarchical multiscale techniques —that do not presuppose either scale separation or periodicity/statistical homogeneity, or both—, namely, in the *multiscale finite element method* [53, 26, 27], in the *heterogeneous multiscale method* [2, 1], and in multiscale approaches based on the Proper Generalized Decomposition (PGD)[21]. However, it should be noted that none of the above cited papers confronts the previously described, crucial question of how to *efficiently integrate* the resulting reduced-order equations, simply because, in most of them [10, 53, 26, 27, 2, 1], integration is not an issue — the fine-scale BVPs addressed in these works bear an *affine* relation with the corresponding coarse-scale, input parameter, as in linear elasticity, and, consequently, all integrals can be *pre-computed*, i.e., evaluated *offline*, with no impact in the online computational cost. Thus, the development of reduced-order models

endowed with efficient, mesh-size independent integration schemes —able to handle any material composition— is a research area that, to the best of the authors' knowledge, still remains uncharted.

1.3.1. Main original contributions

The theory underlying reduced-order models (ROMs) that incorporate *efficient* interpolatory integration schemes is still at its embryonic stage of development —the first general proposal for parametrized BVPs dates back to 2004 [7]— and many fundamental issues remain to be addressed. Foremost among these is the crucial question of *well-posedness* of the resulting system of algebraic equations: does the replacement of the integrand, or *non-affine* term in the integrand, by a reduced-order interpolant always lead to a well-posed, discrete problem ? Examination of the reduced basis literature indicates that apparently no researcher has so far been confronted with ill-posed reduced-order equations, a fact that might certainly promote the view that uniqueness of solution can be taken for granted whenever the full-order model is well-posed. Unfortunately, this is not always so: we demonstrate in this paper that the choice of the reduced-order space in which the interpolant of the integrand resides has a profound impact on the well-posedness of the discrete problem. In particular, we show that, in the case of the fine-scale boundary-value problem, the widely adopted [33] approach of determining the basis functions for this space from (converged) FE snapshots leads invariably to *ill-posed*, discrete formulations. The *main original contribution of the present work to the field of reduced-order modeling is the development of an interpolatory integration method that safely overcomes this type of ill-posedness*. The gist of the method is to *expand* the interpolation space so that it embraces, aside from the span of the POD stress basis functions, the space generated —and herein lies the novelty— by the *gradient of the (reduced-order) shape functions*. Furthermore, it is shown that, in contrast to the situation encountered when using standard interpolatory schemes in other parametrized BVPs [33], in the BVP under consideration, the *number and particular placement of sampling points within the integration domain influence notably the spectral properties* (positive definiteness) *of the Jacobian matrix of the governing equation*, and therefore, the *convergence characteristics of the accompanying Newton-Raphson solution algorithm*. Another innovative ingredient of the present paper is a points selection algorithm that does acknowledge this peculiarity and chooses the desired sampling points guided, not only by accuracy requirements (minimization of the interpolation

error over the FE stress snapshot), but also by stability considerations.

2. RVE equilibrium problem

In this section, we present the variational statement and finite element discretization of the *fine-scale equilibrium problem*, which, recall, is the parameterized BVP we wish to efficiently solve using the reduced-basis approximation.

2.1. Preliminaries

Let $\Omega \subset \mathbb{R}^d\,(d = 2, 3)$ be a subvolume of characteristic length $l << l_M$ (l_M is the characteristic length of the macro-continuum Ω_M, see Figure 1) that is *representative* of the heterogeneous material as a whole. In micro-structures that exhibit statistical homogeneity, this domain receives the name of *Representative Volume Element* (RVE), whereas in micro-structures that display periodicity, it is commonly known as repeating unit cell (RUC), or simply *unit cell* [24]. In the sequel, the acronym RVE will be used to refer to Ω.

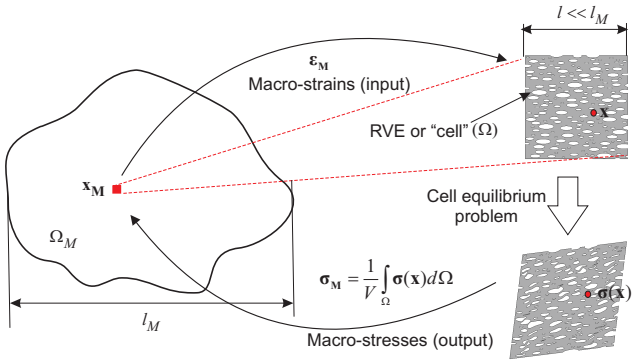

Figure 1: First-order homogenization.

In the homogenization approach adopted in this work —commonly known as *first-order* homogenization [32, 40]—, the strain field $\boldsymbol{\epsilon}(\mathbf{x})$ at any point $\mathbf{x} \in \Omega$ is assumed to be decomposed into macroscopic and fluctuating contributions; under the hypothesis of infinitesimal deformations, this decomposition can be written as:

$$\boldsymbol{\epsilon}(\mathbf{x}) = \boldsymbol{\epsilon_M} + \nabla^s \boldsymbol{u}(\mathbf{x}). \tag{1}$$

Here, $\boldsymbol{\epsilon_M}$ stands[3] for the macroscopic strain tensor (the *input parameter* in the problem) and $\nabla^s \boldsymbol{u}$ denotes the symmetric gradient of the *displacement fluctuation field* (this field is, in turn, the *basic unknown* of the problem).

Implicit in the scale separation assumption is the fact that fine-scale deformations only influence coarse-scale behavior through its volume average over the RVE. It can be shown (see, for instance, Ref. [22]) that this implies that the boundary conditions (BCs) prescribed on the RVE must be homogeneous (i.e., $\boldsymbol{A}_0\boldsymbol{u} = \mathbf{0}$ on $\partial\Omega$, $\boldsymbol{A}_0$ being a certain linear operator). The natural choice for a repeating unit cell is to employ *periodic* boundary conditions (See Refs. [9, 48] for more details on how to prescribe this type of BCs). In statistically homogeneous micro-structures, by contrast, there is a certain latitude in the choice of boundary conditions (vanishing fluctuations, uniform tractions, quasi-periodic conditions ...). In the examples shown later, vanishing boundary conditions are used ($\boldsymbol{u} = \mathbf{0}$ on $\partial\Omega$).

2.2. Variational formulation

2.2.1. Trial and test spaces

The trial space, i.e., the *set of kinematically admissible displacement fluctuation* fields, is defined formally as

$$\mathcal{V}_u = \left\{ \boldsymbol{u} \in H^1(\Omega)^d \mid \boldsymbol{A}_0\boldsymbol{u} = \mathbf{0}, \;\; on \;\; \partial\Omega \right\}, \tag{2}$$

where $H^1(\Omega)^d$ stands for the Sobolev space of functions possessing square integrable derivatives over Ω. Note that this set forms a *vector space*. Since the *test* functions $\boldsymbol{\eta}$ appearing in the variational statement shown in the following are *kinematically admissible variations* ($\boldsymbol{\eta} := \mathbf{u} - \mathbf{v}, \quad \mathbf{u}, \mathbf{v} \in \mathcal{V}_\mathbf{u}$), $\mathcal{V}_u$ having structure of vector space implies that, in the RVE equilibrium problem, the *spaces of trial and test functions coincide*.

2.2.2. Formal statement

Consider a time discretization of the interval of interest $[t_0, t_f] = \bigcup_{n=1}^{n_{stp}} [t_n, t_{n+1}]$. The current value of the microscopic stress tensor $\boldsymbol{\sigma}_{n+1}$ at each $\mathbf{x} \in \Omega$ is presumed to be entirely determined by, on the one hand, the current value of the

[3] Macroscopic variables will be identified by appending a subscript "M", while variables associated to the fine scale will be designated by bare symbols. For instance, we shall write $\boldsymbol{\epsilon_M}$ and $\boldsymbol{\epsilon}(\mathbf{x})$ to denote the macroscopic strain tensor and the fine-scale strain field, respectively.

microscopic strain tensor $\boldsymbol{\epsilon}_{n+1}(\mathbf{x}) = \boldsymbol{\epsilon}_{\boldsymbol{M}n+1} + \nabla^s \boldsymbol{u}_{n+1}(\mathbf{x})$, and, on the other hand, a set of microscopic internal variables $\boldsymbol{\xi}_{n+1}$ —that encapsulate the *history* of microscopic deformations. The relationship between these variables is established by (phenomenological) rate constitutive equations; these equations may vary from point to point within the RVE (multiphase materials). Likewise, the considered RVE may contain also voids distributed all over the domain. The (incremental) RVE equilibrium problem at time t_{n+1} can be stated as follows (see Ref. [22]): given the *initial data* $\{\boldsymbol{u}_n(\mathbf{x}), \boldsymbol{\epsilon}_{\boldsymbol{M}n}, \boldsymbol{\xi}_n(\mathbf{x})\}$ and the *prescribed* macroscopic strain tensor $\boldsymbol{\epsilon}_{\boldsymbol{M}n+1}$, find $\boldsymbol{u}_{n+1} \in \mathcal{V}_u$ such that

$$\int_\Omega \nabla^s \boldsymbol{\eta} : \boldsymbol{\sigma}_{n+1}(\boldsymbol{\epsilon}_{\boldsymbol{M}n+1} + \nabla^s \boldsymbol{u}_{n+1}, \boldsymbol{\xi}_{n+1})\, d\Omega = 0, \tag{3}$$

for all $\boldsymbol{\eta} \in \mathcal{V}_u$. The actual *output of interest* in this fine-scale BVP is not the displacement fluctuation field *per se*, but rather the macroscopic stress tensor $\boldsymbol{\sigma}_{\boldsymbol{M}}|_{n+1}$, which is defined as the volume average over the RVE of the microscopic stresses:

$$\boldsymbol{\sigma}_{\boldsymbol{M}}|_{n+1} := \frac{1}{V} \int_\Omega \boldsymbol{\sigma}_{n+1}\, d\Omega, \tag{4}$$

where V stands for the volume of the RVE. In order to keep the notation uncluttered, the superindex "n+1" will be hereafter dropped out and all quantities will be assumed to be evaluated at time t_{n+1}; only when confusion is apt to show up, the pertinent distinction will be introduced.

2.3. Finite element formulation

Let $\Omega = \bigcup_{n=1}^{n_e} \Omega^e$ be a finite element discretization of the RVE. It will be assumed that this discretization is fine enough to consider the exact and FE approximated solutions indistinguishable at the accuracy level of interest. Let $\{N_1(\mathbf{x}), N_2(\mathbf{x}) \dots N_n(\mathbf{x})\}$ (n denotes the number of nodes of the discretization) be a set of *shape functions* associated to this discretization. Now we approximate $\boldsymbol{u} \in \mathcal{V}_u$ and $\boldsymbol{\eta} \in \mathcal{V}_u$ as

$$\boldsymbol{u}(\mathbf{x}; \boldsymbol{\epsilon}_{\boldsymbol{M}}) \approx \boldsymbol{u}^{(h)}(\mathbf{x}; \boldsymbol{\epsilon}_{\boldsymbol{M}}) = \sum_{I=1}^{n} N_I(\mathbf{x}) \boldsymbol{U}_I(\boldsymbol{\epsilon}_{\boldsymbol{M}}), \tag{5}$$

$$\boldsymbol{\eta}(\mathbf{x}) \approx \boldsymbol{\eta}^{(h)}(\mathbf{x}) = \sum_{I=1}^{n} N_I(\mathbf{x}) \boldsymbol{\eta}_I, \tag{6}$$

where $\boldsymbol{U}_I \in \mathbb{R}^d$ and $\boldsymbol{\eta}_I \in \mathbb{R}^d$ $(I = 1, 2 \ldots n)$ denote the nodal values of the displacement fluctuations and test functions, respectively. Inserting these approximations in Eq.(3), and exploiting the arbitrariness of coefficients $\boldsymbol{\eta}_I$ $(I = 1, 2 \ldots n)$, one arrives at the following set of discrete equilibrium equations (repeated indices implies summation):

$$\int_\Omega \frac{\partial N_I}{\partial x_j} \boldsymbol{\sigma}_{ij}(\boldsymbol{\epsilon_M} + \nabla^s \boldsymbol{u}^{(h)}, \boldsymbol{\xi})\, d\Omega = 0 \;\; (i = 1 \ldots d;\; I = 1 \ldots n). \tag{7}$$

Introducing Voigt's notation[4], the above equation can be expressed in matrix format as:

$$\int_\Omega \boldsymbol{B}^T \boldsymbol{\sigma}(\boldsymbol{\epsilon_M} + \boldsymbol{BU}, \boldsymbol{\xi})\, d\Omega = \mathbf{0}, \tag{8}$$

As usual, numerical evaluation of the integral in Eq.(8) is carried out by Gaussian quadrature:

$$\int_\Omega \boldsymbol{B}^T \boldsymbol{\sigma}\, d\Omega \approx \sum_{g=1}^{n_g} w_g \boldsymbol{B}^T(\mathbf{x}_g) \boldsymbol{\sigma}(\mathbf{x}_g, ;) = \mathbf{0}. \tag{9}$$

Here, $n_g = \mathcal{O}(n)$ stands for the total number of Gauss points of the mesh; w_g denotes the weight associated to the $g - th$ Gauss point $\mathbf{x}_g$ (this weight includes both the *quadrature* weight itself and the corresponding Jacobian determinant.); and $\boldsymbol{B}(\mathbf{x}_g)$ and $\boldsymbol{\sigma}(\mathbf{x}_g, ;)$ stand for the B-matrix and the stress vector at Gauss point $\mathbf{x}_g$, respectively.

3. Computation of reduced basis

A basic, intuitive picture of the strategy for computing the reduced basis onto which to project the RVE equilibrium equation (3) was already given in the introductory section. In the following, we put the idea behind this strategy on a more rigorous footing. We begin by noting that, from a functional analysis standpoint, the term *model reduction* is conceptually akin

[4]Here, it is convenient to use the so-called *modified Voigt's notation* rather than the standard one. In the *modified* Voigt's notation, both stress $\boldsymbol{\sigma}$ and strain $\boldsymbol{\epsilon}$ tensors are represented as column vectors ($\{\boldsymbol{\sigma}\}$ and $\{\boldsymbol{\epsilon}\}$, respectively) in which the shear components are multiplied by $\sqrt{2}$. The advantage of this notation over the conventional, engineering Voigt's notation is the equivalence between norms; viz., $\|\boldsymbol{\sigma}\| = \sqrt{\boldsymbol{\sigma} : \boldsymbol{\sigma}} = \|\{\boldsymbol{\sigma}\}\| = \sqrt{\{\boldsymbol{\sigma}\}^T \{\boldsymbol{\sigma}\}}$. The reader is urged to consult [20] for further details on this notation.

to the more common term *model discretization*, since both connote *transitions* from higher-dimensional to lower-dimensional solution spaces. Whereas *model discretization* is used to refer to the (classical) passage from the infinite dimensional space $\mathcal{V}_u$ to the finite element subspace $\mathcal{V}_u^h \subset \mathcal{V}_u$, *model reduction* denotes a transition from this finite dimensional space $\mathcal{V}_u^h$ to a significantly smaller manifold $\mathcal{V}_u^* \subset \mathcal{V}_u^h$ —the *reduced-order* space. This latter transition is not carried out directly, but in two sequential steps, namely, *sampling of the input parameter space* and *dimensionality reduction*.

3.1. Sampling of the input parameter space

In constructing the finite element space of *kinematically* admissible functions $\mathcal{V}_u^h$, the only restrictions placed on the motion of the mesh nodes are those imposed at the boundaries. The finite element solution space, thus, does not presuppose any constraint on the motion of the *interior* nodes of the mesh.

However, in actuality, interior nodes cannot *fluctuate* freely, independently from each other, but they rather move according to *deformational patterns* dictated by the *constitutive laws* that govern the mechanical behavior of the distinct phases in the RVE[5]. This means that the solution of the finite element equilibrium equation (3) for given values of the macro-strain tensor $\boldsymbol{\epsilon_M}$ actually lives in a smaller subspace $\mathcal{V}_u^\epsilon \subset \mathcal{V}_u^h$ (in the parlance of model reduction [47, 57], $\mathcal{V}_u^\epsilon$ is the manifold induced by the parametric dependence of the BVP on the input variables).

Yet, in general, this subspace cannot be precisely determined; one has to be content to construct an *approximation* of it as the span of the displacement fluctuation solutions obtained for a judiciously chosen set of n_{hst} input strain histories $\{{}^t\boldsymbol{\epsilon_M}^1, {}^t\boldsymbol{\epsilon_M}^2, \dots {}^t\boldsymbol{\epsilon_M}^{n_{hst}}\}$. Suppose, for simplicity, that each of these strain histories is discretized into equal number of steps n_{stp}, and let

$$\boldsymbol{u}^k(\mathbf{x}) = \boldsymbol{u}(\mathbf{x}; {}^t\boldsymbol{\epsilon_M}_j{}^i), \quad k = (i-1)n_{hst} + j \tag{10}$$

denote the displacement fluctuation solution at the $j-th$ time step of the $i-th$ strain history ($i = 1, 2 \dots n_{hst}$, $j = 1, 2 \dots n_{stp}$). The approximating space for $\mathcal{V}_u^\epsilon$, henceforth called the *snapshots space*, is then defined as:

[5] As noted by Lubliner [45], constitutive laws can be regarded as *internal restrictions* on the kinds of deformation a body can suffer

$$\mathcal{V}_u^{snp} = \text{span}\left\{\boldsymbol{u}^1(\mathbf{x}), \boldsymbol{u}^2(\mathbf{x}), \dots \boldsymbol{u}^{n_{snp}}(\mathbf{x})\right\} \subseteq \mathcal{V}_u^{\epsilon}, \tag{11}$$

$n_{snp} = n_{stp} n_{hst}$ being the total number of snapshots. The matrix containing, in columns, the nodal values of these displacement fluctuations solutions:

$$\boldsymbol{X}_u = \begin{bmatrix} \boldsymbol{U}^1 & \boldsymbol{U}^2 & \cdots & \boldsymbol{U}^{n_{snp}} \end{bmatrix} \in \mathbb{R}^{n \cdot d \times n_{snp}} \tag{12}$$

will correspondingly be termed the (displacement fluctuations) *snapshot matrix*.

3.2. Dimensionality reduction

The next and definitive step in the transition from the high-dimensional finite element space $\mathcal{V}_u^h$ to the desired reduced-order space $\mathcal{V}_u^*$ —in which the fine-scale BVP is to be finally posed— is the *dimensionality reduction* process, in which, as pointed out in the introductory section, the dominant deformational patterns of the RVE response are identified and unveiled by washing out the "inessentials". To accomplish this central task, we employ here a partitioned version of the *Proper Orthogonal Decomposition*[6].

3.2.1. Elastic/Inelastic reduced basis functions

The Proper Orthogonal Decomposition is nothing but a multidimensional data fitting procedure intended to obtain a sequence of orthogonal basis functions whose span best approximate the space of snapshots. As such, the POD is a *purely data-driven* process —it is "agnostic" to the physical origin of the data. For instance, for POD basis construction purposes, it is completely immaterial whether a given snapshot corresponds to a purely linear elastic solution or to a solution well into the inelastic regime. The task of discriminating which features of the RVE response are *essential* and which are not is exclusively guided by statistical considerations: if the elastic response happens to be poorly represented within the snapshot ensemble, the POD may regard as unimportant the contribution of these snapshots, and, as a consequence, the basis functions with largest associated singular values —i.e., the *essential* modes— would hardly contain any information of this range. To accurately replicate the apparently trivial linear elastic behavior, thus, one may be forced to take a relatively large number of basis functions, and this

[6]See Appendix A for a brief description of the POD.

may translate into a significant increase in the overall *online* computational cost. This fact certainly places the POD-based reduced basis approach at a competitive disadvantage compared with semi-analytical homogenization approaches such as the Nonlinear Transformation Field Analysis [50], which do capture exactly (and effortlessly) the linear elastic response of the RVE.

To eliminate this shortcoming, we propose here a slightly different strategy for constructing the reduced basis. The essence of the proposal is to partition the space of snapshots $\mathcal{V}_u^{snp}$ into *elastic* ($\mathcal{V}_{u,el}^{snp}$) and *inelastic* ($\mathcal{V}_{u,inel}^{snp}$) subspaces:

$$\mathcal{V}_u^{snp} = \mathcal{V}_{u,el}^{snp} \oplus \mathcal{V}_{u,inel}^{snp}, \tag{13}$$

($\oplus$ symbolizes direct sum of subspaces [55]) and then obtain the reduced basis as the *union* of the bases for both subspaces. Below, we describe this strategy more in detail.

The first step is to determine an orthogonal basis for $\mathcal{V}_{u,el}^{snp}$. One can do this by simply performing m_e independent, linear elastic finite element analysis of the RVE ($m_e = 6$ for 3D problems[7], and $m_e = 3$ for plane strain), and then orthonormalizing the resulting displacement fluctuation fields. These m_e elastic modes will be considered as the first m_e basis functions of the reduced basis:

$$\text{span}\{\boldsymbol{\Phi}_1, \boldsymbol{\Phi}_2, \ldots, \boldsymbol{\Phi}_{m_e}\} = \mathcal{V}_{u,el}^{snp}. \tag{14}$$

Once we have at our disposal this set of elastic basis functions, we compute the (orthogonal) projection of each snapshot $\boldsymbol{u}^k$ onto the orthogonal complement of $\mathcal{V}_{u,el}^{snp}$ (which is precisely the aforementioned *inelastic space* $\mathcal{V}_{u,inel}^{snp}$):

$$\boldsymbol{u}_{inel}^k := \boldsymbol{u}^k - \sum_{i=1}^{m_e} \left\langle \boldsymbol{\Phi}_i, \boldsymbol{u}^k \right\rangle_{L_2(\Omega)} \boldsymbol{\Phi}_i, \quad k = 1, 2 \ldots n_{snp}. \tag{15}$$

It is now on this ensemble of *inelastic* snapshots $\{\boldsymbol{u}_{inel}^k\}_{k=1}^{n_{snp}}$ that the previously described POD is applied to obtain the remaining $n_u - m_e$ basis functions. Thus, we finally have:

$$\mathcal{V}_u^* = \mathcal{V}_{u,el}^{snp} \oplus \mathcal{V}_{u,inel}^{snp} = \text{span}\{\overbrace{\boldsymbol{\Phi}_1, \boldsymbol{\Phi}_2, \ldots, \boldsymbol{\Phi}_6}^{\text{Elastic modes}}, \quad \overbrace{\boldsymbol{\Phi}_7, \ldots, \boldsymbol{\Phi}_{n_u}}^{\text{“Essential” Inelastic modes}} \quad \}. \tag{16}$$

[7]Strictly speaking, the proposed decomposition is only valid for materials governed by rate-independent constitutive equations.

for 3D problems, and

$$\mathcal{V}_u^* = \text{span}\{\overbrace{\boldsymbol{\Phi}_1, \boldsymbol{\Phi}_2, \boldsymbol{\Phi}_3}^{\text{Elastic modes}}, \quad \overbrace{\boldsymbol{\Phi}_4, \ldots, \boldsymbol{\Phi}_{n_u}}^{\text{“Essential” inelastic modes}} \quad \}. \tag{17}$$

for plane strain. In placing the m_e elastic modes within the first m_e positions, the reduced-order model is guaranteed to deliver linear elastic solutions with the same accuracy as the underlying (full-order) finite element model (obviously, provided that $n_u \geq m_e$).

Further details concerning the numerical implementation of this apparently novel —to the best of the authors' knowledge— basis construction strategy can be found in Appendix B.

4. Galerkin projection onto the reduced subspace

We now seek to pose the boundary-value problem represented by Eq.(3) in the reduced-order space $\mathcal{V}_u^* \subseteq \mathcal{V}_u^h$ spanned by the basis functions $\{\boldsymbol{\Phi}_1, \boldsymbol{\Phi}_2, \ldots, \boldsymbol{\Phi}_{n_u}\}$. To this end, we approximate both test $\boldsymbol{\eta} \in \mathcal{V}_u$ and trial $\boldsymbol{u} \in \mathcal{V}_u$ functions by the following linear expansions:

$$\boldsymbol{u}(\mathbf{x}; \boldsymbol{\epsilon_M}) \approx \boldsymbol{u}^*(\mathbf{x}; \boldsymbol{\epsilon_M}) = \sum_{i=1}^{n_u} \boldsymbol{\Phi}_i(\mathbf{x}) U_i^*(\boldsymbol{\epsilon_M}), \tag{18}$$

$$\boldsymbol{\eta}(\mathbf{x}) \approx \boldsymbol{\eta}^*(\mathbf{x}) = \sum_{i=1}^{n_u} \boldsymbol{\Phi}_i(\mathbf{x}) \eta_i^*, \tag{19}$$

$\boldsymbol{u}^*(\mathbf{x})$ and $\boldsymbol{\eta}^*(\mathbf{x})$ being the low-dimensional approximations of trial and test functions, respectively (hereafter, asterisked symbols will be used to denote low-dimensional approximations of the associated variables). Inserting Eqs. (18) and (19) into Eq.(3), and exploiting the arbitrariness of coefficients η_i^* ($i = 1, 2 \ldots n_u$), we arrive at the following set of n_u equilibrium equations:

$$\int_\Omega \nabla^s \boldsymbol{\Phi}_i(\mathbf{x}) : \boldsymbol{\sigma}(\mathbf{x}; \boldsymbol{\epsilon_M} + \nabla^s \boldsymbol{u}^*, \boldsymbol{\xi})\, d\Omega = 0, \quad i = 1, 2 \ldots n_u. \tag{20}$$

Expressing now the reduced basis functions in the above equation in terms of finite element shape functions (through expression $\boldsymbol{\Phi}_i(\mathbf{x}) = \sum_{I=1}^{n} N_I(\mathbf{x}) \boldsymbol{\Phi}_{Ii}$), we get (in Voigt's notation):

$$\int_\Omega \boldsymbol{B}_i^{*T}(\mathbf{x})\, \boldsymbol{\sigma}(\mathbf{x}; \boldsymbol{\epsilon_M} + \boldsymbol{B}^* \boldsymbol{U}^*, \boldsymbol{\xi})\, d\Omega = \mathbf{0}, \quad i = 1, 2 \ldots n_u, \tag{21}$$

or more compactly:

$$\int_{\Omega} \boldsymbol{B}^{*T}(\mathbf{x})\, \boldsymbol{\sigma}(\mathbf{x}; \boldsymbol{\epsilon_M} + \boldsymbol{B}^{*}\boldsymbol{U}^{*}, \boldsymbol{\xi})\, d\Omega = \mathbf{0}. \tag{22}$$

Here, $\boldsymbol{U}^{*} = \begin{bmatrix} U_1^{*} & U_2^{*} & \cdots & U_{n_u}^{*} \end{bmatrix}^{T} \in \mathbb{R}^{n_u}$ denotes the vector containing the *reduced* displacement fluctuations —the basic unknowns of the reduced-order problem— and $\boldsymbol{B}^{*} : \Omega \to \mathbb{R}^{s \times n_u}$ stands for the *reduced* "B-matrix", defined as:

$$\boldsymbol{B}^{*}(\mathbf{x}) := \boldsymbol{B}(\mathbf{x})\boldsymbol{\Phi}. \tag{23}$$

This matrix connects the gradient of the displacement fluctuation field with the vector of reduced displacement fluctuations:

$$\begin{aligned} \nabla^{s}\boldsymbol{u}^{*} = \sum_{i=1}^{n_u} \boldsymbol{B}_i^{*} U_i^{*} &= \overbrace{\begin{bmatrix} \boldsymbol{B}_1^{*} & \boldsymbol{B}_2^{*} & \cdots & \boldsymbol{B}_{n_u}^{*} \end{bmatrix}}^{\boldsymbol{B}^{*}} \overbrace{\begin{bmatrix} U_1^{*} \\ U_2^{*} \\ \vdots \\ U_{n_u}^{*} \end{bmatrix}}^{\boldsymbol{U}^{*}} \\ &= \boldsymbol{B}^{*}\boldsymbol{U}^{*} = \boldsymbol{B}\boldsymbol{\Phi}\boldsymbol{U}^{*}. \end{aligned} \tag{24}$$

For implementational purposes, it is more expedient to express Eq.(23) in terms of elemental $B-$matrices. To this end, we write:

$$\boldsymbol{B}(\mathbf{x}) = \begin{cases} \boldsymbol{B}^{e}(\mathbf{x}), & \text{if } \mathbf{x} \in \Omega^{e} \\ \mathbf{0}, & \text{otherwise} \end{cases} \tag{25}$$

where $\boldsymbol{B}^{e} \in \mathbb{R}^{s \times d \cdot \bar{n}_e}$ denotes the local B-matrix of element Ω^{e} ($\bar{n}_e$, in turn, is the number of nodes in Ω^{e}). Thus,

$$\boldsymbol{B}^{*}(\mathbf{x}) = \boldsymbol{B}(\mathbf{x})\boldsymbol{\Phi} = \boldsymbol{B}^{e}(\mathbf{x})\boldsymbol{\Phi}^{e}. \tag{26}$$

In the above equation, $\boldsymbol{\Phi}^{e} \in \mathbb{R}^{d\bar{n}_e \times n_u}$ represents the block matrix of $\boldsymbol{\Phi}$ corresponding to the $\bar{n}_e$ nodes of finite element Ω^{e} ($e = 1, 2 \ldots n_e$).

5. Stress approximation space

To arrive at an efficient, mesh-size independent integration scheme, two crucial questions have to be addressed, namely, the determination of the

vector space (hereafter denoted by $\mathcal{V}_\sigma^{apr}$) in which the low-dimensional approximation of the *stress field*[8] should lie in order to obtain an accurate and at the same time well-posed ROM; and the calculation of the optimal location of the *sampling or integration points*. Attention here and in the next section is confined to the aspect related to the stress approximation space; the issue related to the selection of sampling points, on the other hand, is examined in Section 7.

5.1. The reduced-order subspace of statically admissible stresses ($\mathcal{V}_\sigma^*$)

At first sight, the problem of constructing a $\mathcal{O}(n_u)$-dimensional representation of the stress field seems quite similar to the problem addressed in Section 3 concerning the reduced basis for the displacement fluctuations: we have to find a set of orthogonal basis functions $\{\boldsymbol{\Psi}_1(\mathbf{x}), \boldsymbol{\Psi}_2(\mathbf{x}) \dots \boldsymbol{\Psi}_{n_\sigma}(\mathbf{x})\}$ ($n_\sigma = \mathcal{O}(n_u)$) such that its span accurately approximates the set of all possible *stress solutions* —that is, the set of all *statically admissible stresses*. Accordingly, following the procedure described in Section 3, we first compute finite element, stress distributions over the RVE for representative macrostrain histories[9]. Then, the elastic/inelastic dimensionality reduction process set forth in Section 3.2.1 is applied to the resulting ensemble of stress solutions $\{\boldsymbol{\sigma}^1(\mathbf{x}), \boldsymbol{\sigma}^2(\mathbf{x}) \dots \boldsymbol{\sigma}^{n_{snp}}(\mathbf{x})\}$, in order to identify both the elastic and the *essential* inelastic stress modes. The space spanned by these modes will be denoted hereafter by $\mathcal{V}_\sigma^*$ and termed the *reduced-order subspace of statically admissible stresses*:

$$\mathcal{V}_\sigma^* = \text{span}\{\overbrace{\boldsymbol{\Psi}_1(\mathbf{x}), \boldsymbol{\Psi}_2(\mathbf{x}), \dots, \boldsymbol{\Psi}_{m_e}(\mathbf{x})}^{\text{Elastic stress modes}}, \overbrace{\boldsymbol{\Psi}_{m_e+1}(\mathbf{x}), \boldsymbol{\Psi}_{m_e+2}(\mathbf{x}), \dots, \boldsymbol{\Psi}_{n_\sigma}(\mathbf{x})}^{\text{“Essential”, inelastic stress modes}}\}. \tag{27}$$

[8] It was mentioned in the introductory section that the central idea of efficient interpolatory approaches for numerical integration of reduced-order BVPs is to replace the nonaffine term in the the integrand by low-dimensional interpolants. In our case, a glance at the reduced-order equilibrium equation (21) readily reveals that such “offending”, nonaffine term is the *stress field* —the reduced B-matrix $\boldsymbol{B}^* = \boldsymbol{B}^*(\mathbf{x})$ is independent of the input parameter $\boldsymbol{\epsilon_M}$ and hence need not be subject to approximation.

[9] The most practical and somehow consistent choice regarding these strain trajectories is to use the same as in the computation of the displacement fluctuations snapshots

5.2. Ill-posedness of the HP-ROM

Let us now try to construct the low-dimensional approximation of the stress field, denoted by[10] $\boldsymbol{\sigma}^*$, as a linear combination of the above described stress reduced basis— hence making $\mathcal{V}_\sigma^{apr} = \mathcal{V}_\sigma^*$—; i.e.,

$$\boldsymbol{\sigma}(\mathbf{x}; \boldsymbol{\epsilon_M}, \boldsymbol{U}^*) \approx \boldsymbol{\sigma}^*(\mathbf{x}; \boldsymbol{\epsilon_M}, \boldsymbol{U}^*) = \sum_{i=1}^{n_\sigma} \boldsymbol{\Psi}_i(\mathbf{x}) c_i(\boldsymbol{\epsilon_M}, \boldsymbol{U}^*), \tag{28}$$

where $c_i \in \mathbb{R}$ $(i = 1, 2 \dots n_\sigma)$. This strategy of approximating the *offending*, *nonaffine* term in the BVP by a linear combination of pre-computed basis functions —obtained, in turn, from samples of the nonaffine term evaluated at the solution— has been successfully applied by several authors, with no apparent —or at least not reported— computational pitfalls, to a wide gamut of problems: nonlinear monotonic elliptic and nonlinear parabolic BPVs [46, 33], nonlinear miscible viscous fingering in porous media [17, 18], uncertainty quantification in inverse problems [31], and nonlinear heat conduction problems [5, 6], to cite but a few.

However, a closer examination of the the RVE equilibrium problem reveals that, in this case, this "standard" strategy proves completely fruitless, for it leads to patently *ill-posed* reduced-order equations. To show this, let us first substitute approximation (28) into Eq.(21):

$$\begin{aligned} &\int_\Omega \boldsymbol{B}^{*T}(\mathbf{x})\, \boldsymbol{\sigma}(\mathbf{x}; \boldsymbol{\epsilon_M}, \boldsymbol{U}^*)\, d\Omega \approx \int_\Omega \boldsymbol{B}^{*T}(\mathbf{x})\, \boldsymbol{\sigma}^*(\mathbf{x}; \boldsymbol{\epsilon_M}, \boldsymbol{U}^*) = \\ &\sum_{i=1}^{n_\sigma} \left(\int_\Omega \boldsymbol{B}^{*T}(\mathbf{x}) \boldsymbol{\Psi}_i(\mathbf{x})\, d\Omega \right) c_i(\boldsymbol{\epsilon_M}, \boldsymbol{U}^*) = \mathbf{0}. \end{aligned} \tag{29}$$

By virtue of Eq.(23), the bracketed integral in the preceding equation can be rephrased as:

$$\int_\Omega \boldsymbol{B}^{*T}(\mathbf{x}) \boldsymbol{\Psi}_i(\mathbf{x})\, d\Omega = \boldsymbol{\Phi}^T \left(\int_\Omega \boldsymbol{B}^T(\mathbf{x}) \boldsymbol{\Psi}_i(\mathbf{x})\, d\Omega \right), \quad i = 1, 2 \dots n_\sigma. \tag{30}$$

Each basis function $\boldsymbol{\Psi}_i(\mathbf{x})$ $(i = 1, 2 \dots n_\sigma)$ is, by construction, a linear combination of the stress snapshots collected during the offline, finite element

[10] Notice that, in keeping with the notational convention introduced in Section 4, the low-dimensional approximation of the stress field is represented by attaching an asterisk to the stress symbol.

analysis; thus, we can write $\boldsymbol{\Psi}_i = \sum_{j=1}^{n_{snp}} \beta_{ij} \boldsymbol{\sigma}^j$ $(i = 1, 2 \dots n_\sigma)$, $\beta_{ij} \in \mathbb{R}$ being the corresponding coefficients in the linear combination. Inserting the above equation into Eq.(30) and considering that $\boldsymbol{\sigma}^j$ $(j = 1, 2 \dots n_{snp})$ are finite element stress solutions —and therefore fulfill the finite element equilibrium equation (8)—, we finally arrive at:

$$\boldsymbol{\Phi}^T \sum_{j=1}^{n_{snp}} \beta_{ij} \overbrace{\left(\int_\Omega \boldsymbol{B}^T \boldsymbol{\sigma}^j \, d\Omega \right)}^{=0} = \mathbf{0}, \quad i = 1, 2 \dots n_\sigma, \tag{31}$$

that is, the integral (30) appearing in the equilibrium equation (29), and hence, the left-hand side of the equation itself, vanishes identically regardless of the value of the modal coefficients $c_i \in \mathbb{R}$ $(i = 1, 2 \dots n_\sigma)$, and therefore, regardless of the value of the reduced displacement fluctuations $\boldsymbol{U}^*$—hence the ill-posedness.

5.3. Proposed remedy: the expanded space approach

It is clear from the foregoing discussion that the root cause of the ill-posedness lies in the fact that the set of all admissible stress fields $(\mathcal{V}_\sigma)$ forms a *vector space*, and, consequently, the POD stress modes $\boldsymbol{\Psi}_i \in \mathcal{V}_\sigma$ $(i = 1, 2 \dots n_\sigma)$ —and any linear combination of them— turn out to be self-equilibrated fields. Thus, for the reduced-order problem to be well-posed, the approximation space $\mathcal{V}_\sigma^{apr}$ cannot be only formed by statically admissible stresses, but *it must also include statically inadmissible fields* —i.e. stress functions that do not satisfy the reduced-order equilibrium equation (21).

One plausible route for determining a low-dimensional approximation space that embraces both statically admissible and statically inadmissible stresses might be to collect, during the offline finite element calculations, not only converged stresses, but also the unconverged ones —i.e., those generated during the corresponding iterative algorithm—, and then perform the POD-based dimensionality reduction over the whole ensemble of snapshots. In the present work, however, we pursue an approach that precludes the necessity of undertaking this computationally laborious and in some aspects objectionable —there is no guarantee that the span of selected, unconverged stress snapshots covers the entire space of statically inadmissible stresses— process. The idea behind the employed approach was originally conceived, but not fully developed, by the authors in a recent monograph [35]. Here, the theory underlying such an idea is further elaborated and cast into the formalisms of functional analysis.

5.3.1. Continuum formulation

To originate our considerations from a general standpoint, it proves convenient first to rephrase the left-hand side of the reduced-order equilibrium equation Eq.(21) as the action of a certain linear operator $\boldsymbol{G} : L_2(\Omega)^s \to \mathbb{R}^{n_u}$ on the stress field over the RVE:

$$\int_\Omega \boldsymbol{B}_i^{*T} \boldsymbol{\sigma} \, d\Omega = \langle \boldsymbol{B}_i^*, \boldsymbol{\sigma} \rangle_{L_2(\Omega)} = (\boldsymbol{G}[\boldsymbol{\sigma}])_i \quad i = 1, 2 \dots n_u. \tag{32}$$

Invoking now the orthogonal decomposition of $L_2(\Omega)^s$ induced by this operator, one obtains:

$$L_2(\Omega)^s = \mathcal{N}(\boldsymbol{G}) \oplus \text{span}\{\boldsymbol{B}_i^*\}_{i=1}^{n_u}, \tag{33}$$

where $\mathcal{N}(\boldsymbol{G})$ stands for the nullspace of $\boldsymbol{G}$. Since the RVE equilibrium equation has a vanishing right-hand side term, it follows that $\mathcal{N}(\boldsymbol{G})$ is actually the space of *statically admissible stress fields*. Its orthogonal complement, $\text{span}\{\boldsymbol{B}_i^*\}_{i=1}^{n_u}$, can be therefore construed as the abovementioned *space of statically inadmissible stresses. The key fact here is that such a space is inherently n_u-dimensional and, thus, there is no need to perform any dimensionality reduction whatsoever over* unconverged *snapshots to arrive at the desired basis: the strain-displacement functions $\{\boldsymbol{B}_1^*, \boldsymbol{B}_2^* \dots \boldsymbol{B}_{n_u}^*\}$ themselves are linearly independent (albeit not orthogonal) and can thereby serve this very purpose.*

According to the preceding decomposition, any $\boldsymbol{\sigma} \in L_2(\Omega)^s$ can be resolved as (see Figure 2):

$$\boldsymbol{\sigma} = \boldsymbol{\sigma}^{ad} + \boldsymbol{\sigma}^{in}, \quad \text{with } \left\langle \boldsymbol{\sigma}^{ad}, \boldsymbol{\sigma}^{in} \right\rangle_{L_2(\Omega)} = 0, \tag{34}$$

where $\boldsymbol{\sigma}^{ad} \in \mathcal{N}(\boldsymbol{G})$ and $\boldsymbol{\sigma}^{in} \in \text{span}\{\boldsymbol{B}_i^*\}_{i=1}^{n_u}$ stand for the statically admissible and statically inadmissible components of $\boldsymbol{\sigma}$, respectively. Following the standard approach, the statically admissible component $\boldsymbol{\sigma}^{ad}$ —i.e., the stress solution we wish to calculate for a given input $\boldsymbol{\epsilon_M}$— is forced to lie in the span of the POD modes $\boldsymbol{\Psi}_i$ $(i = 1, 2 \dots n_\sigma)$ obtained from converged snapshots:

$$\boldsymbol{\sigma}^{ad} \approx \boldsymbol{\sigma}^* = \sum_{i=1}^{n_\sigma} \boldsymbol{\Psi}_i c_i^{ad}, \tag{35}$$

$c_i^{ad} \in \mathbb{R}$ $(i = 1, 2 \dots n_\sigma)$ being the corresponding modal coefficients. The non-equilibrated component $\boldsymbol{\sigma}^{in}$, on the other hand, resides naturally in the span

of the reduced strain-displacement functions, so we can directly write—i.e., without introducing further approximations—:

$$\boldsymbol{\sigma}^{in} = \sum_{i=1}^{n_u} \boldsymbol{B}_i^* c_i^{in}, \tag{36}$$

with $c_i^{in} \in \mathbb{R}$ $(i = 1, 2 \dots n_u)$. The low-dimensional approximation required in the proposed integration method, denoted in what follows by $\boldsymbol{\sigma}^{ex*}$ (the appended superscript "ex" means "stress approximated in the *expanded* space"), is finally obtained as the sum of Eq.(35) and Eq.(36) :

$$\boldsymbol{\sigma}^{ex*} = \sum_{i=1}^{n_\sigma} \boldsymbol{\Psi}_i c_i^{ad} + \sum_{j=1}^{n_u} \boldsymbol{B}_j^* c_j^{in}. \tag{37}$$

Substituting the above approximation into the equilibrium equation, one

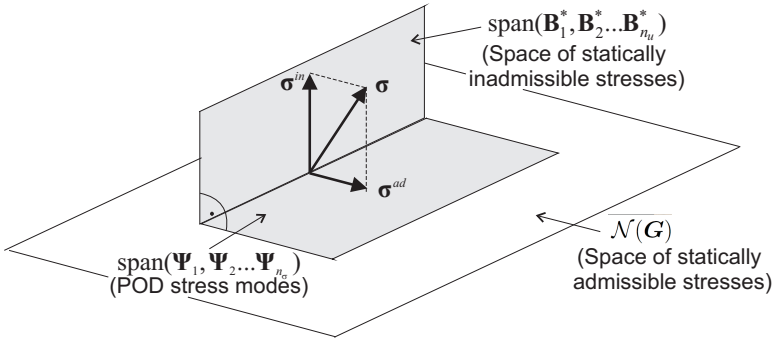

Figure 2: Expanded space approach. The stress approximation space is expanded so that it embraces, not only the span of the stress POD modes, but also the span of the reduced strain-displacement functions $\{\boldsymbol{B}_1^*, \boldsymbol{B}_2^* \dots \boldsymbol{B}_{n_u}^*\}$. The reduced-order RVE equilibrium problem boils down to find the reduced displacement fluctuations vector $\boldsymbol{U}^*$ that makes the *non-equilibrated* component $\boldsymbol{\sigma}^{in}$ to vanish ($\boldsymbol{\sigma}^{in}(\boldsymbol{U}^*, \boldsymbol{\epsilon_M}) = \boldsymbol{0}$).

gets:

$$\int_\Omega \boldsymbol{B}_i^{*T} \boldsymbol{\sigma}^{ex*} = \sum_{j=1}^{n_u} \left(\int_\Omega \boldsymbol{B}_i^{*T} \boldsymbol{B}_j^* d\Omega \right) c_j^{in} = \boldsymbol{0}, \quad i = 1, 2 \dots n_u. \tag{38}$$

Since $\{\boldsymbol{B}_1^*, \boldsymbol{B}_2^* \dots \boldsymbol{B}_{n_u}^*\}$ are linearly independent functions, it becomes immediately clear that the above equations holds only if:

$$c_j^{in}(\boldsymbol{\epsilon_M}, \boldsymbol{U}^*) = 0, \quad j = 1, 2 \dots n_u, \tag{39}$$

i.e., if the n_u coefficients multiplying $\boldsymbol{B}_i^* \in L_2(\Omega)^s$ $(i = 1, 2 \dots n_u)$ are identically zero. In adopting the proposed integration approach, thus, the reduced-order RVE equilibrium problem (21) is transformed into the problem of finding, for a given input macroscopic strain tensor $\boldsymbol{\epsilon_M}$, the reduced displacement fluctuations vector $\boldsymbol{U}^* \in \mathbb{R}^{n_u}$ that makes the non-equilibrated component $\boldsymbol{\sigma}^{in}$ (defined in Eq.(36)) to vanish.

In a nutshell, *the ill-posedness exhibited by the discrete problem when adopting the standard approach of using only POD modes is eliminated by expanding the stress approximation space so that it embraces also the span of the reduced strain-displacement functions* (or strain modes[11]) $\boldsymbol{B}_i^* \in L_2(\Omega)^s$ $(i = 1, 2 \dots n_u)$:

$$\mathcal{V}_\sigma^{apr} = \mathcal{V}_\sigma^* \oplus \text{span}\{\boldsymbol{B}_i^*\}_{i=1}^{n_u} = \text{span}\{\overbrace{\boldsymbol{\Psi}_1, \boldsymbol{\Psi}_2 \dots \boldsymbol{\Psi}_{n_\sigma}}^{n_\sigma \text{ stress modes}}, \overbrace{\boldsymbol{B}_1^*, \boldsymbol{B}_2^* \dots \boldsymbol{B}_{n_u}^*}^{n_u \text{ strain modes}}\}. \quad (40)$$

5.3.2. Discrete formulation

In typical finite element implementations, both stresses and gradients of shape functions are only calculated and stored at the Gauss points of the underlying spatial discretization. For practical reasons, thus, it proves imperative to reformulate the above explained *expanded space* strategy and treat both magnitudes as spatially discrete variables, defined only at such Gauss points.

The *discrete* counterparts of the continuously defined fields $\boldsymbol{\sigma} \in L_2(\Omega)^s$ and $\boldsymbol{B}_i^* \in L_2(\Omega)^s$ $(i = 1, 2 \dots n_u)$ will be denoted by $\boldsymbol{\mathcal{S}} \in \mathbb{R}^{n_g \cdot s}$ and $\boldsymbol{\mathcal{B}^*} = \begin{bmatrix} \boldsymbol{\mathcal{B}_1^*} & \boldsymbol{\mathcal{B}_2^*} & \cdots & \boldsymbol{\mathcal{B}_{n_u}^*} \end{bmatrix} \in \mathbb{R}^{n_g \cdot s \times n_u}$, and termed the *global stress vector*, and the *global matrix of strain modes*, respectively. The *global stress vector* $\boldsymbol{\mathcal{S}}$ is constructed by stacking the stress vectors $\boldsymbol{\sigma}(\mathbf{x}_g; \cdot) \in \mathbb{R}^s$ $(g = 1, 2 \dots n_g)$ at the Gauss points of the finite element grid into a single column vector:

$$\boldsymbol{\mathcal{S}} := \begin{bmatrix} \boldsymbol{\sigma}^T(\mathbf{x}_1; \cdot) & \boldsymbol{\sigma}^T(\mathbf{x}_2; \cdot) & \cdots & \boldsymbol{\sigma}^T(\mathbf{x}_{n_g}; \cdot) \end{bmatrix}^T. \quad (41)$$

Similarly, the global matrix of strain modes $\boldsymbol{\mathcal{B}^*}$ is constructed as:

$$\boldsymbol{\mathcal{B}^*} := \begin{bmatrix} \boldsymbol{B}^{*T}(\mathbf{x}_1) & \boldsymbol{B}^{*T}(\mathbf{x}_2) & \cdots & \boldsymbol{B}^{*T}(\mathbf{x}_{n_g}) \end{bmatrix}^T. \quad (42)$$

[11] Indeed, functions $\boldsymbol{B}_i^* \in L_2(\Omega)^s$ $(i = 1, 2 \dots n_u)$ can be viewed as fluctuating *strain* modes, since they are the symmetric gradient of the displacement fluctuation modes, see Eq. 23.

Having definitions (41) and (42) at hand, the approximation of Eq.(22) by Gauss quadrature can be written as:

$$\begin{aligned} &\int_\Omega \boldsymbol{B}_i^{*T}(\mathbf{x})\boldsymbol{\sigma}(\mathbf{x};\cdot)\,d\Omega \approx \sum_{g=1}^{n_g} w_g \boldsymbol{B}_i^{*T}(\mathbf{x}_g)\boldsymbol{\sigma}(\mathbf{x}_g;\cdot) = 0 \\ &\Rightarrow \boldsymbol{\mathcal{B}}_{\boldsymbol{i}}^{*T}\boldsymbol{W}\boldsymbol{\mathcal{S}} = 0, \qquad i = 1,2\ldots n_u, \end{aligned} \tag{43}$$

where $\boldsymbol{W}$ is a diagonal matrix containing the weights at each Gauss point:

$$\boldsymbol{W} := \begin{bmatrix} w_1\boldsymbol{I} & \mathbf{0} & \mathbf{0} & \cdots & \mathbf{0} \\ \mathbf{0} & w_2\boldsymbol{I} & \mathbf{0} & \cdots & \mathbf{0} \\ \vdots & \vdots & \vdots & \vdots & \vdots \\ \mathbf{0} & \mathbf{0} & \mathbf{0} & \mathbf{0} & w_{n_g}\boldsymbol{I} \end{bmatrix} \tag{44}$$

(here, $\boldsymbol{I}$ denotes the $s\,\mathrm{x}\,s$ identity matrix). Assuming that $w_g > 0$ ($g = 1,2\ldots n_g$) —Gauss quadrature rules with negative weights are excluded from our considerations—, and using the Cholesky decomposition of $\boldsymbol{W}$ ($\boldsymbol{W} = \boldsymbol{W}^{1/2}\boldsymbol{W}^{1/2}$), one can reexpress Eq.(43) as

$$\boldsymbol{\mathcal{B}}^{*T}\boldsymbol{W}\boldsymbol{\mathcal{S}} = (\boldsymbol{\mathcal{B}}^{*T}\boldsymbol{W}^{1/2})(\boldsymbol{W}^{1/2}\boldsymbol{\mathcal{S}}) = \mathbf{0}. \tag{45}$$

Defining now the *weighted* global stress vector and *weighted* matrix of strain modes as

$$\boldsymbol{\Sigma} := \boldsymbol{W}^{1/2}\boldsymbol{\mathcal{S}} = \begin{bmatrix} \sqrt{w_1}\boldsymbol{\sigma}^T(\mathbf{x}_1;\cdot) & \sqrt{w_2}\boldsymbol{\sigma}^T(\mathbf{x}_2;\cdot) & \cdots & \sqrt{w_{n_g}}\boldsymbol{\sigma}^T(\mathbf{x}_{n_g};\cdot) \end{bmatrix}^T, \tag{46}$$

and

$$\mathbb{B}^* := \boldsymbol{W}^{1/2}\boldsymbol{\mathcal{B}}^* = \begin{bmatrix} \sqrt{w_1}\boldsymbol{B}^{*T}(\mathbf{x}_1) & \sqrt{w_2}\boldsymbol{B}^{*T}(\mathbf{x}_2) & \cdots & \sqrt{w_{n_g}}\boldsymbol{B}^{*T}(\mathbf{x}_{n_g}) \end{bmatrix}^T \tag{47}$$

respectively, and inserting these definitions into Eq.(41), one finally arrives at:

$$\mathbb{B}^{*T}\boldsymbol{\Sigma} = \mathbf{0}, \tag{48}$$

or equivalently,

$$\mathbb{B}_i^{*T}\boldsymbol{\Sigma} = 0, \qquad i = 1,2\ldots n_u, \tag{49}$$

which shows that any statically admissible *weighted* stress vector is orthogonal, in the sense of the standard euclidean inner product, to the *weighted* strain modes $\mathbb{B}_i^{*T}$ ($i = 1,2\ldots n_u$).

Comparing Eq.(48) with Eq.(32), it becomes clear that $\mathbb{B}^{*T}$ plays the same role as operator $\boldsymbol{G}$ in Eq.(32). In analogy with Eq.(33), thus, we can write

$$\mathbb{R}^{n_g \cdot s} = \mathcal{N}(\mathbb{B}^{*T}) \oplus \text{Range}(\mathbb{B}^*) \tag{50}$$

where $\mathcal{N}(\mathbb{B}^{*T})$ and $\text{Range}(\mathbb{B}^*)$ denote the null space and the range (or column space) of $\mathbb{B}^{*T}$ and $\mathbb{B}^*$, respectively, and consequently decompose any $\boldsymbol{\Sigma} \in \mathbb{R}^{n_g \cdot s}$ as

$$\boldsymbol{\Sigma} = \boldsymbol{\Sigma^{ad}} + \boldsymbol{\Sigma^{in}} \tag{51}$$

with $\boldsymbol{\Sigma^{ad}} \in \mathcal{N}(\mathbb{B}^{*T})$ and $\boldsymbol{\Sigma^{in}} \in \text{Range}(\mathbb{B}^*)$. As in the continuous case (see Eq.(35)), the statically admissible component $\boldsymbol{\Sigma^{ad}}$ is now *approximated* by a linear combination of POD basis vectors obtained from converged stress snapshots[12]:

$$\boldsymbol{\Sigma^{ad}} \approx \boldsymbol{\Sigma}^* = \sum_{i=1}^{n_\sigma} c_i^{ad} \boldsymbol{\Psi}_i = \boldsymbol{\Psi} \boldsymbol{c}^{ad}, \tag{52}$$

where $\boldsymbol{\Psi} = \begin{bmatrix} \boldsymbol{\Psi}_1 & \boldsymbol{\Psi}_2 & \cdots & \boldsymbol{\Psi}_{n_\sigma} \end{bmatrix}$ denotes the (weighted) stress basis matrix and $\boldsymbol{c}^{ad} \in \mathbb{R}^{n_\sigma}$ stands for the vector of modal coefficients associated to such a basis matrix. Likewise, since the non-equilibrated component $\boldsymbol{\Sigma^{in}}$ pertains to the column space of $\mathbb{B}^*$, we can directly write

$$\boldsymbol{\Sigma^{in}} = \mathbb{B}^* \boldsymbol{c}^{in}, \tag{53}$$

where $\boldsymbol{c}^{in} \in \mathbb{R}^{n_u}$. The low-dimensional (weighted) stress vector $\boldsymbol{\Sigma}^{ex*}$ required in the proposed integration method is finally obtained as the sum of Eq.(53) and Eq.(52).

$$\boldsymbol{\Sigma} \approx \boldsymbol{\Sigma}^{ex*} = \boldsymbol{\Psi} \boldsymbol{c}^{ad} + \mathbb{B}^* \boldsymbol{c}^{in}, \tag{54}$$

or in a more compact format:

$$\boldsymbol{\Sigma}^{ex*} = \boldsymbol{\Psi}^{ex} \boldsymbol{c}. \tag{55}$$

where

$$\boldsymbol{\Psi}^{ex} := \begin{bmatrix} \boldsymbol{\Psi} & \mathbb{B}^* \end{bmatrix}, \tag{56}$$

[12]The methodology for obtaining these modes using the SVD is similar to that explained in Section 3.2 for the displacement fluctuation modes.

and

$$\boldsymbol{c} = \begin{bmatrix} \boldsymbol{c}^{ad} \\ \boldsymbol{c}^{in} \end{bmatrix}. \tag{57}$$

The matrix $\boldsymbol{\Psi}^{ex} \in \mathbb{R}^{n_g \cdot s \times (n_u + n_\sigma)}$ defined by Eq.(56) will be hereafter called the *expanded* basis matrix for the (weighted) stresses, whereas $\boldsymbol{c} \in \mathbb{R}^{n_\sigma + n_u}$ will be correspondingly termed the *expanded* vector of modal coefficients. Inserting approximation (54) into Eq.(48), and considering that $\mathbb{B}^{*T}\boldsymbol{\Psi} = \mathbf{0}$ and that $\mathbb{B}^{*T}$ is a full rank matrix, one finally arrives at the same equilibrium condition derived in the continuum case (see Eq. 39):

$$\boldsymbol{c}^{in}(\boldsymbol{U}^*, \boldsymbol{\epsilon_M}) = \mathbf{0}. \tag{58}$$

Once the above equation is solved for $\boldsymbol{U}^*$, the desired equilibrated stress vector $\boldsymbol{\Sigma}^*$ is obtained by evaluating Eq.(52):

$$\boldsymbol{\Sigma}^* = \boldsymbol{\Psi}\boldsymbol{c}^{ad}(\boldsymbol{U}^*, \boldsymbol{\epsilon_M}). \tag{59}$$

6. The High-Performance ROM

The next step in the development of the proposed integration scheme is to deduce closed-form expressions for the vectors of modal coefficients $\boldsymbol{c}^{ad} \in \mathbb{R}^{n_\sigma}$ and $\boldsymbol{c}^{in} \in \mathbb{R}^{n_u}$ in terms of the stress values computed at a set of $p = \mathcal{O}(n_u)$ *pre-specified sampling points* (to be chosen among the set of Gauss points of the underlying finite element mesh). To this end, we need first to introduce some notation and terminology.

6.1. Gappy vectors

Let $\mathcal{I} = \{\mathcal{I}_1, \mathcal{I}_2 \ldots \mathcal{I}_p\} \subset \{1, 2 \cdots n_g\}$ denote the set of indices of sampling points. Notationally, we write $\hat{\boldsymbol{\Sigma}}_{(\mathcal{I})} \in \mathbb{R}^{p \cdot s}$ to designate the subvector of $\boldsymbol{\Sigma}$ containing the rows associated to these sampling points; viz.:

$$\hat{\boldsymbol{\Sigma}}_{(\mathcal{I})} := \left[\sqrt{w_{\mathcal{I}_1}}\boldsymbol{\sigma}^T(\mathbf{x}_{\mathcal{I}_1}, \cdot) \quad \sqrt{w_{\mathcal{I}_2}}\boldsymbol{\sigma}^T(\mathbf{x}_{\mathcal{I}_2}, \cdot) \quad \cdots \quad \sqrt{w_{\mathcal{I}_p}}\boldsymbol{\sigma}^T(\mathbf{x}_{\mathcal{I}_p}, \cdot)\right]^T \tag{60}$$

(When confusion is not apt to arise, the parenthetical subscript indicating the set of sampling indices will be dropped, and we shall simply write $\hat{\boldsymbol{\Sigma}}$). It proves conceptually advantageous to regard this *restricted* or "gappy" — a terminology that goes back to the work of Everson et al. [28]— stress vector $\hat{\boldsymbol{\Sigma}}_{(\mathcal{I})}$ as the result of the application of a certain boolean operator

$\boldsymbol{\mathcal{P}}_{(\mathcal{I})} : \mathbb{R}^{n_g \cdot s} \to \mathbb{R}^{p \cdot s}$ over the full vector $\boldsymbol{\Sigma}$ (i.e., $\hat{\boldsymbol{\Sigma}} = \boldsymbol{\mathcal{P}}_{(\mathcal{I})}\boldsymbol{\Sigma}$). We call $\boldsymbol{\mathcal{P}}_{(\mathcal{I})}$ the *selection operator* associated to sampling indices $\mathcal{I}$. This operator can be of course applied to any $\mathbf{Y} \in \mathbb{R}^{\mathbf{n_g \cdot s \times z}}$ ($z \in \mathbb{N}$). For instance, the restricted matrix of weighted strain modes is defined as $\hat{\mathbb{B}}^* := \boldsymbol{\mathcal{P}}_{(\mathcal{I})}\mathbb{B}^*$. Furthermore, it is straighforward to show that

$$\boldsymbol{\mathcal{P}}_{(\mathcal{I})}\boldsymbol{\mathcal{P}}_{(\mathcal{I})}^T = \boldsymbol{I}, \tag{61}$$

(here $\boldsymbol{I}$ is the $(n_g \cdot s)$x$(n_g \cdot s)$ identity matrix) and that

$$\boldsymbol{\mathcal{P}}_{(\mathcal{I})}(\mathbf{AY}) = (\boldsymbol{\mathcal{P}}_{(\mathcal{I})}\mathbf{A}\boldsymbol{\mathcal{P}}_{(\mathcal{I})}^{\mathbf{T}})(\boldsymbol{\mathcal{P}}_{(\mathcal{I})}\mathbf{Y}) \tag{62}$$

for any $\mathbf{A} \in \mathbb{R}^{\mathbf{n_g \cdot s \times n_g \cdot s}}$ and $\mathbf{Y} \in \mathbb{R}^{\mathbf{n_g \cdot s \times z}}$.

6.2. Least-squares fit

In the spirit of classical polynomial quadrature, such as Newton-Cotes formulae [36], the modal coefficients $\boldsymbol{c}^{ad} \in \mathbb{R}^{n_\sigma}$ and $\boldsymbol{c}^{in} \in \mathbb{R}^{n_u}$ are determined by *fitting* the low-dimensional approximation (54) to the weighted stresses calculated at the pre-specified sampling points. It should be noticed that, the variable subject to approximation —the stress— being a vector-valued function, the total number of discrete points to be fitted does not coincide with the number of spatial sampling points (p), but rather is equal to the product of such a number times the number of stress components (s). The well-posedness of the fitting problem, thus, demands that $p \cdot s \geq n_\sigma + n_u$, i.e., the number of discrete points must be equal or greater than the number of parameters to be adjusted. For the equality to hold, both $n_\sigma + n_u$ and p have to be multiple of s; thus, an *exact fit* is in general not possible for arbitrary values of n_σ and n_u, and recourse to an *approximate fit* is to be made. In this respect, we follow here the standard approach of using a *least-squares*, best-fit criterion, i.e., minimization of the squares of the deviations between "observed" ($\hat{\boldsymbol{\Sigma}}$) and fitted ($\hat{\boldsymbol{\Sigma}}^{ex*} = \hat{\boldsymbol{\Psi}}\boldsymbol{a} + \hat{\mathbb{B}}^*\boldsymbol{b}$) values (in our context, "observed" signifies "calculated through the pertinent constitutive equation"). This minimization problem can be stated as:

$$\boldsymbol{c} = \begin{bmatrix} \boldsymbol{c}^{ad} \\ \boldsymbol{c}^{in} \end{bmatrix} = \arg \min_{\boldsymbol{a} \in \mathbb{R}^{n_\sigma}, \boldsymbol{b} \in \mathbb{R}^{n_u}} \| \hat{\boldsymbol{\Sigma}} - \left(\hat{\boldsymbol{\Psi}}\boldsymbol{a} + \hat{\mathbb{B}}^*\boldsymbol{b} \right) \| \tag{63}$$

where $\| \cdot \|$ stands for the standard euclidean norm. Let $\hat{\boldsymbol{\Psi}}^{\boldsymbol{ex}} = \boldsymbol{\mathcal{P}}_{(\mathcal{I})}\boldsymbol{\Psi}^{ex} = [\hat{\boldsymbol{\Psi}} \ \hat{\mathbb{B}}^*]$ be the *gappy* expanded basis matrix, and suppose that the sampling indices $\mathcal{I}$ have been chosen so that $\hat{\boldsymbol{\Psi}}^{\boldsymbol{ex}}$ has full rank, i.e.:

$$\text{rank}(\hat{\boldsymbol{\Psi}}^{\boldsymbol{ex}}) = \text{rank}([\hat{\boldsymbol{\Psi}} \ \hat{\mathbb{B}}^*]) = n_\sigma + n_u. \tag{64}$$

Then, it can be shown (see, for instance, Ref. [23]) that the solution of this standard, least-squares problem is provided by the following vector of coefficients:

$$\boldsymbol{c} = \begin{bmatrix} \boldsymbol{c}^{ad} \\ \boldsymbol{c}^{in} \end{bmatrix} = \hat{\boldsymbol{\Psi}}^{ex\dagger} \hat{\boldsymbol{\Sigma}}, \tag{65}$$

where

$$\hat{\boldsymbol{\Psi}}^{ex\dagger} := \overbrace{(\hat{\boldsymbol{\Psi}}^{\boldsymbol{ex}T} \hat{\boldsymbol{\Psi}}^{\boldsymbol{ex}})^{-1}}^{\hat{\boldsymbol{M}}^{-1}} \hat{\boldsymbol{\Psi}}^{\boldsymbol{ex}T} \tag{66}$$

is the so-called *pseudo-inverse* of matrix $\hat{\boldsymbol{\Psi}}^{\boldsymbol{ex}}$.

Recall that our ultimate aim is to derive closed-form expressions for $\boldsymbol{c}^{in}$ and $\boldsymbol{c}^{ad}$ as functions of $\hat{\boldsymbol{\Sigma}}$. Thus, it remains to extricate these two sub-vectors from expression (65). This can be done by first partitioning both $\hat{\boldsymbol{M}} = \hat{\boldsymbol{\Psi}}^{\boldsymbol{ex}T} \hat{\boldsymbol{\Psi}}^{\boldsymbol{ex}}$ and $\hat{\boldsymbol{\Psi}}^{\boldsymbol{ex}T}$ in terms of the gappy stress basis matrix $\hat{\boldsymbol{\Psi}}$ and the gappy matrix of strain modes $\hat{\mathbb{B}}^*$:

$$\boldsymbol{c} = \begin{bmatrix} \boldsymbol{c}^{ad} \\ \boldsymbol{c}^{in} \end{bmatrix} = \begin{bmatrix} \hat{\boldsymbol{\Psi}}^T \hat{\boldsymbol{\Psi}} & \hat{\boldsymbol{\Psi}}^T \hat{\mathbb{B}}^* \\ \hat{\mathbb{B}}^{*T} \hat{\boldsymbol{\Psi}} & \hat{\mathbb{B}}^{*T} \hat{\mathbb{B}}^* \end{bmatrix}^{-1} \begin{bmatrix} \hat{\boldsymbol{\Psi}}^T \\ \hat{\mathbb{B}}^{*T} \end{bmatrix} \hat{\boldsymbol{\Sigma}}. \tag{67}$$

Invoking the blockwise inverse formula for 2x2 block symmetric matrices [11], and upon tedious algebra —that has been relegated to Appendix C— one finally arrives at the following expressions for $\boldsymbol{c}^{ad}$ and $\boldsymbol{c}^{in}$

$$\boldsymbol{c}^{ad} = \hat{\boldsymbol{\Psi}}^{\dagger} (\hat{\boldsymbol{\Sigma}} - \hat{\mathbb{B}}^* \boldsymbol{c}^{in}), \tag{68}$$

$$\boldsymbol{c}^{in} = \mathbf{S}^{-\mathbf{1}} \hat{\mathbb{B}}^{*\mathbf{T}} \left(\boldsymbol{I} - \hat{\boldsymbol{\Psi}} \hat{\boldsymbol{\Psi}}^{\dagger} \right) \hat{\boldsymbol{\Sigma}}, \tag{69}$$

where $\hat{\boldsymbol{\Psi}}^{\dagger}$ denotes the pseudoinverse of the gappy stress basis matrix $\hat{\boldsymbol{\Psi}}$:

$$\hat{\boldsymbol{\Psi}}^{\dagger} = (\hat{\boldsymbol{\Psi}}^T \hat{\boldsymbol{\Psi}})^{-1} \hat{\boldsymbol{\Psi}}^T \tag{70}$$

and $\mathbf{S} := \hat{\mathbb{B}}^{*\mathbf{T}} (\boldsymbol{I} - \hat{\boldsymbol{\Psi}} \hat{\boldsymbol{\Psi}}^{\dagger})$ (note that $\mathbf{S}$ is invertible by virtue of the hypothesis represented by Eq.(64)).

6.2.1. Reconstruction matrix

Let us first examine expression (68) for the modal coefficients $\boldsymbol{c}^{ad}$ —those that multiply the *statically admissible* component of the global stress vector.

Since, at the solution, $\boldsymbol{c}^{in} = \mathbf{0}$, we have that:

$$\boldsymbol{c}^{ad} = \hat{\boldsymbol{\Psi}}^{\dagger}(\hat{\boldsymbol{\Sigma}} - \hat{\mathbb{B}}^{*}\overbrace{\boldsymbol{c}^{in}}^{=\mathbf{0}}) = \hat{\boldsymbol{\Psi}}^{\dagger}\hat{\boldsymbol{\Sigma}}. \tag{71}$$

(Notice that this result can also be obtained by directly solving minimization problem (63) with $\boldsymbol{b} = \mathbf{0}$). Substitution of this equation into Eq.(59) yields:

$$\boldsymbol{\Sigma}^{*} = \boldsymbol{\Psi}\boldsymbol{c}^{ad} = \overbrace{\boldsymbol{\Psi}\hat{\boldsymbol{\Psi}}^{\dagger}}^{\boldsymbol{R}}\hat{\boldsymbol{\Sigma}} = \boldsymbol{R}\,\hat{\boldsymbol{\Sigma}}, \tag{72}$$

where

$$\boldsymbol{R} := \boldsymbol{\Psi}\hat{\boldsymbol{\Psi}}^{\dagger} = \boldsymbol{\Psi}(\hat{\boldsymbol{\Psi}}^{T}\hat{\boldsymbol{\Psi}})^{-1}\hat{\boldsymbol{\Psi}}^{T}. \tag{73}$$

Inspection of Eq.(72) reveals that the matrix $\boldsymbol{R} \in \mathbb{R}^{n_g \cdot s \times p \cdot s}$ defined above is the operator that allows one to *reconstruct* the (weighted) *statically admissible* stress vector $\boldsymbol{\Sigma}^{*} \in \mathbb{R}^{n_g \cdot s}$ using only the (weighted) stress values ($\hat{\boldsymbol{\Sigma}} \in \mathbb{R}^{p \cdot s}$) calculated at the pre-selected sampling points $\mathcal{I}$. For this reason, we shall use the term *weighted reconstruction matrix* (or simply reconstruction matrix) to refer to this operator. It must be emphasized here that this matrix only depends on the POD stress basis matrix $\boldsymbol{\Psi}$ and on the selected sampling indices $\mathcal{I}$ —i.e., it is independent of the input parameter, the macro-strain $\boldsymbol{\epsilon_M}$—and, therefore, it can be pre-computed *offline*.

6.3. "Hyperreduced" RVE equilibrium equation

As for the expression for the set of "statically inadmissible" coefficients $\boldsymbol{c}^{in} \in \mathbb{R}^{n_u}$, we know that, at the solution, these coefficients must vanish; thus, from Eq.(69), we have

$$\boldsymbol{c}^{in}(\boldsymbol{U}^{*}, \boldsymbol{\epsilon_M}) = \mathbf{S}^{-\mathbf{1}}\hat{\mathbb{B}}^{*\mathbf{T}}\left(\boldsymbol{I} - \hat{\boldsymbol{\Psi}}\hat{\boldsymbol{\Psi}}^{\dagger}\right)\hat{\boldsymbol{\Sigma}}(\boldsymbol{U}^{*}, \boldsymbol{\epsilon_M}) = \mathbf{0}. \tag{74}$$

Since $\mathbf{S}$ is a nonsingular matrix, the above condition is equivalent to

$$\hat{\mathbb{B}}^{*T}\left(\boldsymbol{I} - \hat{\boldsymbol{\Psi}}\hat{\boldsymbol{\Psi}}^{\dagger}\right)\hat{\boldsymbol{\Sigma}}(\boldsymbol{U}^{*}, \boldsymbol{\epsilon_M}) = \mathbf{0}. \tag{75}$$

Furthermore, examination of Eq.(73) and Eq.(75) readily shows that the bracketed term $\hat{\boldsymbol{\Psi}}\hat{\boldsymbol{\Psi}}^{\dagger}$ in Eq.(75) is nothing but the submatrix of the reconstruction matrix $\boldsymbol{R}$ formed by the rows associated to sampling points $\mathcal{I}$, i.e.:

$$\hat{\boldsymbol{\Psi}}\hat{\boldsymbol{\Psi}}^{\dagger} = \boldsymbol{\mathcal{P}}_{(\mathcal{I})}(\boldsymbol{\Psi}\hat{\boldsymbol{\Psi}}^{\dagger}) = \boldsymbol{\mathcal{P}}_{(\mathcal{I})}\boldsymbol{R} = \hat{\boldsymbol{R}}. \tag{76}$$

Substitution of expression (76) into Eq.(75) finally leads to:

$$\hat{\mathbb{B}}^{*^T}(\boldsymbol{I}-\hat{\boldsymbol{R}})\hat{\boldsymbol{\Sigma}}(\boldsymbol{U}^*,\boldsymbol{\epsilon_M})=\mathbf{0}. \tag{77}$$

As previously noted (see Figure 2), the purpose of enforcing condition $\boldsymbol{c}^{in}(\boldsymbol{U}^*,\boldsymbol{\epsilon_M})=\mathbf{0}$ is to ensure that the stress solution lies entirely in the space of equilibrated stresses. Equation (77) can be viewed, thus, as the "hyperreduced" form of the original RVE equilibrium equation.

Observation 6.1. *The "hyperreduced" qualifier —coined by D. Ryckelynck [58, 59]— is used here to indicate that Eq.(77) is the result of two subsequent steps of complexity reduction: firstly, in the number of degrees of freedom (when passing from the finite element model to the ROM that employs standard Gauss quadrature), and, secondly, in the number of integration points (when passing from this standard ROM to what we have baptized*[13] *"High-Performance" ROM). This double complexity reduction can be better appreciated by rephrasing both Eq.(77) and the FE equation (9) in a format similar to that of Eq.(48), viz.:*

$$\overbrace{\hat{\mathbb{B}}^{*^T}(\boldsymbol{I}-\hat{\boldsymbol{R}})}^{\hat{\mathbb{B}}^{**^T}}\hat{\boldsymbol{\Sigma}}=\hat{\mathbb{B}}^{**^T}\hat{\boldsymbol{\Sigma}}=\mathbf{0}, \tag{78}$$

and

$$\sum_{g=1}^{n_g} w_g\boldsymbol{B}^T(\boldsymbol{x}_g)\boldsymbol{\sigma}(\boldsymbol{x}_g,;)=\mathbb{B}^T\boldsymbol{\Sigma}=\mathbf{0}, \tag{79}$$

respectively (here, $\mathbb{B}\in\mathbb{R}^{n_g\cdot s\times n\cdot d}$ is the finite element counterpart of $\mathbb{B}^*$, defined in Eq.(42)). With Eq.(79), Eq.(48) and Eq.(78) at our disposal, the abovementioned process of complexity reduction can be symbolically represented as

$$\overbrace{\mathbb{B}^T\boldsymbol{\Sigma}=\mathbf{0}}^{FEM} \quad \overset{1^{st}reduc.}{\underset{n\cdot d\to n_u}{\Longrightarrow}} \quad \overbrace{\mathbb{B}^{*^T}\boldsymbol{\Sigma}=\mathbf{0}}^{Stand.\ ROM} \quad \overset{2^{nd}reduc.}{\underset{n_g\to p}{\Longrightarrow}} \quad \overbrace{\hat{\mathbb{B}}^{**^T}\hat{\boldsymbol{\Sigma}}=\mathbf{0}}^{HP\text{-}ROM}, \tag{80}$$

[13] The term *High-Performance, Reduced-Order Model* (HP-ROM) is used to highlight the tremendous gains in performance that affords this model over the standard ROM, let alone over the full-order, finite model. In the numerical example shown in Section 9, we report speedup factors of above three order of magnitudes.

the relation between $\mathbb{B} \in \mathbb{R}^{n_g \cdot s \times n \cdot d}$, $\mathbb{B}^* \in \mathbb{R}^{n_g \cdot s \times n_u}$ *and* $\hat{\mathbb{B}}^{**} \in \mathbb{R}^{p \cdot s \times n_u}$ *being* $\mathbb{B}^* = \mathbb{B}\boldsymbol{\Phi}$ *and*

$$\hat{\mathbb{B}}^{**} := (\boldsymbol{I} - \hat{\boldsymbol{R}})\hat{\mathbb{B}}^* = (\boldsymbol{I} - \hat{\boldsymbol{R}})\boldsymbol{\mathcal{P}}_{(\mathcal{I})}\mathbb{B}^*, \tag{81}$$

with $p = \mathcal{O}(n_u) << n_g = \mathcal{O}(n)$. *It is interesting to see how the reduction in complexity of the RVE equilibrium equation is reflected in the gradual reduction of the dimensions of the "B" operators that act on the weighted vector of stresses.*

6.3.1. Physical interpretation

Aside from a "compressed" version of the original, full-order cell condition, the *hyperreduced* equation (77) can be alternatively interpreted as a balance between "observed" and "fitted" internal forces at the selected sampling points. Such an interpretation becomes readily identifiable by realizing that the product $\hat{\boldsymbol{R}}\hat{\boldsymbol{\Sigma}}$ appearing in Eq.(77) is but the (weighted) vector of *fitted* stresses at the selected sampling points. Indeed, by virtue of Eq.(72) and, considering the properties of the selection operator $\boldsymbol{\mathcal{P}}_{(\mathcal{I})}$, we have that

$$\hat{\boldsymbol{R}}\hat{\boldsymbol{\Sigma}} = \boldsymbol{\mathcal{P}}_{(\mathcal{I})}(\boldsymbol{R}\hat{\boldsymbol{\Sigma}}) = \boldsymbol{\mathcal{P}}_{(\mathcal{I})}\boldsymbol{\Sigma}^* = \hat{\boldsymbol{\Sigma}}^*. \tag{82}$$

Using the above equality, Eq.(77) is expressible as $\hat{\mathbb{B}}^{*^T}\hat{\boldsymbol{\Sigma}} = \hat{\mathbb{B}}^{*^T}\hat{\boldsymbol{\Sigma}}^*$, or, reverting to the original, summation notation as

$$\sum_{j \in \mathcal{I}} w_j \boldsymbol{B}^{*^T}(\mathbf{x}_j)\boldsymbol{\sigma}(\mathbf{x}_j;\cdot) = \sum_{j \in \mathcal{I}} w_j \boldsymbol{B}^{*^T}(\mathbf{x}_j)\boldsymbol{\sigma}^*(\mathbf{x}_j;\cdot). \tag{83}$$

Note that both sides of the above equation represent the same physical quantity, namely, the sum of internal forces, in reduced coordinates, at the sampling Gauss points $\{\mathbf{x}_{\mathcal{I}_1}, \mathbf{x}_{\mathcal{I}_2} \cdots \mathbf{x}_{\mathcal{I}_p}\}$. The difference lies in the stresses employed for computing these internal forces. In the left-hand side, they are calculated using "observed" stresses $\boldsymbol{\sigma}$ —stresses that arises directly from evaluating the corresponding constitutive equation—, whereas, in the right-hand side, "fitted" stresses $\boldsymbol{\sigma}^*$ are used —that is, stresses obtained from fitting the approximation constructed using the POD stress basis functions $\boldsymbol{\Psi}_1, \boldsymbol{\Psi}_2 \ldots \boldsymbol{\Psi}_{n_\sigma}$ to the observed data. Thus, the HP-ROM equilibrium condition (83) is telling us that, at the solution, *the sum of internal forces —at the pre-selected sampling points— computed using either observed or fitted stresses*[14] *must coincide.*

[14]It should be mentioned in this respect that, in general, $\boldsymbol{\sigma}^*(\mathbf{x}_j;\cdot) \neq \boldsymbol{\sigma}(\mathbf{x}_j;\cdot)$ since the

6.4. Jacobian matrix

Needless to say, the dependence of the stresses on the reduced vector of reduced displacement fluctuations $\boldsymbol{U}^*$ is in general non-linear, and, thereby, an iterative method is required for solving Eq.(77). Here we employ the standard *Newton-Raphson* procedure. The iterative scheme corresponding to this procedure is given by the following expression (the parenthetical superscript indicates iteration number):

$$\boldsymbol{U}^{*(k+1)} = \boldsymbol{U}^{*(k)} - \boldsymbol{K}^{*(k)^{-1}} \boldsymbol{F}^{*(k)}, \tag{84}$$

where

$$\boldsymbol{F}^{*(k)} = \hat{\mathbb{B}}^{*^T} (\boldsymbol{I} - \hat{\boldsymbol{R}})\, \hat{\boldsymbol{\Sigma}}(\boldsymbol{\epsilon_M}, \boldsymbol{U}^{*(k)}) \tag{85}$$

and

$$\boldsymbol{K}^{*(k)} = \hat{\mathbb{B}}^{*^T} (\boldsymbol{I} - \hat{\boldsymbol{R}})\, \hat{\mathbb{C}}(\boldsymbol{\epsilon_M}, \boldsymbol{U}^{*(k)})\, \hat{\mathbb{B}}^*. \tag{86}$$

In the above equation, $\hat{\mathbb{C}} \in \mathbb{R}^{p\cdot s \times p\cdot s}$ denotes a block diagonal matrix containing the algorithmic, constitutive tangent matrices at each sampling point:

$$\hat{\mathbb{C}} := \begin{bmatrix} \boldsymbol{C}(\mathbf{x}_{\mathcal{I}_1}; \cdot) & \mathbf{0} & \mathbf{0} & \cdots & \mathbf{0} \\ \mathbf{0} & \boldsymbol{C}(\mathbf{x}_{\mathcal{I}_2}; \cdot) & \mathbf{0} & \cdots & \mathbf{0} \\ \vdots & \vdots & \vdots & \vdots & \vdots \\ \mathbf{0} & \mathbf{0} & \mathbf{0} & \mathbf{0} & \boldsymbol{C}(\mathbf{x}_{\mathcal{I}_p}; \cdot) \end{bmatrix}. \tag{87}$$

6.4.1. Positive definiteness

Because of its relevance in the overall robustness of the proposed method, it is worthwhile at this point to digress and discuss thoroughly the spectral properties of the Jacobian matrix represented by Eq.(86). In particular, it would be interesting to ascertain whether *positive definiteness* of the algorithmic tangent matrices $\boldsymbol{C}(\mathbf{x}_{\mathcal{I}_1}; \cdot)$, $\boldsymbol{C}(\mathbf{x}_{\mathcal{I}_2}; \cdot), \cdots \boldsymbol{C}(\mathbf{x}_{\mathcal{I}_p})$ at the selected sampling points, and thus of matrix $\hat{\mathbb{C}}$, ensures positive definiteness of the Jacobian matrix $\boldsymbol{K}^*$ —as it occurs when using classical Gauss quadrature rules with positive weights—, and, if not, which remedies can be applied to obtain such desirable property.

number of data items to be fitted ($p \cdot s$) is always greater than the number of stress modes (n_σ). Observed and fitted stresses coincide only when the stress vector $\boldsymbol{\Sigma}$ one wishes to approximate pertains to the column space of the stress basis matrix $\boldsymbol{\Psi}$

Positive definiteness of the Jacobian matrix (86) requires that the function defined as

$$F(\mathbf{U}) = \mathbf{U}^{\mathbf{T}}\boldsymbol{K}^{*}\mathbf{U} = (\hat{\mathbb{B}}^{*}\mathbf{U})^{\mathbf{T}}(\boldsymbol{I} - \hat{\boldsymbol{R}})\,\hat{\mathbb{C}}(\hat{\mathbb{B}}^{*}\mathbf{U}) \tag{88}$$

be positive for all non-zero $\mathbf{U} \in \mathbb{R}^{\mathbf{n_u}}$. Since $\hat{\mathbb{B}}^{*}$ is a full rank matrix —by virtue of Eq.(64)—, condition $F(\mathbf{U}) > \mathbf{0}$ is equivalent to:

$$G(\mathbf{V}) = \mathbf{V}^{\mathbf{T}}(\boldsymbol{I} - \hat{\boldsymbol{R}})\,\hat{\mathbb{C}}\,\mathbf{V} > \mathbf{0} \tag{89}$$

for all non-zero $\mathbf{V} \in \text{Range}(\hat{\mathbb{B}}^{*})$.

To go further, we need to demonstrate that $\hat{\boldsymbol{R}} \in \mathbb{R}^{n_g \cdot s \times n_g \cdot s}$ —recall that $\hat{\boldsymbol{R}}$ is the matrix that maps the vector of "observed" stresses $\hat{\boldsymbol{\Sigma}}$ to the vector of *fitted* stresses $\hat{\boldsymbol{\Sigma}}^{*}$— actually represents an *orthogonal projection*[15] onto the column space of the gappy stress basis matrix $\hat{\boldsymbol{\Psi}}$. This can be shown by simply noting that $\hat{\boldsymbol{R}}$ is, on the one hand, symmetric:

$$\hat{\boldsymbol{R}}^{T} = (\hat{\boldsymbol{\Psi}}(\hat{\boldsymbol{\Psi}}^{T}\hat{\boldsymbol{\Psi}})^{-1}\hat{\boldsymbol{\Psi}}^{T})^{T} = \hat{\boldsymbol{\Psi}}(\hat{\boldsymbol{\Psi}}^{T}\hat{\boldsymbol{\Psi}})^{-T}\hat{\boldsymbol{\Psi}}^{T} = \hat{\boldsymbol{R}} \tag{90}$$

and, on the other hand, idempotent:

$$\hat{\boldsymbol{R}}^{2} = (\hat{\boldsymbol{\Psi}}\hat{\boldsymbol{\Psi}}^{\dagger})^{2} = \hat{\boldsymbol{\Psi}}\overbrace{(\hat{\boldsymbol{\Psi}}^{T}\hat{\boldsymbol{\Psi}})^{-1}\hat{\boldsymbol{\Psi}}^{T}\hat{\boldsymbol{\Psi}}}^{=\boldsymbol{I}}(\hat{\boldsymbol{\Psi}}^{T}\hat{\boldsymbol{\Psi}})^{-1}\hat{\boldsymbol{\Psi}}^{T} = \hat{\boldsymbol{\Psi}}(\hat{\boldsymbol{\Psi}}^{T}\hat{\boldsymbol{\Psi}})^{-1}\hat{\boldsymbol{\Psi}}^{T} = \hat{\boldsymbol{R}}. \tag{91}$$

With this property at hand, we can decompose any $\mathbf{V} \in \text{Range}(\hat{\mathbb{B}}^{*})$ as

$$\mathbf{V} = \mathbf{V}^{||} + \mathbf{V}^{\perp} \tag{92}$$

where $\mathbf{V}^{||} = \hat{\boldsymbol{R}}\mathbf{V} \in \text{Range}(\hat{\boldsymbol{\Psi}})$ —the component of $\mathbf{V}$ along the column space of $\hat{\boldsymbol{\Psi}}$— and $\mathbf{V}^{\perp} = (\boldsymbol{I} - \hat{\boldsymbol{R}})\mathbf{V}$ —the component of $\mathbf{V}$ along the orthogonal complement of $\text{Range}(\hat{\boldsymbol{\Psi}})$. Introducing the above decomposition into Eq.(89), we arrive at

$$G = \mathbf{V}^{\perp T}\hat{\mathbb{C}}\mathbf{V}^{\perp} + \mathbf{V}^{\perp\mathbf{T}}\,\hat{\mathbb{C}}\mathbf{V}^{||}. \tag{93}$$

While the first term $\mathbf{V}^{\perp T}\hat{\mathbb{C}}\mathbf{V}^{\perp}$ in the preceding equation is, in virtue of the positive definiteness of $\hat{\mathbb{C}}$, eminently positive for all nonzero $\mathbf{V}^{\perp} \in \mathbb{R}^{\mathbf{p}\cdot\mathbf{s}}$, nothing can be said in principle about the second term $\mathbf{V}^{\perp T}\,\hat{\mathbb{C}}\mathbf{V}^{||}$: numerical experience shows that the sign and relative magnitude of this term depends further on the chosen *set of sampling indices* $\mathcal{I}$.

[15] $\hat{\boldsymbol{R}}$ is the so-called "hat" matrix of linear regression models [52].

Remark 6.1. *From the above observation, it follows that the positive definiteness of the Jacobian matrix* $\boldsymbol{K}^*$ is determined*, not only by the spectral properties of* $\hat{\mathbb{C}}$*, but —not surprisingly— also by the number and the location within the RVE of the sampling points employed in the integration.*

The foregoing remark naturally leads to wonder whether it is possible to select the sampling indices $\mathcal{I}$ so as to ensure the positive definiteness of $\boldsymbol{K}^*$ (assuming, obviously, that $\hat{\mathbb{C}}$ enjoys this property). To shed light on this question, let us first divide Eq.(93) by $\mathbf{V}^{\perp T}\hat{\mathbb{C}}\mathbf{V}^{\perp}$ (notice that hypothesis (64) precludes the possibility of $\mathbf{V}^{\perp}$ being zero)

$$\bar{G} = \frac{G}{\mathbf{V}^{\perp T}\hat{\mathbb{C}}\mathbf{V}^{\perp}} = 1 + \frac{\mathbf{V}^{\perp T}\hat{\mathbb{C}}\mathbf{V}^{||}}{\mathbf{V}^{\perp T}\hat{\mathbb{C}}\mathbf{V}^{\perp}}. \tag{94}$$

Suppose now, for the sake of argument, that $\hat{\mathbb{C}}$ is also symmetric. Such being the case, the above equation can be legitimately rewritten as:

$$\bar{G} = 1 + \cos(\mathbf{V}^{\perp}, \mathbf{V}^{||})_{\hat{\mathbb{C}}} \frac{\|\mathbf{V}^{||}\|_{\hat{\mathbb{C}}}}{\|\mathbf{V}^{\perp}\|_{\hat{\mathbb{C}}}}, \tag{95}$$

where

$$\cos(\mathbf{V}^{\perp}, \mathbf{V}^{||})_{\hat{\mathbb{C}}} = \frac{\langle \mathbf{V}^{\perp}, \mathbf{V}^{||} \rangle_{\hat{\mathbb{C}}}}{\|\mathbf{V}^{\perp}\|_{\hat{\mathbb{C}}} \|\mathbf{V}^{||}\|_{\hat{\mathbb{C}}}}. \tag{96}$$

In the above equation, $\langle \cdot, \cdot \rangle_{\hat{\mathbb{C}}}$ symbolizes the inner product defined by $\hat{\mathbb{C}}$ (i.e., $\langle \mathbf{x}, \mathbf{y} \rangle_{\hat{\mathbb{C}}} = \mathbf{x}^{\mathbf{T}}\hat{\mathbb{C}}\mathbf{y}$), whereas $\| \cdot \|_{\hat{\mathbb{C}}}$ denotes the norm associated to such an inner product ($\|\mathbf{x}\|^{\mathbf{2}}_{\hat{\mathbb{C}}} = \langle \mathbf{x}, \mathbf{x} \rangle_{\hat{\mathbb{C}}}$). From Eq.(94), it can be deduced that a sufficient (yet not necessary) condition for $\bar{G} > 0$, and thus for $\boldsymbol{K}^*$ to be positive definite, is that

$$\frac{\|\mathbf{V}^{||}\|_{\hat{\mathbb{C}}}}{\|\mathbf{V}^{\perp}\|_{\hat{\mathbb{C}}}} < 1 \tag{97}$$

for all nonzero $\mathbf{V} \in \text{Range}(\hat{\mathbb{B}}^*)$, or equivalently (setting $\mathbf{V} = \hat{\mathbb{B}}^*\mathbf{U}$):

$$\frac{\|\hat{\boldsymbol{R}}\hat{\mathbb{B}}^*\mathbf{U}\|_{\hat{\mathbb{C}}}}{\|(\boldsymbol{I} - \hat{\boldsymbol{R}})\hat{\mathbb{B}}^*\mathbf{U}\|_{\hat{\mathbb{C}}}} < 1 \tag{98}$$

for all nonzero $\mathbf{U} \in \mathbb{R}^{\mathbf{n_u}}$.

Useful guidelines on how to choose $\mathcal{I}$ so as to make positive definite the Jacobian matrix $\boldsymbol{K}^*$ can be inferred from inequality (98). Firstly, given a fixed number of sampling points p, expression (98) indicates that such points should be selected so that the columns of the gappy *strain* basis matrix $\hat{\mathbb{B}}^* = \boldsymbol{\mathcal{P}}_{(\mathcal{I})}\mathbb{B}^* = [\hat{\mathbb{B}}_1^* \, \hat{\mathbb{B}}_2^* \ldots \hat{\mathbb{B}}_{n_u}^*]$ are, loosely speaking, "as orthogonal as possible" to $\text{Range}(\hat{\boldsymbol{R}}) = \text{Range}(\hat{\boldsymbol{\Psi}})$ —the column space of the gappy *stress* basis matrix $\hat{\boldsymbol{\Psi}} = \boldsymbol{\mathcal{P}}_{(\mathcal{I})}\boldsymbol{\Psi}$. In so doing, the factor defined as

$$f_{\hat{\mathbb{C}}} := \frac{\sqrt{\sum_{i=1}^{n_u} \|\hat{\boldsymbol{R}}\hat{\mathbb{B}}_i^*\|_{\hat{\mathbb{C}}}^2}}{\sqrt{\sum_{i=1}^{n_u} \|(\boldsymbol{I} - \hat{\boldsymbol{R}})\hat{\mathbb{B}}_i^*\|_{\hat{\mathbb{C}}}^2}}, \tag{99}$$

would diminish, and so would, consequently, the left-hand side of inequality Eq.(98). In practice, however, factor $f_{\hat{\mathbb{C}}}$ cannot be used as a criterion for guiding the selection of sampling points, simply because it is defined in terms of the norm induced by $\hat{\mathbb{C}}$, and this matrix virtually changes at every time step and iteration. One has to be content to estimate this factor using other norm; for instance, employing the standard euclidean norm $\|\cdot\|$, one gets

$$f_{\hat{\mathbb{C}}} \sim f_F := \frac{\sqrt{\sum_{i=1}^{n_u} \|\hat{\boldsymbol{R}}\hat{\mathbb{B}}_i^*\|^2}}{\sqrt{\sum_{i=1}^{n_u} \|(\boldsymbol{I} - \hat{\boldsymbol{R}})\hat{\mathbb{B}}_i^*\|^2}} = \frac{\|\hat{\boldsymbol{R}}\hat{\mathbb{B}}^*\|_F}{\|(\boldsymbol{I} - \hat{\boldsymbol{R}})\hat{\mathbb{B}}^*\|_F}, \tag{100}$$

where $\|\cdot\|_F$ stands for the Frobenius norm.

Aside from seeking orthogonality between $\hat{\mathbb{B}}^*$ and $\hat{\boldsymbol{R}}$, expression (99) suggests that another way of lowering factor f_F may be to reduce the ratio defined as

$$\beta_F := \frac{\|\hat{\boldsymbol{R}}\|_F}{\|\boldsymbol{I} - \hat{\boldsymbol{R}}\|_F}. \tag{101}$$

Since $\hat{\boldsymbol{R}}$ and, consequently, $\boldsymbol{I} - \hat{\boldsymbol{R}}$ are matrices representing orthogonal projections, we have that $\|\hat{\boldsymbol{R}}\|_F = \sqrt{\text{rank}(\hat{\boldsymbol{R}})} = \sqrt{n_\sigma}$ and $\|\boldsymbol{I} - \hat{\boldsymbol{R}}\|_F = \sqrt{p \cdot s - n_\sigma}$. Therefore,

$$\beta_F = \sqrt{\frac{n_\sigma}{p \cdot s - n_\sigma}}. \tag{102}$$

Observation 6.2. *From the above expression, thus, one can conclude that increasing the number of sampling points p while keeping the number of stress modes n_σ constant also contributes to reduce factor f_F in Eq.(98), and, hence, to improve the spectral properties (positive defineteness) of the Jacobian matrix $\boldsymbol{K}^*$. Notice that this property is totally consistent with the fact that, in the limiting case of taking all Gauss points ($p = n_g$), the reduced matrices $\hat{\boldsymbol{R}}$ and $\hat{\mathbb{B}}^*$ degenerate into their full order counterparts $\boldsymbol{R}$ and $\mathbb{B}^*$, for which the condition $\boldsymbol{R}\,\mathbb{B}^* = \boldsymbol{0}$ holds —they span subspaces that are mutually orthogonal—, hence making $f_F = f_{\hat{\mathbb{C}}} = 0$.*

7. Selection of sampling points

The last theoretical issue to be discussed in the present work is the selection —among the full set of Gauss points of the underlying finite element mesh— of appropriate *sampling or interpolation points*. At the very least, the set of sampling indices $\mathcal{I} = \{i_1, i_2 \dots i_p\}$ must be chosen so that the *gappy* expanded basis matrix has full rank (see section 6.2):

$$\text{rank}(\hat{\boldsymbol{\Psi}}^{ex}_{(\mathcal{I})}) = \text{rank}([\hat{\boldsymbol{\Psi}}_{(\mathcal{I})} \;\; \hat{\mathbb{B}}^*_{(\mathcal{I})}]) = n_\sigma + n_u. \tag{103}$$

Any set of sampling indices fulfilling this necessary condition is said to be *admissible*.

7.1. Optimality criteria

7.1.1. Accuracy

As in any other model reduction problem, the overriding concern when choosing the sampling points is the *accuracy of the approximation*: we would like to position such points so that maximum similarity between the "high-fidelity", finite element solution and its reduced-order counterpart is obtained. More specifically, since the output of interest in our BVP is the *macroscopic* stress response, the aim is to find the set of sampling points $\mathcal{I}$ that minimizes the following error estimate:

$$E_{M,\sigma}(\boldsymbol{\Psi}, \mathcal{I}) := \sqrt{\sum_{i=1}^{n_{snp}} \|\boldsymbol{\sigma_M}^i - \boldsymbol{\sigma_M}^{*\,i}(\boldsymbol{\Psi}, \mathcal{I})\|^2}, \tag{104}$$

where $\boldsymbol{\sigma_M}^i = \boldsymbol{\sigma_M}({}^t\boldsymbol{\epsilon_M}_k{}^j)$ denotes the finite element, macroscopic stress response corresponding to the the $k-th$ ($k = 1, 2 \dots n_{stp}$) time step of the

"training"[16] strain trajectory ${}^t\boldsymbol{\epsilon}_{\boldsymbol{M}}{}^j$ ($j = 1, 2 \dots n_{hst}$); and $\boldsymbol{\sigma}_{\boldsymbol{M}}{}^{*i}(\boldsymbol{\Psi}, \mathcal{I})$ its low-dimensional approximation.

Using the Cauchy-Schwarz inequality, and approximating the pertinent integrals by Gauss quadrature, we can write

$$\begin{aligned} E_{M,\sigma}{}^2 &\leq \frac{1}{V} \sum_{i=1}^{n_{snp}} \int_\Omega \|\boldsymbol{\sigma}^i(\mathbf{x}) - \boldsymbol{\sigma}^{*i}(\mathbf{x}; \boldsymbol{\Psi}, \mathcal{I})\|^2 \, d\Omega \\ &\approx \frac{1}{V} \sum_{i=1}^{n_{snp}} \sum_{g=1}^{n_g} \|\sqrt{w_g}\boldsymbol{\sigma}^i(\mathbf{x}_g) - \sqrt{w_g}\boldsymbol{\sigma}^{*i}(\mathbf{x}_g; \boldsymbol{\Psi}, \mathcal{I})\|^2 \\ &= \frac{1}{V} \sum_{i=1}^{n_{snp}} \|\boldsymbol{\Sigma}^i - \boldsymbol{\Sigma}^{*i}(\boldsymbol{\Psi}, \mathcal{I})\|^2 2 = \frac{1}{V} \|\boldsymbol{X} - \boldsymbol{X}^*(\boldsymbol{\Psi}, \mathcal{I})\|_F^2 \end{aligned} \tag{105}$$

where $\boldsymbol{X} = \begin{bmatrix} \boldsymbol{\Sigma}^1 & \boldsymbol{\Sigma}^2 & \cdots & \boldsymbol{\Sigma}^{n_{snp}} \end{bmatrix}$ and $\boldsymbol{X}^*(\boldsymbol{\Psi}, \mathcal{I}) = \boldsymbol{R}_{(\mathcal{I})}(\boldsymbol{\mathcal{P}}_{(\mathcal{I})}\boldsymbol{X})$. The error estimate for the macroscopic stresses defined in Eq.(104) is, thus, bounded above by the Frobenius norm of the difference between the (weighted) stress snapshot matrix $\boldsymbol{X}$ and its oblique projection, $\boldsymbol{X}^*$, onto Range($\boldsymbol{\Psi}$). This bound, hereafter designated by e_σ, admits the following decomposition[17]

$$e_\sigma{}^2 = \frac{1}{V} \|\boldsymbol{X} - \boldsymbol{X}^{*\perp}(\boldsymbol{\Psi})\|_F^2 + \frac{1}{V} \|\boldsymbol{X}^{*\perp}(\boldsymbol{\Psi}) - \boldsymbol{X}^*(\boldsymbol{\Psi}, \mathcal{I})\|_F^2, \tag{106}$$

$\boldsymbol{X}^{*\perp}$ being the *orthogonal* projection of $\boldsymbol{X}$ onto the range of $\boldsymbol{\Psi}$, i.e., $\boldsymbol{X}^{*\perp} = \boldsymbol{\Psi}\boldsymbol{\Psi}^T\boldsymbol{X}$. Note that the first term of the right-hand side of Eq.(106) only depends on the stress basis matrix, but not on the employed sampling indices; it provides, thus, an estimate of the *stress truncation error*. The term that actually measures the quality, in terms of accuracy, of a given set of admissible sampling points is the second one—it provides an (a priori) estimate of the *stress reconstruction error*. We shall denote this term by e_σ^{rec}:

$$e_\sigma^{rec} := \frac{1}{V} \|\boldsymbol{X}^{*\perp}(\boldsymbol{\Psi}) - \boldsymbol{X}^*(\boldsymbol{\Psi}, \mathcal{I})\|_F. \tag{107}$$

For this reason —and also because the cost of evaluating expression Eq.(107)

[16] The term "training", which, incidentally, is borrowed from the neural network literature [38], is used throughout the text to refer to the offline generation of snapshots.

[17] This decomposition follows easily from the Pythagorean theorem (just notice that $\boldsymbol{\Psi}^T(\boldsymbol{X} - \boldsymbol{X}^{*\perp}) = \boldsymbol{0}$).

is independent of the number of Gauss points[18], and therefore significantly lower than in the case of the original error estimate $E_{M,\sigma}$—, we shall use in what follows e_σ^{rec} as error estimator for guiding the selection of sampling points.

7.1.2. Spectral properties

Yet the optimality of a given set of sampling points cannot be measured only in terms of accuracy of the approximation. As demonstrated in Section 6.4, the number and particular placement of such points influence also the *spectral properties* (positive definiteness) of the Jacobian matrix of the equilibrium equation, and therefore, the convergence characteristics of the accompanying Newton-Raphson algorithm. We saw that, to preserve the positive definiteness of the full-order Jacobian matrix, one should strive to choose the sampling indices $\mathcal{I}$ so as to make the factor —defined previously in Eq.(100)—:

$$f_F(\boldsymbol{\Psi}, \mathbb{B}^*, \mathcal{I}) = \frac{\|\hat{\boldsymbol{R}}_{(\mathcal{I})}\hat{\mathbb{B}}^*_{(\mathcal{I})}\|_F}{\|(\boldsymbol{I} - \hat{\boldsymbol{R}}_{(\mathcal{I})})\hat{\mathbb{B}}^*_{(\mathcal{I})}\|_F} \tag{108}$$

as small as possible.

7.2. Optimization approach: basic and stabilizing sampling points

Unfortunately, the minimization of the approximation error represented by expression Eq.(107) and the minimization of Eq.(108) are in general conflicting goals. For instance, numerical experiments show that when the selection is driven exclusively by accuracy considerations, the resulting Jacobian matrix becomes indefinite at certain states of deformation —especially when inelastic deformations are severe—, leading occasionally to convergence failures. These goals must be therefore balanced in order to arrive at an accurate and at the same time robust solution scheme.

To accomodate these conflicting requirements, we propose here a heuristic strategy that basically consists in treating the minimization of Eq.(107) and

[18]Indeed, since $\boldsymbol{\Psi}$ is column-wise orthogonal, minimizing Eq.(107) is equivalent to minimizing the difference between the coefficients of the respective projections. The number of coefficients is equal to the number of snapshots, which is normally much lower than the number of Gauss points.

Eq.(108) as two separated, sequential problems —in the spirit of the so-called "greedy" optimization algorithms[19] [44]. The set of sampling points is assumed to be divided into two disjoint subsets $\mathcal{I}_\sigma$ and $\mathcal{I}_B$:

$$\mathcal{I} = \mathcal{I}_\sigma \cup \mathcal{I}_B. \tag{109}$$

The first subset $\mathcal{I}_\sigma = \{i_1, i_2, \cdots i_{p_\sigma}\}$ is obtained as the minimizer of the error estimation given in Eq.(107), viz.:

$$\mathcal{I}_\sigma = \arg \min_{\mathcal{K} \subseteq \{1,2 \ldots n_g\}} e_\sigma^{rec}(\boldsymbol{\Psi}, \mathcal{K}). \tag{110}$$

Once the set $\mathcal{I}_\sigma$ is determined, the remaining sampling indices $\mathcal{I}_B = \{j_1, j_2 \cdots j_{p_B}\}$ ($p_\sigma + p_B = p$) are calculated as

$$\mathcal{I}_B = \arg \min_{\mathcal{K} \subseteq \{1,2 \ldots n_g\}} f_F(\boldsymbol{\Psi}, \mathbb{B}^*, \mathcal{I}_\sigma \cup \mathcal{K}). \tag{111}$$

Remark 7.1. *It must be noted here that the minimization problem represented by Eq.(110) is in essence the same problem addressed in (standard) interpolatory-based, model reduction approaches for determining, given a set of empirical basis functions, the optimal location of associated interpolations points. For this reason, we shall refer to the set of points arising from solving this minimization problem as the* standard or basic sampling points *—these are the Best Interpolation Points of Nguyen et al. [54], or the "magic points" of Maday et al. [46].. By contrast, the necessity of introducing points that attempt to solve problem (111) is a consequence of expanding the stress approximation space in the first place —the main innovative feature of our approach—, and it is therefore not present in other model reduction strategies. We shall call* $\{\boldsymbol{x}_{\mathcal{I}_B(1)}, \boldsymbol{x}_{\mathcal{I}_B(2)} \ldots \boldsymbol{x}_{\mathcal{I}_B(p_B)}\}$ *the set of stabilizing sampling points.*

The number of *basic sampling points* must satisfy the necessary condition $p_\sigma \geq n_\sigma/s$. In general, taking $p_\sigma = n_\sigma$ suffices to ensure highly satisfactory approximations. How many, on the other hand, *stabilizing sampling points* have to be added to safely render positive definite the Jacobian matrix —for at least a representative range of macroscopic state deformations— is a

[19] A greedy method is any algorithm that solves the problem by making the locally optimal choice at each step with the hope of finding the global optimum.

question that can only be answered empirically. In the examples presented in the next section, it has been found that a conservative answer is to use as many stabilizing sampling points as displacement basis modes ($p_B = n_u$).

To deal with the discrete minimization problem (110), we have used here the *Hierarchical Interpolation Points* (HPI) method proposed by Nguyen et al. [54]. The essence of this method is to construct, in a *greedy* fashion, the set of indices by solving a *sequence* of one-dimensional minimization problems. The minimization problem (111) is also addressed using a heuristic based on the greedy paradigm. In particular, the $k-th$ ($k = 1, 2 \dots p_B$) index is selected by solving the following, one-dimensional minimization problem:

$$\mathcal{I}_B(k) = \arg \min_{j \in \{1,2 \dots n_g\}} f_F(\boldsymbol{\Psi}, \mathbb{B}^*, \mathcal{K}(j)) \tag{112a}$$

$$\mathcal{K} = \mathcal{I}_\sigma \cup \{\mathcal{I}_B(1), \mathcal{I}_B(2) \cdots \mathcal{I}_B(k-1), j\}. \tag{112b}$$

8. Summary

Lastly, for the reader's convenience and easy reference, the online reduced-order problem, along with the offline steps that leads to the the hyperreduced operators appearing in the online problem, are summarized in Boxes 8.1 and 8.2.

9. Numerical results

This section is intended to illustrate the performance and assess the efficiency of the proposed model reduction strategy in solving the fine scale BVP corresponding to a *porous metal material* under plane strain conditions.

9.1. Microstructure description

The voids are elliptical in shape (with eccentricity equal to 0.3), randomly distributed (with porosity equal to 0.3), and have aligned major axes ranging in length —according to the cumulative probability distribution displayed in figure 3.b— from 0.2 to 1.5 mm. The mechanical behavior of the metal matrix is modeled by a rate-independent, Von Mises elastoplastic model endowed with the following non-linear, isotropic hardening saturation law (consult Ref. [61] for details on the implementation of this elastoplastic model):

$$\sigma_u(\alpha) = \sigma_0 + \bar{H}\alpha + (\sigma_\infty - \sigma_0)(1 - exp(-\alpha\delta)). \tag{118}$$

1. Compute FE displacement fluctuations and stress snaphots for representative, input macro-strain histories. Apply —see Appendix B— the elastic/inelastic POD to the resulting snapshot matrices to obtain the displacement fluctuation and stress basis matrices ($\boldsymbol{\Phi} \in \mathbb{R}^{n\cdot d\times n_u}$ and $\boldsymbol{\Psi} \in \mathbb{R}^{n_g\cdot s\times n_\sigma}$, respectively).
2. Calculate the weighted matrix of fluctuating strain modes $\mathbb{B}^* \in \mathbb{R}^{n_g\cdot s\times n_\sigma}$ using Eqs. (26) and (47).
3. Select a set $\mathcal{I}$ of sampling indices optimal for the basis matrices $\boldsymbol{\Psi}$ and $\mathbb{B}^*$ following the procedure sketched in Section 7.
4. Finally, using $\boldsymbol{\Psi}$, $\mathbb{B}^*$ and $\mathcal{I}$, construct the *hyperreduced*-order matrices $\hat{\mathbb{B}}^{**} \in \mathbb{R}^{p\cdot s\times n_u}$ and $\mathbb{T} \in \mathbb{R}^{s\times p\cdot s}$; the expressions for these matrices read:

$$\hat{\mathbb{B}}^{**} = (\boldsymbol{I} - \hat{\boldsymbol{R}})\hat{\mathbb{B}}^* = (\boldsymbol{I} - \boldsymbol{\mathcal{P}}_{(\mathcal{I})}\boldsymbol{R})(\boldsymbol{\mathcal{P}}_{(\mathcal{I})}\mathbb{B}^*) \tag{113}$$

and

$$\mathbb{T} := \frac{1}{V}\left[\sqrt{w_1}\boldsymbol{I} \quad \sqrt{w_2}\boldsymbol{I} \quad \cdots \quad \sqrt{w_{n_g}}\boldsymbol{I}\right]\boldsymbol{R} \tag{114}$$

where $\boldsymbol{R} = \boldsymbol{\Psi}(\hat{\boldsymbol{\Psi}}^T\hat{\boldsymbol{\Psi}})^{-1}\hat{\boldsymbol{\Psi}}^T$ and $\hat{\boldsymbol{\Psi}} = \boldsymbol{\mathcal{P}}_{(\mathcal{I})}\boldsymbol{\Psi}$.

Box 8.1: Offline stage. Pre-computation of reduced basis and hyperreduced operators.

Here, σ_u stands for the yield stress, $\alpha \geq 0$ denotes the equivalent plastic strain; and $\sigma_0 = 75.0\ MPa$, $\sigma_\infty = 100.0\ MPa$, $\delta = 2500.0$ and $\bar{H} = 5000\ MPa$ are material constants. The Young's modulus and Poisson's coefficient, on the other hand, are equal to $E_m = 75\,GPa$ and $\nu_m = 0.3$, respectively (these material constants corresponds approximately to Aluminum).

9.2. RVE and finite element discretization

The size of the RVE was determined by conducting finite element analyses on square domains of increasing size subject to vanishing displacement fluctuations boundary conditions. It was found that the macroscopic stress responses calculated under representative macroscopic strain paths (stretching along the longitudinal and transversal directions, and shearing) of all samples above 20x20 mm^2 were practically indistinguishable. This fact indicates that any subvolume of 20x20 mm^2 (or greater) can be considered as a Representative Volume Element (RVE) of the porous material under study.

1. *Initial data*: $\boldsymbol{U}_n^* \in \mathbb{R}^{n_u}$ (reduced vector of displacement fluctuations at t_n), $\boldsymbol{\epsilon}_{\boldsymbol{M}n}$ (macroscopic strain vector at t_n), and $\{\boldsymbol{\xi}_n(\mathbf{x}_{\mathcal{I}_1}), \boldsymbol{\xi}_n(\mathbf{x}_{\mathcal{I}_2}), \ldots \boldsymbol{\xi}_n(\mathbf{x}_{\mathcal{I}_p})\}$ (internal variables at t_n *at the selected sampling points*).
2. *Input data*: $\boldsymbol{\epsilon}_{\boldsymbol{M}n+1}$ (macroscopic strain vector at t_{n+1})
3. Given the above initial and input data, find $\boldsymbol{U}_{n+1}^* \in \mathbb{R}^{n_u}$ such that

$$\hat{\mathbb{B}}^{**^T} \hat{\boldsymbol{\Sigma}}(\boldsymbol{\epsilon}_{\boldsymbol{M}n+1}, \boldsymbol{U}_{n+1}^*) = \mathbf{0}, \tag{115}$$

   where

$$\hat{\boldsymbol{\Sigma}} = \left[\sqrt{w_{\mathcal{I}_1}}\boldsymbol{\sigma}^T(\mathbf{x}_{\mathcal{I}_1}, \cdot) \quad \sqrt{w_{\mathcal{I}_2}}\boldsymbol{\sigma}^T(\mathbf{x}_{\mathcal{I}_2}, \cdot) \quad \cdots \quad w_{\mathcal{I}_p}\boldsymbol{\sigma}^T(\mathbf{x}_{\mathcal{I}_p}, \cdot)\right]^T \tag{116}$$

   (here, $\boldsymbol{\sigma}(\mathbf{x}_{\mathcal{I}_i}, \cdot)$ denotes the stress vector evaluated at the $i-th$ sampling point through the corresponding constitutive equation).
4. *Output data:* Once Eq.(116) has been solved for $\boldsymbol{U}_{n+1}^*$, update the macroscopic stress vector as

$$\boldsymbol{\sigma}_{\boldsymbol{M}}|_{n+1} = \mathbb{T}\, \hat{\boldsymbol{\Sigma}}(\boldsymbol{\epsilon}_{\boldsymbol{M}n+1}, \boldsymbol{U}_{n+1}^*). \tag{117}$$

Box 8.2: Online stage (solution of the hyperreduced-order RVE equilibrium problem for given macroscopic strains).

The finite element discretization corresponding to the particular 20x20 mm^2 RVE employed in the ensuing simulations is shown in figure 3.a. The number of (four-node bilinear) elements is $n_e = 9746$, and the number of nodes $n = 11825$. The employed quadrature formula, on the other hand, is the standard 2x2 Gauss rule, the total number of Gauss points amounting thus to $n_g = 4\, n_e = 38984$. To overcome incompressibility issues while maintaining the displacement-based formulation presented in the preceding sections, the commonly known as "B-bar" approach is adopted[20]. The constitutive differential equations are integrated in time using the classical (fully

[20]This means that, in this case, the reduced "B-matrix" $\boldsymbol{B}^*(\mathbf{x})$ appearing in the formulation of the HP-ROM is not constructed using the gradients of the shape functions, as indicated by Eq.(23), but rather using the modified "B-matrix" emanating from the three-field Hu-Washizu variational principle [61]

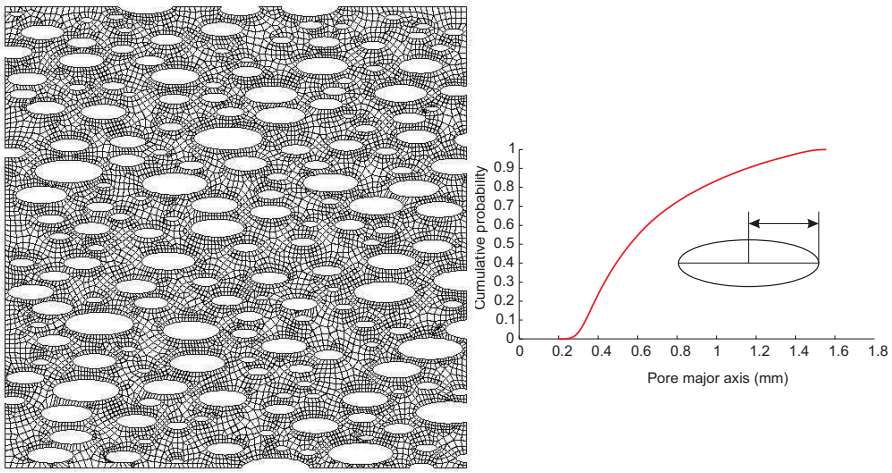

Figure 3: a) Finite element mesh of the RVE corresponding to the porous metal material. b) Cumulative probability distribution followed by the length of the pore major axes.

implicit) backward-Euler scheme.

9.3. Sampling of parameter space

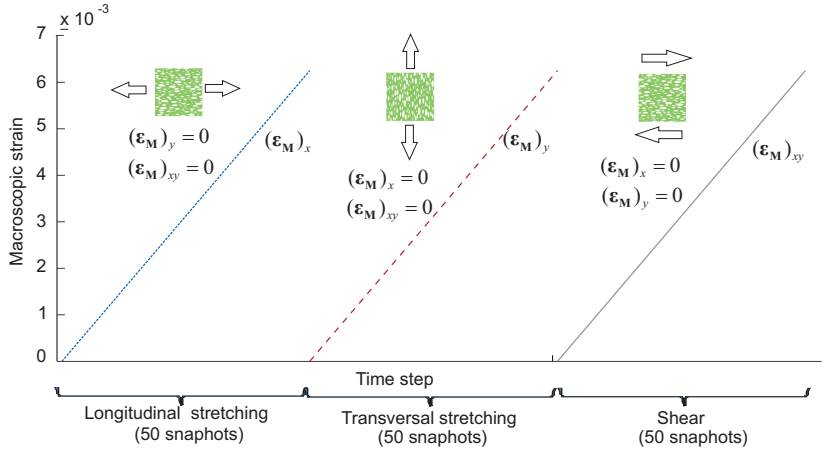

Figure 4: Macro-strain trajectories used for generating the displacement and stress snapshots.

The first step in the process of constructing the reduced basis is the *sampling of the input parameter space*; we saw in Section 3.1 that, in the fine-scale BVP, this process amounts to select *representative macroscopic strain histories*. The three macroscopic strain histories ($n_{hst} = 3$) used in the case under study are depicted in figure 4. In each of these strain trajectories, one of the (independent) strain components follows a linear ascending path while the magnitude of the other two components is set to zero. The time domain for each strain history is discretized into $n_{stp} = 50$ equally spaced steps, resulting in a total number of $n_{snp} = n_{hst} \cdot n_{stp} = 150$ snapshots.

Remark 9.1. *The task of sampling the input parameter space is somehow akin to the experimental process whereby material parameters of standard phenomenological models are calibrated in a laboratory. In this analogy, the RVE plays the role of the corresponding experimental specimen, whereas the macro-strain training trajectories represent the loading paths of the pertinent calibration tests. Hindsight and elementary physical considerations can therefore aid in restricting the number of strain histories (and hence of snapshots) necessary to characterize the response. For instance, if the behavior of the materials that compose the RVE is governed by rate-independent constitutive models (as in the case at hand), we know beforehand that it is not necessary to study the response under varying rates of deformation.*

Strategies for efficiently sampling the input parameter space *in general model reduction contexts can be found in Refs. [12, 13, 15, 42].*

9.4. Dimensionality reduction: a priori error analysis

The finite element displacement fluctuation and stress fields computed at each time step of the input strain trajectories shown above are multiplied by their corresponding weighting matrices ($\bar{\mathbf{M}}$ and $\boldsymbol{W}^{1/2}$) and stored, in the snapshot matrices $\bar{\boldsymbol{X}}_u \in \mathbb{R}^{n \cdot d \times n_{snp}}$ ($n \cdot d = 11825 \cdot 2 = 23650$) and $\boldsymbol{X} \in \mathbb{R}^{n_g \cdot s \times n_{snp}}$ ($n_g \cdot s = 38984 \cdot 4 = 155936$), respectively. Then, these matrices are subjected to the SVD-based, elastic/inelastic dimensionality reduction process sketched in Section 3.2.1 —and described more in detail in Appendix B— in order to generate an optimal set of basis vectors for both the displacements fluctuation and stress solution spaces.

To elucidate which of these basis vectors constitute the "essential" modes of the response, we plot in Figure 5 the dimensionless POD truncation error estimates defined, for the displacement fluctuations, as:

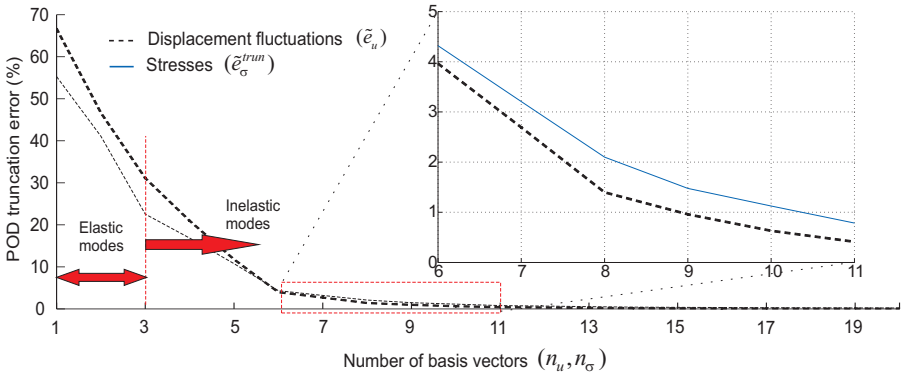

Figure 5: POD truncation error estimates $\tilde{e}_u$ (for the displacement fluctuations, see Eq.(119)) and $\tilde{e}_\sigma^{trun}$ (for the stresses, see Eq.(120)) versus number of basis vectors employed in the approximation (n_u and n_σ, respectively). The portion between 6 and 11 modes is shown in magnified form.

$$\tilde{e}_u(n_u) := \frac{\|\bar{\boldsymbol{X}}_u - \bar{\boldsymbol{X}}_u^*(n_u)\|_F}{\|\bar{\boldsymbol{X}}_u\|_F}, \tag{119}$$

and for the stresses:

$$\tilde{e}_\sigma^{trun}(n_\sigma) := \frac{\|\boldsymbol{X} - \boldsymbol{X}^{*\perp}(n_\sigma)\|_F}{\|\boldsymbol{X}\|_F}, \tag{120}$$

$\bar{\boldsymbol{X}}_u^*(n_u)$ and $\boldsymbol{X}^{*\perp}(n_\sigma)$ being the orthogonal projection of $\bar{\boldsymbol{X}}_u$ and $\boldsymbol{X}$ onto the span of the first n_u and n_σ basis vectors, respectively. It can be observed in Figure 5 that both error measures decrease monotonically with increasing order of truncation —this is a mere consequence of the optimality properties of the SVD—, and at approximately the same rate; the decay is more pronounced from 1 to 6 modes, and becomes more gradual thereafter, tending asymptotically to zero as the number of modes increases. The truncation error for both stresses and displacement fluctuations at $n_\sigma = n_u = 6$ is around 5%. In terms of dimensionality reduction, this means that the data contained in the snapshot matrices can be "compressed" to a factor of $(n_u/n_{snp}) \cdot 100 = (6/150) \cdot 100 = 4\%$ and still retain 95% of the information —the *essential* information. The first 6 basis functions (3 elastic and 3 inelastic) for both stresses and displacement fluctuations, therefore, are to be regarded as *essential* modes in the characterization of the mechanical

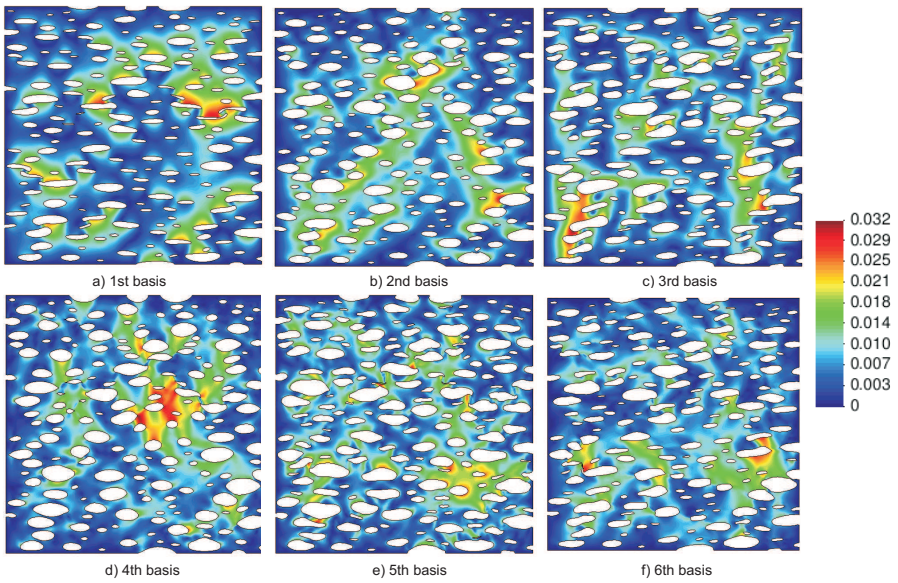

Figure 6: Contour plots of the euclidean norm of the first 6 displacement fluctuations modes ($\|\boldsymbol{\Phi}_i\|$, $i = 1, 2 \dots 5$). Deformed shapes are scaled up by a factor of 15.

response of the concerned RVE. By way of illustration, we plot in Figure 6 the contour plots of the euclidean norm of such 6 *essential* displacement fluctuations modes ($\|\boldsymbol{\Phi}_i\|$, $i = 1, 2 \dots 6$).

9.5. Sampling points

9.5.1. Basic sampling points

Once the stress and displacement fluctuation basis vectors have been determined, the next *offline* step consists in the selection —among the full set of finite element Gauss points—of an optimal set of *sampling points*. Following the strategy described in Section 7.2, we carry out such a selection by first computing the location of what we have called *basic sampling points* $\{\mathbf{x}_{\mathcal{I}_\sigma(1)}, \mathbf{x}_{\mathcal{I}_\sigma(2)} \dots \mathbf{x}_{\mathcal{I}_\sigma(p_\sigma)}\}$. To assess the efficiency of the employed Hierarchical Interpolation Points Method, abbreviated HIPM, we plot in Figure 7 the estimates for both the POD truncation (shown previously in Figure 5) and *total stress error* versus the number of stress modes n_σ (in using this algorithm, it is assumed that $p_\sigma = n_\sigma$). The total stress error estimate is

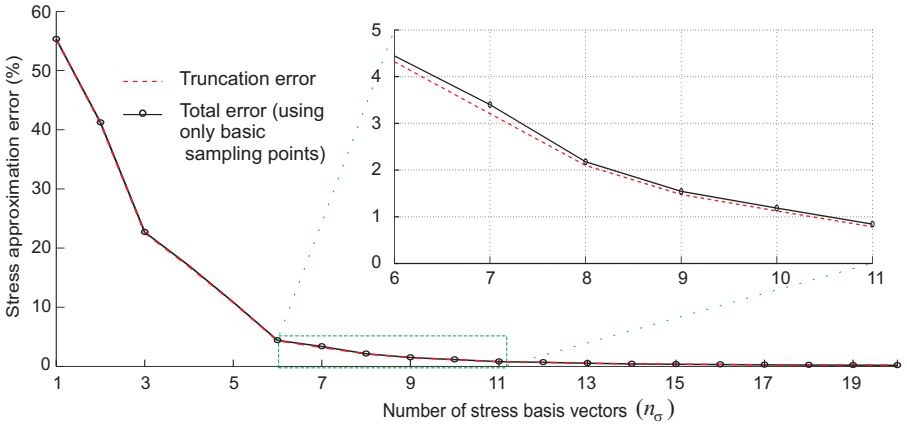

Figure 7: Estimates for the POD truncation ($\tilde{e}_\sigma^{trun}$, see Eq.(120)) and total ($\tilde{e}_\sigma$, see Eq.(121)) stress error versus number of basis vectors employed in the approximation (n_σ). The total error estimate is computed using only the set of *basic sampling points* ($\tilde{e}_\sigma = \tilde{e}_\sigma(n_\sigma, \mathcal{I}_\sigma)$, with $p_\sigma = n_\sigma$). The portion between 6 and 11 modes is shown in magnified form.

defined as

$$\tilde{e}_\sigma(n_\sigma, \mathcal{I}_\sigma) := \frac{\|\boldsymbol{X} - \boldsymbol{X}^*(n_\sigma, \mathcal{I}_\sigma)\|_F}{\|\boldsymbol{X}\|_F} \tag{121}$$

where $\boldsymbol{X}^*(n_\sigma, \mathcal{I}_\sigma)$ denotes the *oblique* projection (calculated using sampling points $\mathcal{I}_\sigma$) of $\boldsymbol{X}$ onto the span of the first n_σ basis vectors $(\boldsymbol{\Psi}_1, \boldsymbol{\Psi}_2 \ldots \boldsymbol{\Psi}_{n_\sigma})$. It can be appreciated in Figure 7 that both the total error and the truncation error curves are practically coincident, a fact that indicates that the contribution of the *reconstruction error*:

$$\tilde{e}_\sigma^{rec} = \sqrt{\tilde{e}_\sigma^2 - \tilde{e}_\sigma^{trun\,2}} = \frac{\|\boldsymbol{X}^{*\perp}(n_\sigma) - \boldsymbol{X}^*(n_\sigma, \mathcal{I}_\sigma)\|_F}{\|\boldsymbol{X}\|_F} \tag{122}$$

(the error introduced as a result of using only p_σ sampling points instead of the entire set of finite element Gauss points, see Section 7.1.1) is *negligible in comparison to the discrepancies due to truncation of the POD basis*. For $n_\sigma = p_\sigma = 6$, for instance, the reconstruction error is less than 3% of the total stress error. In view of these results, it becomes clear that *further refinements in the algorithm for selecting the basic sampling points are in principle not necessary: the employed HIPM optimization algorithm, however*

heuristic, satisfactorily fulfills this purpose. If one wishes to lower the stress approximation error, it is far more effective to simply increase the level of truncation.

9.5.2. Stabilizing sampling points

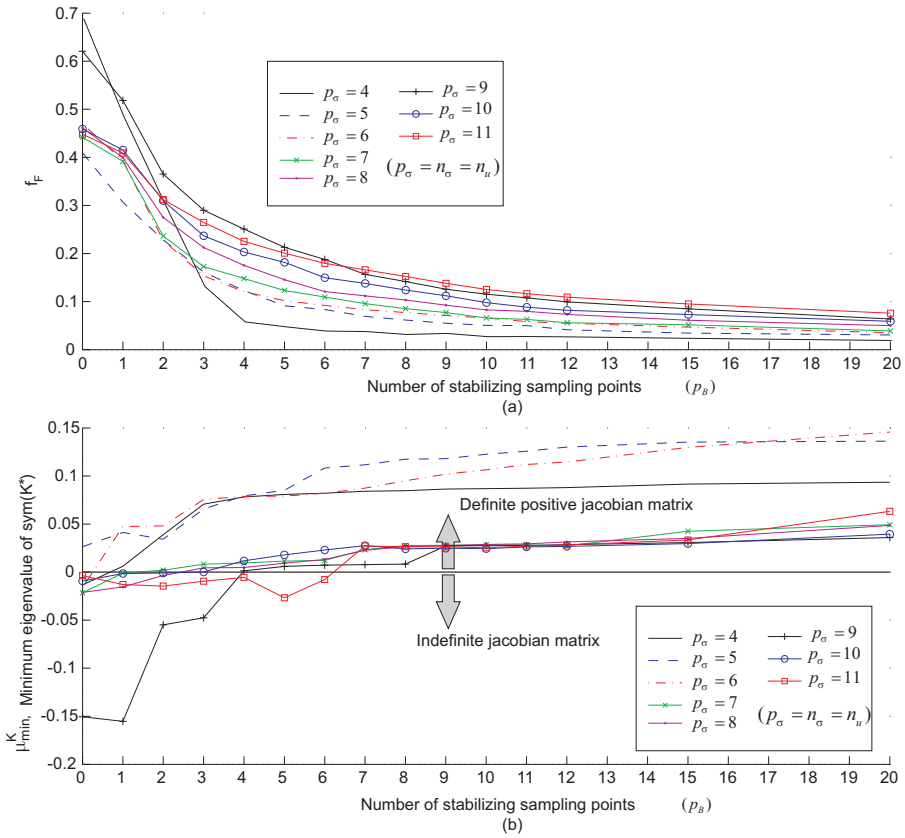

Figure 8: a) Factor f_F (defined in Eq.(99)) versus number of stabilizing sampling points p_B for varying numbers of basic sampling points p_σ (with $p_\sigma = n_\sigma = n_u$). b) Minimum eigenvalue μ^K_{min} (over all time steps and iterations for each p_σ) of the symmetric part of the reduced-order Jacobian matrix $\boldsymbol{K}^*$ versus number of stabilizing sampling points p_B.

Concerning what we have termed "stabilizing sampling points", Figure 8.a contains the graphs, for varying levels of truncation, of factor f_F defined

in Eq.(100) as a function of the number of stabilizing sampling points p_B. To study the influence of including such points on the spectral properties — positive defineteness— of the stiffness matrix, these graphs are accompanied, see figure 8.b, by the plots of the minimum eigenvalue μ^K_{min} (over all time steps and iterations for each case) of the symmetric part of the reduced-order Jacobian matrix $\boldsymbol{K}^*$ versus p_B. It can be seen that f_F decreases monotonically as the number of stabilizing sampling points increases, and such a decrease is reflected, as theoretically anticipated in Section 6.4.1, in the improvement of the spectral properties of the reduced-order Jacobian matrix (higher μ^K_{min} as p_B raises). For clarity, the minimum number of stabilizing sampling points required, for each level of truncation, to render positive definite $\boldsymbol{K}^*$ is plotted in Figure 9. From this plot, it can be gleaned that, roughly, the higher

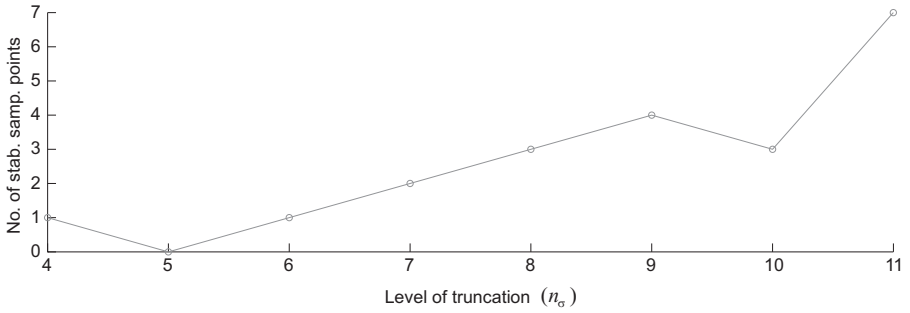

Figure 9: Minimum number of stabilizing sampling points required to make the Jacobian matrix $\boldsymbol{K}^*$ definite positive for each level of truncation $n_\sigma = n_u = p_\sigma$ (deduced from Figure 8).

the level of truncation (and thus the number of basic sampling points), the more stabilizing sampling points appear to be needed to ensure the positive definiteness of $\boldsymbol{K}^*$. For $n_\sigma = p_\sigma = 6$, adding just one stabilizing sampling points suffices, while for $n_\sigma = p_\sigma = 11$, 7 points are required.

Observation 9.1. *The values shown in Figure 9 correspond to the minimum p_B that leads to positive definite $\boldsymbol{K}^*$ when the prescribed strain path coincides with any of the "training" strain trajectory (displayed in Figure 4). Unfortunately, there is no guarantee that the Jacobian matrix will also exhibit this desirable property for prescribed strain histories different from the training ones. Thus, in view of such uncertainty, and in the interest of robustness, it is preferable to stay on the side of "caution" in this regard and use more*

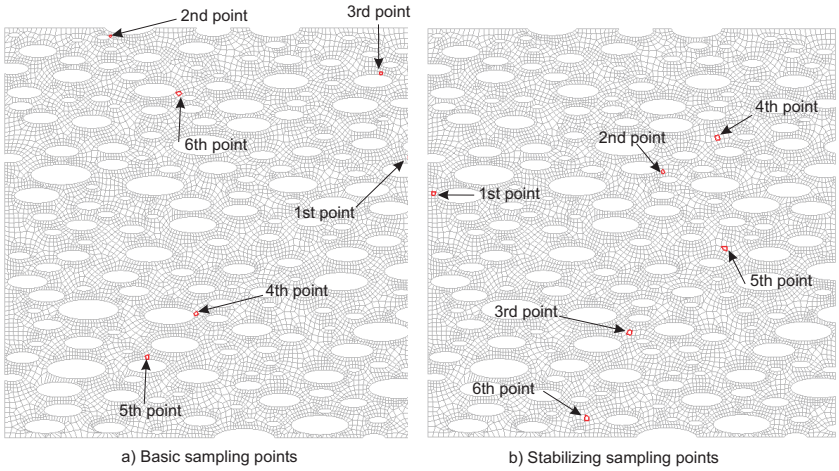

Figure 10: Location within the RVE of the finite elements (marked in red) that contains the first $p_\sigma = p_B = 6$ *basic* and *stabilizing* sampling points.

stabilizing sampling points that the minimum number indicated by the analysis based on the training strain trajectories. It is the authors' experience that a "safe" estimate for p_B is to simply take $p_B = p_\sigma$ —that is, equal number of basic and stabilizing sampling points. In adopting such a rule, the authors have not observed any convergence failures whatsoever, neither in the example under consideration nor in other cases not shown here.

The location of the first $p_\sigma = 6$ basic sampling points and the corresponding $p_B = 6$ stabilizing sampling points is depicted in Figure 10.

9.6. A posteriori errors: consistency analysis

The error measures displayed previously in Figures 5 and 7 only depend on the outcome of the SVD of the snapshot matrices; they can be calculated, thus, *before* actually constructing the reduced-order model. Error analyses based on such measures serve the useful purpose of providing a first hint of how many stress and displacement fluctuations modes are needed to satisfactorily replicate the full-order, finite element solution, and thereby, of prospectively evaluating the *viability* of the reduced basis approach itself.

However, these *a priori* error estimates do not tell the whole story. Expression (121) for the stress approximation error presumes that the stress

solution at the chosen sampling points is the one provided by the finite element model, thus ignoring the fact that, actually, in the reduced-order model, and for the general case of nonlinear, dissipative materials, the stress information at such points at a given time step is already polluted by truncation (in displacement fluctuations and stresses) and reconstruction (in stresses) errors originated in previous time steps. To quantify the extent to which this amalgam of accumulated errors affects the predictions furnished by the HP-ROM, it is necessary to perform a *consistency analysis*.

Generally speaking, a reduced basis approximation is said to be *consistent* if, in the limit of no truncation, it introduces no additional error in the solution of the same problem for which the data used in constructing the basis functions were acquired [14]. In the BVP under consideration, thus, consistency implies that, when using as input macro-strain paths the same trajectories employed in the "training" process, results obtained with the HP-ROM should converge, as n_σ and n_u increase, to the solution furnished by the full-order, finite element model. This condition can be checked by

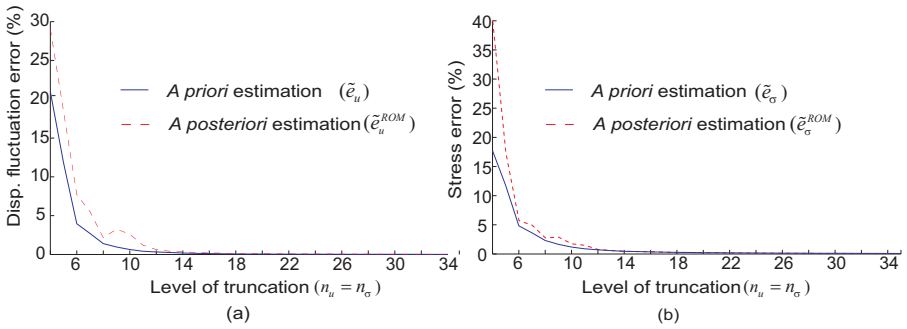

Figure 11: Comparison of the evolution of a priori and a posteriori error measures versus the level of truncation (using $n_u = n_\sigma = p_\sigma = p_B$). a) Displacement fluctuations (see Eqs. 119 and 123). b) Stresses (see Eqs. 121 and 124)

studying the evolution of the error measures defined as

$$\tilde{e}_u^{ROM}(n_u, n_\sigma, \mathcal{I}) := \frac{\|\bar{\boldsymbol{X}}_u - \bar{\boldsymbol{X}}_u^{*ROM}(n_u, n_\sigma, \mathcal{I})\|_F}{\|\bar{\boldsymbol{X}}_u\|_F}, \tag{123}$$

for the displacement fluctuations, and

$$\tilde{e}_\sigma^{ROM}(n_u, n_\sigma, \mathcal{I}_\sigma) := \frac{\|\boldsymbol{X} - \boldsymbol{X}^{*ROM}(n_u, n_\sigma, \mathcal{I}_\sigma)\|_F}{\|\boldsymbol{X}\|_F}, \tag{124}$$

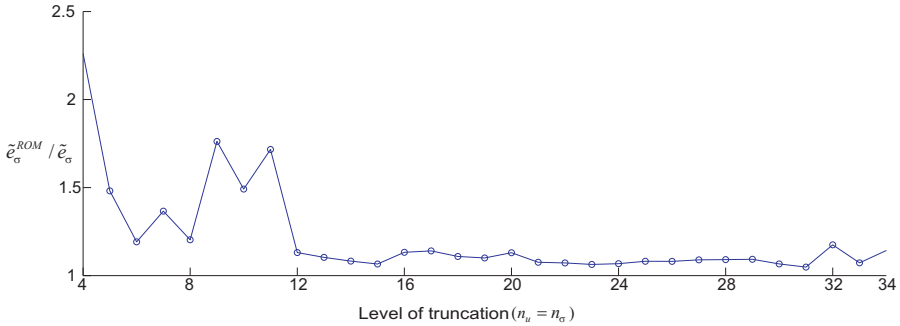

Figure 12: Ratio $\tilde{e}_\sigma^{ROM}/\tilde{e}_\sigma$ between the a posteriori and a priori measures for the stress approximation error against the level of truncation (using $n_u = n_\sigma = p_\sigma = p_B$).

for the stresses. (The superscript "ROM" is appended to highlight that, unlike $\bar{\boldsymbol{X}}_u^*$ and $\boldsymbol{X}^*$ in Eqs. (119) and (121), $\bar{\boldsymbol{X}}_u^{*ROM}$ and $\boldsymbol{X}^{*ROM}$ are matrices of displacement fluctuation and stress snapshots computed using the HP-ROM). Figures 11.a and 11.b contain the graphs of these *a posteriori* error measures, along with their respective *a priori* counterparts $\tilde{e}_u$ (Eq. 119) and $\tilde{e}_\sigma$ (Eq. 121), versus the level of truncation. It becomes clear from these graphs that consistency, in the sense given above, is observed in terms of both displacement fluctuations and stresses: the a posteriori error measures $\tilde{e}_u^{ROM}$ and $\tilde{e}_\sigma^{ROM}$ mimic essentially the decreasing tendency of their a priori counterparts $\tilde{e}_u$ and $\tilde{e}_\sigma$, respectively. It can be seen also that the *a priori error estimations* $\tilde{e}_u$ and $\tilde{e}_\sigma$ *constitute (rather tight) lower bounds* for *their a posteriori counterparts* $\tilde{e}_u^{ROM}$ and $\tilde{e}_\sigma^{ROM}$, respectively. This can be better appreciated, for the stresses, in Figure 12, where the ratio $\tilde{e}_\sigma^{ROM}/\tilde{e}_\sigma$ versus the level of truncation is plotted.

The degree of approximation that can be achieved using the proposed HP-ROM is quantified in a more "engineering" fashion in Figure 13, where we plot, for the case of the first training strain history (stretching in the longitudinal direction), the longitudinal, *macroscopic* stress-strain curves computed using the FE model, on the one hand, and the HP-ROM with $n_u = n_\sigma = 6, 7, 8$ modes, on the other hand. Observe that the maximum deviation from the FE response when using 6 modes (3 elastic and 3 inelastic) takes place at the onset of plastic yielding and is below 8%; remarkably, as deformation continues, this deviation gradually diminishes, being practically

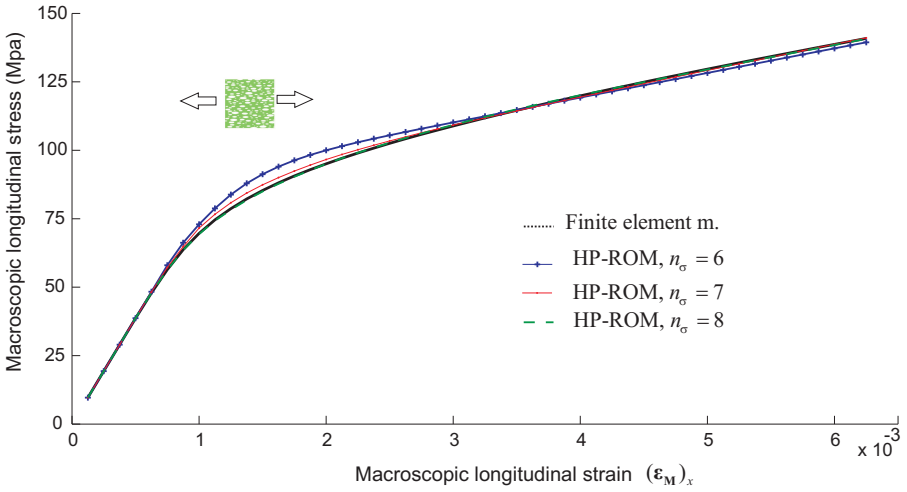

Figure 13: Longitudinal macroscopic stress versus longitudinal macroscopic strain computed using FEM and HP-ROM with $n_\sigma = n_u = 6, 7, 8$.

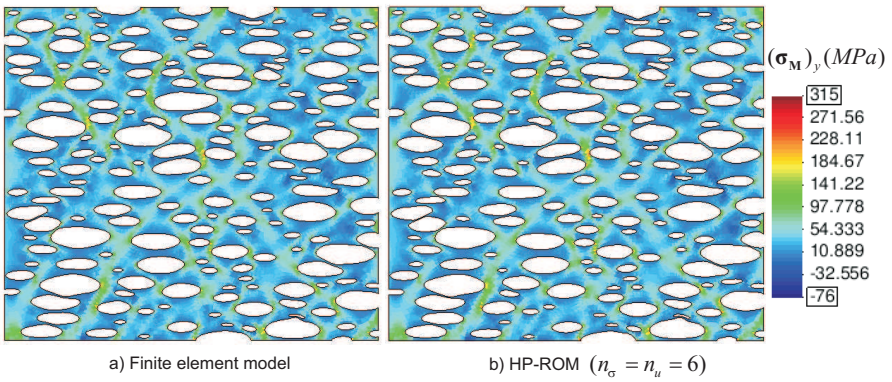

Figure 14: Contour plot of transversal stresses computed at the end of the first "training" strain history using a) FEM (b) HP-ROM with $n_\sigma = n_u = 6$. Deformed shapes are exaggerated (by a factor of 20).

negligible at the end of the process. Furthermore, by just increasing the order of truncation to $n_\sigma = n_u = 8$, differences between the HP-ROM and the FEM responses become virtually imperceptible at all levels of deformation.

Resemblance between HP-ROM and FEM results can also be appreciated in terms of stress distribution in the contour plots shown in Figure 14. Visually, there are no discernible differences between the two contour plots.

9.7. "Training" errors

The studies presented in the preceding subsections were aimed at examining the errors incurred in approximating the *snapshot solution space* $\mathcal{V}_u^{snp}$ by the reduced-order subspace $\mathcal{V}_u^* \in \mathcal{V}_u^{snp}$ spanned by the POD basis vectors —in the terminology of Section 3.1—, and to check that when $\mathcal{V}_u^* \to \mathcal{V}_u^{snp}$, the solution provided by the HP-ROM converges to that obtained with the FEM. But recall that the snapshot space $\mathcal{V}_u^{snp}$ is but a (presumably representative) subspace of $\mathcal{V}_u^\epsilon$, the manifold of $\mathcal{V}_u^h$ induced by the parametric dependence of the fine-scale BVP on the prescribed macroscopic strain history. Consequently, in general —for an arbitrary input strain trajectory— the HP-ROM solution will not converge to the solution provided by the FEM. To complete the error assessment analysis, thus, it is necessary to estimate also the errors inherent to the sampling of the parameter space —we call them *training errors*— and judge whether the selected training strain trajectories generate a snapshot subspace that is indeed *representative* of such a solution space[21] $\mathcal{V}_u^\epsilon$.

Ideally, one should carry out this error assessment by picking up, guided by some sound, statistically-based procedure, a sufficiently large set of strain paths and by comparing the solutions computed by the FEM and HP-ROM under such input strain paths for varying levels of truncation. Such a degree of rigor, however, is beyond the scope of the present work. Here, we limit ourselves here to analyze the quality of the HP-ROM approximation obtained for two different input strain histories, namely, a *uniaxial compression test*, and a *biaxial loading/unloading test*.

[21] To put it in less mathematical terms —by appealing to the the analogy, introduced in Remark 9.1, between the training of the RVE reduced-order model and the calibration of standard phenomenological models— we have "calibrated" our HP-ROM using the training tests displayed previously in Figure 4, and we have shown that the model is able to *exactly* replicate the behavior of the RVE in these tests when $n_u = n_\sigma$ is sufficiently large. Similarly to the situation encountered when dealing with standard phenomenological models, it remains now to assess the capability of the proposed HP-ROM to predict the behavior of the RVE under conditions different from those used in the "calibration" (training) process.

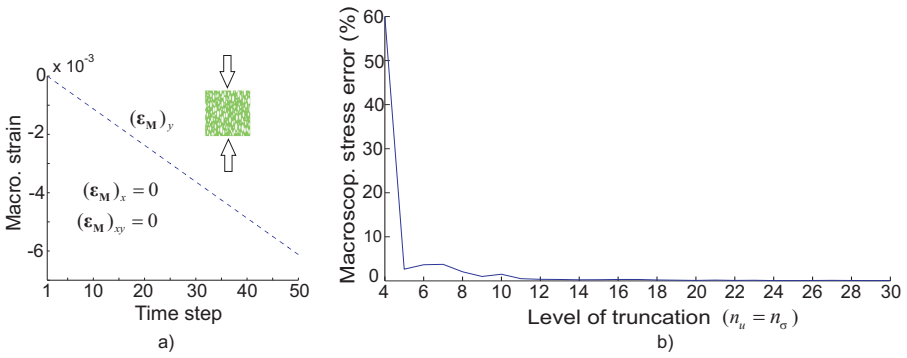

Figure 15: a) First strain trajectory employed for assessing training errors. b) Plot of the macroscopic error estimator $\tilde{E}^{ROM}_{\sigma,M}$ (see Eq.(125)) corresponding to this testing trajectory versus level of truncation ($n_\sigma = n_u$)

9.7.1. Uniaxial compression

The first strain path employed for the assessment is displayed in Figure 15.a; it represents a monotonic compression in the transversal direction (the model, see Figure 4, was trained using only stretching and shear, but not compression, tests). For purposes of evaluating the quality of the HP-ROM approximation, it is convenient to introduce the following macroscopic[22] stress error estimate:

$$\tilde{E}^{ROM}_{\sigma,M} := \sqrt{\frac{\sum_{i=1}^{n^t_{stp}} \|\boldsymbol{\sigma_M}^i - \boldsymbol{\sigma}_M^{*\,i,ROM}(n_\sigma, n_u, \mathcal{I})\|^2}{\sum_{i=1}^{n^t_{stp}} \|\boldsymbol{\sigma_M}^i\|^2}}, \tag{125}$$

where $\boldsymbol{\sigma_M}^i$ and $\boldsymbol{\sigma}_M^{*\,i,ROM}$ denote the macroscopic stress at the $i-th$ time step computed by the FEM and the HP-ROM, respectively. This error estimate is plotted in Figure 15.b versus the level of truncation $n_u = n_\sigma$. Observe that the error goes to zero as the number of employed modes increase. In this particular case, thus, *there is no additional error due to sampling of the*

[22]Recall that the output of interest in solving the fine-scale BVP is the macroscopic stress tensor; thus, the error estimate defined in Eq.(125) ($\tilde{E}^{ROM}_{\sigma,M}$) provides a more meaningful indication of the quality of the approximation than the stress error measure defined previously in Eq.(124) ($\tilde{e}^{ROM}_{\sigma}$). The latter is more suited for examining convergence properties of the HP-ROM approximation, since the minimization problem that underlies the SVD is posed in terms of the Frobenis norm.

parameter space.

Remark 9.2. *This simple example fittingly illustrates one of the acclaimed advantages of POD/Galerkin reduced-order approaches over "black box" methods such as artificial neural networks —that are also based on the partitioned offline-online computational paradigm—: POD/Galerkin reduced-order approaches preserve the "physics" of the problem one wishes to model and, as a consequence, are able to make physically-based extrapolations. For instance, in this case, the reduced-order model is able to exactly replicate (for sufficiently large $n_u = n_\sigma$) the macroscopic compressive behavior of the RVE, even though no information regarding this deformational state has been supplied to the model in the calibration (training) phase; the HP-ROM is "aware", figuratively speaking, that the matrix material in the RVE exhibits similar behavior in tension and compression (J2 plasticity).*

9.7.2. Biaxil loading/unloading test

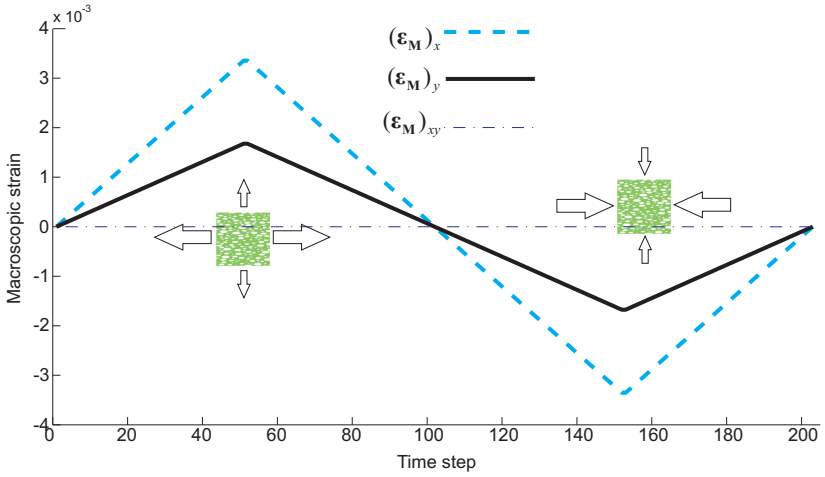

Figure 16: Second strain trajectory employed for assessing training errors.

A more severe test for assessing errors associated to the training process is provided by the strain trajectory shown in Figure 16. Indeed, while the training strain histories of Figure 4 only included monotonic, uniaxial stretching, the strain history displayed in Figure 16 consists of a cycle of *biaxial, loading/unloading stretching* (time steps 1 to 100) and biaxial loading/unloading

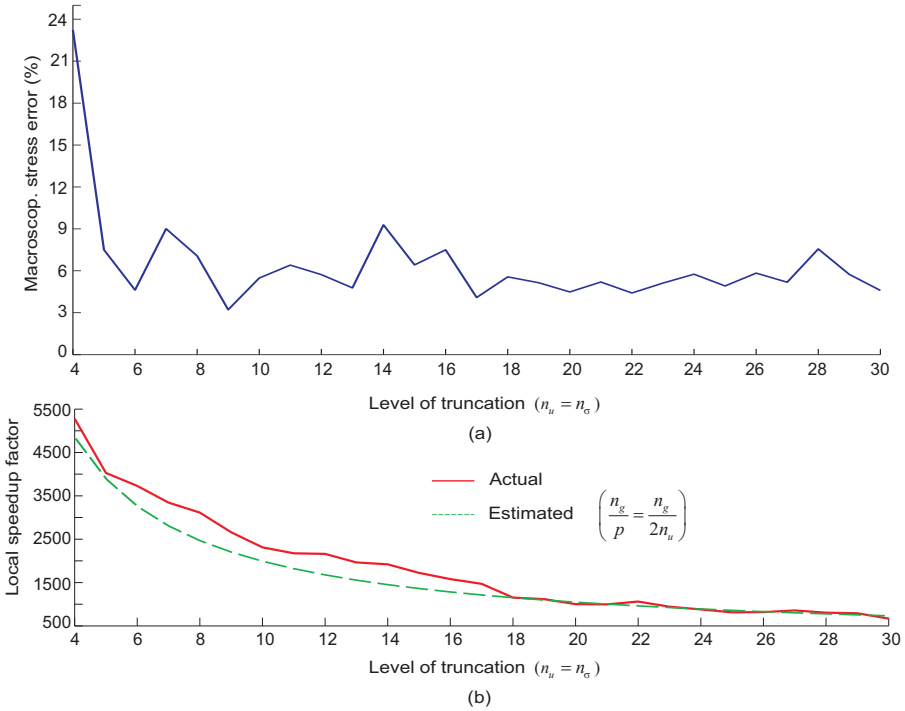

Figure 17: a) Macroscopic error estimator $\tilde{E}^{ROM}_{\sigma,M}$ (see Eq.(125)) versus level of truncation ($n_\sigma = n_u$) for the case of testing trajectory shown in Figure 16,. b) Local speedup factor S_{loc} (defined in Eq.(126)) reported for this case versus level of truncation. This plot is accompanied by the graph of the ratio n_g/p, where $n_g = 38984$ is the total number of Gauss points of the finite element mesh, and $p = 2n_\sigma$ the number of sampling points employed for numerically integrating the HP-ROM.

compression (time steps 101 to 200). The graph of the macroscopic error estimator (125) corresponding to this input strain path as a function of the level of truncation is represented in Figure 17.a. It can be readily perceived that, in this case, and in contrast to the situation encountered in the previously discussed input strain trajectory, the macroscopic stress does not go to zero as the number of POD modes included in the basis increases. Rather, the graph drops sharply from 24% to approximately 5% at $n_\sigma = n_u = 5$ (second inelastic mode), and then fluctuates erratically, with no apparent trend, between 3% and 10% —a level of accuracy that, nevertheless, may be deemed

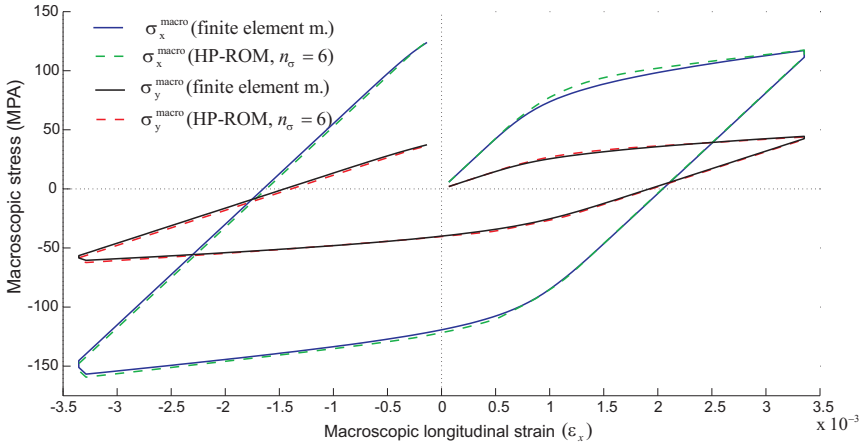

Figure 18: Longitudinal and transversal macroscopic stress versus longitudinal macroscopic strain computed using the FEM and the HP-ROM with $n_\sigma = n_u = 6$ (for the case of the testing trajectory shown in Figure 16)

.

more than acceptable in most practical applications. A more clear picture of the accuracy of the approximation for the particular case of $n_\sigma = n_u = 6$ can be obtained from the stress-strain diagrams shown in figure 18.

9.8. Speedup analysis

Lastly, we turn our attention to one of the main concerns of the present work: the issue of computational efficiency. For a given error level, how many times can the proposed HP-ROM speed up the calculation of the RVE response with respect to the reference finite element model? Let us define the local *speedup factor* as the ratio

$$S_{loc} := \frac{t_{FE}(n, n_g)}{t_{ROM}(n_\sigma, n_u, p)}, \tag{126}$$

where t_{FE} and t_{ROM} denote the CPU times required to compute the FE and HP-ROM macro-stress responses, respectively, induced by a given input strain history[23] In Figure 17.b, we show the graph of the speedup factor

[23]The computational cost associated to the offline stage —generation of snapshots plus the comparatively negligible expenses of applying the POD and selecting the sampling

reported in the the case of the input strain path of Figure 16 as a function of the number of POD modes included in the analysis (recall in this respect that $n_u = n_\sigma = p/2$). We plot also in Figure 17.b the ratio n_g/p, i.e., the relation between the total number of integration points in the finite element model ($n_g = 38984$) and in the reduced order model (p). It can be gleaned from Figure 17.b that the *reported speedup factors are of the same order of magnitude as the ratio* n_g/p; i.e.:

$$S_{loc} \sim \frac{n_g}{p} = \frac{n_g}{2n_\sigma}, \tag{127}$$

(this indicates that the evaluation of the stresses at the integration points dominates the total computational cost). Although these results are no doubt influenced and biased by the particular programming language and coding style employed —we use an in-house, non-vectorized Matlab program operating in a Linux platform—, and, consequently, this trend may not be exactly observed when using other programming languages and/or platforms, they serve to provide an idea of the tremendous *gains in performance* that can be achieved using the proposed ROM; for $n_\sigma = p = 6$ modes, for instance, the *computational cost is reduced by a factor above* 3600, while still capturing 95% of the full-order, high-fidelity information —the *essential information*.

10. Concluding remarks

One of the the most striking features of the proposed reduced-order model is perhaps the conceptual simplicity of the RVE equilibrium equation in its hyperreduced-order form: the sum of (reduced) internal forces at the preselected sampling points must give identical result either calculated using *observed* stresses or *fitted* stresses. Although this condition appears, in hindsight, rather reasonable, even obvious —it ensures maximum resemblance between reduced-order and full-order responses at the sampling points— it seems difficult to arrive at it without the benefit of the integration procedure —based on the notion of *expanded approximation space*— advocated in the present paper.

points—has been deliberately ruled out from this speedup analysis because, in two-scale homogenization contexts, the RVE equilibrium problem is to be solved a sheer number of times and, consequently, this overhead cost is quickly amortized.

The hyperreduced form of the RVE equilibrium equation excels not only in its conceptual simplicity; the corresponding solution scheme is also very simple to implement. Taking as departure point an existing FE code, one only has to replace the typical loop over elements in the FE code by a loop over the pre-selected sampling points $\{\mathbf{x}_{\mathcal{I}_1}, \mathbf{x}_{\mathcal{I}_2}, \ldots \mathbf{x}_{\mathcal{I}_p}\}$. The stress vectors and corresponding constitutive tangent matrices obtained at each stage of the loop are stored in the gappy weighted vector $\hat{\boldsymbol{\Sigma}}$ and the matrix $\hat{\mathbb{C}}$, respectively, and, then the residual vector and the Jacobian matrix are computed as $\hat{\mathbb{B}}^{**^T}\hat{\boldsymbol{\Sigma}}$ and $\hat{\mathbb{B}}^{**^T}\hat{\mathbb{C}}\,\hat{\mathbb{B}}^{*}$, respectively. Notice that *no assembly process is needed*, nor has one to worry about imposing *boundary conditions*. Once convergence is achieved, the macroscopic stress value is simply calculated as $\boldsymbol{\sigma_M} = \mathbb{T}\hat{\boldsymbol{\Sigma}}$. It should be emphasized again that the *operation count in both solving this hyperreduced RVE equation and updating the macroscopic stress vector depends exclusively on the reduced dimensions* n_u and p (number of fluctuation modes and number of sampling points, respectively). Likewise, *storage of history data (internal variables) is only required at the pre-selected sampling points*. Computational savings accrue, thus, not only in terms of number of operations, but also in terms of memory requirements.

The success of the proposed homogenization strategy is predicated on the assumption that displacement and stress fields induced by the parametric dependence on the input macroscopic strain can be approximated by (relatively) low-dimensional functions. Numerical results shown in the preceding section seem to suggest that, in general, this assumption may be expected to hold in the case of *materials governed by strain hardening laws in the small strain regime* —regardless of the geometrical complexity, number and distribution of heterogeneities within the RVE. However, it is by no means apparent that this conclusion can be easily extended to more (kinematically and phenomenologically) complex scenarios, involving large deformations, strain localization, decohesion, etc. For instance, can the deformational behavior of an RVE affected by multiple propagating cracks be represented also in a parsimonious manner, as in the case of strain hardening? Or will the number of modes necessary to accurately replicate its response combinatorially increase with the number of potential crack paths (i.e., with the geometrical complexity of the RVE)? Undoubtedly, in these complex, nonlinear scenarios, the task of sampling the parameter space —i.e., of choosing the macro-strain histories at which to obtain the snapshots— will become quite complicated, due to the richness of possible deformational patterns (void closure, propagating discontinuities ...), and thus difficult to carry out

on intuitive basis (as it has been done in the present paper). Therefore, it would be desirable to systematize this crucial task, as well as to provide some statistical means to *certify*, so to speak, the representativeness of the chosen snapshots. Likewise, topological variations caused by these phenomena may render POD-based compression algorithms inappropriate for collapsing the dimensions of the snapshots space; in such cases, nonlinear dimensionality reduction methods such as the Isomap algorithm [43] may be more suitable. Research in these fronts is currently in progress and will be reported in forthcoming publications.

Acknowledgements

The research leading to these results has received funding from, on the one hand, the European Research Council under the European Union's Seventh Framework Programme (FP/2007-2013) / ERC Grant Agreement n. 320815, Advanced Grant Project COMP-DES-MAT, and, on the other hand, the Spanish Ministry of Science and Innovation under grant BIA2011-24258.

A. Proper Orthogonal Decomposition

The formal statement of the POD problem goes as follows: given the ensemble of snapshots $\{\boldsymbol{u}^1, \boldsymbol{u}^2, \dots \boldsymbol{u}^{n_{snp}}\}$, find a set of $n_u < n_{snp}$ orthogonal basis functions $\{\boldsymbol{\Phi}_1, \boldsymbol{\Phi}_2, \dots \boldsymbol{\Phi}_{n_u}\}$ ($\boldsymbol{\Phi}_i \in \mathcal{V}_u^{snp}$) such that the error defined as

$$e_u(n_u) := \sqrt{\sum_{k=1}^{n_{snp}} \|\boldsymbol{u}^k - \mathbf{P}^* \boldsymbol{u}^k\|^2_{L_2(\Omega)}} \tag{128}$$

is minimized. Here, $\mathbf{P}^* \boldsymbol{u}^k$ represents the projection of $\boldsymbol{u}^k$ onto the subspace spanned by the basis functions $\{\boldsymbol{\Phi}_i\}_{i=1}^{n_u}$, and $\|\cdot\|_{L_2(\Omega)}$ symbolizes the L_2 norm. We shall denote by $\boldsymbol{\Phi}_i$ ($i = 1, 2 \dots n_u$) the column vector containing the values of basis function $\boldsymbol{\Phi}_i$ at the nodes of the underlying finite element mesh. Likewise, the matrix formed by such vectors, $\boldsymbol{\Phi} = \begin{bmatrix} \boldsymbol{\Phi}_1 & \boldsymbol{\Phi}_2 & \cdots \end{bmatrix} \in \mathbb{R}^{n \cdot d \times n_u}$, will be hereafter called the *reduced basis matrix*.

The reduced basis matrix $\boldsymbol{\Phi}$ can be computed from the snapshot matrix $\boldsymbol{X}_u$ by means of the Singular Value Decomposition (SVD) as follows (see

Ref. [16] for more details). We first define the matrix[24]

$$\mathbf{M}_{IJ} := \int_{\Omega} N_I(\mathbf{x}) N_J(\mathbf{x})\, d\Omega \qquad I, J = 1, 2 \ldots n. \tag{129}$$

Let $\mathbf{M} = \bar{\mathbf{M}}^T \bar{\mathbf{M}}$ be the Cholesky decomposition of $\mathbf{M}$, and let $\bar{\boldsymbol{X}}_u$ denote the matrix defined as:

$$\bar{\boldsymbol{X}}_u := \bar{\mathbf{M}} \boldsymbol{X}_u. \tag{130}$$

Then, we compute the reduced SVD [37] of $\bar{\boldsymbol{X}}_u$, that is, the factorization

$$\bar{\boldsymbol{X}}_u = \bar{\boldsymbol{U}} \bar{\boldsymbol{S}} \bar{\boldsymbol{V}}^T, \tag{131}$$

where $\bar{\boldsymbol{V}} \in \mathbb{R}^{n_{snp} \times r}$ (r is the rank of $\bar{\boldsymbol{X}}_u$) and $\bar{\boldsymbol{U}} \in \mathbb{R}^{n \cdot d \times r}$ stand for the matrices of *right and left singular vectors*, respectively; and $\bar{\boldsymbol{S}} \in \mathbb{R}^{r \times r}$ is a diagonal matrix containing the *singular values* of $\boldsymbol{X}_u$. The $i-th$ column of the reduced basis matrix $\boldsymbol{\Phi}$ is finally related to the $i-th$ *left singular vector* of $\bar{\boldsymbol{X}}_u$ through expression

$$\boldsymbol{\Phi}_i = \bar{\mathbf{M}}^{-1} \bar{\boldsymbol{U}}_i, \quad i = 1, 2 \ldots n_u. \tag{132}$$

B. Elastic/Inelastic reduced basis matrix

This appendix is devoted to provide further details concerning the actual numerical implementation of the elastic/inelastic partitioned strategy, presented in Section 3.2.1, for the computation of the *reduced basis matrices* $\boldsymbol{\Phi}$ (displacement fluctuations). The steps to arrive at the desired matrix basis $\boldsymbol{\Phi}$ are summarized in the following.

1. Compute finite element stress solutions for representative, input macro-strain histories.
2. Store the displacement fluctuation solutions computed at each time step of these macro-strain trajectories in the displacement fluctuations *snapshot matrix* $\boldsymbol{X}_u \in \mathbb{R}^{n \cdot d \times n_{snp}}$:

$$\boldsymbol{X}_u = \begin{bmatrix} \boldsymbol{U}^1 & \boldsymbol{U}^2 & \cdots & \boldsymbol{U}^{n_{snp}} \end{bmatrix} \tag{133}$$

[24] Note that, except for the density factor, this matrix $\mathbf{M}$ is similar to the "mass matrix" appearing in finite element implementations of dynamical problems. For implementational purposes, one can simply use a lumped version of such a matrix.

3. Pick up from $\boldsymbol{X}_u$ a minimum of m_e ($m_e = 6$ for 3D problems, and $m_e = 3$ for plane strain) linearly independent columns corresponding to purely elastic solutions. Store these columns in a matrix $\boldsymbol{Z}_u^{el}$.
4. Perform the *reduced singular value decomposition* (SVD) of the matrix defined as
$$\bar{\boldsymbol{Z}}_u^{el} := \bar{\mathbf{M}}\boldsymbol{Z}_u^{el} \tag{134}$$
where $\bar{\mathbf{M}}$ is the matrix of the Cholesky factorization of $\mathbf{M}$ ($\mathbf{M} = \bar{\mathbf{M}}^T\bar{\mathbf{M}}$). A basis matrix for Range($\boldsymbol{Z}_u^{el}$) is finally obtained as
$$\boldsymbol{D}^{el} := \bar{\mathbf{M}}^{-1}\bar{\boldsymbol{D}}^{el} \tag{135}$$
$\bar{\boldsymbol{D}}^{el} \in \mathbb{R}^{n\cdot d\times m_e}$ being the matrix of left singular vectors arising from the SVD of $\bar{\boldsymbol{Z}}_u^{el}$. In principle, $\boldsymbol{D}^{el}$ may be used as the desired elastic basis matrix $\boldsymbol{\Phi}^{el}$. However, $\boldsymbol{D}^{el}$ does not enjoy any optimality property with respect to $\boldsymbol{X}_u$—it is only optimal with respect to the matrix $\boldsymbol{Z}_u^{el}$ of chosen elastic snapshots.
5. For consistency in the approximation, thus, it is preferable to derive $\boldsymbol{\Phi}^{el}$ from the the "elastic component" of $\boldsymbol{X}_u$ —the orthogonal projection of $\boldsymbol{X}_u$ onto Range($\boldsymbol{D}^{el}$)—; the expression for this projection reads:
$$\boldsymbol{X}_u^{el} = \boldsymbol{D}^{el}(\boldsymbol{D}^{el^T}\mathbf{M}\boldsymbol{X}_u) \tag{136}$$
The elastic basis matrix can be finally calculated from $\boldsymbol{X}_u^{el}$ as:
$$\boldsymbol{\Phi}^{el} := \bar{\mathbf{M}}^{-1}\bar{\boldsymbol{\Phi}}^{el}. \tag{137}$$
where $\bar{\boldsymbol{\Phi}}^{el}$ is the matrix of left singular vectors emerging from the reduced SVD of $\bar{\boldsymbol{X}}_u^{el} := \bar{\mathbf{M}}\boldsymbol{X}_u^{el}$; i.e $\bar{\boldsymbol{X}}_u^{el} = \bar{\boldsymbol{\Phi}}^{el}\bar{\boldsymbol{S}}_u^{el}\bar{\boldsymbol{V}}_u^{el^T}$.
6. Calculate the "inelastic component" $\boldsymbol{X}_u^{in}$ of the snapshot matrix $\boldsymbol{X}_u$ as:
$$\boldsymbol{X}_u^{in} = \boldsymbol{X}_u - \boldsymbol{X}_u^{el}; \tag{138}$$
that is, $\boldsymbol{X}_u^{in}$ is the orthogonal projection of $\boldsymbol{X}_u$ onto the orthogonal complement, in Range($\boldsymbol{X}_u$), of Range($\boldsymbol{\Phi}^{el}$).
7. It is now on this *inelastic* snapshot matrix $\boldsymbol{X}_u^{in}$ that we apply the POD in order to identify and unveil the *essential* or most "energetic" inelastic fluctuation modes. This is done by first carrying out the reduced SVD of $\bar{\boldsymbol{X}}_u^{in} = \bar{\mathbf{M}}\boldsymbol{X}_u^{in}$:
$$\bar{\boldsymbol{X}}_u^{in} = \bar{\boldsymbol{D}}^{in}\bar{\boldsymbol{S}}_u^{in}\bar{\boldsymbol{V}}_u^{in^T}. \tag{139}$$

The $i-th$ POD basis vector of $\boldsymbol{X}_u^{in}$ is then given by:

$$\boldsymbol{\Phi}_i^{in} = \bar{\mathbf{M}}^{-1}\bar{\boldsymbol{D}}_i^{in}, \quad i = 1, 2 \ldots n_u - m_e. \tag{140}$$

8. The desired basis matrix $\boldsymbol{\Phi} \in \mathbb{R}^{n\cdot d \times n_u}$ adopts finally the form:

$$\boldsymbol{\Phi} = [\boldsymbol{\Phi}^{el}\ \boldsymbol{\Phi}^{in}] = [\overbrace{\boldsymbol{\Phi}_1^{el}\ \boldsymbol{\Phi}_2^{el}\ \cdots\ \boldsymbol{\Phi}_{m_e}^{el}}^{\text{Elastic modes}}\ \overbrace{\boldsymbol{\Phi}_1^{in}\ \boldsymbol{\Phi}_2^{in}\ \cdots\ \boldsymbol{\Phi}_{n_u-m_e}^{in}}^{\text{Essential inelastic modes}}] \tag{141}$$

C. Block matrix pseudoinverse of the expanded basis matrix

The inverse of a 2x2 *symmetric* block matrix is given by the following expression (see, for instance, Ref. [11]):

$$\mathbf{M}^{-1} = \begin{bmatrix} \mathbf{A} & \mathbf{B} \\ \mathbf{B^T} & \mathbf{C} \end{bmatrix}^{-1} = \begin{bmatrix} \mathbf{A^{-1}} + \mathbf{A^{-1}BS^{-1}B^TA^{-1}} & \mathbf{-A^{-1}BS^{-1}} \\ \mathbf{-S^{-1}B^TA^{-1}} & \mathbf{S^{-1}} \end{bmatrix} \tag{142}$$

where

$$\mathbf{S} = \mathbf{C} - \mathbf{B^TA^{-1}B} \tag{143}$$

is the so-called Schur complement of $\mathbf{A}$ in $\mathbf{M}$. This formula can be used to derive closed-form expressions for the modal coefficients $\boldsymbol{c}^{ad}$ and $\boldsymbol{c}^{in}$ (see Section 6.2). The departure point is equation Eq.(67):

$$\begin{bmatrix} \boldsymbol{c}^{ad} \\ \boldsymbol{c}^{in} \end{bmatrix} = ([\hat{\boldsymbol{\Psi}}\ \hat{\mathbb{B}}^*])^{\dagger}\hat{\boldsymbol{\Sigma}} = \begin{bmatrix} \hat{\boldsymbol{\Psi}}^T\hat{\boldsymbol{\Psi}} & \hat{\boldsymbol{\Psi}}^T\hat{\mathbb{B}}^* \\ \hat{\mathbb{B}}^{*T}\hat{\boldsymbol{\Psi}} & \hat{\mathbb{B}}^{*T}\hat{\mathbb{B}}^* \end{bmatrix}^{-1} \begin{bmatrix} \hat{\boldsymbol{\Psi}}^T \\ \hat{\mathbb{B}}^{*T} \end{bmatrix} \hat{\boldsymbol{\Sigma}}, \tag{144}$$

where $([\hat{\boldsymbol{\Psi}}\ \hat{\mathbb{B}}^*])^{\dagger}$ designates the pseudo-inverse of the *gappy* expanded basis matrix. By setting:

$$\mathbf{A} = \hat{\boldsymbol{\Psi}}^{\mathbf{T}}\hat{\boldsymbol{\Psi}}, \quad \mathbf{B} = \hat{\boldsymbol{\Psi}}^{\mathbf{T}}\hat{\mathbb{B}}^*, \qquad \mathbf{C} = \hat{\mathbb{B}}^{*\mathbf{T}}\hat{\mathbb{B}}^*, \tag{145}$$

and by inserting Eq.(142) into Eq.(144), one obtains upon expansion:

$$\boldsymbol{c}^{in} = \mathbf{S^{-1}}\left(\mathbf{-B^TA^{-1}}\hat{\boldsymbol{\Psi}}^{\mathbf{T}} + \hat{\mathbb{B}}^{*\mathbf{T}}\right)\hat{\boldsymbol{\Sigma}} \tag{146}$$

and

$$\begin{aligned} \boldsymbol{c}^{ad} &= \left(\left(\mathbf{A^{-1}} + \mathbf{A^{-1}BS^{-1}B^TA^{-1}}\right)\hat{\boldsymbol{\Psi}}^T - \mathbf{A^{-1}BS^{-1}}\hat{\mathbb{B}}^{*\mathbf{T}}\right)\hat{\boldsymbol{\Sigma}} \\ &= \mathbf{A^{-1}}\hat{\boldsymbol{\Psi}}^{\mathbf{T}}\hat{\boldsymbol{\Sigma}} + \mathbf{A^{-1}B}\overbrace{\mathbf{S^{-1}}\left(\mathbf{-B^TA^{-1}}\hat{\boldsymbol{\Psi}}^{\mathbf{T}} + \hat{\mathbb{B}}^{*\mathbf{T}}\right)\hat{\boldsymbol{\Sigma}}}^{\boldsymbol{c}^{\mathbf{in}}} \\ &= \mathbf{A^{-1}}\hat{\boldsymbol{\Psi}}^{\mathbf{T}}\hat{\boldsymbol{\Sigma}} + \mathbf{A^{-1}B}\boldsymbol{c}^{\mathbf{in}}. \end{aligned} \tag{147}$$

By substituting back Eq.(145) into the above equation, and taking into account that:

$$\hat{\boldsymbol{\Psi}}^{\dagger} = (\hat{\boldsymbol{\Psi}}^{T}\hat{\boldsymbol{\Psi}})^{-1}\hat{\boldsymbol{\Psi}}^{T} \tag{148}$$

one finally gets:

$$\boldsymbol{c}^{ad} = \hat{\boldsymbol{\Psi}}^{\dagger}(\hat{\boldsymbol{\Sigma}} - \hat{\mathbb{B}}^{*}\boldsymbol{c}^{in}), \tag{149}$$

$$\boldsymbol{c}^{in} = \mathbf{S}^{-\mathbf{1}}\hat{\mathbb{B}}^{*\mathbf{T}}\left(\boldsymbol{I} - \hat{\boldsymbol{\Psi}}\hat{\boldsymbol{\Psi}}^{\dagger}\right)\hat{\boldsymbol{\Sigma}}, \tag{150}$$

where

$$\mathbf{S} = \hat{\mathbb{B}}^{*\mathbf{T}}(\boldsymbol{I} - \hat{\boldsymbol{\Psi}}\hat{\boldsymbol{\Psi}}^{\dagger})\hat{\mathbb{B}}^{*}. \tag{151}$$

References

[1] Abdulle, A., Bai, Y., 2012. Adaptive reduced basis finite element heterogeneous multiscale method.

[2] Abdulle, A., Bai, Y., 2012. Reduced basis finite element heterogeneous multiscale method for high-order discretizations of elliptic homogenization problems. Journal of Computational Physics.

[3] An, S., Kim, T., James, D., 2009. Optimizing cubature for efficient integration of subspace deformations. ACM transactions on graphics 27 (5), 165.

[4] Ashby, M., 1992. Physical modelling of materials problems. Materials Science and Technology 8 (2), 102–111.

[5] Astrid, P., 2004. Reduction of process simulation models: a proper orthogonal decomposition approach. Technische Universiteit Eindhoven.

[6] Astrid, P., Weiland, S., Willcox, K., Backx, T., 2008. Missing point estimation in models described by proper orthogonal decomposition. Automatic Control, IEEE Transactions on 53 (10), 2237–2251.

[7] Barrault, M., Maday, Y., Nguyen, N., Patera, A., 2004. An empirical interpolation'method: application to efficient reduced-basis discretization of partial differential equations. Comptes Rendus Mathematique 339 (9), 667–672.

[8] Bishop, C., en ligne), S. S., 2006. Pattern recognition and machine learning. Vol. 4. springer New York.

[9] Bohm, H., 1998. A short introduction to basic aspects of continuum micromechanics. CDL-FMD Report 3.

[10] Boyaval, S., 2007. Reduced-basis approach for homogenization beyond the periodic setting. Arxiv preprint math/0702674.

[11] Boyd, S., Vandenberghe, L., 2004. Convex optimization. Cambridge Univ Pr.

[12] Bui-Thanh, T., 2007. Model-constrained optimization methods for reduction of parameterized large-scale systems. Ph.D. thesis, Citeseer.

[13] Bui-Thanh, T., Willcox, K., Ghattas, O., 2008. Model reduction for large-scale systems with high-dimensional parametric input space. SIAM Journal on Scientific Computing 30 (6), 3270–3288.

[14] Carlberg, K., Bou-Mosleh, C., Farhat, C., 2011. Efficient non-linear model reduction via a least-squares petrov–galerkin projection and compressive tensor approximations. International Journal for Numerical Methods in Engineering 86 (2), 155–181.

[15] Carlberg, K., Farhat, C., 2008. A Compact Proper Orthogonal Decomposition Basis for Optimization-Oriented Reduced-Order Models. AIAA Paper 5964, 10–12.

[16] Carlberg, K., Farhat, C., 2011. A low-cost, goal-oriented compact proper orthogonal decompositionbasis for model reduction of static systems. International Journal for Numerical Methods in Engineering 86 (3), 381–402.

[17] Chaturantabut, S., Sorensen, D., 2009. Application of POD and DEIM on Dimension Reduction of Nonlinear Miscible Viscous Fingering in Porous Media.

[18] Chaturantabut, S., Sorensen, D., 2010. Discrete empirical interpolation for nonlinear model reduction. In: Decision and Control, 2009 held jointly with the 2009 28th Chinese Control Conference. CDC/CCC 2009. Proceedings of the 48th IEEE Conference on. IEEE, pp. 4316–4321.

[19] Cook, R., 1995. Finite element modeling for stress analysis. John Wiley and Sons., New York.

[20] Couégnat, G., 2008. Approche multiéchelle du comportement mécanique de matériaux composites à renfort tissé. Ph.D. thesis, Université Sciences et Technologies-Bordeaux I.

[21] Cremonesi, M., Néron, D., Guidault, P.-A., Ladevèze, P., 2013. A pgd-based homogenization technique for the resolution of nonlinear multi-scale problems. Computer Methods in Applied Mechanics and Engineering 267, 275–292.

[22] de Souza Neto, E., Feijóo, R., 2006. Variational foundations of multi-scale constitutive models of solid: small and large strain kinematical formulation. LNCC Research & Development Report 16.

[23] DeVore, R., Iserles, A., Suli, E., 2001. Foundations of computational mathematics. Cambridge Univ Pr.

[24] Drago, A., Pindera, M., 2007. Micro-macromechanical analysis of heterogeneous materials: Macroscopically homogeneous vs periodic microstructures. Composites science and technology 67 (6), 1243–1263.

[25] Dvorak, G., Wafa, A., Bahei-El-Din, Y., 1994. Implementation of the transformation field analysis for inelastic composite materials. Computational Mechanics 14 (3), 201–228.

[26] Efendiev, Y., Galvis, J., Gildin, E., 2012. Local-global multiscale model reduction for flows in high-contrast heterogeneous media. Journal of Computational Physics.

[27] Efendiev, Y., Galvis, J., Thomines, F., 2012. A systematic coarse-scale model reduction technique for parameter-dependent flows in highly heterogeneous media and its applications.

[28] Everson, R., Sirovich, L., 1995. Karhunen–Loeve procedure for gappy data. Journal of the Optical Society of America A 12 (8), 1657–1664.

[29] Feyel, F., Chaboche, J., 2000. Fe-2 multiscale approach for modelling the elastoviscoplastic behaviour of long fibre sic/ti composite materials. Computer methods in applied mechanics and engineering 183 (3), 309–330.

[30] Fish, J., Shek, K., Pandheeradi, M., Shephard, M., 1997. Computational plasticity for composite structures based on mathematical homogenization: Theory and practice. Computer Methods in Applied Mechanics and Engineering 148 (1-2), 53–73.

[31] Galbally, D., Fidkowski, K., Willcox, K., Ghattas, O., 2010. Non-linear model reduction for uncertainty quantification in large-scale inverse problems. International Journal for Numerical Methods in Engineering 81 (12), 1581–1608.

[32] Geers, M., Kouznetsova, V., Brekelmans, W., 2010. Multi-scale computational homogenization: Trends and challenges. Journal of computational and applied mathematics 234 (7), 2175–2182.

[33] Grepl, M., Maday, Y., Nguyen, N., Patera, A., 2007. Efficient reduced-basis treatment of nonaffine and nonlinear partial differential equations. Mathematical Modelling and Numerical Analysis 41 (3), 575–605.

[34] Gross, D., Seelig, T., 2011. Fracture mechanics: with an introduction to micromechanics. Springer.

[35] Hernández, J. A., Oliver, J., Huespe, A., Caicedo, M., 2012. High-performance model reduction procedures in multiscale simulations. Monograph CIMNE (ISBN:978-84-9939640-6-1).
URL http://centrovnet.cimne.upc.edu/cvdata/cntr7/dtos/img/mdia/Download

[36] Hoffman, J. D., 2001. Numerical Methods for Engineers and Scientists. Marcel Dekker.

[37] Hogben, L., 2006. Handbook of linear algebra. Chapman & Hall/CRC.

[38] Hu, Y., Hwang, J., Perry, S., 2002. Handbook of neural network signal processing. The Journal of the Acoustical Society of America 111, 2525.

[39] Kim, T., James, D., 2009. Skipping steps in deformable simulation with online model reduction. In: ACM SIGGRAPH Asia 2009 papers. ACM, pp. 1–9.

[40] Kouznetsova, V., 2002. Computational homogenization for the multi-scale analysis of multi-phase materials.

[41] Krysl, P., Lall, S., Marsden, J., 2001. Dimensional model reduction in non-linear finite element dynamics of solids and structures. International Journal for Numerical Methods in Engineering 51 (4), 479–504.

[42] Kunisch, K., Volkwein, S., 2010. Optimal snapshot location for computing pod basis functions. ESAIM: Mathematical Modelling and Numerical Analysis 44 (3), 509.

[43] Li, Z., Wen, B., Zabaras, N., 2010. Computing mechanical response variability of polycrystalline microstructures through dimensionality reduction techniques. Computational Materials Science 49 (3), 568–581.

[44] Lovasz, L., Pelikan, J., Vesztergombi, K., 2003. Discrete Mathematics: Elementary and Beyond. Springer.

[45] Lubliner, J., 1990. Plasticity Theory. McMillan, New York.

[46] Maday, Y., Nguyen, N., Patera, A., Pau, G., 2007. A general, multipurpose interpolation procedure: the magic points.

[47] Maday, Y., Patera, A., Turinici, G., 2002. Reliable real-time solution of parametrized partial differential equations: Reduced-basis output bound methods.

[48] Michel, J., Moulinec, H., Suquet, P., 1999. Effective properties of composite materials with periodic microstructure: a computational approach. Computer methods in applied mechanics and engineering 172 (1-4), 109–143.

[49] Michel, J., Suquet, P., 2003. Nonuniform transformation field analysis. International journal of solids and structures 40 (25), 6937–6955.

[50] Michel, J., Suquet, P., 2004. Computational analysis of nonlinear composite structures using the nonuniform transformation field analysis. Computer methods in applied mechanics and engineering 193 (48-51), 5477–5502.

[51] Monteiro, E., Yvonnet, J., He, Q., 2008. Computational homogenization for nonlinear conduction in heterogeneous materials using model reduction. Computational Materials Science 42 (4), 704–712.

[52] Montgomery, D., Runger, G., 2010. Applied statistics and probability for engineers. Wiley.

[53] Nguyen, N., 2008. A multiscale reduced-basis method for parametrized elliptic partial differential equations with multiple scales. Journal of Computational Physics 227 (23), 9807–9822.

[54] Nguyen, N., Patera, A., Peraire, J., 2008. A best points interpolation method for efficient approximation of parametrized functions. Int. J. Numer. Meth. Engng 73, 521–543.

[55] Quarteroni, A., Sacco, R., Saleri, F., 2000. Numerical Mathematics. Springer, New York.

[56] Roussette, S., Michel, J., Suquet, P., 2009. Nonuniform transformation field analysis of elastic-viscoplastic composites. Composites Science and Technology 69 (1), 22–27.

[57] Rozza, G., 2009. Reduced basis methods for stokes equations in domains with non-affine parameter dependence. Computing and Visualization in Science 12 (1), 23–35.

[58] Ryckelynck, D., 2005. A priori hyperreduction method: an adaptive approach. Journal of computational physics 202 (1), 346–366.

[59] Ryckelynck, D., 2009. Hyper-reduction of mechanical models involving internal variables. International Journal for Numerical Methods in Engineering 77 (1), 75–89.

[60] Salomon, D., 2004. Data compression: the complete reference. Springer-Verlag New York Incorporated.

[61] Simo, J. C., Hughes, T. J. R., 1998. Computational inelasticity. Springer, New York.

[62] Yvonnet, J., He, Q., 2007. The reduced model multiscale method (R3M) for the non-linear homogenization of hyperelastic media at finite strains. Journal of Computational Physics 223 (1), 341–368.

B.2 Paper #2

Title: Continuum approach to computational multiscale modeling of propagting fracture.
Authors:

- **J. Oliver**: Professor of Continuum Mechanics and Structural analysis at the Escola Tecnica Superior d'Enginyers de Camins, Canals i Ports (Civil Engineering School) of the Universitat Politècnica de Catalunya (Technical University of Catalonia BarcelonaTech). Senior researcher at the International Center for Numerical Methods in Engineering (CIMNE).
- **M. Caicedo**: PhD Candidate in Structural Analysis in UPC BarcelonaTech and International Center for Numerical Methods in Engineering (CIMNE).
- **E. Roubin**: Maître de conférence at the 3SR (Sols, Solides, Structures et Risques) and the IUT DGGC in Grenoble.
- **A. E. Huespe**: Professor of Mechanics at the Faculty of Chemical Engineering, Dept. of Materials, National University of Litoral, Santa Fe, Argentina. Independent researcher of Conicet at CIMEC (Centro de Investigaciones en Mecánica Computacional), National University of Litoral (UNL).
- **J. A. Hernández**: Assistant Professor of Structural Engineering and Strength of Materials at the School of Industrial and Aeronautic Engineering of Terrassa, of the Technical University of Catalonia. Senior researcher at the International Center for Numerical Methods in Engineering (CIMNE).

Journal of Computer Methods in Applied Mechanics and Engineering
Editors: Thomas J.R. Hughes, J. Tinsley Oden, Manolis Papadrakakis
ISSN: 0045-7825
Elsevier Editors
http://dx.doi.org/10.1016/j.cma.2015.05.012
Link to Publisher

ATTENTION ¡
Pages 144 to 188 of the thesis, containing the text mentioned above, are available at the editor's web
https://www.sciencedirect.com/science/article/pii/S0045782515001851

B.3 Paper #3

Title: Reduced Order Modeling strategies for Computational Multiscale Fracture.
Authors:

- **J. Oliver**: Professor of Continuum Mechanics and Structural analysis at the Escola Tecnica Superior d'Enginyers de Camins, Canals i Ports (Civil Engineering School) of the Universitat Politècnica de Catalunya (Technical University of Catalonia BarcelonaTech). Senior researcher at the International Center for Numerical Methods in Engineering (CIMNE).
- **M. Caicedo**: PhD Candidate in Structural Analysis in UPC BarcelonaTech and International Center for Numerical Methods in Engineering (CIMNE).
- **A. E. Huespe**: Professor of Mechanics at the Faculty of Chemical Engineering, Dept. of Materials, National University of Litoral, Santa Fe, Argentina. Independent researcher of Conicet at CIMEC (Centro de Investigaciones en Mecánica Computacional), National University of Litoral (UNL).
- **J. A. Hernández**: Assistant Professor of Structural Engineering and Strength of Materials at the School of Industrial and Aeronautic Engineering of Terrassa, of the Technical University of Catalonia. Senior researcher at the International Center for Numerical Methods in Engineering (CIMNE).
- **E. Roubin**: Maître de conférence at the 3SR (Sols, Solides, Structures et Risques) and the IUT DGGC in Grenoble.

Journal of Computer Methods in Applied Mechanics and Engineering
Editors: Thomas J.R. Hughes, J. Tinsley Oden, Manolis Papadrakakis
ISSN: 0045-7825
Elsevier Editors

ATTENTION ¡
Pages 190 to 226 of the thesis, containing the text mentioned above, are available at the editor's web
https://www.sciencedirect.com/science/article/pii/S0045782516303322

B.4 Paper #4

Title: Dimensional hyper-reduction of nonlinear finite element models via empirical cubature.
Authors:

- **J. A. Hernández**: Assistant Professor of Structural Engineering and Strength of Materials at the School of Industrial and Aeronautic Engineering of Terrassa, of the Technical University of Catalonia. Senior researcher at the International Center for Numerical Methods in Engineering (CIMNE).
- **M. Caicedo**: PhD Candidate in Structural Analysis in UPC BarcelonaTech and International Center for Numerical Methods in Engineering (CIMNE).
- **A. Ferrer**: PhD Candidate in Structural Analysis in UPC BarcelonaTech and International Center for Numerical Methods in Engineering (CIMNE).

Journal of Computer Methods in Applied Mechanics and Engineering
Editors: Thomas J.R. Hughes, J. Tinsley Oden, Manolis Papadrakakis
ISSN: 0045-7825
Elsevier Editors

ATTENTION ¡
Pages 228 to 264 of the thesis, containing the text mentioned above, are available at the editor's web
https://www.sciencedirect.com/science/article/pii/S004578251631355X

B.5 Paper #5

Title: Continuum Approach to Computational Multi-Scale Modeling of Fracture.
Authors:

- **J. Oliver**: Professor of Continuum Mechanics and Structural analysis at the Escola Tecnica Superior d'Enginyers de Camins, Canals i Ports (Civil Engineering School) of the Universitat Politècnica de Catalunya (Technical University of Catalonia BarcelonaTech). Senior researcher at the International Center for Numerical Methods in Engineering (CIMNE).
- **M. Caicedo**: PhD Candidate in Structural Analysis in UPC BarcelonaTech and International Center for Numerical Methods in Engineering (CIMNE).
- **E. Roubin**: Maître de conférence at the 3SR (Sols, Solides, Structures et Risques) and the IUT DGGC in Grenoble.
- **A. E. Huespe**: Professor of Mechanics at the Faculty of Chemical Engineering, Dept. of Materials, National University of Litoral, Santa Fe, Argentina. Independent researcher of Conicet at CIMEC (Centro de Investigaciones en Mecánica Computacional), National University of Litoral (UNL).

Key Engineering Materials Vol. 627
Advances in Fracture and Damage Mechanics XIII
Editors: J. Alfaiate and M.H. Aliabadi
ISSN: 1662-9795
Trans Tech Publications
DOI: 10.4028/www.scientific.net/KEM.627.349
Link to Publisher

Continuum approach to computational multi-scale modeling of fracture

J. Oliver[1,a], M. Caicedo[1,b], E. Roubin[1,c] and A.E. Huespe[1,2,d]
[1]Technical University of Catalonia (UPC)/International Center for Numerical Methods in Engineering (CIMNE), Campus Nord UPC, Edifici C-1, 08034 Barcelona, Spain
[2]CIMEC-Universidad del Litoral (UNL), Santa Fe, Argentina
[a]xavier.oliver@upc.edu, [b]mcaicedo@cimne.upc.edu, [c]eroubin@cimne.upc.edu, [d]ahuespe@intec.unl.edu.ar

Keywords: Fracture, computational multi-scale modeling, strain injection, crack path field, Continuum Strong Discontinuity Approach

Abstract. This paper presents a FE^2 multi-scale framework for numerical modeling of the structural failure of heterogeneous quasi-brittle materials. The model is assessed by application to cementitious materials. Using the Continuum Strong Discontinuity Approach (CSD), innovative numerical tools, such as strain injection and crack path field techniques, provide a robust, and mesh-size, mesh-bias and RVE-size objective, procedure to model crack onset and propagation at the macro-scale.

Introduction

In view of the significant impact of low-scale material morphology in regards to macroscopic responses, numerical strategies has been wildly developed in order to both analyze and model the complex relationship between scales. Among the different issues that yet remain to be explored, this paper focuses on softening behavior modeling, i.e. non-smooth behaviors, and complex small scale failure mechanisms. These problematic find their applications, inter alia, in multi-scale modeling of the quasi-brittle fracture of cementitious materials.

The theoretical framework used in this work is based on the so-called (FE^2) methods. A coupled FEM is used in both scales. Homogenized quantities at the lower scale, represented by a so-called failure-cell, are therefore transferred, in a one-way fashion, to material points (Gauss points) of the macroscopic structure. Such a direct homogenization procedure eventually links this failure-cell to the notion of statistical Representative Volume Element (hereafter referred to as RVE). However, in case of softening behavior, the non-smooth kinematical description of the thin scale raises the problematic of existence of an RVE and the lack of objectivity of the response with respect to its size. Solutions have been provided, for example, in the context of regularized non-local damage models [1], or in the context of homogenized discrete models [4].

In contrast, this work is an attempt to address this issue in the context of local and continuum models and the Continuum Strong Discontinuity Approach (hereafter referred to as CSDA) [2]. The different key ingredients of the theoretical and numerical framework, which unlock the different issues and flaws mentioned above are: a) at the macroscopic level, the non-smooth kinematics representation is captured using strain-localization and FE with embedded regularized strong discontinuities, b) at the mesoscopic level, the failure-cell fracture behavior is fitted with cohesive-bands with predefined position, even though there is no “a priori” limitation on the considered failure mechanisms, c) from the standard homogenization at the RVE the usual set of macroscopic quantities, in terms of a strain/stress relationship, emerges, together with, and specifically for this approach, *a physically meaningful internal length linked with the size of the RVE and the activated microscopic fracture mechanism*. This internal length is exported to the upper scale and used as the macroscopic strain localization bandwidth, this providing both an objective regularization parameter ---leading to a macroscopic response completely insensitive to RVE size--- and a consistent up-scaling scheme of the failure material properties ---such as the fracture energy.

Model description

Mesoscopic scale description and homogenization procedure. The dissipative processes that occur at the mesoscale are modeled using cohesive bands (that are much thinner than the cell dimensions) scattered within the matrix, the aggregates and the interfaces between them. In this way, they can model a set of predefined crack patterns including several mechanisms such as percolation of the crack through the matrix (necessary for softening behavior), mortar/aggregate decohesion and rupture within the aggregates. Eventually, as the damage stage increases, a dominant mechanism naturally prevails, thus representing the final pattern of the micro-crack. This mechanism is now referred to as *mesoscopic failure mechanism*.

The meso-structure constitutive behavior is considered elastic outside these cohesive bands, whereas the material exhibits strain softening inside the bands (using a classical isotropic damage model), thus, eventually leading to strain localization. From the CSDA [2] it is well known that this kind of narrow bands represents, in a consistent way, a strong discontinuity in which the regularized parameter is given by its bandwidth, ensuring the equivalence of the fracture energy in both scales.

The approach is based on a first order homogenization of strains under a small strain framework in both scales, ensuring energetic balance through the Mandel-Hill principle). Though the mathematical framework is not developed here, attention is focused on the outcome of this homogenization procedure within the overall framework of the strong discontinuity kinematics. The macroscopic constitutive response is point-wise equivalent to an inelastic law (in an incremental fashion) as a function of the homogenized elastic tangent tensor, $\boldsymbol{C^{hom}}$, and the incremental homogenized inelastic strain rate $\dot{\boldsymbol{\varepsilon}}^{(i)}$ i.e.

$$\dot{\boldsymbol{\sigma}} = \boldsymbol{C^{hom}} : (\dot{\boldsymbol{\varepsilon}}(\boldsymbol{x}) - \dot{\boldsymbol{\varepsilon}}^{(i)}). \tag{1}$$

The main interest of this result lies in the evolution of the latter inelastic strain tensor, as it can be expressed in terms of failure mechanism variables at the meso-scale:

$$\dot{\boldsymbol{\varepsilon}}^{(i)} = \frac{1}{l_\mu} \overline{(\boldsymbol{n} \otimes \dot{\boldsymbol{\beta}})^{\boldsymbol{s}}}_{S_k}, \tag{2}$$

where the barked notation represents the average value the symmetrical tensor product between the strong discontinuity normal, $\boldsymbol{n}$, and the rate of the displacement jump, $\dot{\boldsymbol{\beta}}$, of each cohesive band, belonging to the manifold of the mesoscopic failure mechanism S_k, i.e. the mesoscopic crack. In addition, and defined as the ration between the measure (volume or area) of the RVE and the measure (surface or length) of S_k, l_μ stands the aforementioned *material internal length*.

Numerical aspects at the meso-cell. The cohesive bands are modeled by quadrilateral elements of very small thickness. Even though more general phenomenological models can be set, herein a constitutive *only tension constitutive model* [2] governs the softening behavior in order, first, to represent the typical tensile failure mechanisms of cementitious materials and second, to exhibit the structural impact of the heterogeneities that can lead to complex macroscopic responses.

The external force for the equilibrium equation is the macroscopic strain tensor since, consistently with the considered homogenization theory, no external force comes into play. Furthermore, and following the usual minimal boundary restrictions at the RVE, Dirichlet boundary conditions, avoiding rigid body motions, are applied.

Finally, it is worth noticing that the mesoscopic failure mechanism propagates naturally through the strain localization that takes place within the cohesive bands. At each time step of the problem, the in-loading cohesive bands define the active failure mechanism and therefore they define the set of elements used to upscale non-linear features such as the characteristic length of Eq. (2).

Material failure propagation at the structural level. The *strain injection technique* [5] is used in order to provide a robust and efficient model that can capture failure propagation even with high

strain localization states. Two specific strain-rate modes (*weak and strong discontinuity modes*) are injected within two evolving sets of elements, following criteria based on up-scaled non-linear features, such as bifurcation analysis of the homogenized localization tensor, or based on the dissipated energy. In addition, the crucial matter of positioning strong discontinuities is tackled by a parallel technique termed *crack path field* [5]. This technique uses a directional derivative of a scalar field, based on the internal strain-like variables, whose zero level set defines the crack path.

Based on physical considerations of the crack characteristics ---both in terms of path and kinematics---, the coupling of these methods leads to a numerical framework capable of drastically reducing the classical drawbacks of propagating fracture approaches, such as stress locking, hourglass modes, mesh bias, etc. More details can be found, in a one-scale framework in [5].

Numerical results: application to classical concrete-like simulations

Mesoscopic material properties. The description of the meso-cell is taken to be the same for both tests. The FE discretization is depicted in Fig. 1a where the morphology and the considered pattern of cohesive bands can be seen (from dark to light gray: elastic aggregates, elastic mortar matrix and cohesive bands). The material elastic properties are taken to be the same for elastic and cohesive band elements.

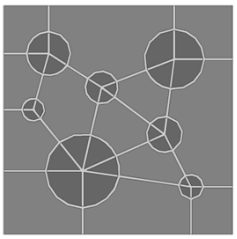

	Mortar	**Aggregates**	
Young Modulus	21 220	100 000	[MPa]
Poisson ratio	0.15	0.15	[-]
Yield stress	3	-	[MPa]
Fracture energy	20	-	[N/m]

Fig. 1. Mesoscopic FE discretization and considered material properties

Nooru-Mohamed test. This test has been simulated following the detail in [3] (load-path 1) where prior to a tension loading, the specimen is subjected to shear load up to 5kN and 10kN. First, a typical mesoscopic failure mechanism is depicted in Fig. 2a, where the activated cohesive bands are clearly shown. Figs. 2b and 2c represent the injection state (light gray for weak and dark gray for strong injection) for two different time steps, thus showing its evolving aspect. By enhancing the kinematics only in a narrow zone around the strain localization, the displacement discontinuity can be well capture and yet, instable modes (hourglass) are avoided. It can be checked that the injection pattern follows the crack path field shown Fig. 2d.

a) b) c) d)

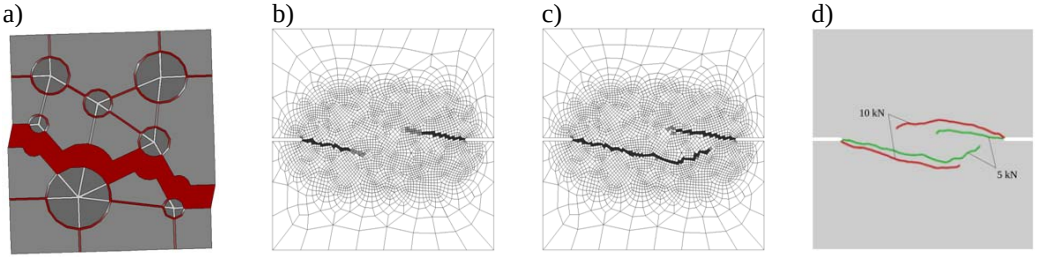

Fig. 2a: a) Damage in cell, b) Strain-injection pattern (5kN), c) Strain-injection pattern (10kN) and d) Crack path fields for 5kN and 10kN.

The latter figure also represents the crack path field in the case of a shear loading of 10kN. Matching the results of [3], a larger spacing between the two cracks along with a larger curvature can be noticed.

Four point bending test. This example shows the impact of the meso-cell failure mechanisms onto the macroscopic response. The meso-cell (Fig. 1) has been slightly modified in order to perform four different tests whose results are depicted in Figs. 3a and 3b, in terms of the crack path field and the macroscopic responses, respectively. The first two meso-cells (top left and top right in Fig. 3a) allow and preclude, respectively, intra-aggregate failure. Therefore, they could correspond to typical failure mechanisms for hard and light-aggregate concrete. The other two tests (bottom right and bottom left) have the cohesive bands *locked for failure* excepting one horizontal and one vertical path, respectively, therefore restricting the set of possible mesoscopic failure mechanisms to a predetermined one. In Fig. 3a, the link of the mesoscopic failure mechanisms and the obtained macroscopic crack path can clearly be observed. Furthermore, in Fig. 3b, the translation of the considered failure-mechanisms into structural responses can be observed.

a) b)

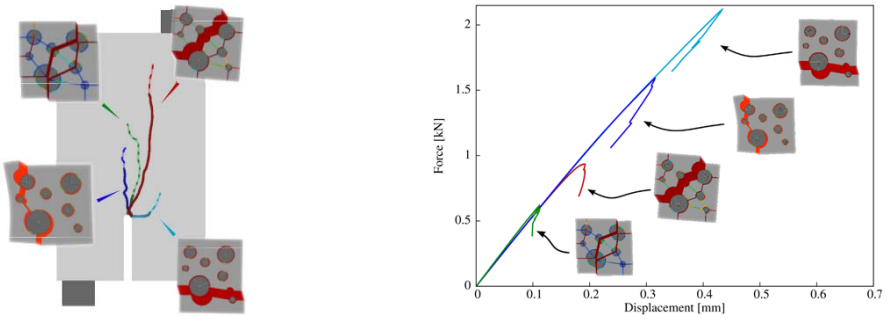

Fig. 3. Four-point bending test: a) crack path fields for different activated mesoscopic failure mechanisms (crack patterns), b) macroscopic (structural) responses

Conclusions

The result of this work is a multi-scale framework that preserves the correct dissipation and objectivity with respect to the size and bias of the FE mesh. Furthermore, the two presented simulations show the, physically meaningful, effects of the activated meso-scale failure mechanisms on the structural response. The proposed framework allows extending the classical FE^2 computational homogenization procedures from smooth problems to fracture mechanics analyzes.

Acknowledgments

The research leading these results has received funding from the European Research Council under the European Union's Seventh Framework Program (FP/2007-2013) / ERC Grant Agreement n. 320815, Advanced Grant Project COMP-DES-MAT. The third author would also like to thanks the École Normale Supérieur de Cachan (FR) for their financial support.

References

[1] V.P. Nguyen, O. Lloberas-Valls, M. Stroeven and L. J. Sluys, in: *Computer Methods in Applied Mechanics and Engineering*, (2010)
[2] J. Oliver, A.E. Huespe, M.D.G Pulido and E. Chaves, in: *Engineering Fracture Mechanics*, 2002
[3] M.B Nooru-Mohamed, E. Schlangen and J.G.M. Van Mier, in: *Cement Based Materials*, 1993
[4] P.J. Sánchez, P.J. Blanco, A.E. Huespe, and R.A. Feijóo in: *Comp. Meth. In Appl. Mech. And Eng.*, 2013.
[5] J. Oliver, A. Huespe and I.F. Dias, in: *Comp. Meth. In Appl. Mech. And Eng.*, 2014

B.6 Paper #6

Title: Model Order Reduction in computational multiscale fracture mechanics.
Authors:

- **M. Caicedo**: PhD Candidate in Structural Analysis in UPC BarcelonaTech and International Center for Numerical Methods in Engineering (CIMNE).
- **J. Oliver**: Professor of Continuum Mechanics and Structural analysis at the Escola Tecnica Superior d'Enginyers de Camins, Canals i Ports (Civil Engineering School) of the Universitat Politècnica de Catalunya (Technical University of Catalonia BarcelonaTech). Senior researcher at the International Center for Numerical Methods in Engineering (CIMNE).
- **A. E. Huespe**: Professor of Mechanics at the Faculty of Chemical Engineering, Dept. of Materials, National University of Litoral, Santa Fe, Argentina. Independent researcher of Conicet at CIMEC (Centro de Investigaciones en Mecánica Computacional), National University of Litoral (UNL).
- **O. Lloberas-Valls**: Postdoctoral researcher at the International Center for Numerical Methods in Engineering (CIMNE).

Key Engineering Materials Vol. 713
Advances in Fracture and Damage Mechanics XV
Editors: Jesús Toribio, Vladislav Mantic, Andrés Sáez, M.H. Ferri Aliabadi
ISSN: 1662-9795
Trans Tech Publications
DOI: 10.4028/www.scientific.net/KEM.713.248

Model Order Reduction in computational multiscale fracture mechanics

M. Caicedo[1,a], J. Oliver[1,b], A.E. Huespe[2,c], O. Lloberas-Valls[1,d]

[1] E.T.S. d'Enginyers de Camins, Canals i Ports, Technical University of Catalonia (BarcelonaTech)/International Center for Numerical Methods in Engineering (CIMNE) Campus Nord UPC, Edifici C-1, c/ Jordi Girona 1-3, 08034 Barcelona, SPAIN.

[2] CIMEC-UNL-CONICET, Gemes 3450, Santa Fe, Argentina.

[a]mcaicedo@cimne.upc.edu,[b]oliver@cimne.upc.edu,[c]ahuespe@intec.unl.edu.ar,[d]olloberas@cimne.upc.edu

Keywords: Model Order Reduction, Reduced-Order Cubature, Fracture, Computational Multi-scale modeling, Continuum Strong Discontinuituy Approach.

Abstract. Nowadays, the model order reduction techniques have become an intensive research field because of the increasing interest in the computational modeling of complex phenomena in multi-physic problems, and its consequent increment in high-computing demanding processes; it is well known that the availability of high-performance computing capacity is, in most of cases limited, therefore, the *model order reduction* becomes a novelty tool to overcome this paradigm, that represents an immediately challenge in our research community. In computational multiscale modeling for instance, in order to study the interaction between components, a different numerical model has to be solved in each scale, this feature increases radically the computational cost. We present a reduced model based on a multi-scale framework for numerical modeling of the structural failure of heterogeneous quasi-brittle materials using the Strong Discontinuity Approach (CSD). The model is assessed by application to cementitious materials. The *Proper Orthogonal Decomposition* (POD) and the *Reduced Order Integration Cubature* are the proposed techniques to develop the reduced model, these two techniques work together to reduce both, the complexity and computational time of the *high-fidelity* model, in our case the FE^2 standard model.

1 Introduction

The present model departs from the multiscale framework developed in [2] for the numerical modeling of failure via hierarchical multi-scale models, taking advantage of the reduced order techniques developed in [1], the theoretical framework used in this work is based on the so-called (FE^2) methods via *first order computational homogenization* for the coupling between scales, in which homogenized quantities at the lower scale, represented by a so-called failure-cell, are therefore transferred, in a one-way fashion, to material points (Gauss points) of the macroscopic structure. The formulation is presented in terms of strains in a non-conventional format imposing the *natural* multiscale boundary conditions via Lagrange multipliers.

This work attempts to solve the problematic of excessive computational time in multi-scale models, in our case an additional complexity is induced by the discontinuous displacement field produced by the strain localization at both scales. Nonetheless, the methodology can also be straightforward extended to problems with continuous fields.

2 Model description

2.1 Generalities of the FE^2 method applied to multiscale fracture problems

This approach is developed under a small strain framework, the equality of internal power at both scales is guaranteed via *Hill-Mandell Macro-Homogeneity principle*. In virtue of the finite element method, the dissipative processes that occur at the meso-scale are modeled using *cohesive bands*, represented by quadrilateral elements endowed with a regularized continuum damage model. These bands are characterized by a *high aspect ratio* (width smaller than its length and, in turn, that width being much thinner than the representative cell dimensions). In addition, scattered within the matrix, the aggregates and the interfaces between them are also included. In this way, they can model a set of predefined crack patterns including several mechanisms such as percolation of the crack through the matrix (necessary for softening behavior), mortar/aggregate decohesion and rupture between aggregates. Depending on the loading process at the large scale, these crack patterns are loading and unloading until the full consolidation, finally, a dominant mechanism naturally prevails, thus representing the final pattern of the micro-crack. This mechanism is now referred to as *mesoscopic failure mechanism*. That mechanism has several features, its form and orientation will be as precise as the richness of the lower scale, and is closely related to the crack orientation obtained at the large scale.

In this approach, the macroscopic constitutive response is proven to be point-wise equivalent to an inelastic law (in an incremental fashion) as a function of the homogenized elastic tangent tensor, $\mathbf{C}^{hom}$, and the incremental homogenized inelastic strain rate $\dot{\boldsymbol{\varepsilon}}^{(i)}$ i.e.:

$$\dot{\boldsymbol{\sigma}} = \mathbf{C}^{hom} : (\dot{\boldsymbol{\varepsilon}}(x) - \dot{\boldsymbol{\varepsilon}}^{(i)}) \qquad \dot{\boldsymbol{\varepsilon}}^{(i)} = \frac{1}{l_\mu}(\mathbf{n} \otimes \dot{\boldsymbol{\beta}}) \tag{1}$$

Where, the inelastic strain component $\dot{\boldsymbol{\varepsilon}}^{(i)}$ is expressed as a function of the homogenized variables taken from the lower scale, and represent the average value of the symmetrical tensor product between the strong discontinuity normal $\mathbf{n}$, and the rate of displacement jump $\dot{\boldsymbol{\beta}}$ of each cohesive band, belonging to the manifold of the mesoscopic failure mechanism $\mathcal{S}_\mu$, i.e. the mesoscopic crack. In addition, the so-called *material characteristic length* l_μ is defined as the ratio between the measure (volume or area) of the representative volume and the measure (surface or length) of the mesoscopic failure mechanism. The equations that govern the lower scales are the next:

PROBLEM I: Given a macroscale strain $\boldsymbol{\varepsilon}$, Find $\tilde{\boldsymbol{u}}_\mu$ such that $\boldsymbol{\varepsilon}_\mu = \boldsymbol{\varepsilon} + \nabla^s \tilde{\boldsymbol{u}}_\mu$ and:

$$\int_{\mathcal{B}_\mu} \boldsymbol{\sigma}_\mu(\boldsymbol{\varepsilon}_\mu) : \nabla^s \tilde{\boldsymbol{u}}_\mu \, d\mathcal{B}_\mu = 0 \quad ; \forall \tilde{\boldsymbol{u}}_\mu \in \mathcal{V}_\mu^u := \{\tilde{\boldsymbol{u}}_\mu \quad | \quad \int_{\mathcal{B}_\mu} \nabla^s \tilde{\boldsymbol{u}}_\mu \, d\mathcal{B}_\mu = \mathbf{0}\}; \tag{2}$$

Regarding the large scale (macro-scale), it is modeled via the finite element method. The strain injection technique [3] is used in order to provide a robust and efficient model that can capture failure propagation even in high strain localization scenarios. In addition, the crucial matter of positioning strong discontinuities is tackled by a parallel technique termed *crack-path field*. This technique uses a directional derivative of a scalar field, based on a location variable (in our case, the average of mesoscale dissipated energy) whose zero level set defines the crack path.

2.2 Model Order Reduction techniques

The reduction process is divided into two sequential stages. The first stage consists of a common Galerkin projection, via *Proper Orthogonal Decomposition* POD for the meso-scale strain field, onto a small space (*reduced-order space*). For the second stage, the main goal is to reduce the number of integration points given by the standard Gauss quadrature, by defining a new scheme that efficiently determines optimal points and its corresponding weights so that the error in the integration of the reduced model is minimized (*Reduced Order Cubature* - ROC).
In order to provide the reduced model with the input parameters and entities, the general procedure is also divided into two parts, the first one (*offline part*) in which the projection operators for the meso-scale strain field and the parameters of the new integration cubature are computed. These data, together with the material and geometrical parameters, define the set of input parameters for the first and second stage (online part).
By comparison with the standard (FE^2) scheme, the proposed model in (2) can be redefined in term of strains in a generalized fashion, imposing the kinematic constraint (2-b) in an explicit way via Lagrange multipliers.

PROBLEM IB: Given a macro-scale strain $\boldsymbol{\varepsilon}$, find $\tilde{\boldsymbol{\varepsilon}}_\mu$ and $\boldsymbol{\lambda}$ satisfying:

$$(\tilde{\boldsymbol{\varepsilon}}_\mu(\boldsymbol{\varepsilon}, d_\mu), \boldsymbol{\lambda}(\boldsymbol{\varepsilon}, d_\mu)) = \arg\{\min_{\tilde{\boldsymbol{\varepsilon}}_\mu} \max_{\boldsymbol{\lambda}} \Pi(\tilde{\boldsymbol{\varepsilon}}_\mu, \boldsymbol{\lambda})\}; \quad \text{such that} \quad \dot{d}_\mu(\boldsymbol{y}, \boldsymbol{\varepsilon}_\mu) = g(\boldsymbol{\varepsilon}_\mu, d_\mu) \tag{3}$$

Where Π is the homogenized potential of energy in the meso-scale, expressed in the following way:

$$\Pi(\tilde{\boldsymbol{\varepsilon}}_\mu, \boldsymbol{\lambda}) = \int_{\mathcal{B}_\mu} \psi_\mu(\tilde{\boldsymbol{\varepsilon}}_\mu) \, d\mathcal{B}_\mu + \boldsymbol{\lambda} \int_{\mathcal{B}_\mu} \tilde{\boldsymbol{\varepsilon}}_\mu \, d\mathcal{B}_\mu \qquad \psi_\mu(\tilde{\boldsymbol{\varepsilon}}_\mu) = \frac{1}{2}(1 - d_\mu)(\boldsymbol{\varepsilon} + \tilde{\boldsymbol{\varepsilon}}_\mu) \cdot \mathbb{C}_\mu^{el} \cdot (\boldsymbol{\varepsilon} + \tilde{\boldsymbol{\varepsilon}}_\mu) \tag{4}$$

Being ψ_μ, d_μ and $\mathbb{C}_\mu^{el}$ the internal energy, the damage internal variable and the elastic constitutive tensor at each point $\boldsymbol{y}$ in the meso-scale, respectively.

2.2.1 Projection of strain field via POD

The reduction of the meso-scale strain field is based on the projection of the weak form of the discrete mechanical problem into a reduced *manifold* (reduced-order space), this reduced space is spanned by Ritz (globally supported) basis functions obtained via *Singular Value Decomposition* (SVD) of a set of *snapshots* taken from *training tests* computed during the offline part. Following this reasoning, the meso-scale strain fluctuation can be expressed as:

$$\tilde{\boldsymbol{\varepsilon}}_\mu(\boldsymbol{y}, t) = \sum_{i=1}^{n_{\boldsymbol{\varepsilon}}} \boldsymbol{\Phi}_i(\boldsymbol{y}) c_i(t) = \boldsymbol{\Phi}(\boldsymbol{y}) \boldsymbol{c}(t) \tag{5}$$

Where $\boldsymbol{c}(t) = \{c_1, c_2, c_3, \ldots, c_{n_{\boldsymbol{\varepsilon}}}\}$ is time dependent ($\boldsymbol{c} \in \mathbb{R}^{n_{\boldsymbol{\varepsilon}}}$) and represents the amplitude of the corresponding meso-scale strain mode updated during the online part. Now, introducing (5) and (4) into the **PROBLEM IB** and, after some straightforward manipulations, results into a new model written in terms of the reduced basis:

PROBLEM II: Given a macro-scale strain $\boldsymbol{\varepsilon}$, find $\boldsymbol{c} \in \mathbb{R}^{n_{\boldsymbol{\varepsilon}}}$ satisfying:

$$\int_{\mathcal{B}_\mu} \boldsymbol{\Phi}^T [\boldsymbol{\sigma}_\mu(\boldsymbol{\varepsilon} + \boldsymbol{\Phi}\boldsymbol{c}) + \boldsymbol{\lambda}] \, d\mathcal{B}_\mu = \mathbf{0}; \quad \text{tal que} \quad \int_{\mathcal{B}_\mu} \boldsymbol{\Phi}(\boldsymbol{y}) \, \boldsymbol{c}(t) \, d\mathcal{B}_\mu = \mathbf{0}; \tag{6}$$

Solving the system of equations (6) for $\boldsymbol{c}$ and $\boldsymbol{\lambda}$ (Lagrange multiplier to ensure the equality of internal power at both scales via Hill-Mandel Macro-Homogeneity principle), it can be immediately noticed that this problem with $n_{\boldsymbol{\varepsilon}}+n_{\sigma}$ equations will be cheaper, (in computational cost terms), than the standard (FE^2) framework. However, the matricial form of **PROBLEM II** has to be computed (in a standard way) prior its projection onto the reduced-order space. This fact highlights that the actual bottleneck for fast online computation is not the solution of the discrete balance equations but, rather, the determination of the stresses, internal forces and stiffness matrices at all the integration points of the underlyung finite element mesh and its posterior projection. Alternatively, this approach proposes a second stage based on the **PROBLEM II**, that intends to reduce the amount of integration points in which the constitutive equation is computed.

2.2.2 Hyper-reduced model

As pointed out in the previous section, the next objective is to introduce an additional reduction step to diminish the computational burden for equation (6-a). In addition, in order to guarantee the good performance for the second stage, all possible operators have to be computed during the offline part. Particularly, the term (6-b) can be computed entirely in the offline part. To persue the main objective of the second stage, we develop a *Hyperreduced Order Model* (HPROM) via Reduced Optimized Cubature (ROC), this technique is based on a discrete minimization problem that allows determining the optimized location of integration points and the corresponding weights. Once these positions and weigths are at one's disposal, the equation (6-a) can be easily determined as:

$$\int_{\mathcal{B}_\mu} \boldsymbol{\Phi}^T [\boldsymbol{\sigma}_\mu(\varepsilon + \boldsymbol{\Phi}\boldsymbol{c})]\, d\mathcal{B}_\mu \approx \sum_{j=1}^{n_r} (\Phi(\boldsymbol{z}_j)^T \boldsymbol{\sigma}_\mu(\boldsymbol{z}_j, \boldsymbol{c}))\, \omega_j \tag{7}$$

The success of our proposed scheme, relies on the fact that it is possible to find a set of integration points n_r, substantially smaller than the ones given by the Gauss standard quadrature, minimizing the error in the assessment of (6). Introducing the expression (7) into the **PROBLEM II**, we get:

PROBLEM III: Given the macro-scale strain $\boldsymbol{\varepsilon}$, find $\boldsymbol{c} \in \mathbb{R}^{n_{\boldsymbol{\varepsilon}}}$ satisfying:

$$\sum_{j=1}^{n_r} (\boldsymbol{\Phi}(\boldsymbol{z}_j)^T \boldsymbol{\sigma}_\mu(\boldsymbol{z}_j, \boldsymbol{c}))\, \omega_j + \int_{\mathcal{B}_\mu} \boldsymbol{\Phi}^T \boldsymbol{\lambda}\, d\mathcal{B}_\mu = 0; \quad \text{tal que} \quad \int_{\mathcal{B}_\mu} \boldsymbol{\Phi}(\boldsymbol{y})\, \mathbf{c}(t)\, d\mathcal{B}_\mu = \mathbf{0}; \tag{8}$$

3 Numerical Results

3.1 Application to simulation of fracture in cementitious materials

The macro-scale will be splitted into two subdomains, the dark gray domain will be modeled using an elastic monoscale constitutive law, taking the elastic homogenized constitutive tangent tensor, and, in the green domain the Hiper-Reduced Order Model (HPROM). The finite element mesh of the meso-scale is also depicted in figure (1-b), where the morphology and the considered pattern of cohesive bands can be seen (in light green the aggregates, in pink the mortar matrix, in light gray the *intra-matrix* cohesive bands, and finally, in blue the interface *matrix/aggregate* cohesive bands). The mechanical behavior of the cohesive bands is modeled by a rate-independent continuum damage model endowed with a linear isotropic regularized softening, whose material properties have been taken from the experimental test in [4].

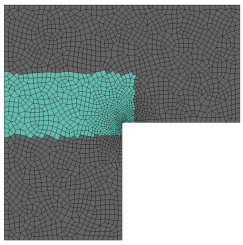

(a) Macroscale FE discretization

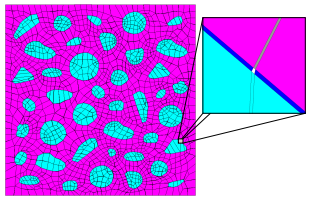

(b) Meso-scale FE discretization

Mortar Matrix			
Young modulus	E_m	[MPa]	18500
Poisson's ratio	ν_m	[-]	0.18
Tensile strength	$f_{t,m}$	[MPa]	2.60
Fracture energy	$G_{f,m}$	[N/m]	140
Aggregates			
Young modulus	E_a	[MPa]	37000
Poisson's ratio	ν_a	[-]	0.18

(Unger & Eckard 2011)

(c) Material properties

Figure 1: Finite element discretization and material properties

The figure (2-a) shows the structural response in terms of load-displacement ($\mathbf{P}-\delta$) curve (vertical load of the bottom, rightmost corner node versus displacement at the same place) for each set of strain modes $n_{\boldsymbol{\varepsilon}}$ and integration points n_r. It is shown the sensitivity in the convergence of the structural behavior as $n_{\boldsymbol{\varepsilon}}$ increases. As a consequence, the

amount of integration points will increase in order to guarantee the numerical stability and the exact integration of the scheme. For instance, with $n_{\boldsymbol{\varepsilon}} = 60$ and $n_r = 188$, we get a speed-up of 130 times with respect to the time consumed by the standard (FE^2) formulation. In this case the reduced model matches the peak load of the experimental test; however, the softening branch (post-peak behavior) is not as precise as expected, the improvement of this branch is achieved increasing the amount of strain modes in the online part.
Lastly, in figure (2-b) it can be observed the convergence results for the meso-scale tests using the Hiper-Reduced Order Model; fixing a number of strain modes $n_{\boldsymbol{\varepsilon}}$, we get an optimal number of integration points for the second stage, (with an error less than 5% in homogenized tractions for the CSDA taking as a reference the HF solution). In addition, it can be immediately noticed that, as the number of strain modes $n_{\boldsymbol{\varepsilon}}$ increases, the error decreases monotonically. However, the rate of decrement in the error is considerably smaller than the rate of increment of integration points, leading to an increment in the computational cost of the HPROM model, therefore, the imposition of a judicious equilibrium between error and number of integration points plays an important role in the good performance of our method, specially in low-performance computing platforms.

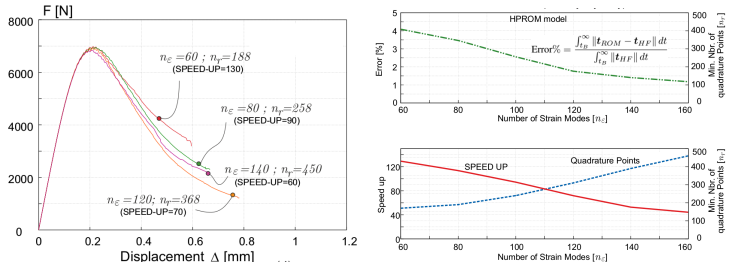

(a) Macro-structural response - L Shape Panel (b) Convergence analysis of the meso-scale

Figure 2: Convergence error in macro and meso scales

4 Conclusions

The result of this work is a reduced model based on a hierarchical (FE^2) multiscale approach for material failure in cementitious materials, that preserves all features of the standard FE model [2]. Furthermore, the two presented simulations show the convergence of the meso-scale and the sensitivity of the macro-structural behavior, as a function of the amount of strain modes, $n_{\boldsymbol{\varepsilon}}$, and the number of integration points, n_r. The reduced model solves the problem of unafordable computational cost widely known in multiscale hierachical (FE^2) approaches. This methodology can be straighforward extended to problems with smooth fields.

5 Acknowledgments

The research leading to these results has received funding from, on the one hand, the European Research Council under the European Union's Seventh Framework Program (FP/2007-2013) / ERC Grant Agreement n. 320815, Advanced Grant Project COMP-DES-MAT, and, on the other hand, the Spanish Ministry of Economy and Competitiveness through the National Research Plan 2014: MAT2014-60919-R. Oriol Lloberas-Valls gratefully acknowledges the funding received from the Spanish Ministry of Economy and Competitiveness through the "Juan de la Cierva" Postdoctoral Junior Grant: JCI-2012-13782 and the National Research Plan 2014: MAT2014-60919-R.

References

[1] J.A. Hernndez, J. Oliver, A.E. Huespe, M.A. Caicedo, and J.C. Cante. High-performance model reduction techniques in computational multiscale homogenization. *Computer Methods in Applied Mechanics and Engineering*, 276:149–189, 2014.

[2] J. Oliver, M. Caicedo, E. Roubin, A. E. Huespe, and J.A. Hernandez. Continuum approach to computational multi-scale modeling of propagating material failure. *Computer Methods in Applied Mechanics and Engineering*, 294:384–427, 2015.

[3] J. Oliver, I.F. Dias, and A.E. Huespe. Crack-path field and strain-injection techniques in computational modeling of propagating material failure. *Computer Methods in Applied Mechanics and Engineering*, 274:289–348, 2014.

[4] J. F. Unger and S. Eckardt. Multiscale modeling of concrete - from mesoscale to macroscale. *Archives of Computational Methods in Engineering*, 18:341–393, 2011.

B.7 Chapter in Book

Title: Multi-scale (FE^2) analysis of material failure in cement/aggregate-type composite structures
Authors:

- **J. Oliver**: Professor of Continuum Mechanics and Structural analysis at the Escola Tecnica Superior d'Enginyers de Camins, Canals i Ports (Civil Engineering School) of the Universitat Politècnica de Catalunya (Technical University of Catalonia BarcelonaTech). Senior researcher at the International Center for Numerical Methods in Engineering (CIMNE).
- **M. Caicedo**: PhD Candidate in Structural Analysis in UPC BarcelonaTech and International Center for Numerical Methods in Engineering (CIMNE).
- **A. E. Huespe**: Professor of Mechanics at the Faculty of Chemical Engineering, Dept. of Materials, National University of Litoral, Santa Fe, Argentina. Independent researcher of Conicet at CIMEC (Centro de Investigaciones en Mecánica Computacional), National University of Litoral (UNL).
- **E. Roubin**: Maître de conférence at the 3SR (Sols, Solides, Structures et Risques) and the IUT DGGC in Grenoble.
- **J. A. Hernández**: Assistant Professor of Structural Engineering and Strength of Materials at the School of Industrial and Aeronautic Engineering of Terrassa, of the Technical University of Catalonia. Senior researcher at the International Center for Numerical Methods in Engineering (CIMNE).

Computational Modelling of Concrete Structures
Proceedings of EURO–C 2014
Editors: N. Bićanić; H Mang; Gunther Meschke; Reneé de Borst
ISBN: 978-1-138-00145-9
Taylor & Francis Group: CRC Press–Balkema, 2014

Multi-scale (FE^2) analysis of material failure in cement/aggregate-type composite structures

J. Oliver, M. Caicedo, E. Roubin, J.A. Hernández
Technical University of Catalonia (UPC)/International Center for Numerical Methods in Engineering (CIMNE), Barcelona, Spain

A. Huespe
CIMEC-Universidad del Litoral (UNL), Santa Fe, Argentina

ABSTRACT: The work proposes a FE^2 multiscale approach to computational modeling of material failure in concrete-like structures, made of cement/aggregate-type composite materials. Keeping the approach in a classical homogenization setting, a multiscale model is proposed, which naturally provides a microscopic length-scale to be exported to the macrostructure. There, this length scale is used as regularization parameter in the context of the Continuum Strong Discontinuity Approach to material failure, and finite elements with embedded strong discontinuities (E-FEM). The resulting technique allows robust modeling of crack propagation at the structural scale, accounting for the mesostructure morphology, supplies proper energy dissipation and solutions independent of the finite element and RVE sizes. Application to a number of examples, in the range from light-aggregate concrete to regular concrete, shows the potentiality of the method.

1 INTRODUCTION

Two-scale computational modeling of materials is a subject of increasing interest in computational mechanics. When dealing with materials displaying a spatially smooth behavior there is wide consensus, and some suitable mechanical approaches to the problem are available in the literature. For instance, the so-called *FE^2 methods*, based on the hierarchical, bottom-up one-way coupled, description of the material using the finite element method in both scales, and computational homogenization procedures at the low scale, is nowadays one of the most popular approaches. At the heart of the direct computational homogenization procedure lies the notion of representative volume element (RVE) defined as the smallest possible region representative of the whole heterogeneous media on average.

Alternatively, two-scale computational modeling for *material failure analysis* is more controversial, and exhibits additional complexity. Either if *discrete approaches* (based on non-linear softening cohesive models), or *continuum approaches* (strain localization-based or regularized models) are used at the lower scale, the kinematic description of some, or both, scales cannot be considered smooth anymore, and the existence of the RVE can be questioned arguing that, in this case, the material loses the statistical homogeneity. A crucial consequence of this issue is the lack of objectivity of the results with respect to the size of the RVE. In (Nguyen et al., 2010) a recent attempt to overcome this flaw, for regularized non-local models, can be found.

This work is an attempt to address this issue in the setting of the Continuum Strong Discontinuity Approach (CSDA) to material failure, developed by the authors in the past (Oliver, 1995, Oliver et al., 2002). The essentials of the method are:

1) At the macroscopic level, material failure is captured via *strain-localization and finite elements with embedded regularized strong discontinuities.*

2) The microstructure of the smooth-strain part of the body is represented by a classical RVE, whose size is associated to standard statistic representativeness concepts.

3) A *failure-cell* at the microscopic scale, with the same size and topological properties than the RVE is associated to material points at the strain-localizing part of the microstructure. This failure-cell is enriched with appropriated material failure mechanisms with, apparently, no restriction on their type. Though, for the sake of simplicity, cohesive-bands with a predefined position have been used in this work, there is no "a priori" limitation on using more sophisticated material failure mechanisms, e.g. arbitrarily propagating cracks or strong discontinuities (Oliver, 1995, Armero and Garikipati, 1996,

Alfaiate et al., 2003). In contrast, this failure-cell is not claimed to be a RVE, in the sense of being statistically representative of any part of the macrostructure, although standard homogenization procedures are applied to it.

4) It is proven that homogenization of the RVE and failure-cell returns a macroscopic constitutive model (stress vs. strain) with the same format than classical inelastic-strain-based phenomenological models. A set of macroscopic inelastic-strain-like internal variables emerge naturally, whose evolution equation is ruled by the activation of material non-linearities and failure mechanisms at the failure-cell. In addition, a internal-length arises from that homogenization procedure, and it is naturally determined by the size of the chosen RVE and the amount of activated material failure mechanisms at the microstructure. This internal length is of the same order then the RVE and, determines the bandwidth of the macroscopic regularized strain-localization or displacement-discontinuity bands.

5) Based on this internal length, imported from the microstructure, the macrostructure is equipped with finite elements with embedded regularized strain-localization and displacement-discontinuities. Through this method, complete insensitivity of the structural response, with respect to the RVE size, and the macroscopic and microscopic finite element meshes is achieved, and material failure properties, like the fracture energy, are consistently up-scaled.

The mechanical derivation of the model is done in section 2, in section 3 the numerical aspects are presented and, in section 4, representative simulations are presented. Finally, section 5 is devoted to some concluding remarks.

2 MULTISCALE MODEL FOR FRACTURE

Let us consider the body $\mathcal{B}$, in Figure 1. At the macroscopic scale, the body is considered to exhibit strain-localization bands, with typical bandwidth h (very small in comparison with the dimensions of the macrostructure L, $h \ll L$), which, in turn, are h-regularizations of the discontinuities (cracks) observed at the macroscopic scale.

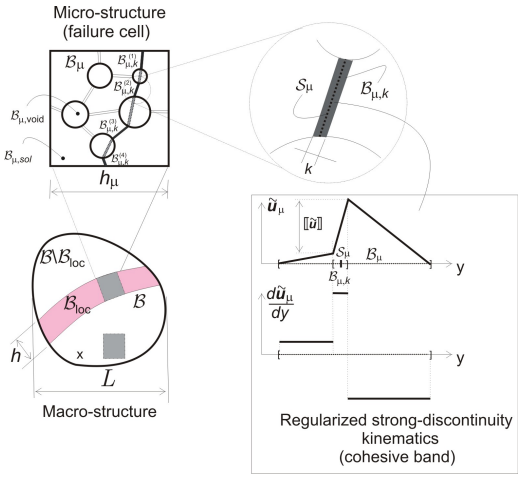

Figure 1. Multiscale failure model

2.1 *Microscopic scale: RVE/failure cell*

We assume microstructures characterized by a RVE/failure-cell like that shown in Figure 2, having cohesive bands, $\mathcal{B}_{\mu,k}$, of very small thickness ($k << h_\mu$) where the dissipative processes can take place and strain localizes.

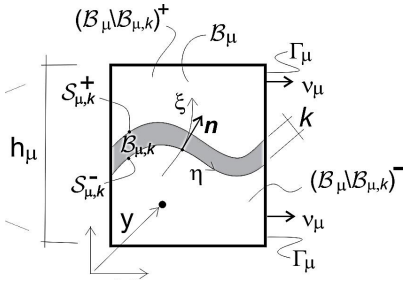

Figure 2. Multiscale model: microstructure with cohesive bands

2.1.1 *Kinematics: microscopic strain field*

Without loss of generality, we are considering cohesive bands of constant width k. Thus, we define the band length $meas(\mathcal{S}_\mu) = \mathcal{B}_{\mu,k} / k$. Then, we assume that: $meas(\mathcal{B}_{\mu,k}) << meas(\mathcal{B}_\mu)$. In $\mathcal{B}_\mu$, we define the microscopic displacement:

$$\mathbf{u}_\mu(\mathbf{y}) = \mathbf{u}(\mathbf{x}) + \varepsilon(\mathbf{x}) \cdot \mathbf{y} + \tilde{\mathbf{u}}_\mu(\mathbf{y}) \tag{1}$$

where, $\mathbf{u}(\mathbf{x})$ and $\varepsilon(\mathbf{x})$ are, respectively, the macroscopic displacement and strain of the point $\mathbf{x}$ in $\mathcal{B}$, respectively, and $\tilde{\mathbf{u}}_\mu$ is the microscopic displacement fluctuation that, for the cohesive bands is defined, in a local coordinate system (ξ, η) aligned with the band $\mathcal{B}_{\mu,k}$ (see Figure 2), as follows:

$$\tilde{\mathbf{u}}(\xi,\eta) = \hat{\tilde{\mathbf{u}}}(\xi,\eta) + H^k_{\mathcal{S}}(\xi)\, \beta(\eta) \tag{2}$$

In equation (2), the displacement $\hat{\mathbf{u}}$ is a smooth field (see Figure 3) whereas the second term of the RHS, is the k-regularized (k-ramp) function $H_{\mathcal{S}}(\xi(\mathbf{y}))$ given by the expressions:

$$H_{\mathcal{S}}(\xi(\mathbf{y})) = \begin{cases} 0 & \forall \quad \mathbf{y} \in (\mathcal{B}_\mu \setminus \mathcal{B}_{\mu,k})^- \\ 1 & \forall \quad \mathbf{y} \in (\mathcal{B}_\mu \setminus \mathcal{B}_{\mu,k}))^+ \\ \dfrac{\xi}{k} & \forall \quad \mathbf{y} \in \mathcal{B}_{\mu,k}) \end{cases}; \tag{3}$$

$$\boldsymbol{\beta}(\eta) \equiv \tilde{\mathbf{u}}_{\mathcal{B}_k^+}(\eta) - \tilde{\mathbf{u}}_{\mathcal{B}_k^-}(\eta).$$

where, $\boldsymbol{\beta}(\eta)$ is the displacement jump across the cohesive band. A sketch of the displacement fluctuation field along ξ is displayed in Figure 3.

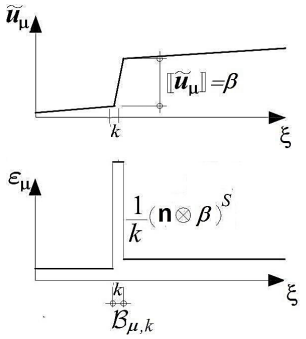

Figure 3. Multiscale model: micro-displacement fluctuations and micro-strains at the cohesive band

From equation (1), the micro strain $\boldsymbol{\varepsilon}_\mu$, assuming infinitesimal strain settings can be obtained as follows:

$$\boldsymbol{\varepsilon}_\mu(\mathbf{y}) = \nabla^s_{\mathbf{y}} \mathbf{u}_\mu = \boldsymbol{\varepsilon}(\mathbf{x}) + \tilde{\boldsymbol{\varepsilon}}_\mu(\mathbf{y}) = \boldsymbol{\varepsilon}(\mathbf{x}) + \nabla^s_{\mathbf{y}} \tilde{\mathbf{u}}_\mu(\mathbf{y}) \tag{4}$$

where $\tilde{\boldsymbol{\varepsilon}}_\mu$ is the micro strain fluctuation and supra-index $(\bullet)^s$ denotes the symmetric part of the corresponding tensor.

2.1.2 *Microscopic constitutive model*

The microstructure is considered constituted of a hardening material outside the cohesive bands, whereas this material exhibits strain-softening inside the bands. Then, the stress-strain relationship, in rate form, is given by:

$$\dot{\boldsymbol{\sigma}}_\mu(\mathbf{y}) = \begin{cases} \mathcal{C}_\mu^{hard} : \dot{\boldsymbol{\varepsilon}}_\mu(\mathbf{y}); & \forall\, \mathbf{y} \in \mathcal{B}_\mu \setminus \mathcal{B}_{\mu,k} \quad (a) \\ \mathcal{C}_\mu^{soft} : \dot{\boldsymbol{\varepsilon}}_\mu(\mathbf{y}); & \forall\, \mathbf{y} \in \mathcal{B}_{\mu,k} \quad (b) \end{cases} \tag{5}$$

where $\boldsymbol{\sigma}_\mu$ are the micro-stresses, and $\mathcal{C}_\mu^{hard}$ and $\mathcal{C}_\mu^{soft}$ are the microscopic tangent constitutive operators corresponding with the (rate) constitutive behavior at domains $\mathcal{B}_\mu \setminus \mathcal{B}_{\mu,k}$ and $\mathcal{B}_{\mu,k}$, respectively (see Figure 4). At $\mathcal{B}_\mu \setminus \mathcal{B}_{\mu,k}$, $\mathcal{C}_\mu^{hard}$ corresponds with a strain-hardening constitutive behavior, so that no strain localization can take place. At $\mathcal{B}_k$, $\mathcal{C}_\mu^{soft}$ defines a strain-softening model which gives raise to strain localization. From the Continuum Strong Discontinuity Approach (CSDA) (Oliver and Huespe, 2004b, Oliver and Huespe, 2004a)) it is well known that, as this strain localization takes place in the narrow bands of bandwidth k (the cohesive bands $\mathcal{B}_{\mu,k}$), regularization of the softening parameter as $H_\mu = k\bar{H}_\mu$; $\bar{H}_\mu = 1/2(\sigma_u^2)/(EG_\mu^f)$, G_μ^f standing for the microscopic fracture energy (see Figure 4), the continuum constitutive model in equation (5)-b, degenerates in an (implicit) traction-separation law, ruling the decohesion of the modeled discrete crack.

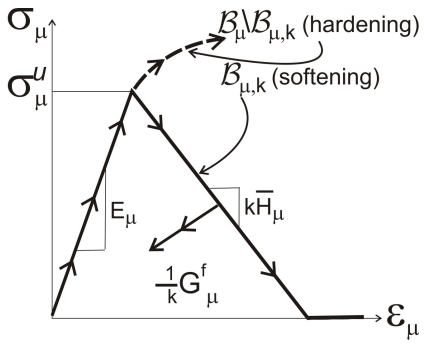

Figure 4. Constitutive model at the microstructure

2.2 *Computational homogenization elements*

Computational homogenization is based on standard procedures lying on the strain homogenization concept and the Mandell-Hill principle (de Souza Neto and Feijóo, 2006) as described next.

2.2.1 *Strain homogenization. Minimal kinematic restrictions*

The strain homogeneity condition requires that[1]:

$$\boldsymbol{\varepsilon}(\mathbf{x}) = \frac{1}{\mathcal{B}_\mu} \int_{\mathcal{B}_\mu} \boldsymbol{\varepsilon}_\mu \, d\mathcal{B}_\mu \tag{6}$$

and replacing (4) in (6), this equation results:

$$\boldsymbol{\varepsilon}(\mathbf{x}) = \boldsymbol{\varepsilon}(\mathbf{x}) + \frac{1}{\mathcal{B}_\mu} \int_{\mathcal{B}_\mu} \nabla^s \tilde{\mathbf{u}}_\mu \, d\mathcal{B}_\mu \tag{7}$$

which, in turn, yields:

$$\int_{\mathcal{B}_\mu} \nabla^s \tilde{\mathbf{u}}_\mu \, d\mathcal{B}_\mu = \int_{\Gamma_\mu} \big(\tilde{\mathbf{u}}_\mu \otimes^s \mathbf{v}_\mu\big) d\Gamma_\mu = \mathbf{0} \tag{8}$$

Thus, we define the space $\boldsymbol{V}_\mu$ of kinematically admissible displacements fluctuations at the micro-scale, as being:

$$\boldsymbol{V}_\mu := \{\tilde{\mathbf{u}}_\mu \quad | \quad \int_{\Gamma_\mu} \big(\tilde{\mathbf{u}}_\mu \otimes^s \mathbf{v}_\mu\big) d\Gamma_\mu = \mathbf{0}\}. \tag{9}$$

[1] From now on, and with some abuse of the notation, we will denote with the same symbol the *domain and its measure*, i.e.: $meas(\mathcal{B}_\mu) \equiv \mathcal{B}_\mu$.

Then, all micro displacement fluctuations: $\tilde{\mathbf{u}}_\mu \in \boldsymbol{V}_\mu$ should be compatible with micro strain fluctuations satisfying the homogeneity condition.

2.2.2 *Hill-Mandel variational principle*

The Hill-Mandel principle equating the macroscopic point internal power and the average value of the microscopic internal power reads

$$\boldsymbol{\sigma}(\mathbf{x}) : \delta\boldsymbol{\varepsilon}(\mathbf{x}) = \frac{1}{\mathcal{B}_\mu}\int_{\mathcal{B}_\mu} \boldsymbol{\sigma}(\mathbf{y}) : \delta\boldsymbol{\varepsilon}_\mu(\mathbf{y}) d\mathcal{B}_\mu = \\ = \frac{1}{\mathcal{B}_\mu}\int_{\mathcal{B}_\mu} \boldsymbol{\sigma}(\mathbf{y}) : (\delta\boldsymbol{\varepsilon}(\mathbf{x}) + \nabla^s_{\mathbf{y}}\delta\tilde{\mathbf{u}}_\mu(\mathbf{y})) d\mathcal{B}_\mu \\ \forall\, \delta\boldsymbol{\varepsilon}, \delta\tilde{\mathbf{u}}_\mu \in \boldsymbol{V}_\mu. \tag{10}$$

Replacement of the appropriate values of $\delta\boldsymbol{\varepsilon}, \delta\tilde{\mathbf{u}}_\mu$ in equation (9) returns the classical strain homogenization principle

$$\boldsymbol{\sigma}(\mathbf{x}) = \frac{1}{\mathcal{B}_\mu}\int_{\mathcal{B}_\mu} \boldsymbol{\sigma}_\mu d\mathcal{B}_\mu\,. \tag{11}$$

which supplies the homogenized macro stresses, $\boldsymbol{\sigma}(\mathbf{x})$, and the RVE virtual work principle (de Souza Neto and Feijóo, 2006)

$$\int_{\mathcal{B}_\mu} \nabla^s\delta\tilde{\mathbf{u}}_\mu : \boldsymbol{\sigma}_\mu(\boldsymbol{\varepsilon} + \nabla^s_{\mathbf{y}}\tilde{\mathbf{u}}_\mu)\, d\mathcal{B}_\mu = 0 \\ \forall\, \delta\tilde{\mathbf{u}}_\mu \in \boldsymbol{V}_\mu \tag{12}$$

Equation (12) provides the solution for the micro-fluctuation field $\tilde{\mathbf{u}}_\mu$.

2.3 *Macroscopic scale: homogenized constitutive model*

Substitution of the solution $\tilde{\mathbf{u}}_\mu(\mathbf{y}, \boldsymbol{\varepsilon})$ of equation (12) into equation (11) yields the macroscopic constitutive equation, whose rate form reads

$$\dot{\boldsymbol{\sigma}}(\boldsymbol{\varepsilon}) = \frac{1}{\mathcal{B}_\mu}\int_{\mathcal{B}_\mu} \dot{\boldsymbol{\sigma}}_\mu(\boldsymbol{\varepsilon} + \nabla^s_{\mathbf{y}}\tilde{\mathbf{u}}_\mu(\mathbf{y}, \boldsymbol{\varepsilon}) d\mathcal{B}_\mu\,. \tag{13}$$

Then, algebraic elaboration on equation (13), considering equations (4) and (5), yields the following *macroscopic homogenized constitutive model*

$$\dot{\boldsymbol{\sigma}} = \boldsymbol{\mathcal{C}}^{\text{hom}} : (\dot{\boldsymbol{\varepsilon}}(\mathbf{x}) - \dot{\boldsymbol{\varepsilon}}^{(i)}) \tag{14}$$

where $\boldsymbol{\mathcal{C}}^{\text{hom}}$ is the macroscopic homogenized value of the hardening constitutive operator $\boldsymbol{\mathcal{C}}_\mu^{hard}$ (de Souza Neto and Feijóo, 2006).

In equation (14) $\dot{\boldsymbol{\varepsilon}}^{(i)}$ are macroscopic internal variables, playing the role of inelastic strains, whose evolution is described in terms of the micro-structural variables as

$$\dot{\boldsymbol{\varepsilon}}^{(i)} = \frac{1}{l_\mu}\boldsymbol{\zeta} = \frac{1}{l_\mu}\overline{\left(\mathbf{n} \otimes^s \dot{\boldsymbol{\beta}}\right)}_{\mathcal{S}_k} \tag{15}$$

i.e.: in terms of the activated failure mechanism and the band opening process at the microscale. In equation (15) notation $(\cdot)_{\mathcal{S}_k}$ stands for the mean value of $(\cdot)$ along the microscopic activated failure mechanism, i.e.:

$$\overline{\left(\mathbf{n} \otimes^s \dot{\boldsymbol{\beta}}\right)^S}_{\mathcal{S}_k} = \frac{1}{\mathcal{S}_k}\int_{\mathcal{S}_k}\left(\mathbf{n} \otimes^s \dot{\boldsymbol{\beta}}\right)^S d\mathcal{S} \tag{16}$$

In addition, the evolution equation (15) incorporates the microscale length l_μ, defined as:

$$l_\mu = \frac{\mathcal{B}_\mu}{\mathcal{S}_k} = \mathcal{O}(h_\mu) \tag{17}$$

In summary, in the context of the description of complex materials equipped with morphological descriptors (Oliver et al., 2012, Huespe et al., 2013) equations (14) to (17) retrieve a *constitutive equation equipped with an internal length and with internal variables described by the microstructure behavior.*

3 NUMERICAL ASPECTS. FINITE ELEMENT MODEL

The multiscale formulation described above is implemented by means of a finite element model following the outlines given by the FE^2 technology (Özdemir et al., 2008). Accordingly, two finite element models are used, one for the macroscopic structure and another for the microstructure through a discretized RVE/failure-cell.

3.1 *RVE/failure-cell finite element model*

Standard quadrilateral finite elements are adopted for the numerical simulation of the RVE/failure-cell response. The cohesive bands, $\mathcal{B}_{k,\mu}$, are also modeled by quads of very small thickness ($k \ll h_\mu$) as shown in Figure 5. They are equipped with the constitutive models defined in Figure 4 and equation (5), so that only elements on the cohesive band can exhibit strain localization. The model is solved according with the RVE virtual work principle in equation (12).

Notice that the driving force (external action) for the equation solution is the macroscopic strain $\boldsymbol{\varepsilon}$ and no external force is explicitly applied.

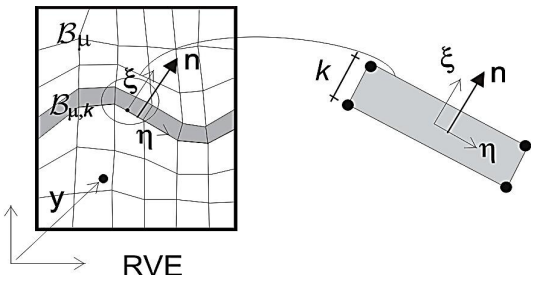

Figure 5. Micro-scale numerical model

The corresponding non-linear problem in the RVE/failure-cell is then solved for the micro-displacements fluctuation discretized as

$$\tilde{\mathbf{u}}_{\mu}(\mathbf{y},\boldsymbol{\varepsilon}) = \sum_{1}^{nnode} N_i(\mathbf{y})\mathbf{d}_{\mu,i}(\boldsymbol{\varepsilon}) \tag{18}$$

where $N_i(\mathbf{y})$ are the standard interpolation functions for quadrilaterals and $\mathbf{d}_{\mu,i}$ are the nodal values. Dirichlet boundary conditions precluding the rigid body motions and, in addition, the minimal boundary restriction in equations (9) are also imposed.

Then, material failure propagates naturally, as the softening behavior and, therefore, strain localization, is incepted in the finite elements defining the cohesive bands. At every time step of the analysis, those elements who are in in-loading state, define the active set of cohesive bands $\mathcal{B}_{\mu,k}$ (see Figure 5) or the *active failure mechanism.*

3.2 *Finite element model at the macro-structure. Material failure propagation.*

At the macroscopic scale, propagation of material failure is modeled using the *crack path field* and *strain injection* techniques recently developed by the authors (Oliver et al., 2014). They are based on using goal oriented assumed-strain fields injected in selected domains, via mixed formulations.

- In a ***first injection stage,*** embedded localization bands, of bandwidth l_{μ}, are incrementally injected (prior to development of displacement discontinuities) in an evolving subdomain of the macro-structure, $\mathcal{B}_{loc}$ (see Figure 6) were both the material discontinuous bifurcation (Willam and Sobh, 1987) an the in-loading conditions are fulfilled.

- These embedded localization bands have an isotropic character (there is no preferred direction in them), but exhibit extremely good ability to propagate material failure in the right material directions. Therefore, its evolving position and intensity is used to determine a scalar field (the crack propagation field) whose zero level set constitutes a reliable approximation to the actual crack path.

- In a ***second injection stage,*** the obtained crack path field, $\mathcal{S}$ (see Figure 6) is used to determine the correct position of an elemental embedded strong-discontinuity strain field, which is incrementally injected in the set of elements, $\mathcal{B}_{dis}$ (see Figure 6).

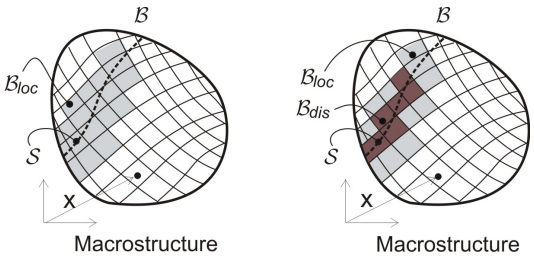

Figure 6. Strain injection procedures. Left: embedded strain localization bands injection in $\mathcal{B}_{loc}$. Right: embedded strong discontinuity injection in $\mathcal{B}_{dis}$

The resulting procedure is a robust and efficient technique to model propagating material failure in a finite element discretized body. Its intra-elemental character (one-element bandwidth band captures the regularized strain-localization) makes it especially appropriate for capturing material failure propagation in coarse meshes, in contraposition of the alternative extra elemental character techniques (e.g. phase field models) for capturing propagating material failure, where several elements have to span the localization band, this leading to, some-times unaffordably fine finite element meshes (B. Bourdin et al., 2000, Miehe et al., 2010). In addition, its implementation in an existing finite element code has a little invasive character.

4 REPRESENTATIVE SIMULATIONS. TWO-SCALE MODELING OF FAILURE PROPAGATION IN A CONCRETE-LIKE MATERIAL.

In order to explore the potential of the proposed formulation, numerical experimentation is performed on the basis of a material whose mesostructure mimics the cement-aggregate composition of concrete. This is not an attempt to obtain quantitative results, to fit some specific experiment, but, rather, to evaluate the potential of multiscale modeling, incorporating the microstructure morphology, in simulation of *complex macroscopic behavior using simple microscopic/mesoscopic models*. It should be mentioned that, unlike what is regularly done in the literature, the issue tackled here is not only modeling the macroscopic homogenized behavior at a single point of the macrostructure, but, also, *the full macroscopic structural behavior, including material failure onset and propagation* and obtaining a *complete action/response behavior during the structural failure*.

The strip in
Figure 7, incorporating a central opening to break the inhomogeneity, is subjected to horizontal stretch-

ing, induced by a constant displacement, Δ, under the action of the external force $\mathbf{F}$.

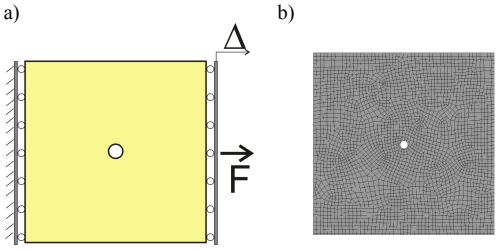

Figure 7. Strip with central opening under uniaxial stretching: a) macroscopic (structural) geometry. Dimensions (1m x1m). b) Finite element mesh (quadrilaterals)

The mesostructure morphology is sketched by the failure-cell of Figure 8 roughly characterized by some cylindrical aggregates of different sizes, immersed in a matrix of mortar. Grains and matrix are numerically modeled by quadrilateral finite elements. Additionally, the failure cell is equipped with a number of, very narrow, cohesive bands; some of them surrounding the aggregates (thus its failure representing possible aggregate/mortar decohesion) and some others crossing the matrix and connecting grains (its failure corresponding to mortar cracks).

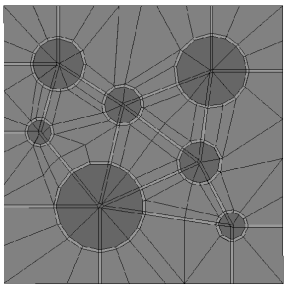

Figure 8. Strip with central opening under uniaxial stretching. 2D microscopic failure cell incorporating: a) cylindrical-shaped aggregates, immersed in a matrix and b) intra-granular, extra-granular and grain-matrix cohesive bands. Dimensions (1mm x 1mm)

Their activation allows modeling a number of failure mechanisms: those excluding the interior of the aggregates i.e.: *extra-granular failure mechanisms* or those including the grains breakage i.e.: *intra-granular failure mechanisms.*

Constitutive behavior at the matrix is assumed to be elastic; at the cohesive bands it is assumed to be ruled by a very simple model: the *only-tension-failure* constitutive model developed by the authors in the past (Oliver et al., 1990) that precludes inelastic behavior in pure compression stress states (see Figure 9).

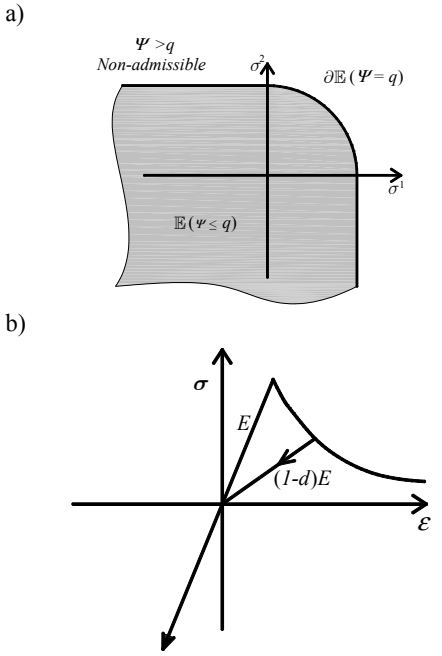

Figure 9. Only-tension-failure continuum damage model: a) elastic domain in the 2D principal stress, $\sigma^{(1)} - \sigma^{(2)}$, space, b) resulting uniaxial stress-strain constitutive model.

Then, three different types of concrete are analyzed, using the mesostructure in Figure 8, equipped with different material properties, i.e.:

- Regular-weight-aggregate (RWA) concrete: properties of matrix and aggregates are taken as those typically described in the literature for standard concrete.
- Light-weight-aggregate (LWA) concrete: properties of aggregates are taken as those typically described in the literature for light (ceramic) aggregates.
- Medium-weight-aggregate (MWA) concrete: aggregate properties are taken in between the other two cases.

The goal of the experiments is to observe how, for the same experiment, the mechanical properties of the aggregates affect the mesoscopic failure mechanism and, in turn, the macroscopic structural response.

4.1 *Regular weight aggregate (RWA) concrete modeling*

The mesostructure in Figure 8 is equipped with the material properties displayed in Table 1.

Table 1: Regular Weight Aggregate (RWA) concrete. Material properties at the mesoscopic level.

	Young modulus E	Poisson ratio ν	Ultimate stress σ_u	Fracture energy G_{μ}^{f}
Mortar (bulk)	20 Gpa	0.2	(elastic)	(elastic)
Mortar (cohesive bands)	20 Gpa	0.2	3.0 Mpa	700 J/m^2
Aggregates (bulk)	100 Gpa	0.2	(elastic)	(elastic)
Aggregates (cohesive bands)	100 Gpa	0.2	15.0 Mpa	3500 J/m^2

In Figure 10, qualitative results at the macroscopic level are presented.

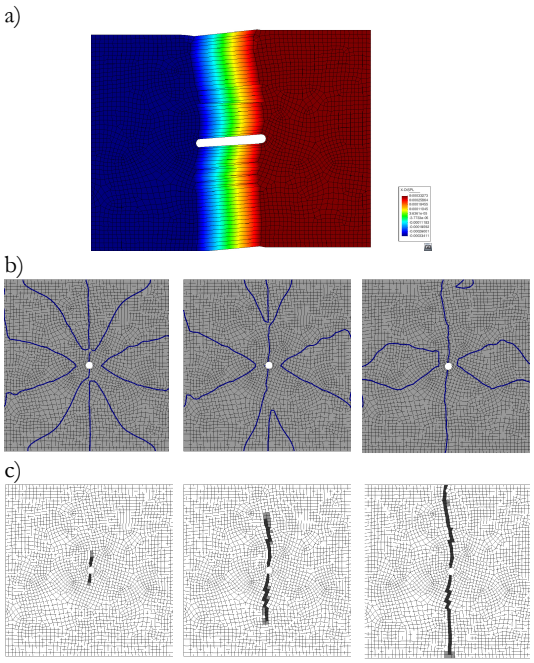

Figure 10 *Regular weight aggregate (RWA) concrete. Macroscopic results*. a) Deformed (amplified) shape showing the contours of horizontal displacements. b) Evolution, at sequential stages of the analysis, of the captured crack-path field. c) Evolution, at sequential stages of the analysis, of the strain injection pattern (darker zones correspond to strain-injected elements).

Those results show a macroscopic, approximately vertical, crack starting at the opening and exhibiting a mixed Mode I failure.

At the mesoscopic level, results for the deformation (fluctuations) of a typical failure-cell (nearby the opening in the macroscopic failure path) can be seen, conveniently amplified, in Figure 11. There it can be checked that, at an initial stage of the macroscopic localization, the failure-cell displays several (very small in amplitude) competing failure mechanisms (Figure 11-a)). Later on, an *extra-granular failure mechanism,* involving aggregate/matrix decohesion and mortar cracking, prevails (Figure 11-b)), characterizing the mesoscopic failure for this type of concrete.

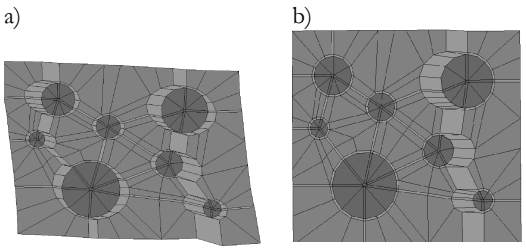

Figure 11. *Regular weight aggregate (RWA) concrete. Mesoscopic results*. Deformation of a typical failure cell displaying the failure modes: a) at the initiation of the macroscopic localization (amplification factor =1000), b) at the end of the loading process (amplification factor = 200).

In Figure 12 the evolution of the macroscopic energy along the process is presented. It can be noticed that the numerically observed dissipated energy computed as

$$E^{numerical} = \int_{t=0}^{t=\infty} \mathrm{F}(t) \cdot \dot{\Delta}(t) dt \qquad (19)$$

, where F and Δ are defined in Figure 7-a), see also Figure 16) matches very well the theoretical value computed as:

$$E^{theoretical} = L_{macro} G^{f}_{macro}$$

$$G^{f}_{macro} \equiv \overline{\left(G_{\mu}^{f}\right)}_{\mathcal{S}_{\mu}} = \frac{1}{\mathcal{S}_{\mu}} \int_{\mathcal{S}_{\mu}} G_{\mu}^{f}(\mathbf{y}) d\mathcal{S} \qquad (20)$$

i.e.: the length of the macroscopic crack, L_{macro}, times the macroscopic fracture energy G^{f}_{macro}. The theoretical value of G^{f}_{macro} is computed as the average, along the mesoscopic failure-cell failure path in Figure 11-b), of the mesoscopic fracture energy (G_{μ}^{f} in Table 1).

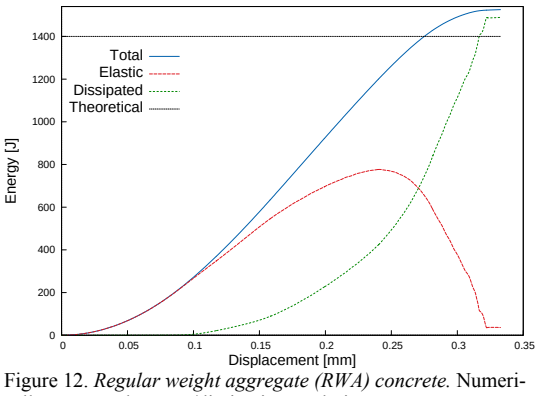

Figure 12. *Regular weight aggregate (RWA) concrete.* Numerically computed energy/dissipation evolution curves.

4.2 *Light weight aggregate (LWA) concrete modeling*

Now, light weight aggregate (LWA) concrete is considered. The material properties, for a ceramic-type aggregate are presented in Table 2.

Table 2: Light Weight Aggregate (LWA) concrete. Material properties at the mesoscopic level.

	Young modulus E	Poisson ratio ν	Ultimate stress σ_u	Fracture energy G_μ^f
Mortar (bulk)	28.6 Gpa	0.2	(elastic)	(elastic)
Mortar (cohesive bands)	28.6 Gpa	0.2	3.0 Mpa	700 J/m^2
Aggregates (bulk)	6.8 Gpa	0.2	(elastic)	(elastic)
Aggregates (cohesive bands)	6.8 Gpa	0.2	0.7 Mpa	166 J/m^2

Figure 13 displays a macroscopic failure mechanism fairly similar to the one in the previous (RWA) case.

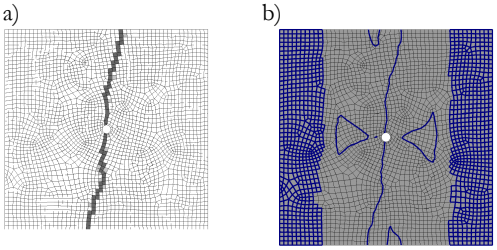

Figure 13 *Light-weight-aggregate (LWA) concrete. Macroscopic results*. a) strain injection pattern (darker zones correspond to strain-injected elements) at the end of the loading process, b) captured crack-path field.

However the mesoscopic failure mechanism is substantially different: the activated mechanism goes through the aggregates (see Figure 14-b), thus defining an intra-*granular failure mechanism*.

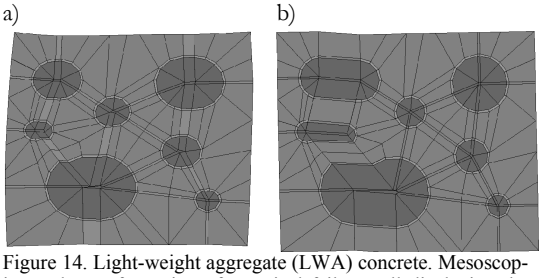

Figure 14. Light-weight aggregate (LWA) concrete. Mesoscopic results. Deformation of a typical failure cell displaying the failure modes: a) at the initiation of the macroscopic localization (amplification factor =1000), b) at the end of the loading process (amplification factor = 200).

As for the energy dissipation, in Figure 15 good agreement of the theoretical energy dissipation and the numerical one (computed according equation (19), see also Figure 16) is shown.

Notice that the energy dissipation of the process for this LWA concrete (850 J) is smaller than the one for NWA concrete in Figure 12 (1500 J). This is due to the fact that, in the present case, the mesoscopic failure mechanism, in Figure 14-b), crosses the (weaker) aggregates, which are endowed with a lower fracture energy (check G_μ^f in Table 2 versus Table 1). Therefore the macroscopic fracture energy, G_{macro}^f, in equation (20) is smaller .

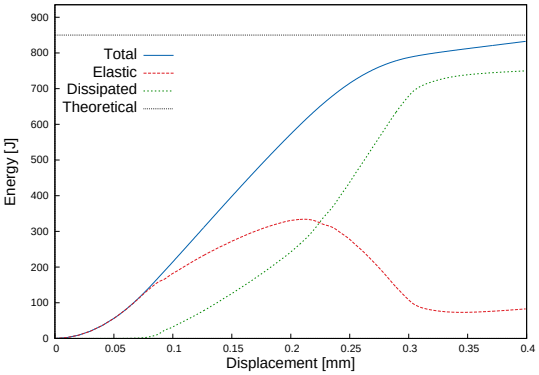

Figure 15. *Light-weight aggregate (LWA) concrete.* Numerically computed energy/dissipation evolution curves.

4.3 *Medium weight aggregate (MWA) concrete modeling*

As an intermediate case, the numerical experiment is repeated with the material properties presented in Table 3.

Table 3: Medium Weight Aggregate (MWA) concrete. Material properties at the mesoscopic level.

	Young modulus E	Poisson ratio ν	Ultimate stress σ_u	Fracture energy G_μ^f
Mortar (bulk)	28.6 Gpa	0.2	(elastic)	(elastic)
Mortar (cohesive bands)	28.6 Gpa	0.2	3.0 Mpa	700 J/m^2
Aggregates (bulk)	19.9 Gpa	0.2	(elastic)	(elastic)
Aggregates (cohesive bands)	19.9Gpa	0.2	2.1 Mpa	487 J/m^2

The macroscopic and mesoscopic failure mechanisms (not displayed) are similar to the ones, in Figure 10 and Figure 11, for RWA concrete. However, even if the qualitative effects of the different mesoscopic properties are not relevant, the quantitative structural response is very affected as it will be shown in next paragraph.

4.4 *Structural response*

Quantitative responses are now measured in terms of the force-displacement evolution curves, $F-\Delta$ in Figure 7-a), as shown in Figure 16.

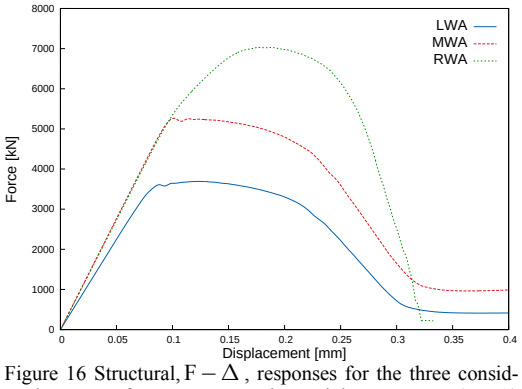

Figure 16 Structural, $F-\Delta$, responses for the three considered types of concrete. Regular weight aggregate (RWA) concrete, light weight aggregate (LWA) concrete and medium weight aggregate (MWA) concrete.

There it can be observed that:

- RWA concrete (regular concrete) behaves as observed in normal plain concrete. After an initial elastic branch, the structure exhibits some inelastic hardening and then fails abruptly (brittle failure).

- Introduction of light aggregate (MWA, LWA) concrete translates into substantial loss of the maximum carrying capacity but, also, in a more ductile failure: the non-linear hardening branch disappears and, immediately after the elastic branch, the structure softens in a smoother manner (ductile failure).

Both observations coincide with the expectations for this types of concrete.

5 CONCLUDING REMARKS

Along this work, multiscale (FE^2) techniques have been used to model material failure of concrete-like materials.

A computational homogenization setting has been proposed which, keeping the essentials of classical computational homogenization techniques, naturally introduces a length scale, related to the RVE size and the mesoscale failure mechanism, into the induced macroscopic homogenized model. This microscopic length scale can be interpreted as the actual width of the fracture process zone, defining the bandwidth of the macroscopic localization band that captures the crack at the structural level. It has been frequently claimed in modeling of concrete materials (Bazant and Jirásek, 2002) and it is automatically retrieved here through the homogenization process.

At the macroscopic scale, this microscopic length scale is locally used in the context of the Continuum Strong Discontinuity Approach to material failure (Oliver and Huespe, 2004a) , and introduced, as a regularization parameter, into a new technique (Oliver et al., 2014) for capturing the macroscopic propagation of cracks by means of finite elements with embedded discontinuities.

The result is a multiscale approach, that preserves the correct dissipation and objectivity, with respect both the macroscopic size of the finite element mesh and the size of the failure cell, which, in turn, can be readily connected with recent proposals for similar purposes (Sánchez et al., 2013).

Finally, the proposed techniques have been applied to modeling concrete like materials (i.e., materials that, at the mesoscopic level, are constituted by aggregates and mortar). Although the complexity of the mesoscale morphology is very limited by the computational cost of the combined multiscale computations, the potential of the approach is clearly stated by the presented examples.

ACKNOWLEDGMENT

The research leading to these results has received funding from the European Research Council under the European Union's Seventh Framework Programme (FP/2007-2013) / ERC Grant Agreement n. 320815, Advanced Grant Project COMP-DES-MAT.

REFERENCES

Alfaiate, J., Simone, A. & Sluys, L. J. 2003. Non-homogeneous displacement jumps in strong embedded discontinuities. *International Journal of Solids and Structures,* 40**,** 5799-5817.

Armero, F. & Garikipati, K. 1996. An analysis of strong discontinuities in multiplicative finite strain plasticity and their relation with the numerical simulation of strain localization in solids. *Int.J. Solids and Structures,* 33**,** 2863-2885.

B. Bourdin, Francfort, G. A. & J-J. Marigo 2000. Numerical experiments in revisited brittle fracture. *Journal of the Mechanics and Physics of Solids,,* 48**,** 797-826.

Bazant, Z. P. & Jirásek, M. 2002. Nonlocal Integral Formulations of Plasticity and Damage: Survey of Progress. *Journal of Engineering Mechanics,* 1119**,** 1125:1149.

De Souza Neto, E. A. & Feijóo, R. A. 2006. Variational foundations of multi-scale constitutive models of solid: small and large strain kinematical formulation. *LNCC Research & Development Report,* 16.

Huespe, A., Oliver, J. & Mora, D. 2013. Computational modeling of high performance steel fiber reinforced concrete using a micromorphic approach. *Computational Mechanics***,** 1-22.

Miehe, C., Welschinger, F. & Hofacker, M. 2010. Thermodynamically consistent phase-field models of fracture: Variational principles and multi-field FE implementations. *Int. J. Numer. Meth. Engng.,* 83.

Nguyen, V. P., Lloberas-Valls, O., Stroeven, M. & Sluys, L. J. 2010. On the existence of representative volumes for softening quasi-brittle materials-a failure zone averaging scheme. *Computer Methods in Applied Mechanics and Engineering*.

Oliver, J. 1995. Continuum modelling of strong discontinuities in solid mechanics using damage models. *Computational Mechanics,* 17**,** 49-61.

Oliver, J., Cervera, M., Oller, S. & Lubliner, J. Isotropic damage models and smeared crack analysis of concrete. *In:* AL., N. B. E., ed. Proc. SCI-C Computer Aided Analysis and Design of Concrete Structures, 1990. 945-957.

Oliver, J. & Huespe, A. E. 2004a. Continuum approach to material failure in strong discontinuity settings. *Computer Methods in Applied Mechanics and Engineering,* 193**,** 3195-3220.

Oliver, J. & Huespe, A. E. 2004b. Theoretical and computational issues in modelling material failure in strong discontinuity scenarios. *Computer Methods in Applied Mechanics and Engineering,* 193**,** 2987-3014.

Oliver, J., Huespe, A. E. & Dias, I. F. 2014. Crack-path field and strain-injection techniques in computational modeling of propagating material failure. *Comp. Meth. in Appl. Mech. and Eng.,* Submitted.

Oliver, J., Huespe, A. E., Pulido, M. D. G. & Chaves, E. 2002. From continuum mechanics to fracture mechanics: the strong discontinuity approach. *Engineering Fracture Mechanics,* 69**,** 113-136.

Oliver, J., Mora, D., Huespe, A. & Weyler, R. 2012. A micromorphic model for steel fiber reinforced concrete. *International Journal of Solids and Structures,* 49**,** 2990-3007.

Özdemir, I., Brekelmans, W. & Geers, M. 2008. FE2 computational homogenization for the thermo-mechanical analysis of heterogeneous solids. *Computer Methods in Applied Mechanics and Engineering,* 198**,** 602-613.

Sánchez, P. J., Blanco, P. J., Huespe, A. E. & Feijóo, R. A. 2013. Failure-Oriented Multi-scale Variational Formulation: Micro-structures with nucleation and evolution of softening bands. *Comput. Methods Appl. Mech. Engrg.,* 257**,** 221–247.

Willam, K. & Sobh, N. 1987. Bifurcation analysis of tangential material operators. *In:* PANDE, G. N. & MIDDLETON, J. (eds.) *Transient/Dynamic Analysis and Constitutive Laws for Engineering Materials.* Martinus-Nijhoff Publishers.

This Thesis focuses on the numerical modeling of fracture and its propagation in heterogeneous materials by means of hierarchical multiscale models based on the FE2 method, addressing at the same time, the problem of the excessive computational cost through the development, implementation and validation of a set of computational tools based on reduced order modeling techniques.

For fracture problems, a novel multiscale model for propagating fracture has been developed, implemented and validated. This multiscale model is characterized by the following features:

At the macroscale level, were adapted the last advances of the Continuum Strong Discontinuity Approach (CSDA), devising a new finite element exhibiting good ability to capture and model strain localization in bands which can be intersect the finite element in random directions. At the microscale level, the use of cohesive-band elements, endowed with a regularized isotropic continuum damage model aiming at representing the material decohesion, is proposed. These cohesive-band elements are distributed within the microscale components, and their boundaries.

For model order reduction purposes, the microscale Boundary Value Problem (VBP), is rephrased using Model Order Reduction techniques. The use of two subsequent reduction techniques, known as: Reduced Order Model (ROM) and HyPer Reduced Order Model (HPROM or HROM), respectively, is proposed.

First, the standard microscale finite element model High Fidelity (HF), is projected and solved in a low-dimensional space via Proper Orthogonal Decomposition (POD). Second, two techniques have been developed and studied for multiscale models, namely: a) interpolation methods, and b) Reduced Order Cubature (ROQ) methods (An/2009). The reduced bases for the projection of the primal variables, are computed by means of a judiciously training, defining a set of pre-defined training trajectories.

Taking into account the discontinuous pattern of the strain field in problems exhibiting softening behavior. A domain separation strategy, is proposed. A cohesive domain, which contains the cohesive elements, and the regular domain, composed by the remaining set of finite elements. Each domain has an individual treatment. The microscale Boundary Value Problem (BVP) is rephrased as a saddle-point problem which minimizes the potential of free-energy, subjected to constraints fulfilling the basic hypotheses of multiscale models.

UNIVERSITAT POLITÈCNICA
DE CATALUNYA

ESCOLA TÈCNICA SUPERIOR D'ENGINYERS
DE CAMINS, CANALS I PORTS
DEPARTAMENT DE RESISTÈNCIA DE
MATERIALS I ESTRUCTURES A L'ENGINYERIA